Study of B0 to D(*)0h0 Decay and Measurement of sin(2beta)

Marco Bomben

SLAC-R-863

Prepared for the Department of Energy
under contract number DE-AC02-76SF00515

Printed in the United States of America. Available from the National Technical Information Service, U.S. Department of Commerce, 5285 Port Royal Road, Springfield, VA 22161.

Università degli Studi di Trieste

Facoltà di Scienze Matematiche, Fisiche e Naturali
Dottorato di Ricerca in Fisica Sperimentale - FIS/01
XIX Ciclo di Dottorato (2004-2006)

Marco Bomben

Study of $B^0 \to \overline{D}^{(*)0} h^0$ decay and measurement of $\sin(2\beta)$

Advisor:
Chiar.mo Prof. Livio Lanceri

Coordinator:
Chiar.mo Prof. Gaetano Senatore

Referee:
Chiar.mo Prof. Giovanni Carboni

Study of $B^0 \to \overline{D}^{(*)0} h^0$ decay and measurement of $\sin(2\beta)$

Marco Bomben

April 2nd 2007

Ai miei amici...

"Forse un mattino andando in un'aria di vetro,
arida, rivolgendomi, vedrò compirsi il miracolo:
il nulla alle mie spalle, il vuoto dietro
di me, con un terrore di ubriaco.

Poi come s'uno schermo, s'accamperanno di gitto
alberi case colli per l'inganno consueto.
Ma sarà troppo tardi; ed io me n'andrò zitto
tra gli uomini che non si voltano, col mio segreto."

Eugenio Montale

Contents

Introduzione

Tra le caratteristiche piu' importanti nella descrizione dei fenomeni fisici vanno sicuramente menzionate le simmetrie.

Il teorema di Nöther [1] stabilisce che a ciascuna simmetria di trasformazioni continue è associata una quantità conservata. Ad esempio, la conservazione del momento angolare è una conseguenza dell'invarianza delle leggi fisiche per rotazioni.

Oltre alle trasformazioni continue, esistono tre importanti transformazioni discrete:

- l'inversione temporale, T, che cambia il segno della coordinata temporale ($t \to -t$) nelle equazioni del moto;
- l'operazione di parità, P, che inverte le coordinate spaziali ($\vec{x} \to -\vec{x}$) di una particella;
- la coniugazione di carica, C, che trasforma ciascuna particella nella sua antiparticella, cambiando segno alla sua carica elettrica e ad altri numeri quantici, lasciando invariate le coordinate spazio-temporali

La meccanica classica e l'elettrodinamica sono invarianti sotto l'effetto di T e P. Intuitivamente ci si aspetterebbe che le interazioni tra particelle elementari fossero invarianti per effetto delle stesse trasformazioni. Invece, la violazione di P-parità fu scoperta nel 1957 da C. Wu *et al.* nel decadimento dei nuclei ^{60}Co [3]. Inoltre, lo studio dei neutrini rivela che i neutrini sono sempre levogiri (lo spin $\vec{s}$ è anti-parallelo al momento $\vec{p}$). Il fatto che neutrini destrogiri e antineutrini levogiri non siano stati osservati in natura è una chiara violazione della simmetria per coniugazione di carica C. Una prima misura dell'elicità dei neutrini si deve a M. Goldhaber *et al.* [4] nel 1958.

Si pensò che la trasformazione combinata di C e P fosse una simmetria delle interazioni fondamentali, ma si trovò che la simmetria CP era violata nel decadimento dei mesoni K; l'esperimento decisivo, nel 1964 si deve a J. Christenson, J. Cronin, V. Fitch e R. Turlay che osservarono l'esistenza della asimmetria CP nel decadimento $K^0_L \to \pi\pi$ [5].

In tempi recenti, la misura di asimmetria CP agli esperimenti *BABAR* [6] e BELLE [7] ha dimostrato la presenza dell'effetto anche nei decadimenti dei mesoni B.

Le asimmetrie osservate sono inquadrabili nell'ambito del Modello Standard [8] delle interazioni delle particelle elementari. Le interazioni di corrente carica tra *quark* sono descritte da una matrice unitaria a termini complessi; i suoi termini possono essere parametrizzati da tre parametri reali e una fase ineliminabile; quest'ultima è l'unica sorgente dell'asimmetria CP prevista dal Modello Standard. La verifica di questa predizione è al momento uno dei test cruciali della fisica delle particelle elementari.

La violazione della simmetria CP è argomento di rilievo anche per le moderne teorie cosomologiche. Secondo queste teorie, eguali quantità di materia e antimateria erano presenti nell'Universo primordiale dopo il Big Bang. Ma ora, invece, l'Universo appare essere composto principalmente di materia e radiazione. Nella nostra galassia, ad esempio, i nuclei contenuti nella radiazione cosmica primaria che osserviamo sono composti in maggioranza di particelle piuttosto che di antiparticelle [9]. Grandi ammassi di antimateria risulterebbero visibili dalle emissioni di fotoni provenienti dalle annichilazioni

con la materia cosmica. Fenomeni simili non sono stati ancora osservati. L'esistenza della asimmetria *CP*, secondo Sakharov [11], è uno degli ingredienti necessari per spiegare l'abbondanza osservata di materia nell'Universo attuale. L'effetto della differenza di interazione tra materia e antimateria dovuto alla violazione della simmetria *CP* fornisce un meccanismo quindi per generare la asimmetria osservata tra materia e antimateria. Le misure odierne indicano però che l'effetto della violazione di *CP* nel Modello Standard non è sufficiente per spiegare la asimmetria osservata tra materia e antimateria. Infatti l'effetto previsto dal Modello Standard è di gran lunga inferiore a quello necessario per produrre l'asimmetria osservata. Questa inconsistenza spinge a verificare origine ed effetti della violazione di *CP* nelle interazioni fondamentali. Alcune teorie che estendono il Modello Standard forniscono in generale diverse spiegazioni della violazione di *CP*; le loro predizioni differiscono da quelle del Modello Standard stesso e possono essere quindi messe alla prova mediante esperimenti: la misura di asimmetrie nei decadimenti dei mesoni B, potrà fornire indicazioni al riguardo.

Questa tesi descrive la misura di asimmetria *CP* nei decadimenti dei mesoni B neutri, $B^0 \to \overline{D}^{(*)0} h^0$, dove $\overline{D}^{(*)0}$ è un mesone con "charm" e h^0 è un mesone leggero (π^0, η, η' o ω), utilizzando dati registrati dall'esperimento *BABAR* al collisionatore PEP-II presso lo Stanford Linear Accelerator Center (SLAC); in tale acceleratore elettroni e positroni collidono con energie diverse in modo da rendere possibile lo studio della asimmetria *CP*.

Nei decadimenti dei mesoni B neutri in stati finali accessibili sia da B^0 che da $\overline{B}^0$, l'interferenza tra l'ampiezza di decadimento e quella di oscillazione tra B^0 e $\overline{B}^0$ si può tradurre in violazione della simmetria *CP*, come risultato di una fase relativa tra le ampiezze.

Se il mesone D^0 ($\overline{D}^0$) decade in un autostato dell'operatore *CP*, sia mesoni B^0 che $\overline{B}^0$ possono contribuire allo stato finale, dando luogo ai fenomeni di interferenza appena citati che possono che possono risultare in asimmetria *CP*.

Risulta interessante misurare la asimmetria di *CP* nel decadimento $B^0 \to \overline{D}^{(*)0} h^0$ in quanto le incertezze teoriche nell'ambito del Modello Standard sono ben conosciute, siccome i contributi successivi all'ampiezza dominante sono soppressi [12]. L'eventuale osservazione di una sensibile differenza da quanto previsto dal Modello Standard per la violazione di *CP* in questo decadimento darebbe modo di sondare possibili contributi di nuova fisica.

Il Capitolo 1 è dedicato ad una introduzione alla fisica dei mesoni B, della violazione della simmetria *CP* e del processo $B^0 \to \overline{D}^{(*)0} h^0$. Nel Capitolo 2 viene descritto il rivelatore *BABAR*. Il Capitolo 3 è dedicato ai criteri di selezione del cananle $B^0 \to \overline{D}^{(*)0} h^0$ nel Capitolo 4 invece è descritto il fit dell'asimmetria dipendente dal tempo fit. Nel Capitolo 5 è presentato il fit ai dati e i risultati ottenuti. Infine, vengono discussi i resultati e loro possibili interpretazioni nel Capitolo 5.9.

Introduction

Symmetries are among the most important features in the description of physics phenomena. Nöther's theorem [1] states that for each symmetry of a continuous transformation of a theory, there is an associated conserved quantity. For example, the conservation of angular momentum is a consequence of the invariance of physical laws under rotations.

In addition to continuous transformations, there exist three important discrete transformations:

- *Time reversal*, T, that changes the sign of the time coordinate ($t \rightarrow -t$) in equations of motion;
- *Parity*, P, that inverts the space coordinates ($\vec{x} \rightarrow -\vec{x}$) of a particle;
- *Charge conjugation*, C, that transforms each particle to its antiparticle by changing its electrical charge and other *quantum numbers*, but leaves its space-time coordinates unchanged.

Classical mechanics and electrodynamics are invariant under T and P transformations. Naively, one would expect all fundamental particle interactions to obey the same symmetries. However, P violation was discovered in 1957 by C. Wu *et al.* in the decays of ^{60}Co nuclei [3]. Further, the study of neutrinos reveals that neutrinos are always left-handed (its spin $\vec{s}$ anti-parallel to momentum $\vec{p}$). The fact that right-handed neutrinos and left-handed anti-neutrinos do not exist in nature is a clear violation of C. A measurement of neutrino helicity was demonstrated first in 1958 by M. Goldhaber *et al.* [4].

Even the combined transformation of C and P, that was thought to be a symmetry of all particle interactions, was found to be violated in the decays of kaons. In 1964, J. Christenson, J. Cronin, V. Fitch and R. Turlay discovered the existence of *CP* asymmetries in the decay $K_L^0 \rightarrow \pi\pi$ [5].

More recently, measurements of *CP* asymmetries by the *BABAR* [6] and BELLE [7] collaborations established this effect in the decays of B mesons.

These small symmetry violations, however, can be accounted for in the context of the Standard Model [8] of particle interactions. The weak charged currents interactions between quarks are governed by complex coupling constants that can be parameterized by three real parameters and one irreducible complex phase, that is the unique source of all *CP* violating effects according to the Standard Model. Nowadays this test has become one of the most important for particle physics.

The violation of *CP* symmetry is also relevant for modern theories of cosmology. According to these theories, there are reasons to believe that an equal amount of matter and antimatter was present in the early universe after the Big Bang. Presently, however, the universe appears to be predominantly composed of matter and radiation. In our galaxy, for example, the primary cosmic-ray nuclei that we observe are composed of particles rather than antiparticles [9]. Large amounts of antimatter could be detected through γ emission from annihilation processes with cosmic matter. No such phenomena have been observed. The existence of *CP* violation is, according to Sakharov [11], an essential ingredient to explain the abundance of matter in the universe. The small differences in the interactions of matter and antimatter due to *CP* violation could provide a mechanism to generate the observed matter-antimatter asymmetry. However, the predicted size of *CP*-violating effects in the Standard Model is not able to account for the small observed amount of antimatter. In fact, the effect predicted by the Standard

Model is many orders of magnitude too small to produce this asymmetry. This inconsistency motivates physicists to probe the sources and effects of *CP*-violation in fundamental particle interactions. Theories of physics beyond the Standard Model generally provide more sources of *CP* violation; their predictions differ from those of the Standard Model and can be tested in experiments: measurements of asymmetries in B decays, in particular, probe for new physics contributions.

This thesis describes a measurement of a *CP* violating asymmetry in neutral B meson decays, $B^0 \to \overline{D}^{(*)0} h^0$, where $\overline{D}^{(*)0}$ is a charmed meson and h^0 is a light meson such like a π^0, η, η' or ω, performed on data collected by the *BABAR* experiment at the Stanford Linear Accelerator Center (SLAC) asymmetric-energy electron-positron collider PEP-II.

A possible manifestation of *CP* violation in neutral B meson decays appears in final states accessible to both B^0 and $\overline{B}^0$; a B^0 can mix into a $\overline{B}^0$ and this gives an extra phase that translates into a *CP* violating effect.

If the D^0 ($\overline{D}^0$) meson decays into a *CP* eigenstate, then both B^0 and $\overline{B}^0$ can contribute to the final state, realizing the condition for possible *CP* violation.

The interesting point in measuring *CP* violation using $B^0 \to \overline{D}^{(*)0} h^0$ modes is that theoretical uncertainties are well under control since SM contributions other than leading amplitude are highly suppressed [12]. Observation of a sizeable difference from the SM expectation in *CP* violating asymmetries for this decay would be an evidence for new physics contributions.

Chapter 1 is devoted to a theoretical introduction to B physics, *CP* violation and the $B^0 \to \overline{D}^{(*)0} h^0$ process. In Chapter 2 we briefly describe the *BABAR* detector. In Chapter 3 a detailed explanation of selection criteria for $B^0 \to \overline{D}^{(*)0} h^0$ channel is given; in Chapter 4 the time dependent fit is described. In Chapter 5 we present the fit to the data and results. In the end we discuss the results and their possible interpretation in Chapter 5.9.

Chapter 1

Theoretical introduction

To motivate the study of B mesons physics, and then in particular of the $B^0 \to \overline{D}^{(*)0} h^0$ process, we will first present a description of the Standard Model (SM) [8] of particle physics. We explore predictions of SM that are relevant in the $B^0 \to \overline{D}^{(*)0} h^0$ process and more in general for our discussion of CP violation in B meson sector. We also explore CP violation, its general quantum mechanical phenomenology, as well as how the SM provides for it. The B meson system and its connection to CP violation will be explained as well. Finally, motivations for studying the decay $B^0 \to \overline{D}^{(*)0} h^0$ will be given, as well as a discussion of the implications of measurements in this mode.

1.1 Standard Model of fundamental interactions

The Standard Model (SM) of fundamental particle physics is the theory that describes strong and electroweak interactions among elementary particles.

Elementary particles are grouped in *fermions* (half-integer *spin* particles) and in *bosons* (integer spin particles). Matter is made of 1/2 spin fermions: leptons and quarks; the formers feel no strong interactions. Spin 1/2 particles are ordered in families and so far we have three of them, both for quarks and leptons. Quarks, flavor eigenstates (that is conserved in strong and electromagnetic interactions), are u and d, c and s, t and b; leptons are e and ν_e, μ and ν_μ, τ and ν_τ.

A spin 1/2 fermion can be described by a Dirac spinor; it means that left-handed (L) components can be separated from right-handed (R) components. Left-handed components of each family are weak isospin $SU(2)_L$ doublets members:

$$\begin{pmatrix} u_L \\ d_L \end{pmatrix} \quad \begin{pmatrix} c_L \\ s_L \end{pmatrix} \quad \begin{pmatrix} t_L \\ b_L \end{pmatrix} \tag{1.1}$$

$$\begin{pmatrix} \nu_e \\ e_L \end{pmatrix} \quad \begin{pmatrix} \nu_\mu \\ \mu_L \end{pmatrix} \quad \begin{pmatrix} \nu_\tau \\ \tau_L \end{pmatrix} \tag{1.2}$$

Right-hand components are weak isospin singlets:

$$\begin{array}{ccc} e_R & \mu_R & \tau_R \\ u_R & c_R & t_R \\ d_R & s_R & b_R \end{array} \tag{1.3}$$

Neutrinos ν_e, ν_μ and ν_τ are massless in the minimal SM model and have only the left-handed component.

Elementary particles interact exchanging spin 1 particles (vector bosons). Interactions are described by a renormalizable gauge theory based on the

$$SU(3)_C \otimes SU(2)_L \otimes U(1)_Y \text{ group}, \tag{1.4}$$

where $SU(2)_L \otimes U(1)_Y$ is the combined electroweak symmetry group and $SU(3)_C$ is the quantum chromo-dynamics group, QCD [15].

Electroweak symmetry group has four generators, each of them is linked to a vector field; corresponding quanta are *gauge* bosons: the photon and vector bosons. Spontaneous symmetry breaking and Higgs [14] mechanism provide mass to quarks, leptons, $W^{\pm}$ and Z^0. Strong interactions are mediated by gluon exchange, massless vector bosons. Strong interactions occur among "colored" particles, quarks and gluons.

1.1.1 Discrete symmetries and Standard Model interactions

The existence and study of discrete symmetries has been crucial to understand particle properties and interactions. Symmetry properties have been used to infer Lagrangian structure of fundamental interactions.

It was initially assumed that the symmetries of the classical mechanics should work also for quantum mechanics: fundamental interactions were supposed to be symmetric with respect to Parity (P) and Time-reversal (T) transformations, like classical dynamics and electromagnetism. Another discrete transformation for quantum systems is charge-conjugation (C), that transforms particle in antiparticles and *viceversa*.

Experiments showed some that nuclear decays violated parity symmetry [3], while other experiments showed that all neutrinos were left-handed, indicating C violation. Since C violation seemed to always occur in conjunction with P violation in the weak interactions, it was natural to assume that the combined operation of C and P is a symmetry in nature, and to a good approximation CP symmetry is conserved indeed for most weak interactions. However, in 1964, Christensen *et al.* [5] discovered CP violation, observing the decay $K_L^0 \to \pi\pi$. In 2001, the *BABAR* and BELLE experiments discovered CP violation in B meson decays [6,7].

By now CP violation has been firmly established in these two neutral meson systems. The nature of CP violation in the SM is the subject of next Sections.

1.1.2 Mass terms in Standard Model Lagrangian

In SM, elementary particles gain their mass through the so-called Higgs mechanism [14]. Adding a scalar field with a vacuum expectation value v, the Lagrangian has appropriate mass terms. The simplest model uses a Higgs doublet scalar field:

$$\phi = \begin{pmatrix} \phi^+ \\ \phi^0 \end{pmatrix} \tag{1.5}$$

where $\phi^{0,+}$ are complex fields.

The Yukawa couplings of fermions to Higgs field in the SM Lagrangian are given by:

$$\mathcal{L}_Y = -\sum_{i,j} \left(g_d^{ij} \overline{Q}_L^i \phi d_R^j + g_u^{ij} \overline{Q}_L^i \overline{\phi} u_R^j + g_\ell^{ij} \overline{L}_L^i \phi \ell_R^j \right) + \text{h.c.} \tag{1.6}$$

where $Q(L)$ represents the left handed quarks (leptons) doublets, the indices i,j run over the generations of fermions and $\overline{\phi}$ is the SU(2) doublet conjugate of ϕ. Couplings g_u, g_d and g_ℓ are in general represented by complex matrices.

Inserting the expectation value v in the Yukawa Lagrangian 1.6, we obtain:

$$\mathcal{L}_\text{Y} = -\sum_{k=u,d,\ell} \overline{k}_L \mathcal{M}_k k_R \tag{1.7}$$

where $\mathcal{M}_k^{ij} = v g_k^{ij}$ are mass matrices. In general these matrices are not diagonal and therefore introduce mixing between the different generations of quarks. Hence, the SM Lagrangian is not expressed in terms of mass eigenstates but instead in terms of the eigenstates of the weak interactions. We can, however, rewrite the fields using a unitary transformation:

$$\begin{array}{lll} u_l = V_L^u u'_L & , & u_R = V_R^u u'_R \\ d_l = V_L^d d'_L & , & d_R = V_R^d d'_R \end{array} \tag{1.8}$$

so $\mathcal{M}' = V_L^{\dagger k} \mathcal{M}_k V_R^k$ is the diagonal mass matrix.

1.1.3 Weak interactions and quarks mixing

Quark mass eigenstates are different from weak interaction eigenstates; we may want to write weak interactions in the mass eigenstate base.

Charged current weak interactions can be described in SM by the product of an operator J^μ (with $V-A$ structure) and the W boson:

$$\mathcal{L}_{int} = -\frac{g}{\sqrt{2}}(\mathcal{J}^\mu W_\mu^+ + \mathcal{J}^{\mu\dagger} W_\mu^-) \tag{1.9}$$

where g is the weak charge related to Fermi coupling constant by $G_F/\sqrt{2} = g^2/8M_W^2$, where M_W is the W boson mass.

Weak charged current for quarks are written then in this way:

$$\mathcal{J}^\mu = \sum_{i,j} V_{ij} J_{ij}^\mu = \sum_{i,j} \overline{u}'_i \gamma^\mu \frac{1}{2}(1-\gamma_5) V_{ij}^{CKM} d'_j \tag{1.10}$$

where V_{ij}^{CKM} are the terms of Cabibbo, Kobayashi and Maskawa (CKM) matrix [19], which is defined as $V_L^{\dagger u} V_L^d$ (see eq. 1.8), and is usually written in this form:

$$V = \begin{pmatrix} V_{ud} & V_{us} & V_{ub} \\ V_{cd} & V_{cs} & V_{cb} \\ V_{td} & V_{ts} & V_{tb} \end{pmatrix} \tag{1.11}$$

Quark mixing idea was first introduced by Cabibbo [17] in 1963 to explain weak transition among different quark generations. Christensen *et al.* [5] observed *CP* violation in neutral kaon system in 1964 Kobayashi and Maskawa [18] in 1973 proposed a third quark family and a complex phase in quark mixing matrix to accommodate *CP* violation in Standard Model.

Quark mixing matrix parameters are unbounded from theory and need to be experimentally determined.

1.1.4 *CP* violation in the flavor sector

We have to identify which terms in the SM Lagrangian can be source of *CP* violation. Only flavor changing term can contribute; applying the *CP* operation we obtain:

$$1/2(CP) g \overline{u'}^i_L \gamma^\mu (1-\gamma_5)(V_{CKM}^{ij}) d'^j_L W_\mu^+ (CP)^\dagger \;=\; 1/2 g e^{i\phi} u'^i_L \gamma^\mu (1-\gamma_5)(V_{CKM}^{ij}) d'^j_L W_\mu^- \tag{1.12}$$

The right-hand side of Equation 1.12 is different from its hermitian conjugate by a phase. *CP* conservation would require:

$$V_{ij}^{*} = e^{i\phi} V_{ij} \tag{1.13}$$

Here ϕ is an arbitrary phase which can be properly set for one matrix element but maybe not for all of them. So if there is more than one complex element in the matrix then *CP* is violated in SM.

We have now to consider how many independent parameters are present in CKM matrix.

Quark mixing matrix elements are complex since *quarks* and weak boson fields are complex. Quark mixing matrix has to be unitary; therefore, with three quark families, then CKM matrix written in 1.11 has to be unitary ($\equiv V^{\dagger}V = 1$). Unitarity constraints impose restrictions on the number of free parameters, reducing them from 18 (9 modules and 9 phases) to only 3 real parameters and one phase. Usually the CKM matrix is parameterized by means of three real angles, θ_{12}, θ_{13} and θ_{23}, and one phase δ_{13}; then we can rewrite it in this way:

$$V = \begin{pmatrix} c_{12}c_{13} & s_{12}c_{13} & s_{13}e^{-i\delta_{13}} \\ -s_{12}c_{23} - c_{12}s_{23}s_{13}e^{i\delta_{13}} & c_{12}c_{23} - s_{12}s_{23}s_{13}e^{i\delta_{13}} & s_{23}c_{13} \\ s_{12}s_{23} - c_{12}c_{23}s_{13}e^{i\delta_{13}} & -c_{12}s_{23} - s_{12}c_{23}s_{13}e^{i\delta_{13}} & c_{23}c_{13} \end{pmatrix}, \tag{1.14}$$

where $c(s)_{ij} = \cos(\sin)\theta_{ij}$.

Experimentally the magnitude of off-diagonal terms is considerably smaller than the magnitude of on-diagonal terms. Wolfenstein [20] proposed an expansion of CKM matrix elements in terms of $\lambda_C = \theta_C$, the Cabibbo angle; experimentally $\lambda_C \approx 0.22$. By means of this expansion we get:

$$V_{CKM} = \begin{pmatrix} 1 - \frac{1}{2}\lambda_C^2 & \lambda_C & A\lambda_C^3(\rho - i\eta) \\ -\lambda_C & 1 - \frac{1}{2}\lambda_C^2 & A\lambda_C^2 \\ A\lambda_C^3(1 - \rho - i\eta) & -A\lambda_C^2 & 1 \end{pmatrix} + \mathcal{O}(\lambda_C^4) \tag{1.15}$$

In the Wolfenstein parametrization the four free parameters are A, λ_C, ρ and η; we can also define $(\bar{\rho}, \bar{\eta})$: $s_{13} = e^{i\delta} = V_{ub}^{*} = \dfrac{A\lambda_C^3(\bar{\rho} + i\bar{\eta})\sqrt{1 - A^4\lambda_C^4}}{\sqrt{1 - \lambda_C^2}[1 - A^2\lambda_C^4(\bar{\rho} + i\bar{\eta})]}$; this definition ensures that CKM matrix is unitary to all orders of λ_C. The hierarchy in quarks couplings is explicit and is expressed in powers of λ_C; the irreducible phase appears in V_{ub} and V_{td}.

1.1.5 Unitary triangles

The CKM matrix is unitary, whatever the number of generations of *quarks* and leptons. The number of light neutrino flavors contributing to Z^0 boson width [16] indicates that there are three generations of fermions. In the following we will use the Wolfenstein parameterization (Equation 1.15).

Requiring unitarity, we obtain these constraints on the CKM matrix elements:

$$\sum_j V_{ji}^{*} V_{jk} = \sum_j V_{ij} V_{kj}^{*} = \delta_{ik} \tag{1.16}$$

that translate in nine independent relations. In particular, the relations $\sum_j V_{jk}^{*} V_{ik} = 0$, $i \neq j$ can be represented by triangles in complex plane, for three generations of quarks. Their equal areas ("Jarlskog invariants" [21]) are proportional to the size of *CP* violation. We will focus our attention on the relation that involves all *b quark* CKM elements:

$$V_{ub}^{*} V_{ud} + V_{cb}^{*} V_{cd} + V_{tb}^{*} V_{td} = 0; \tag{1.17}$$

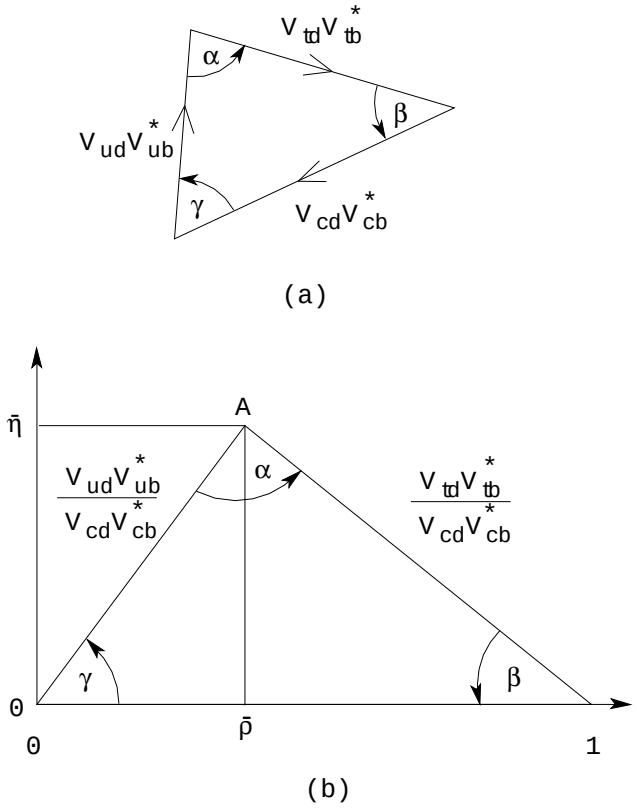

Figure 1.1: Unitarity triangle; (b) one is rotated by $V_{cd}V_{cb}^*$ quantity.

we will refer to this relation as the "Unitarity Triangle" (UT), represented in Figure 1.1.5 We define the angles of UT as:

$$\alpha = \arg\Big[-\frac{V_{td}V_{tb}^*}{V_{ud}V_{ub}^*}\Big],\ \ \beta = \arg\Big[-\frac{V_{cd}V_{cb}^*}{V_{td}V_{tb}^*}\Big],\ \ \gamma = \arg\Big[-\frac{V_{ud}V_{ub}^*}{V_{cd}V_{cb}^*}\Big]; \tag{1.18}$$

we will show that these angles are measurable from B meson decays. Moreover, measurements on B meson decays test the CKM mechanism by checking experimentally that: $\alpha + \beta + \gamma = \pi$.

1.2 *CP* violation in neutral pseudo-scalar mesons

We have seen in 1.1.4 that the source of *CP* violation in SM is the irreducible phase in the CKM matrix. Now we will present how this *CP* violating phase can appear in neutral meson system.

We consider a system with two neutral pseudo-scalar mesons, particle and anti-particle X^0 and $\overline{X}^0$, that can mix and decay; these are the flavor eigenstates. The time-evoluted state $|\psi(t)\rangle = a(t)|X^0\rangle + b(t)|\overline{X}^0\rangle$, is determined by Schrödinger equation:

$$i\frac{\partial}{\partial t}\begin{pmatrix} a \\ b \end{pmatrix} = \mathcal{H}\begin{pmatrix} a \\ b \end{pmatrix} \equiv \begin{pmatrix} m_{11} - \frac{i}{2}\Gamma_{11} & m_{12} - \frac{i}{2}\Gamma_{12} \\ m_{21} - \frac{i}{2}\Gamma_{21} & m_{22} - \frac{i}{2}\Gamma_{22} \end{pmatrix}\begin{pmatrix} a \\ b \end{pmatrix} \tag{1.19}$$

Assuming *CPT* invariance, $m_{11} = m_{22}$ and $\Gamma_{11} = \Gamma_{22}$, and $m_{21} = m_{12}^*$, $\Gamma_{21} = \Gamma_{12}^*$.

Figure 1.2: Lowest order SM box diagrams for B^0 meson mixing.

The mass eigenstates are obtained by a rotation of flavor eigenstates:

$$\begin{aligned} |X_L\rangle &= p|X^0\rangle + q|\overline{X}^0\rangle \\ |X_H\rangle &= p|X^0\rangle - q|\overline{X}^0\rangle \end{aligned} \tag{1.20}$$

where $L(H)$ denotes the lighter (heavier) mass eigenstate and

$$\frac{q}{p} = \sqrt{\frac{m_{12}^* - \frac{1}{2}i\Gamma_{12}^*}{m_{12} - \frac{1}{2}i\Gamma_{12}}} = \frac{\Delta m - \frac{i}{2}\Delta\Gamma}{2(m_{12} - i\frac{1}{2}\Gamma_{12})} \tag{1.21}$$

with q, p: $|q|^2 + |p|^2 = 1$. The mass and decay width differences, $\Delta m = m_H - m_L$ and $\Delta\Gamma = \Gamma_H - \Gamma_L$ respectively, are obtained diagonalizing the Hamiltonian matrix 1.19. A pure $|X^0\rangle$ state at $t = 0$ is a superposition of $|X_L\rangle$ and $|X_H\rangle$ and will evolve into a superposition of $|X^0\rangle$ and $|\overline{X}^0\rangle$ at a later time. For B meson system, mixing amplitudes are represented by "box" diagrams (see Figure 1.2).

Mass eigenstates $|X_{L,H}\rangle$ evolve in time according to:

$$|X_{L,H}(t)\rangle = e^{-im_{L,H}t - \Gamma_{L,H}t/2}|X_{L,H}\rangle \tag{1.22}$$

Using relations written in Equation 1.20, the evolution of flavor eigenstates is given by:

$$\begin{aligned} |X^0(t)\rangle &= e^{-iMt-\Gamma t/2}(\cos(\Delta m t/2)|X^0\rangle + i\frac{q}{p}\sin(\Delta m t/2)|\overline{X}^0\rangle) \\ |\overline{X}^0(t)\rangle &= e^{-iMt-\Gamma t/2}(\cos(\Delta m t/2)|\overline{X}^0\rangle + i\frac{q}{p}\sin(\Delta m t/2)|X^0\rangle) \end{aligned} \tag{1.23}$$

where $M = \frac{1}{2}(M_L + M_H)$ and we assume $\Delta\Gamma \ll \Delta m$ (this is true in particular for B^0 mesons).

We now consider the decay of a B meson to a CP eigenstate f whose eigenvalue is η_f:

$$CP|f\rangle = \eta_f|f\rangle \tag{1.24}$$

Decay amplitudes for B^0 and $\overline{B}^0$ to the final f state are:

$$\begin{aligned} A_f &= \langle f|\mathcal{H}|B^0\rangle \\ \overline{A}_f &= \langle f|\mathcal{H}|\overline{B}^0\rangle \end{aligned} \tag{1.25}$$

The corresponding decay rates are:

$$\begin{aligned} |\langle f|\mathcal{H}|B^0(t)\rangle|^2 &= e^{-\Gamma t}|A|^2|\cos(\Delta m t/2) + i\lambda \sin(\Delta m t/2)|^2 \\ &= \frac{e^{-\Gamma t}|A|^2}{2}\left[(1+|\lambda|^2) + (1-|\lambda|^2)\cos(\Delta m t) - 2\Im\lambda \sin(\Delta m t)\right] \end{aligned} \tag{1.26}$$

$$|\langle f|\mathcal{H}|\overline{B}^0(t)\rangle|^2 = \frac{e^{-\Gamma t}|A|^2}{2}\left[(1+|\lambda|^2) - (1-|\lambda|^2)\cos(\Delta m t) + 2\Im\lambda \sin(\Delta m t)\right] \tag{1.27}$$

where the λ parameter is defined as:

$$\lambda = \frac{q}{p}\frac{\overline{A}_f}{A_f} \tag{1.28}$$

Considering the time-dependent asymmetry among decay rates for mesons initially tagged as B^0 or $\overline{B}^0$, from Equations 1.26 and 1.27 we get:

$$a_{CP}(t) \equiv \frac{\Gamma(B^0(t)\to f) - \Gamma(\overline{B}^0(t)\to f)}{\Gamma(B^0(t)\to f) + \Gamma(\overline{B}^0(t)\to f)} = \frac{(1-|\lambda|^2)}{(1+|\lambda|^2)}\cos(\Delta m t) - \frac{2\Im\lambda}{(1+|\lambda|^2)}\sin(\Delta m t) \tag{1.29}$$

The time dependent asymmetry 1.29 shows how the *CP*-violating parameter λ parameter is connected with B meson decays to *CP* eigenstates and also how *CP* violation can be measured.

It is useful define *CP* violating parameters $\mathcal{C}$ and $\mathcal{S}$:

$$\mathcal{C} = \frac{1-|\lambda|^2}{1+|\lambda|^2} \quad \mathcal{S} = \frac{2\Im\lambda}{1+|\lambda|^2} \tag{1.30}$$

Now we will discuss how *CP* violation can arise in B meson decays.

1.2.1 *CP* violation in B decays

The possible manifestations of *CP* violation can be classified in a model-independent way:

1. "*CP* violation in decay", which occurs both in neutral and charged decays, when the amplitudes for a decay and its *CP* conjugate process have different magnitudes;
2. "*CP* violation in mixing", which occurs when the two neutral mass eigenstates cannot be chosen to be *CP* eigenstates;
3. "*CP* violation in the interference between decays with and without mixing", which may occur in decays into final states that are common to B^0 and $\overline{B}^0$.

Whatever the final state f, the $|\frac{\overline{A}_f}{A_f}|$ ratio is related to direct *CP* violation. There are two types of phases that may appear in A_f and $\overline{A}_f$.

Complex parameters in any Lagrangian term that contributes to the amplitude will appear in complex conjugate form in the *CP* conjugate amplitude. Thus, phases that appear in A_f will also appear in $\overline{A}_f$ with opposite signs; these are called "weak" phases. In the SM they can only occur in the CKM matrix. A second type of phase can appear in decay amplitudes even when the Lagrangian is real. Such phases (designated "strong" phases) do not violate *CP*, since they appear in A_f and in $\overline{A}_f$ with the same sign. Further, only the relative phases of different terms in an amplitude have physical

content; an overall phase rotation of an amplitude will have no physical consequences. It is therefore useful to write contributions to A in three parts: the magnitudes A_i, the weak-phase terms $e^{i\phi_i}$ and the strong-phase terms $e^{i\delta_i}$. If several terms contribute to the $B^0 \to f$ total amplitude:

$$A_f = \sum_i A_i e^{i(\delta_i+\phi_i)}, \overline{A}_f = \sum_i A_i e^{i(\delta_i-\phi_i)}. \tag{1.31}$$

The phase convention-independent quantity is then

$$\left|\frac{\overline{A}_f}{A_f}\right| = \left|\frac{\sum_i A_i e^{i(\delta_i-\phi_i)}}{\sum_i A_i e^{i(\delta_i+\phi_i)}}\right| \tag{1.32}$$

If *CP* is conserved it means that the weak phases are all equal and can be eliminated. Therefore if $|\overline{A}_f|/|A_f| \neq 1$, then "*CP* violation in decay" is manifest. It is interesting to note that *CP* violation of this type will not occur unless at least two terms with different weak phases also have different strong phases; the difference in decay rates is indeed proportional to:

$$|A_f|^2 - |\overline{A}_f|^2 = -2\sum_{i,j} A_i A_j \sin(\phi_i - \phi_j)\sin(\delta_i - \delta_j) \tag{1.33}$$

The second type of *CP* violation is in the mixing between neutral meson. Relative phase between m_{12} and Γ_{12} (see Equation 1.21) vanish if *CP* is conserved, leading to $|q/p| = 1$. Therefore, if *CP* is conserved, mass eigenstates must be *CP* eigenstates.

For the neutral B system, this effect could be observed through the asymmetries in semileptonic decays.

Finally, the last type of *CP* violation is observed from the interference between decay with and without mixing, where a neutral B mesons decay into the same final *CP* eigenstate, f. The relevant physically meaningful quantity is λ, as shown in 1.28. Assuming no *CP* violation of type 1 or 2, therefore

$$\begin{aligned} A_f = Ae^{i(\delta+\phi_D)}, \overline{A}_f = Ae^{i(\delta-\phi_D)} &\Rightarrow |A_f| = |\overline{A}_f| \\ q/p = e^{2i\phi_M} &\Rightarrow |q/p| = 1, \end{aligned} \tag{1.34}$$

allowing for a strong phase δ, but denote different decay and mixing weak phases, ϕ_D and ϕ_M. Hence we see that

$$\lambda = \frac{q}{p}\frac{\overline{A}_f}{A_f} = e^{2i(\phi_M-\phi_D)} \tag{1.35}$$

If $|\lambda| \neq 1$, then *CP* violation is manifest through either mixing or decay, and if $\Im\lambda \neq 0$ then *CP* violation is manifest through the interference between decays with and without mixing. This is a consequence of the non vanishing phase between q/p (from mixing) and $\overline{A}_f/A_f$ (from decay). It is clear, then, that the asymmetry in 1.29 provides a very powerful means for probing *CP* violation in B decays, via the parameter λ. We will see how λ is directly related to the CKM matrix elements in Standard Model.

1.2.2 Unitarity Triangle and *CP* violating parameters

We can relate the Unitarity Triangle (UT) and measurements performed on B meson decay processes as summarized in Figure 1.3.

The parameter λ defined above can be expressed in terms of CKM matrix elements. In general, the amplitudes for B decays can carry contributions from multiple Feynman diagrams, each of which

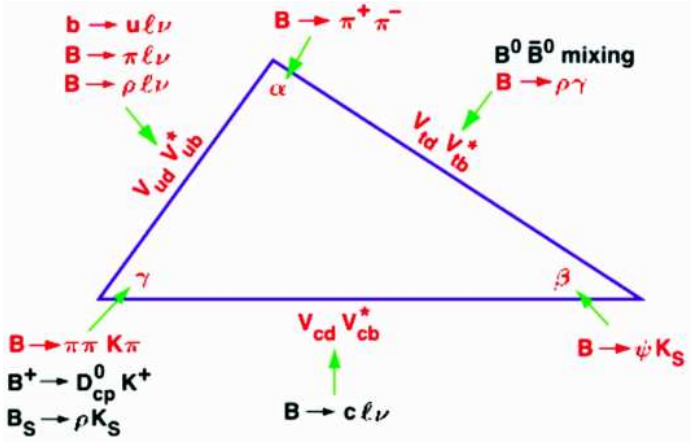

Figure 1.3: Unitary Triangle and related B meson decay processes.

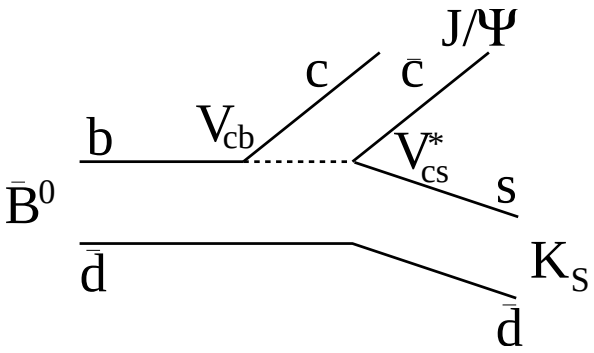

Figure 1.4: The $B \to J/\psi\, K^0_S$ decay tree-diagram.

contains different CKM elements. Let us consider as an example the dominant tree contribution to the decay $B \to J/\psi\, K^0_S$, shown in Figure 1.4.

Let us recall the λ parameter:

$$\lambda = \frac{q}{p}\frac{\overline{A}}{A}, \tag{1.36}$$

where q/p is the mixing-related term and $\overline{A}/A$ is the ratio of the decay amplitudes, and find the corresponding expressions in $B \to J/\psi\, K^0_S$ decay.

The usual mixing term q/p (see also Figure 1.2) is:

$$\frac{q}{p} = \left(\frac{V^*_{tb}V_{td}}{V_{tb}V^*_{td}}\right) \tag{1.37}$$

.

The quark subprocess in $B \to J/\psi\, K^0_S$ is $b \to c\bar{c}s$ (Figure 1.4), that is dominated by the W^- mediated tree diagram:

$$\frac{\overline{A}_{J/\psi\, K^0_S}}{A_{J/\psi\, K^0_S}} = \eta_{J/\psi\, K^0_S}\left(\frac{V_{cb}V^*_{cs}}{V^*_{cb}V_{cs}}\right); \tag{1.38}$$

the CP-parity of the state is $\eta_{J/\psi\, K^0_S} = -1$. An additional ingredient is $K - \overline{K}$ mixing in the final state. For decays with a single K^0_S in the final state, $K - \overline{K}$ is essential because $B^0 \to K^0$ and $\overline{B}^0 \to \overline{K}^0$ only;

therefore the interference of B^0 and $\overline{B}^0$ is possible only due to $K - \overline{K}$ mixing. Therefore the decay $B \to J/\psi K^0_S$ is an example of *CP*-violating process of the third type (see Subsection 1.2.1). The $K - \overline{K}$ mixing adds a factor:

$$\left(\frac{q}{p}\right)_K = \left(\frac{V_{cs}V^*_{cd}}{V^*_{cs}V_{cd}}\right). \tag{1.39}$$

into $(\overline{A}/A)$, that becomes:

$$\frac{\overline{A}_{J/\psi K^0_S}}{A_{J/\psi K^0_S}} = \eta_{J/\psi K^0_S}\left(\frac{V_{cb}V^*_{cs}}{V^*_{cb}V_{cs}}\right)\left(\frac{V_{cs}V^*_{cd}}{V^*_{cs}V_{cd}}\right) \tag{1.40}$$

Combining equations 1.37 and 1.40 using Equation 1.36, one finds [47]:

$$\begin{aligned} \lambda_{J/\psi K^0_S} &= -\left(\frac{V^*_{tb}V_{td}}{V_{tb}V^*_{td}}\right)\left(\frac{V_{cb}V^*_{cs}}{V^*_{cb}V_{cs}}\right)\left(\frac{V_{cs}V^*_{cd}}{V^*_{cs}V_{cd}}\right) \\ &\Rightarrow \quad \Im(\lambda_{J/\psi K^0_S}) = \sin 2\beta \end{aligned} \tag{1.41}$$

A measurement of the asymmetry in Equation 1.29 with this decay provides a measurement of $\sin 2\beta$. The *BABAR* and BELLE collaborations used this mode to establish *CP* violation in B meson system [6,7].

Measurements of the other two angles and of the sides of UT are still ongoing. The idea is to over-constrain UT parameters to test the flavor sector of SM. Recent results are summarized in Figure 1.5 [22].

The $b \to s$ penguin transition results for $\eta_f \mathcal{S}$, reported in Figure 1.6, are individually compatible with the $B^0 \to J/\psi K^0_S$ result, takens as a reference; however, they appear to be systematically on the low side.

This is interesting, but cannot yet be considered as an indication of a discrepancy with respect to the SM predictions: in fact SM corrections to $\sin 2\beta^{\rm eff} (\equiv -\eta_f \mathcal{S})$ must be taken into account for a meaningful comparison [23–25].

Recent theoretical efforts to calculate the difference of *CP*-asymmetries between penguin-dominated and tree-dominated modes, using different methods, indicate that differences $\Delta\mathcal{S} = \sin 2\beta^{\rm eff} - \sin 2\beta$ should be within a few %, predicting mostly the positive shifts, to be compared with the observed negative differences.

Among the channels one can investigate to over-constrain the UT elements, $B^0 \to \overline{D}^{(*)0} h^0$ decays are interesting because it has only tree amplitudes in the SM. We will describe in detail its characteristics in the next Section.

1.3 The $B^0 \to \overline{D}^{(*)0} h^0$ decays

We describe here $B^0 \to \overline{D}^{(*)0} h^0$ decays, where $\overline{D}^{(*)0}$ is a charmed meson and h^0 is a light meson such as π^0, η, ω and η'. We introduce the $B^0 \to \overline{D}^{(*)0} h^0$ process starting from B decays in general and moving then to possible *CP* violation in this channel.

1.3.1 Color suppressed $b \to c$ transitions

Weak decays like $\overline{B}^0 \to D^{(*)+} h^-$ can proceed through the emission of a virtual W^-, which then can materialize as a charged hadron [1]. Because the W^- carries no color, no exchange of gluons with the rest of the final state is required. Such decays are called *color-allowed*. By contrast, decays like $B^0 \to \overline{D}^{(*)0} h^0$ cannot occur in this way. The quark from the decay of the virtual W^- must be combined

[1] Unless differently specified, charge conjugation is always assumed in the following

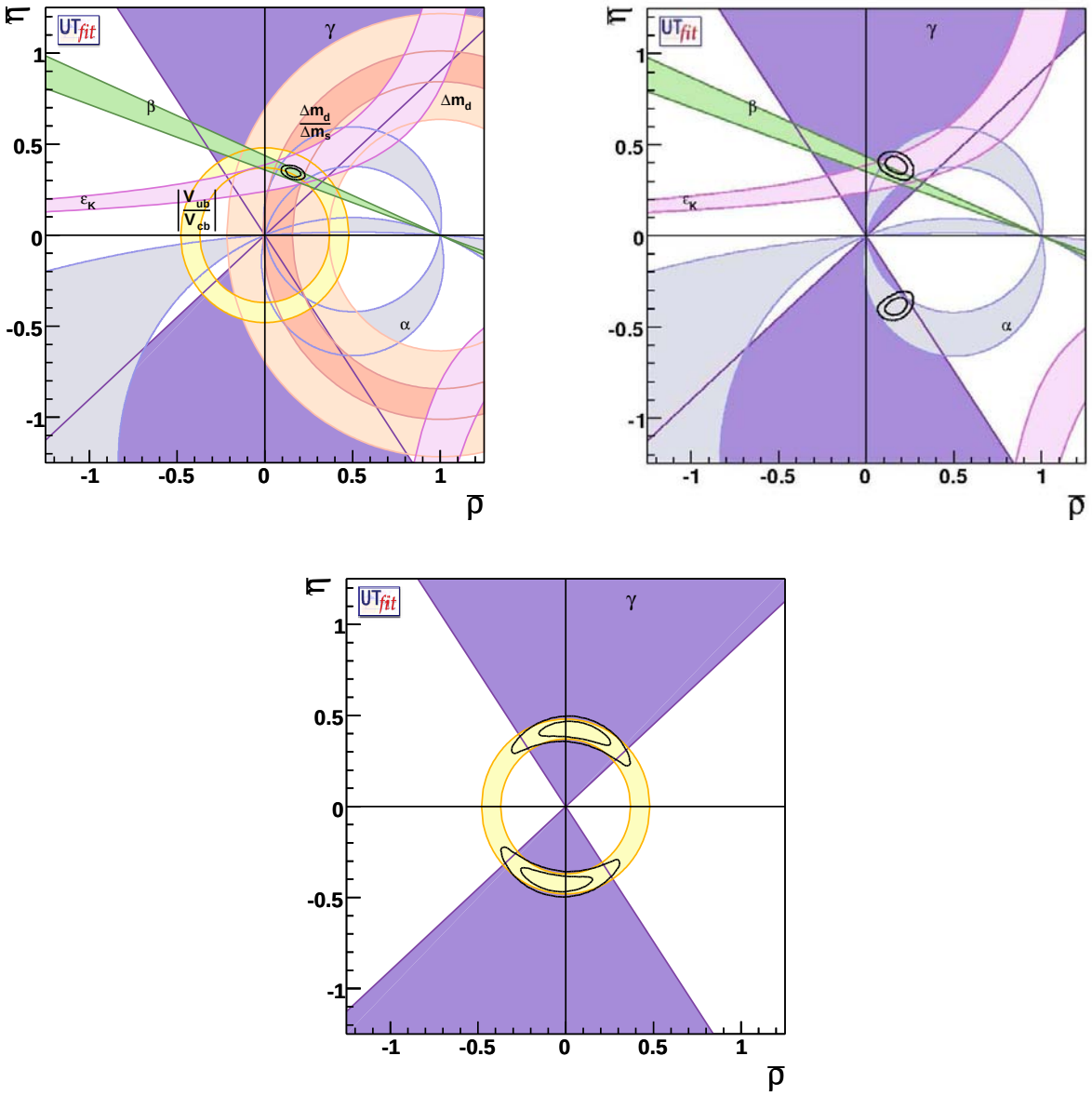

Figure 1.5: Allowed regions for $(\overline{\rho}-\overline{\eta})$; 8% and 95% regions are shown. Top left plot shows region for the constraints given by the measurements of $|V_{ub}|/|V_{cb}|$, ϵ_K, Δm_d,$\Delta m_d/\Delta m_s$, α, β, γ, $\Delta\Gamma_d/\Gamma_d$, $\Delta\Gamma_s/\Gamma_s$, A^d_{SL}, and the di-muon asymmetry. Top right plot shows allowed regions for $(\overline{\rho}-\overline{\eta})$ as selected by the measurements of $|V_{ub}|/|V_{cb}|$, Δm_d and Δm_s are compared to the bounds (at 95% probability) from the measurements of *CP* violating quantities in the kaon (ϵ_K) and in the B (α, β andγ) sectors. Bottom plot shows constraints given by the measurements two constraints which are almost unchanged by the presence of New Physics: $|V_{ub}|/|V_{cb}|$

with some anti-quark other than its partner from the W^-. However, other anti-quarks will have the right color to make a color singlet only one-third of the time (when q and $\overline{q}$ are in color singlet state). As a result, these decays are "color-suppressed". The tree level diagrams for the color-allowed and color-suppressed decays are shown in Fig. 1.7.

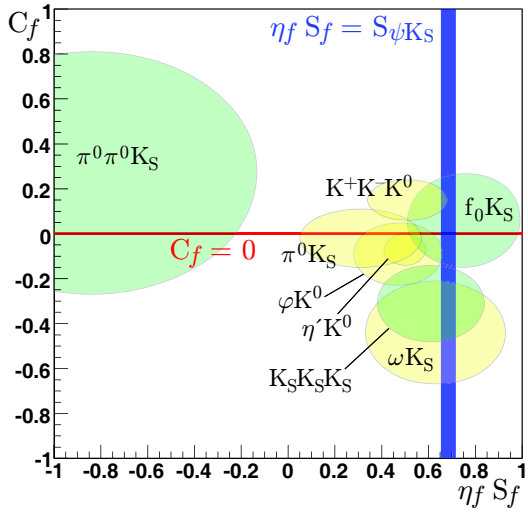

Figure 1.6: Two-dimensional ($\mathcal{S}$ $\mathcal{C}$) comparison of averages in several $b \to q\overline{q}$ s modes. The $J/\psi K^0_S$ result is also reported for comparison.

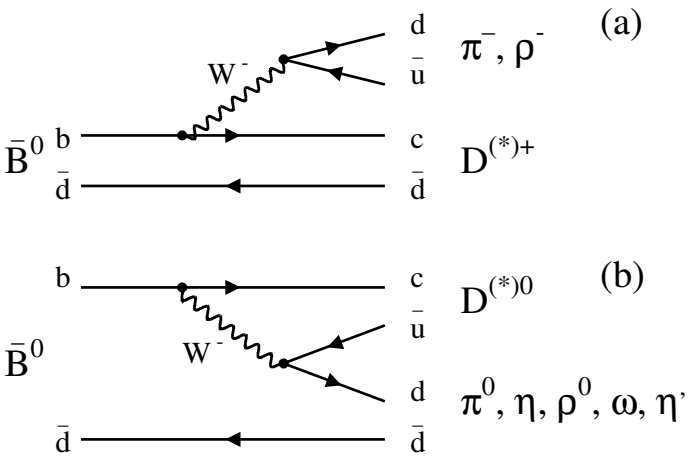

Figure 1.7: The (a) color-allowed and (b) color-suppressed spectator tree diagrams for $\overline{B}^0 \to D\ h$ decays.

Since non-perturbative calculations of decay rates are at present not possible, we must rely on models to describe the above processes. In an early model [28,29], the "naive" (or "generalized") factorization model, that is successful in describing charmed meson decays, the decay amplitudes of exclusive two-body non-leptonic weak decays of heavy flavor mesons are estimated by replacing hadronic matrix elements of four-quark operators in the effective weak Hamiltonian by products of current matrix elements. These current matrix elements are determined in terms of form factors describing the transition of the B meson into the meson containing the spectator quark, and a second factor proportional to a decay constant describing the creation of a single meson from the remaining quark–anti-quark pair. In this approach, the decay amplitudes corresponding to the Figures. 1.7(a) and 1.7(b) are proportional to a_1 and a_2 [30], respectively, where the a_i are effective QCD Wilson coefficients [27].

As an example, using the naive factorization model, the decay amplitude for the $\overline{B}^0 \to D^+\pi^-$ mode corresponding to the Figure 1.7(a) can be written as [31]

$$\mathcal{A}^f(\overline{B}^0 \to D^+\pi^-) = i\frac{G_F}{\sqrt{2}}V_{cb}V_{ud}^*(m_B^2 - m_D^2)a_1(D\pi)f_\pi F_0^{B\to D}(m_\pi^2), \tag{1.42}$$

while the decay amplitude for the $\overline{B}^0 \to D^0\pi^0$ mode corresponding to Fig. 1.7(b) can be expressed as

$$\sqrt{2}\mathcal{A}^f(\overline{B}^0 \to D^0\pi^0) = i\frac{G_F}{\sqrt{2}}V_{cb}V_{ud}^*(m_B^2 - m_\pi^2)a_2(D\pi)f_D F_0^{B\to\pi}(m_D^2), \tag{1.43}$$

where G_F is the Fermi coupling constant, V_{cb} and V_{ud} are CKM matrix elements, f_π and f_D are the decay constants of the π and D mesons, and $F_0^{B\to M}(q^2)$ are the longitudinal form factors of the B-meson decays to M mesons at momentum transfer q^2. The coefficients a_1 and a_2 are used to parameterize the "non-factorizable" strong-interaction effects. These coefficients are real in the absence of final state interactions (FSI) and ideally would be process independent [28–30].

The $\overline{B}^0 \to D^{(*)+}M^-$ with $M = \pi$, ρ, a_1, and $D_s^{(*)}$ decays are well described in this model using a universal value $|a_1| = 1.1 \pm 0.1$ [30,32]. It has been proposed [30,31] that a value of $|a_2|$ in the range 0.2 to 0.3 accommodates most of the two-body color-suppressed charm $\overline{B}^0$ or charmonium B decays, without the need for FSI. Nevertheless, from low-energy hadronic physics it is known that FSI not only introduce phases but also interchange particles. The introduction of FSI has also completely changed the conclusions of the models that describe non-leptonic D^0 decays, especially for decay modes such as $D^0 \to \overline{K}^0\pi^0$ [33].

The color-suppressed amplitude for $\overline{B}^0 \to D^{(*)0}h^0$, where h is an isovector meson, is a linear combination of the amplitudes with $I = 3/2$ and $I = 1/2$ isospin [34]. Final state interactions in the $I = 3/2$ and $I = 1/2$ channels might be expected to be independent and thus "mitigate" the destructive interference between the channels that would otherwise make the color-suppressed amplitude small.

The $B^0 \to \overline{D}^{(*)0}h^0$ decays have been observed for instance by the CLEO collaboration [39], while the $\overline{B}^0$ decays into $D^{*0}\pi^0$, $D^0\eta$, $D^0\omega$, and $D^0\rho^0$ have also been measured by the Belle collaboration [40]. We present in Table 1.1 the average of existing measurements of branching fractions of the B^0 color-suppressed decays. The level of color-suppression can be estimated from the branching fractions for the $D^*\pi$ decay modes, as reported in Table 1.2.

The naive factorization model predicts branching fractions for the color-suppressed modes in the range $(0.3\text{–}1.7) \times 10^{-4}$ [30–32,34–38]. The inclusion of FSI will increase these rates, as explained above (see, for example, Ref. [36]). The measured branching fractions, as listed in Table 1.1, are larger than the predictions of the naive factorization model; further investigation is needed.

1.3.2 *CP* violation in $B^0 \to \overline{D}^{(*)0}h^0$ decay

Here we discuss in more detail the color-suppressed decay of neutral B mesons into $D^{(*)0}$ and a light meson (h^0). The *CP*-asymmetry analysis reported in this thesis is the first measurement in $B^0 \to \overline{D}^{(*)0}h^0$ decays with D^0 meson going to *CP*-eigenstates.

The leading diagrams are shown in Fig. 1.8 for the $D^0\pi^0$ final state; similar considerations hold for other h^0 (η, ω and η') mesons. We consider final states where D^0 decays into a *CP*-eigenstate, and h^0 is a CP-eigenstate as well. The *CP* conservation in these decays is violated due to the interference between the decay amplitude and $B\bar{B}$ mixing, containing the phase 2β. The asymmetry vanishes if integrated over time, so that the measurement requires a time dependent decay asymmetry fit, with a flavor tag of the opposite side B meson.

Within Standard Model, theory predicts the amplitude of the *CP* asymmetry to be equal to $\sin 2\beta$ (just like in charmonium and "penguin" modes) within 5% accuracy [12]. The SM deviation from $\sin 2\beta$

Table 1.1: Measured branching fractions [16] for $B^0 \to \overline{D}^{(*)0} h^0$.

B^0 mode	$\mathcal{BR}$ ($\times 10^{-4}$)
$D^0\pi^0$	2.91± 0.28
$D^0\eta$	2.2± 0.5
$D^0\omega$	2.5± 0.6
$D^0\eta'$	1.25± 0.23
$D^{*0}\pi^0$	2.7± 0.5
$D^{*0}\eta$	2.6± 0.6
$D^{*0}\omega$	4.2± 1.1
$D^{*0}\eta'$	1.23± 0.35

Table 1.2: Ratio of $\mathcal{BR}$ of colour suppressed and colour favored $B \to Dh$

Decay modes	$\mathcal{BR}$ (x10^{-4})
$B^0 \to \overline{D}^0\pi^0$	2.91 ± 0.28
$\overline{B}^0 \to D^-\pi^+$	34 ± 9
$\mathcal{BR}$ Ratio	value
$\frac{\overline{D}^0\pi^0}{D^-\pi^+}$	0.09 ± 0.03

mainly occurs due to the presence of sub-leading $b \to u$ transition amplitude (Fig. 1.9), that is strongly suppressed as compared to the leading $b \to c$ contribution.

According to Grossman and Worah [12], we can express time-dependent *CP* asymmetry (see Equation 1.29) for process having different quark level decay channels that measure the same phase when only one amplitude contributes, in this way:

$$a_{CP}(t) = -\sin 2(\phi_0 + \delta\phi)\sin(\Delta m t) \tag{1.44}$$

where ϕ_0 is the phase predicted at leading order in the Standard Model, and $\delta\phi$ is the correction to it. They estimate for $B^0 \to \overline{D}^{(*)0} h^0$ decays the phase correction due to Cabibbo suppressed amplitude, $\delta\phi_{SM}$, to be:

$$\delta\phi_{SM}(b \to c\bar{u}d) = \frac{V_{ub}V_{cd}^*}{V_{cb}V_{ud}^*} r_{FA} \leq 0.05 \tag{1.45}$$

where r_{FA} is the ratio of matrix elements; $r_{FA} = 1$ in the factorization approximation, $r_{FA} < 2$ is a reasonable limit to obtain the upper bound. The absence of penguin diagrams also makes the SM calculation easier [41].

However, possible non-SM effects, such as Supersymmetry without R-parity conservation may increase this deviation to a larger values. As reported in [12,13], $B^0 \to \overline{D}^{(*)0} h^0$ decays could receive

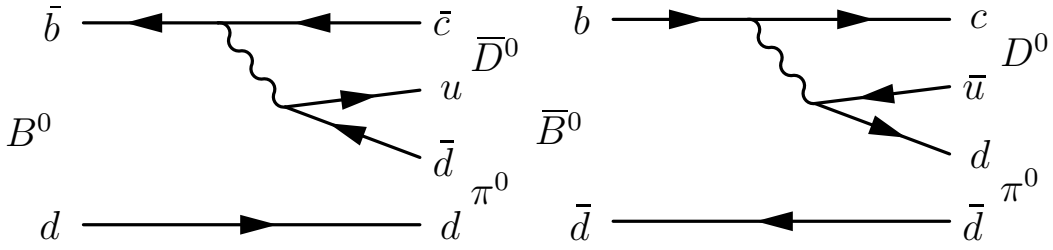

Figure 1.8: Leading diagrams for $B^0 \to D^0\pi^0$ decays.

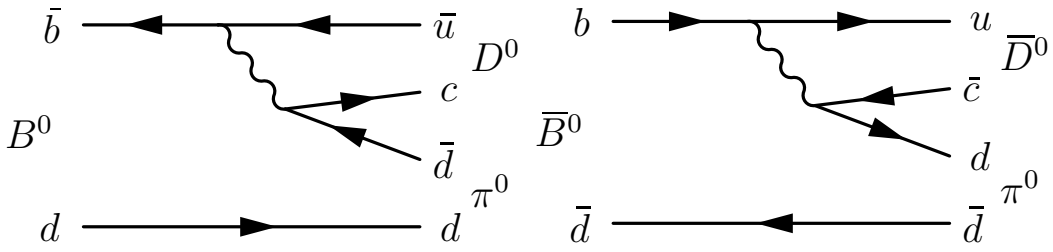

Figure 1.9: Diagrams for $B^0 \to D^0\pi^0$ decays, suppressed by $\mathcal{O}(\sin^2\theta_C)$.

contribution from R-parity violating diagrams; assuming lepton number conservation and baryon number violation, diagrams with vertices like the one reported in Figure 1.10 can contribute. In this vertex the propagator is a squark (Supersimmetric partner of a quark) coupled to a pair of quarks or anti-quarks, thus violating baryon number. In this model, the tree diagram reported in Figure 1.11 would contribute to the total amplitude; here the b quark goes to a $\overline{u}$ quark (thus violating baryon number), while a $\tilde{s}_R$ squark is emitted; this squark "hadronizes" then in a c and d pair, thus violating baryon number again. Globally the baryon number is conserved, as it should be. The λ'' parameter can carry an extra non-trivial phase. The possible effect is of order of $\delta\phi \leq 0.5$.

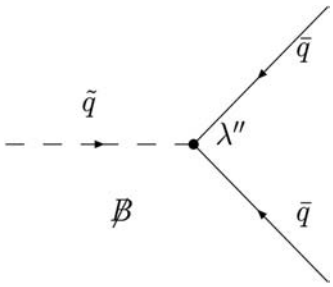

Figure 1.10: Basic R-parity violating tree diagram, associated with λ'' couplings; this vertex violates baryon conservation number [12,13]. q ($\tilde{q}$) denote (s)quarks; the arrows on the (s)quark indicate the flow of the baryon number.

The $B^0 \to \overline{D}^{(*)0}h^0$ process provides a way to measure sin2β and test the Standard Model in an independent way from the "Golden Mode" $J/\psi\, K^0_S$. If SM holds, then we expect:

$$|\phi(B^0 \to J/\psi\, K^0_S) - \phi(B^0 \to \overline{D}^{(*)0}h^0)| < 0.05 \tag{1.46}$$

Deviations from this relation could be an indication of possible new physics in decay amplitudes;

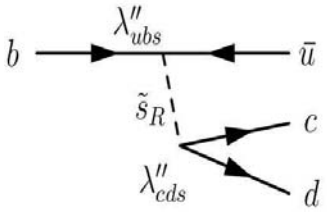

Figure 1.11: R-parity violating tree diagram for $B^0 \to \overline{D}^{(*)0} h^0$ decays [12,13]. q ($\tilde{q}$) denote (s)quarks; the arrows on the quarks indicate the flow of the baryon number.

experimental results compatible with this prediction would constrain non-SM contributions.

1.3.3 Comparison with other modes

Apart from $B^0 \to J/\psi K^0_S$ decay, already presented in Subsection 1.2.2, process of the type $b \to q\overline{q}q'$ [42,47] can be used to measure *CP*-violating parameters, in the interference between mixing and decay (see Subsection 1.2.1). In particular, the $B \to \phi K^0_S$ decay is dominated by electroweak penguin diagrams (Fig. 1.12), possibly with smaller contributions from electroweak penguins, while other (SM) amplitudes are strongly suppressed. Neglecting CKM-suppressed contributions, the time-dependendent *CP*-violating asymmetry in the decay $B \to \phi K^0$ is proportional to the parameter $\sin 2\beta$, like $B^0 \to J/\psi K^0_S$; SM corrections to mixing phase are of order of 0.04 [12].

Since many models of physics beyond the SM introduce additional diagrams with heavy particles in the penguin loops and new *CP*-violating phases, discrepancy between $\mathcal{S}$ parameter in $B \to \phi K^0$ and in $B^0 \to J/\psi K^0_S$ can probe New Physics; according to Grossman and Worah [12], some Supersymmetric extensions of SM can result in really sizable extra phases (up to order 1).

The *CP*-asymmetry in $B^0 \to \phi K^0_S$ was measured by *BABAR* [43] and BELLE [44] and the most recent average is: $\sin(2\beta^{eff}) = 0.39 \pm 0.18$ [98].

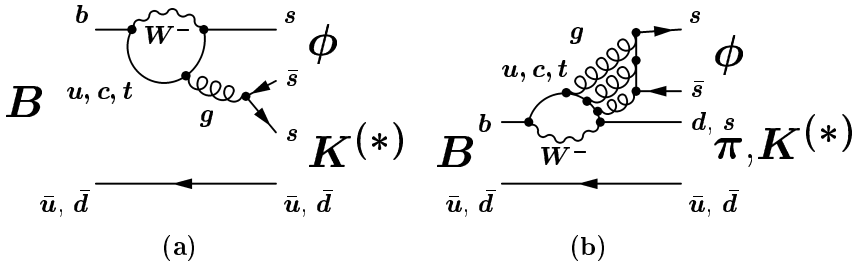

Figure 1.12: Examples of quark-level diagrams for $B \to \phi K(\pi)$. Left: internal penguin, right: flavor-singlet penguin.

Since $B^0 \to \overline{D}^{(*)0} h^0$ receives no contributions from loop digrams and on the contrary $B^0 \to \phi K^0_S$ has no tree amplitude allowed, the measured *CP*-asymmetries in these two channels could result in a pattern of $\sin 2\beta$ that allows to determine which New Physics is likely to be correct. Therefore $B^0 \to J/\psi K^0_S$, $B^0 \to \phi K^0_S$ and $B^0 \to \overline{D}^{(*)0} h^0$ are really interesting channels to test the flavor sector of SM and to probe potential New Physics. Moreover, the *CP*-asymmetry measurement in $B^0 \to \overline{D}^{(*)0} h^0$ decays with D^0 meson going to *CP*-eigenstates was never performed before.

A general comparison of the results in different modes will be shown and discussed in the conclusions.

Chapter 2

The *BABAR* Detector

BABAR, the detector for the SLAC PEP-II asymmetric e^+e^- B Factory operating at the $\Upsilon(4S)$ resonance is presented here. It was designed to allow comprehensive studies of CP-violation in B-meson decays. In what follows we briefly present a summary of the PEP-II collider (Section 2.2); after that we will review main characteristics of *BABAR* subdetectors: the multi-layer silicon vertex tracker SVT (Section 2.4) for charged particle tracks measurement, surrounded by a cylindrical wire chamber, Drift Chamber (DCH, Section 2.5); these two systems provide accurate and reliable tracks measurement (Section 2.6); an Electromagnetic Calorimeter (EMC, Section 2.8) measures showers from electrons and photons by means of an array of CsI crystals located just inside the solenoidal coil of a superconducting magnet (Section 2.3). Muons and neutral hadrons are identified by arrays of resistive plate chambers and limited streamer tubes, inserted into gaps in the steel flux return of the magnet (Section 2.9). Charged hadrons are identified by dE/dx measurements in the tracking detectors and by the Cherenkov angle measured in a ring-imaging Cherenkov detector (DIRC, Section 2.7) surrounding the drift chamber.

I have been involved in operation of SVT in 2005; a more detailed presentation for SVT will be then given, reporting activities and recent results.

2.1 Introduction

The primary physics goal of the *BABAR* experiment is the systematic study of CP-violating asymmetries in the decay of neutral B mesons to CP eigenstates. Secondary goals are precision measurements of decays of bottom and charm mesons and of τ leptons, and searches for rare processes that become accessible with the high luminosity of the PEP-II B Factory [45]. The design of the detector is optimized for CP violation studies, but it is also well suited for these other physics topics.

The PEP-II B Factory is an asymmetric e^+e^- collider designed to operate at a luminosity of 3×10^{33} $\mathrm{cm}^{-2}\mathrm{s}^{-1}$ and it has reached more than $10^{34}\,\mathrm{cm}^{-2}\mathrm{s}^{-1}$ [46], at a center-of-mass energy of 10.58 GeV, the invariant mass of the $\Upsilon(4S)$ resonance. This resonance decays almost exclusively ($> 96\%$ [16]) to B^0 $\overline{B}^0$ and B^+B^- pairs and thus provides an ideal laboratory for the study of B mesons. In PEP-II, the electron beam of 9.0 GeV collides head-on with the positron beam of 3.1 GeV resulting in a Lorentz boost to the $\Upsilon(4S)$ resonance of $\beta\gamma = 0.56$. This large boost makes it possible to better reconstruct the decay vertices of the two B mesons, to determine their relative decay times, and thus to measure the time dependence of their decay rates. The crucial test of CP violation is a comparison of the time-dependent decay rates for B^0 and $\overline{B}^0$ to a self-conjugate state. For the cleanest experimental test, this requires events in which one B meson decays to a CP eigenstate that is fully reconstructed and the other B meson is tagged as a B^0 or a $\overline{B}^0$ by its decay products: a charged lepton, a charged kaon, or other flavor sensitive features such as a low momentum charged pion from a D^* decay.

The small branching ratios of B mesons to CP eigenstates, typically 10^{-4}, the need for full recon-

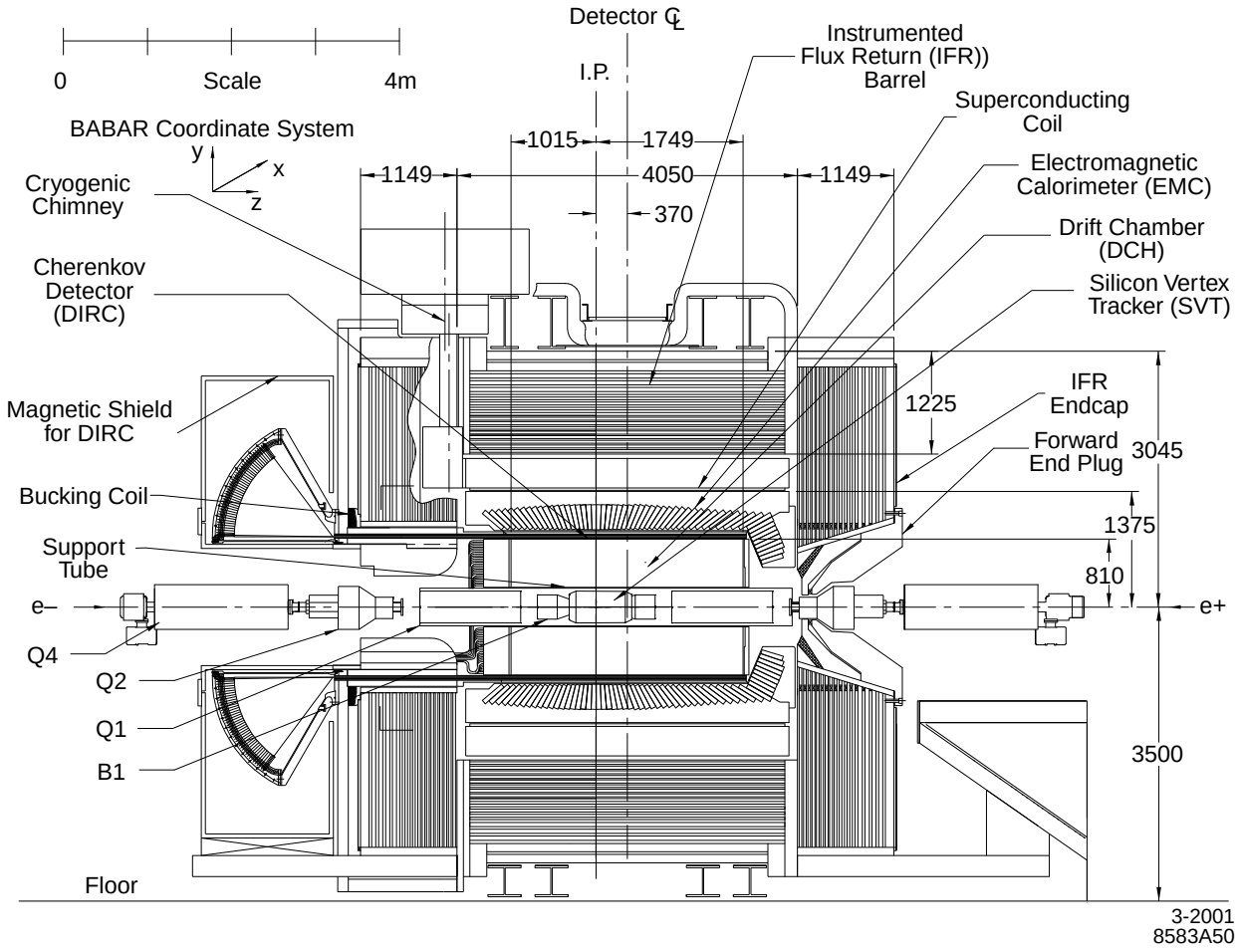

Figure 2.1: *BABAR* detector longitudinal section.

struction of final states with two or more charged particles and several π^0's, plus the need to tag the second neutral B, place stringent requirements on the detector:

- a large and uniform acceptance down to small polar angles relative to the boost direction;
- excellent reconstruction efficiency for charged particles down to 60 MeV/c and for photons to 20 MeV;
- very good momentum resolution to separate small signals from background;
- excellent energy and angular resolution for the detection of photons from π^0 and η^0 decays, and from radiative decays in the range from 20 MeV to 4 GeV;
- very good vertex resolution, both transverse and parallel to the beam direction;
- efficient electron and muon identification, with low mis-identification probabilities for hadrons. This feature is crucial for tagging the B flavor, for the reconstruction of charmonium states, and is also important for the study of decays involving leptons;
- efficient and accurate identification of hadrons over a wide range of momenta for B flavor-tagging, and for the reconstruction of exclusive states; modes such as $B^0 \to K^{\pm}\pi^{\mp}$ or $B^0 \to \pi^+\pi^-$, as well as in charm meson and τ decays;

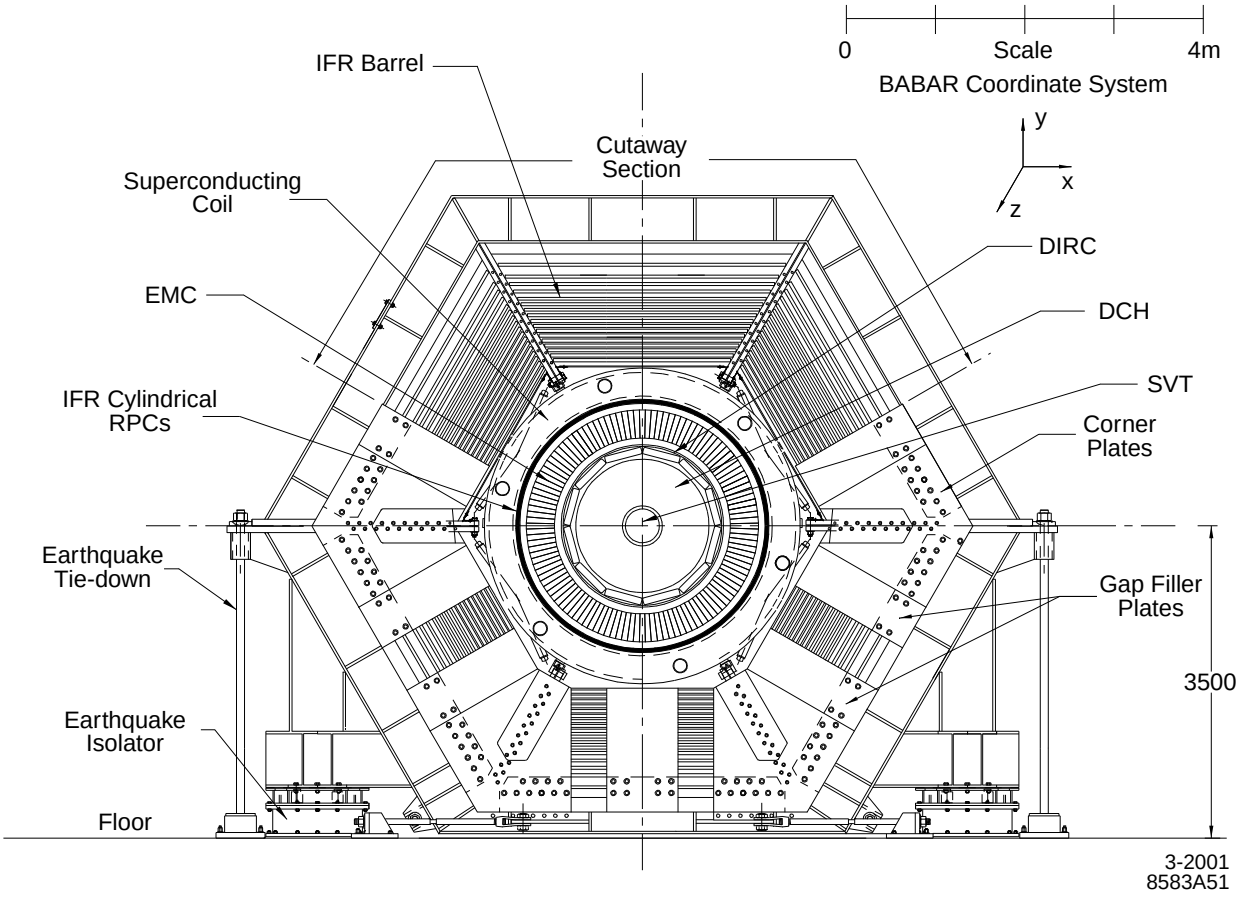

Figure 2.2: *BABAR* detector end view.

- a flexible, redundant, and selective trigger system;
- low-noise electronics and a reliable, high bandwidth data-acquisition and control system;
- detailed monitoring and automated calibration;
- an online computing and network system that can control, process, and store the expected high volume of data; and
- detector components that can tolerate significant radiation doses and operate reliably under high-background conditions.

To reach the desired sensitivity for the most interesting measurements, data sets of order 10^8 B mesons are needed. For the peak cross section at the $\Upsilon(4S)$ of about 1.1 nb, the design project required an integrated luminosity of order $100\,\mathrm{fb}^{-1}$ in three years of reliable and highly efficient operation of the detector. This target has been fully achieved.

In the following, a brief descriptions of the PEP-II interaction region, the beam characteristics, and of the impact of the beam generated background is given. Finally, a detailed presentation of the *BABAR* detector systems is provided.

2.2 The PEP-II Storage Rings

2.2.1 PEP-II Storage Rings

PEP-II is an e^+e^- storage ring system designed to operate at a center of mass (c.m.) energy of 10.58 GeV, corresponding to the $\Upsilon(4S)$ resonance. In Table 2.1 there are listed the approximate production cross sections.

Table 2.1: Approximate production cross sections at PEP-II [47].

$e^+e^- \rightarrow$	Cross-section(nb)
$b\overline{b}$	1.10
$c\overline{c}$	1.30
$s\overline{s}$	0.35
$u\overline{u}$	1.39
$d\overline{d}$	0.35
$\tau^+\tau^-$	0.94
$\mu^+\mu^-$	1.16
e^+e^-	≈ 40

The design and 2006 parameters of these asymmetric energy storage rings are presented in Table 2.2 [46]; PEP-II has surpassed its design goals, both in terms of the peak and the integrated daily luminosity. A detailed description of the design and operational experience of PEP-II can be found in references [49] and [50].

PEP-II operates in continuous injection or "trickle injection" mode. Continuous injection was made to work in November 2003 when the PEP-II and *BABAR* teams reduced the backgrounds to an acceptable level to allow *BABAR* to take data continuously. The improved efficiency for data delivery was about 30% within a few days. Trickle injection for positrons uses about five injection pulses per second from the SLAC linac, resulting in the positron current being stable to about 0.1% with *BABAR* recording more than 98% of the data. The electron ring at PEP-II proved more difficult and studies continued until March 2004 before trickle injection was successful. About three linac pulses per second are needed to keep the electron current stable to 0.1%. Since March 2004, both PEP-II rings are trickle injected simultaneously with *BABAR* taking data. So PEP-II has true trickle injection with either beam injected pulse-by-pulse with very steady currents and steady luminosity. The overall integrated luminosity efficiency increased by 10% with the HER ring above and by just over 40% with both rings together in trickle injection mode.

2.2.2 Monitoring of Beam Parameters

The beam parameters most critical for *BABAR* performance are the luminosity, the energies of the two beams, the interaction region position, angles, and size of the interaction region.

Luminosity

While PEP-II measures radiative Bhabha scattering to provide a fast monitor of the relative luminosity for operations, *BABAR* derives the absolute luminosity offline from other QED processes, primarily e^+e^-, and $\mu^+\mu^-$ pairs. The measured rates are consistent and stable as a function of time. For a data sample of $1\,\mathrm{fb}^{-1}$, the statistical error is less than 1%. The systematic uncertainty on the relative changes of

Table 2.2: Some of the PEP-II beam parameters. Values are given both for the design and for typical colliding beam operation in year 2006. HER and LER refer to the high energy e^- and low energy e^+ ring, respectively. σ_z refer to the longitudinal rms size of the luminous region.

Parameters	Design	Present [46]
Energy HER/LER (GeV)	9.0/3.1	9.0/3.1
Current HER/LER (A)	0.75/2.14	1.776/2.95
Number of bunches	1658	1722
σ_z (mm)	11	11-12
Luminosity ($10^{33}\,\mathrm{cm}^{-2}\mathrm{s}^{-1}$)	3	10.88
Integrated luminosity (fb^{-1}/month)	3.3	17.04
Total integrated luminosity (fb^{-1})	30/year	375

the luminosity is less than 0.5%, while the systematic error on the absolute value of the luminosity is estimated to be about 1.5%. This error is currently dominated by uncertainties in the Monte Carlo generator and the simulation of the detector.

Beam Energies

During operation, the mean energies of the two beams are calculated from the total magnetic bending strength (including the effects of off-axis quadrupole fields, steering magnets, and wigglers) and the average deviations of the accelerating frequencies from their central values. While the systematic uncertainty in the PEP-II calculation of the absolute beam energies is estimated to be 5–10 MeV, the relative energy setting for each beam is accurate and stable to about 1 MeV. The rms energy spreads of the LER and HER beams are 2.3 MeV and 5.5 MeV, respectively.

To ensure that data are recorded close to the peak of the $\Upsilon(4S)$ resonance, the observed ratio of $B\overline{B}$ enriched hadronic events to lepton pair production is monitored online. Near the peak of the resonance, a 2.5% change in the $B\overline{B}$ production rate corresponds to a 2 MeV change in the c.m. energy, a value that is close to the tolerance to which the energy of PEP-II can be held. However, a drop in the $B\overline{B}$ rate does not distinguish between energy settings below or above the $\Upsilon(4S)$ peak. The sign of the energy change must be determined from other indicators. The best monitor and absolute calibration of the c.m. energy is derived from the measured c.m. momentum of fully reconstructed B mesons combined with the known B-meson mass.

The beam energies are necessary input for the calculation of two kinematic variables that are commonly used to separate signal from background in the analysis of exclusive B-meson decays. These variables, which make optimum use of the measured quantities and are largely uncorrelated, are Lorentz-invariants which can be evaluated both in the laboratory and c.m. frames.

The first variable, ΔE, can be expressed in Lorentz invariant form as

$$\Delta E = (2q_B q_0 - s)/2\sqrt{s}, \tag{2.1}$$

where $\sqrt{s} = 2E^*_{beam}$ is the total energy of the e^+e^- system in the c.m. frame, and q_B and $q_0 = (E_0, \vec{p}_0)$ are the Lorentz vectors representing the momentum of the B candidate and of the e^+e^- system, $q_0 = q_{e+} + q_{e-}$. In the c.m. frame, ΔE takes the familiar form

$$\Delta E = E^*_B - E^*_{beam}, \tag{2.2}$$

here E^*_B is the reconstructed energy of the B meson. The ΔE distribution receives a sizable contribution from the beam energy spread, but is generally dominated by detector resolution.

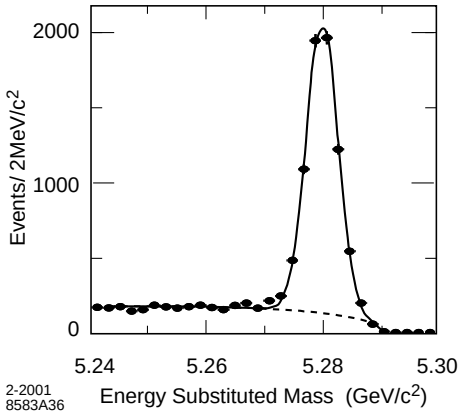

Figure 2.3: The energy-substituted mass for a sample of 6,700 neutral B mesons reconstructed in the final states $D^{(*)-}\pi^+, D^{(*)-}\rho^+, D^{(*)-}a_1^+$, and $J/\psi K^{*0}$. The background is extrapolated from events outside the signal region.

The second variable is the energy-substituted mass, $m_{\rm ES}$, defined as $m_{\rm ES}{}^2 = q_B^2$. In the laboratory frame, $m_{\rm ES}$ can be determined from the measured three-momentum $\vec{p}_B$ of the B candidate without explicit knowledge of the masses of the decay products:

$$m_{\rm ES} = \sqrt{(s/2 + \vec{p}_B \cdot \vec{p}_0)^2/E_0^2 - p_B^2}. \tag{2.3}$$

In the c.m. frame ($\vec{p}_0 = 0$), this variable takes the familiar form

$$m_{\rm ES} = \sqrt{E_{beam}^{*2} - p_B^{*2}}, \tag{2.4}$$

where p_B^* is the c.m. momentum of the B meson, derived from the momenta of its decay products, and the B-meson energy is substituted by E_{beam}^*. Figure 2.3 shows the $m_{\rm ES}$ distribution for a sample of fully reconstructed B mesons. The resolution in $m_{\rm ES}$ is dominated by the spread $\sigma_{E_{beam}^*} = 2.6\,\mathrm{MeV}$ in E_{beam}^*.

Beam Direction

The direction of the beams relative to *BABAR* is measured iteratively run-by-run using $e^+e^- \to e^+e^-$ and $e^+e^- \to \mu^+\mu^-$ events. The resultant uncertainty in the direction of the boost from the laboratory to the c.m. frame, $\vec{\beta}$, is about 1 mrad, dominated by alignment errors. This translates into an uncertainty of about 0.3 MeV in m_{ES}. $\vec{\beta}$ is consistent to within 1 mrad with the orientation of the elongated beam spot (see below).

Beam Size and Position

The size and position of the interaction region are critical parameters for the decay-time-dependent analysis and their values are monitored continuously online and offline. The vertical size is too small to be measured directly. It is inferred from the measured luminosity, the horizontal size, and the beam currents; it varies typically by 1–2 μm.

The transverse position, size, and angles of the luminous region relative to the *BABAR* coordinate system are determined by analyzing the distribution of the distance of closest approach to the z-axis of the tracks in well measured two-track events as a function of the azimuth ϕ. The longitudinal parameters are derived from the longitudinal vertex distribution of the two tracks. A combined fit to

nine parameters (three average coordinates, three widths, and three small angles) converges readily, even after significant changes in the beam position. The uncertainties in the average beam position are of the order of a few μm in the transverse plane and 100 μm along the collision axis. Run-by-run variations in the beam position are comparable to these measurement uncertainties, indicating that the beams are stable over the period of a typical run. The fit parameters are stored run-by-run in the *conditions database*. These measurements are also checked offline by measuring the primary vertices in multi-hadron events. The measured horizontal and longitudinal beam sizes, corrected for tracking resolution, are consistent with those measured by PEP-II.

2.2.3 Beam Background Sources

The primary sources of steady-state accelerator backgrounds are, in order of increasing importance: synchrotron radiation in the vicinity of the interaction region; interactions between the beam particles and the residual gas in either ring; and electromagnetic showers generated by beam-beam collisions [52–54]. In addition, there are other background sources that fluctuate widely and can lead to very large instantaneous rates, thereby disrupting stable operation.

2.3 The Solenoid Magnet and Flux Return

The *BABAR* magnet system consists of a super-conducting solenoid [55], a segmented flux return and a field compensating or *bucking coil*. This system provides the magnetic field which enables charged particle momentum measurement, serves as the hadron absorber for hadron/muon separation, and provides the overall structure and support for the detector components. Figures 2.1 and 2.2 show key components of the *BABAR* magnet system and some of the nearby PEP-II magnets.

The magnet coil cryostat is mounted inside the hexagonal barrel flux return by four brackets on each end. The total weight of the flux return is approximately 870 metric tons.

To optimize the detector acceptance for unequal beam energies, the center of the *BABAR* detector is offset by 370 mm in the electron beam direction. The principal component of the magnetic field, B_z, lies along the $+z$ axis; this is also the approximate direction of the electron beam. The backward end door is tailored to accommodate the DIRC bar boxes and to allow access to the drift chamber electronics. Both ends allow space and adequate shielding for the PEP-II quadrupoles.

A solenoid magnetic field of 1.5 T was specified in order to achieve the desired momentum resolution for charged particles. To simplify track finding and fast and accurate track fitting, the magnitude of the magnetic field within the tracking volume was required to be constant within a few percent.

2.3.1 Magnetic Flux Return

The magnet flux return supports the detector components on the inside, but this load is not a major issue. Far greater demands are placed on the structural design by the magnetic forces and the mechanical forces from a potential earthquake.

Magnetic forces are of three kinds. First, there is a symmetric magnetic force on the end doors which was taken into consideration in their design and construction. Second, there is an axial force on the solenoid due to the forward-backward asymmetry of the steel. Because the steel is highly saturated in places, the magnitude of the field asymmetry changes when the current is raised from zero, and there is no position of the solenoid at which the force remains zero at all currents. Because it is important that this axial force should not change sign, which could cause a quench, the superconducting solenoid was deliberately offset by 30 mm towards the forward door. This offset was chosen to accommodate a worst case scenario, including uncertainties in the calculation. Third, during a quench of the superconducting coil, eddy currents in conducting components inside the magnetic volume could generate

sizable forces. These forces were analyzed for components such as the end-plates of the drift chamber and the electromagnetic calorimeter and were found not to be a problem.

2.3.2 Magnet Coils

The solenoid is indirectly cooled to an operating point of 4.5K.

To reduce the leakage fields into the PEP-II components and the DIRC photomultipliers, an additional external bucking coil is installed [57]. This is a conventional water cooled copper coil consisting of ten layers. Although the nominal operating current is 200 A, a current of up to 575 A is attainable, if needed, to demagnetize the DIRC shield.

To optimally control the stray fields and avoid a magnetization of the DIRC magnetic shield, the currents in the solenoid and the bucking coil are ramped together under computer control. High precision transducers are used to measure the currents and provide the feedback signals to the power supplies. The values of the currents are recorded in the *BABAR* database.

2.4 Silicon Vertex Tracker

2.4.1 Charged Particle Tracking

The Silicon Vertex Tracker is the most relevant detector for the measurement of time dependent *CP* asymmetries in *BABAR*. The finite precision in the reconstruction of the z difference is required not to degrade the error in the *CP* asymmetry by more than 10%. In order to achieve this goal, the resolution is required to be better than 80 μm on fully reconstructed B decay vertices.

Accurate vertex reconstruction is the crucial goal for SVT, so high precision in tracks measurement is required. Track measurements are also important for the extrapolation to the DIRC, EMC, and IFR. At lower momenta, the DCH measurements are more important, while at higher momenta the SVT measurements dominate. Most critical are the angles at the DIRC, because the uncertainties in the charged particle track parameters add to the uncertainty in the measurement of the Cherenkov angle. Thus, the track errors from the combined SVT and DCH measurements should be small compared to the average DIRC Cherenkov angle measurements, *i.e.,* of order of 1 mrad, particularly at the highest momenta.

2.4.2 SVT Goals and Design Requirements

The SVT has been designed to provide precise reconstruction of charged particle trajectories and decay vertices near the interaction region. The design choices were driven primarily by direct requirements from physics measurements and constraints imposed by the PEP-II interaction region and *BABAR* experiment. In this Section the mechanical and electronic design of the SVT are discussed, with some discussion of the point resolution per layer and dE/dx performance. The tracking performance and efficiency of the SVT alone and in combination with the DCH are described in Section 2.6.

As already said, the mean vertex resolution along the z-axis for a fully reconstructed B decay has to be better than 80 μm [48]; the required resolution in the x–y plane arises from the need to reconstruct final states in B decays as well as in τ and charm decays. The SVT needs to provide resolution of order $\sim$100 μm in the plane perpendicular to the beam line.

Many of the decay products of B mesons have low transverse momentum p_t. The SVT must provide stand-alone tracking for particles with transverse momentum less than 120 MeV/c, the minimum that can be measured reliably in the DCH alone. This feature is fundamental for the identification of slow pions from D^*-meson decays: a tracking efficiency of 70% or more was desirable for tracks with a

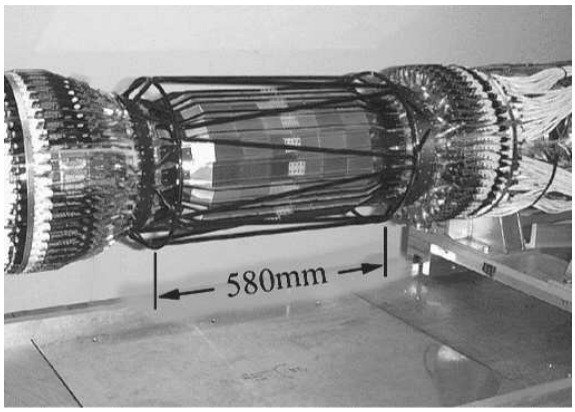

Figure 2.4: Fully assembled SVT. The silicon sensors of the outer layer are visible, as is the carbon-fiber space frame (black structure) that surrounds the silicon.

transverse momentum in the range 50–120 MeV/c. The stand-alone tracking capability and the need to link SVT tracks to the DCH were crucial in choosing the number of layers.

Beyond the stand-alone tracking capability, the SVT provides the best measurement of track angles, which is required to achieve design resolution for the Cherenkov angle for high momentum tracks. Additional constraints are imposed by the storage ring components. The SVT is located inside the ∼4.5 m-long support tube, that extends all the way through the detector. To maximize the angular coverage, the SVT must extend down to 350 mrad (20°) in polar angle from the beam line in the forward direction. The region at smaller polar angles is occupied by the B1 permanent magnets. In the backward direction, it is sufficient to extend the SVT sensitive area down to 30°. The SVT was designed to withstand at least to 2 MRad of integrated ionizing radiation. A radiation monitoring system capable of aborting the beams is required. The expected radiation dose is 1 Rad/day in the horizontal plane immediately outside the beam pipe (where the highest radiation is concentrated), and 0.1 Rad/day on average otherwise. The SVT is cooled to remove the heat generated by the electronics. In addition, it operates in the 1.5 T magnetic field.

To achieve the position resolution necessary to carry out physics analysis, the relative position of the individual silicon *sensors* should be stable over long time periods. The assembly allows for relative motion of the support structures with respect to the B1 magnets.

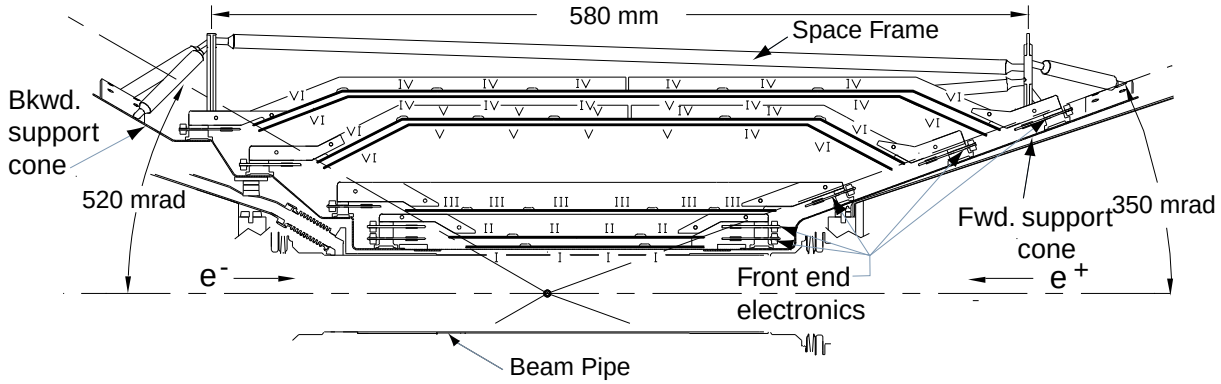

Figure 2.5: Schematic view of SVT: longitudinal section.

These requirements and constraints have led to the choice of a SVT made of five layers of double-sided silicon strip sensors. To fulfill the physics requirements, the spatial resolution, for perpendicular tracks, must be 10–15 μm in the three inner layers and about 40 μm in the two outer layers. The inner three layers perform the impact parameter measurements, while the outer layers are necessary for pattern recognition and low p_t tracking.

2.4.3 SVT Layout

The five layers of double-sided silicon strip sensors, which form the SVT detector, are organized in 6, 6, 6, 16, and 18 modules, respectively; a photograph is shown in Figure 2.4. The strips on the opposite sides of each sensor are oriented orthogonally to each other: the ϕ measuring strips (ϕ *strips*) run parallel to the beam and the z measuring strips (z *strips*) are oriented transversely to the beam axis. The modules of the inner three layers are straight, while the modules of layers 4 and 5 are *arch*-shaped (Figures 2.5 and 2.6).

This arch design was chosen to minimize the amount of silicon required to cover the solid angle, while increasing the crossing angle for particles near the edges of acceptance. A photograph of an outer layer arch module is shown in Figure 2.7. The modules are divided electrically into two half-modules, which are read out at the ends.

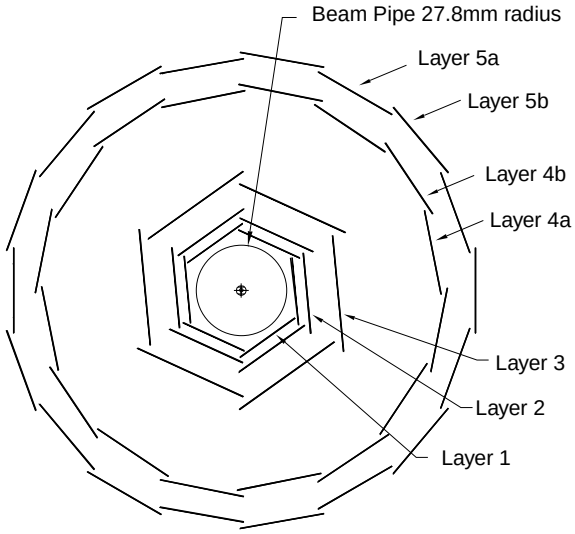

Figure 2.6: Schematic view of SVT: transverse section.

To satisfy the different geometrical requirements of the five SVT layers, five different sensor shapes are required to assemble the planar sections of the layers. The smallest detectors are $43 \times 42\,\mathrm{mm}^2$ ($z \times \phi$), and the largest are $68 \times 53\,\mathrm{mm}^2$. Two identical trapezoidal sensors are added (one each at the forward and backward ends) to form the arch modules. The half-modules are given mechanical stiffness by means of two carbon fiber/kevlar ribs, which are visible in Figure 2.7. The ϕ strips of sensors in the same half-module are electrically connected with wire bonds to form a single readout strip. This results in a total strip length up to 140 mm (240 mm) in the inner (outer) layers.

The signals from the z strips are brought to the readout electronics using fanout circuits consisting of conducting traces on a thin (50 μm) insulating Upilex [58] substrate. For the innermost three layers, each z strip is connected to its own preamplifier channel, while in layers 4 and 5 the number of z strips on a half-module exceeds the number of electronics channels available, requiring that two z

Figure 2.7: Photograph of an SVT arch module in an assembly jig.

strips on different sensors be electrically connected (ganged) to a single electronics channel. The length of a z strip is about 50 mm (no ganging) or 100 mm (two strips connected). The ganging introduces an ambiguity on the z coordinate measurement, which must be resolved by the pattern recognition algorithms. The total number of readout channels is approximately 150,000.

The inner modules are tilted in ϕ by 5°, allowing an overlap region between adjacent modules, a feature that provides full azimuthal coverage and is advantageous for alignment. The outer modules cannot be tilted, because of the arch geometry. To avoid gaps and to have a suitable overlap in the ϕ coordinate, layers 4 and 5 are divided into two sub-layers (4a, 4b, 5a, 5b) and placed at slightly different radii (see Figure 2.6). The relevant geometrical parameters of each layer are summarized in Table 2.3.

In order to minimize the material in the acceptance region, the readout electronics are mounted entirely outside the active detector volume. The forward electronics must be mounted in the 10 mm space between the 350 mrad stay-clear space and B1 magnet. This implies that the hybrids carrying the front-end chip must be positioned at an angle of 350 mrad relative to the sensor for the layers 3, 4, and 5 (Figure 2.5). In the backward direction, the available space is larger and the inner layer electronics can be placed in the sensor plane, allowing a simplified assembly.

The module assembly and the mechanics are quite complicated, especially for the arch modules, and are described in detail elsewhere [59]. The SVT support structure (Figure 2.4) is a rigid body made from two carbon-fiber cones, connected by a *space frame*, also made of carbon-fiber epoxy laminate.

An optical survey of the SVT on its assembly jig indicated that the global error in placement of the sensors with respect to design was $\sim$200 μm, FWHM. Subsequently, the detector was disassembled and shipped to SLAC, where it was re-assembled on the IR magnets. The SVT is attached to the B1 magnets by a set of gimbal rings in such a way as to allow for relative motion of the two B1 magnets while fixing the position of the SVT relative to the forward B1 and the orientation relative to the axis of both B1 dipoles. The support tube structure is mounted on the PEP-II accelerator supports, independently of *BABAR*, allowing for movement between the SVT and the rest of *BABAR*. Precise monitoring of the beam interaction point is necessary, as is described in Section 2.4.5.

The total active silicon area is 0.96 m ^{2} and the material traversed by particles is $\sim$ 4% of a radiation

Table 2.3: Geometric parameters for each layer and readout plane of the SVT. Floating strips refers to the number of strips between readout (R-O) strips. Note: parts of the ϕ sides of layers 1 and 2 are bonded at 100 μm and 110 μm pitch, respectively, with one floating strip. Strip length of z-strips for layers 4 and 5 includes ganging. The radial range for layers 4 and 5 includes the radial extent of the arched sections.

Layer/ view	Radius (mm)	R-O pitch (μm)	Floating strips	Strip length (mm)
1 z	32	100	1	40
1 ϕ	32	50-100	0-1	82
2 z	40	100	1	48
2 ϕ	40	55-110	0-1	88
3 z	54	100	1	70
3 ϕ	54	110	1	128
4 z	91-127	210	1	104
4 ϕ	91-127	100	1	224
5 z	114-144	210	1	104
5 ϕ	114-144	100	1	265

length. The geometrical acceptance of SVT is 90% of the solid angle in the c.m. system, typically 86% are used in charged particle tracking.

2.4.4 SVT Components

A block diagram of SVT components is shown in Figure 2.8. The basic components of the detector are the silicon sensors, the *fanout* circuits, the *Front End Electronics* (FEE) and the data transmission system. Each of these components is discussed below.

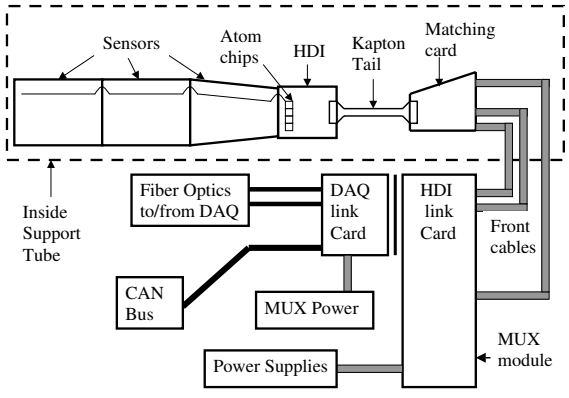

Figure 2.8: Schematic block diagram showing the different components of the SVT.

Silicon Sensors

The SVT sensors [60] are 300 μm thick double-sided silicon strip devices. They were designed at INFN Pisa and Trieste (Italy) and fabricated commercially [61]. They are built on high-resistivity (6–15 kΩ-

Table 2.4: Electrical parameters of the SVT, shown for the different layers and views. C_{input} refers to the total input capacitance, R_{series} is the series resistance. The amplifier peaking time is 200 ns for layers 1–3 and 400 ns for layers 4–5.

Layer/ view	$C_{\rm input}$ (pF)	$R_{\rm series}$ (Ω)	Noise, calc. (elec)	meas. (elec)
1 z	6.0	40.	550	880
1 ϕ	17.2	164.	990	1200
2 z	7.2	48.	600	970
2 ϕ	18.4	158.	1030	1240
3 z	10.5	70.	700	1180
3 ϕ	26.8	230.	1470	1440
4 z	16.6	104.	870	1210
4 ϕ	33.6	224.	1380	1350
5 z	16.6	104.	870	1200
5 ϕ	39.7	265.	1580	1600

cm) n-type substrates with p^+ strips and n^+ strips on the two opposite sides. The insulation of the n^+ strips is provided by individual p-stops, so as to achieve an inter-strip linear resistance greater than 100 MΩ at operating bias voltage, normally about 10 V above the depletion voltage.

Typical depletion voltages are in the range 25–35 V. The strips are biased on both sides with polysilicon resistors (4–20 MΩ) to ensure the required radiation hardness, keeping the voltage drop across resistors and the parallel noise as low as possible. Strips are AC-coupled to the electronics via integrated decoupling capacitors, the capacitance of which depends on the sensor shape, but is always greater than 14 pF/cm. The sensors were designed to maximize the active area, which extends to within 0.7 mm of the physical edges. Another design goal was to control the inter-strip capacitance: values between 0.7 pF/cm and 1.1 pF/cm were obtained for the various sensor shapes. To achieve the required spatial resolution, while keeping the number of readout channels as low as possible, most of the modules have a *floating strip* (*i.e.,* not read out) between two readout strips.

The leakage currents, because of the excellent performance of the manufacturing process, were as low as 50 nA/cm^2 on average, measured at 10 V above depletion voltage. The silicon sensor parameters have been measured after irradiation with ^{60}Co sources. Apart from an increase in the inter-strip capacitance of about 12% during the first 100 krad, the main effect was an increase of the leakage current by 0.7 μA/cm^2/MRad. However, in a radiation test performed in a 1 GeV/c electron beam, an increase in leakage current of about 2 μA/cm^2/MRad and a significant shift in the depletion voltage, dependent on the initial dopant concentration, were observed. A shift of about 8–10 V was seen for irradiation corresponding to a dose of approximately 1 MRad. These observations indicate significant bulk damage caused by energetic electrons. As indicated by the change in depletion voltage, the SVT sensors could undergo type inversion after about 1–3 MRad. Preliminary tests show that the sensors continue to function after type inversion [62]. Studies of the behavior of SVT modules as a function of radiation dose continue.

Fanout Circuits

The fanout circuits, which route the signals from the strips to the electronics, have been designed to minimize the series resistance and the inter-strip capacitance. As described in ref. [63], a trace on the fanout has a series resistance about 1.6 Ω/cm, an inter-strip resistance > 20 MΩ, and an inter-strip capacitance < 0.5 pF/cm. The electrical parameters of the final assembly of sensors and fanouts

(referred to as *Detector Fanout Assemblies* or DFAs) are summarized in Table 2.4. Due to the different strip lengths, there are large differences between the inner and the outer layers. Smaller differences are also present between the forward and backward halves of the module, that are of different lengths.

Front End Electronics

The electrical parameters of a DFA and the general *BABAR* requirements are the basic inputs that drove the design of the SVT front-end custom integrated circuit (IC); the ATOM (*A Time-Over-Threshold Machine*). In particular, the front-end IC had to satisfy the following requirements:

- signal to noise ratio greater than 15 for *minimum ionizing particle* (MIP) signals for all modules;
- signals from all strips must be retained, in order to improve the spatial resolution through interpolation, while keeping the number of transmitted hits as low as possible. A *hit* refers to a deposited charge greater than 0.95 fC, corresponding to 0.25 MIP;
- the amplifier must be sensitive to both negative and positive charge;
- the peaking time must be programmable, with a minimum of 100 ns (in layers 1 and 2, because of the high occupancy), up to 400 ns (outer layers, with high capacitance);
- capability to accept random triggers with a latency up to 11.5 μs and a programmable jitter up to $\pm 1\,\mu$s, without dead time;
- radiation hardness greater than 2.5 MRad;
- small dimensions: 128 channels in a 6.2 mm-wide chip.

These requirements are fully satisfied by the ATOM IC [64], which is depicted schematically in Figure 2.9.

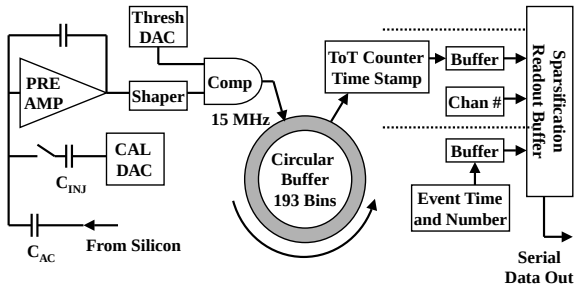

Figure 2.9: Schematic diagram of the ATOM front end IC.

The linear analog section consists of a charge-sensitive preamplifier followed by a shaper. Gains of 200 mV/fC (low) or 300 mV/fC (high) may be selected. The channel gains on a IC are uniform to 5 mV/fC. Signals are presented to a programmable-threshold comparator, designed so that the output width of the pulse (*Time over Threshold* or ToT) is a quasi-logarithmic function of the collected charge. This output is sampled at 30 MHz and stored in a 193 location buffer. Upon receipt of a *Level 1* (L1) trigger, the time and ToT is retrieved from this latency buffer, sparsified, and stored in a four event buffer. Upon the receipt of an *L1 Accept* command from the data acquisition system, the output data (the 4 bits for the ToT, 5 bits for the time stamp, and 7 bits for the strip address) are formatted, serialized, and delivered to the ROM. The IC also contains a test charge injection circuit. The typical

Table 2.5: ATOM chip ENC parameters at different peaking times

Peaking time	ENC (0 pF)	Noise slope
100 ns	380 e^-	40.9 e^-/pF
200 ns	280 e^-	33.9 e^-/pF
400 ns	220 e^-	25.4e^-/pF

noise behavior of the ATOM, as described by the *Equivalent Noise Charge* (ENC) of the linear analog section is given in Table 2.5.

The average noise for the various module types is shown in Table 2.4. Given that shot noise due to sensor leakage current is negligible, the expected noise may be calculated from the parameters of Tables 2.4 and 2.5. The results of such a calculation are also shown in Table 2.4. The maximum average noise is 1,600 electrons, leading to a signal-to-noise ratio greater than 15.

The power consumption of the IC is about 4.5 mW/channel. Radiation hardness was studied up to 2.4 MRad with a ^{60}Co source. At that dose, the gain decreased 20%, and the noise increased less than 15%.

The ATOM ICs are mounted on thick-film double-sided hybrid circuits (known as *High Density Interconnects* or HDIs) based on an aluminum-nitride substrate with high thermal conductivity. The electronics are powered through a floating power supply system, in such a way as to guarantee a small voltage drop (< 1 V) across the detector decoupling capacitors.

Data Transmission

The digitized signals are transmitted from the ATOM ICs through a thin *kapton tail* or cable to the *matching cards*, from where they are routed to more conventional cables. Just outside the detector, signals are *multiplexed* by the MUX modules, converted into optical signals and transmitted to the *Readout Modules* (ROMs). The MUX modules also receive digital signals from the DAQ via a fiber optical connection. The SVT is connected to the *BABAR* online detector control and monitoring system via the industry standard CAN bus. Details on SVT data transmission system and DAQ can be found in references [65,66]. Power to SVT modules (silicon sensor bias voltage and ATOM low voltages) is provided by a CAEN A522 power supply system [67].

2.4.5 Monitoring and Calibration

To identify immediately any operational problems, the SVT is integrated in the control and monitoring system. Major concerns for SVT monitoring are temperature and humidity, mechanical position, and radiation dose.

Temperature and Humidity Monitors

The total power dissipation of the SVT modules is about 350 W, mainly dissipated in the ATOM ICs. External cooling is provided by chilled water at 8°C. In addition, humidity is reduced by a stream of dry air in the support tube.

Since condensation or excessive temperature can permanently damage the FEE, temperature and humidity monitoring are very important to the safe operation of the SVT. Thermistors are located on the HDIs (for the measurements of FEE temperature), around the SVT, along the cooling systems,

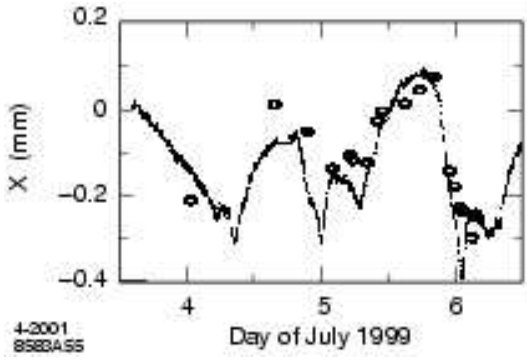

Figure 2.10: Horizontal motion between the DCH and the support tube measured with the capacitive sensors (curve) compared to the mean x coordinate of the interaction point (circles) measured with e^+e^- and $\mu^+\mu^-$ events over a three-day period in July 1999. An arbitrary offset and scale has been applied to the beam position data.

and in the electronics (MUX) crates. The absolute temperatures are monitored to 0.2°C and relative changes of 0.1°C. Additionally, a series of humidity sensors are employed to monitor the performance of the dry air system. The temperature and humidity monitors also serve as an interlock to the HDI power supplies.

Position Monitors

A system of capacitive sensors was installed to identify and track changes in the position of the SVT with respect to the PEP-II B1 magnets and the position of the support tube with respect to the DCH. An example of the understanding that can be achieved by this system is given in Figure 2.10, where the measured changes in the horizontal position of the SVT relative to the DCH are shown for a period of three days in the summer of 1999. These position changes can be attributed to local temperature variations. The sensor data are compared to measurements of the mean position of the interaction point (in the horizontal plane) determined with e^+e^- and $\mu^+\mu^-$ events recorded over this period. While the amplitude of motion at the time was uncharacteristically large, the strong correlation between these independent measurements is quite evident. Alignment with charged particle tracks is now performed routinely to correct for relative motion of the tracking systems.

Radiation Monitors

Radiation monitoring is extremely important to ensure the SVT does not exceed its radiation budget, which could cause permanent damage to the device. To date, the measured radiation absorbed by the SVT is well within the allowed budget.

Calibrations

Once a day, and each time the SVT configuration of data acquisition has changed, calibrations are performed in absence of circulating beams. All electronic channels are tested with pulses through test capacitors, for different values of the injected charge. Gains, thresholds, and electronic noise are measured, and defective channels are identified. The calibration results have proven very stable and repeatable. The main variation in time is the occasional discovery of a new defective channel. The calibration procedures have also been very useful for monitoring noise sources external to the SVT.

Defects

Due to a series of minor mishaps incurred during the installation of the SVT, nine out of 208 readout sections (each corresponding to one side of a half-module) were damaged and are currently not functioning. There is no single failure mode, but several causes: defective connectors, mishandling during installation, and not-fully-understood problems on the FEE hybrid. There has been no module failure due to radiation damage. It should be noted that due to the redundancy afforded by the five layers of the SVT, the presence of the defective modules has minimal impact on physics analysis.

In addition, there are individual channel defects, of various types, at a level of about 1%. Calibrations have revealed an increase in the number of defective channels at a rate of less than 0.2%/year.

2.4.6 Data Analysis and Performance

This Section describes the reconstruction of space points from signals in adjacent strips on both sides of the sensors, the SVT internal and global alignment, single hit efficiency, and resolution and dE/dx performance of the SVT.

Cluster and Hit Reconstruction

Under normal running conditions, the average occupancy of the SVT in a time window of 1 μs is about 3% for the inner layers, with a significant azimuthal variation due to beam-induced backgrounds, and less than 1% for the outer layers, where noise hits dominate. Figure 2.11 shows the typical occupancy as a function of IC index (equivalent to azimuthal angle, in this case) for layer 1, ϕ side. In the inner layers, the occupancy is dominated by machine backgrounds, which are significantly higher in the horizontal plane, seen in the plot as the peaks near IC indices 3 and 25.

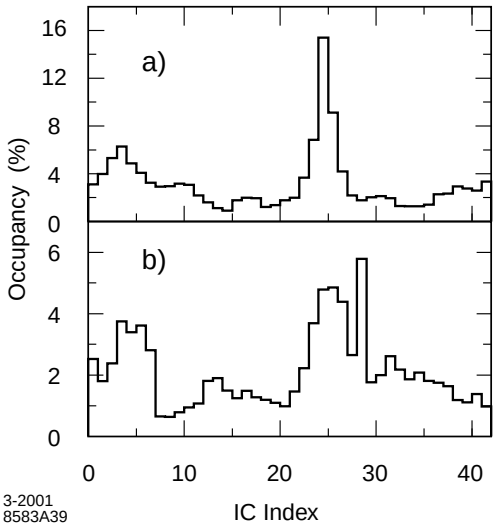

Figure 2.11: Typical occupancy in percent as a function of IC index in layer 1, ϕ side for a) forward half-modules and b) backward half-modules. The IC index increases with azimuthal angle and the higher occupancy in the horizontal plane is visible near chip indices 3 and 25.

The first step of the reconstruction program consists in discarding out-of-time channels. A time correction, *i.e.,* the time between the passage of the particle and the time the shaper exceeds threshold, is performed, after which hits with times more than 200 ns from the event time (determined by the DCH) are discarded. The loss of real hits from this procedure is negligible. The resulting in-time hits

are then passed to the cluster finding algorithm. First, the charge pulse height (Q) of a single pulse is calculated from the ToT value, and clusters are formed grouping adjacent strips with consistent times. In a second pass, clusters separated by just one strip are merged into one cluster. The two original clusters plus the merged cluster are made available to the pattern recognition algorithm, which chooses among the three.

The position x of a cluster formed by n strips is determined, with the "head-to-tail" algorithm:

$$x = \frac{(x_1 + x_n)}{2} + \frac{p}{2}\frac{(Q_n - Q_1)}{(Q_n + Q_1)},$$

where x_i and Q_i are the position and collected charge of i-th strip, respectively, and p is the readout pitch. This formula results in a cluster position that is always within $p/2$ of the geometrical center of the cluster. The cluster pulse height is simply the sum of the strip charges, while the cluster time is the average of the signal times.

Alignment

The alignment of the SVT is performed in two steps. The first step consists of determining the relative positions of the 340 silicon sensors. Once this is accomplished, the next step is to align the SVT as a whole within the global coordinate system defined by the DCH. The primary reason for breaking the alignment procedure into these two steps is that the local positions are relatively stable in time compared to the global position. Also, the local alignment procedure is considerably more complex than the global alignment procedure. Thus, the global alignment can be updated on a run-by-run basis, while the local alignment constants are changed as needed, typically after magnet quenches or detector access.

The local alignment procedure is performed with tracks from $e^+e^- \to \mu^+\mu^-$ events and cosmic rays. Well isolated, high momentum tracks from hadronic events are also used to supplement di-muon and cosmic data. Data samples sufficient to perform the local alignment are collected in one to two days of typical running conditions.

In $\mu^+\mu^-$ events, the two tracks are simultaneously fit using a Kalman filter technique and the known beam momentum. The use of tracks from cosmic rays reduces any systematic distortion that may be introduced due to imprecise knowledge of the beam momenta. No information from the DCH is used, effectively decoupling the SVT and DCH alignment.

In addition to the information from tracks, data from an optical survey performed during the assembly of the SVT are included in the alignment procedure. The typical precision of these optical measurements is $4\,\mu$m. This survey information is only used to constrain sensors relative to other sensors in the same module, but not one module to another or one layer to another. Furthermore, only degrees of freedom in the plane of the sensor are constrained as they are expected to be the most stable, given the assembly procedure.

Using the hit residuals from the aforementioned set of tracks and the optical survey information, a χ^2 is formed for each sensor and minimized with respect to the sensor's six local parameters. The constraints coming from the overlapping regions of the silicon sensors, the di-muon fit, the cosmic rays, and the optical survey result in internally consistent local alignment constants.

After the internal alignment, the SVT is considered as a rigid body. The second alignment step consists in determining the position of the SVT with respect to the DCH. Tracks with sufficient numbers of SVT and DCH hits are fit two times: once using only the DCH information and again using only the SVT hits. The six global alignment parameters, three translations and three rotations, are determined by minimizing the difference between track parameters obtained with the SVT-only and the DCH-only fits. As reported above, because of the diurnal movement of the SVT with respect to the DCH, this global alignment needs to be performed once per run ($\sim$ every 2–3 hours). The alignment constants

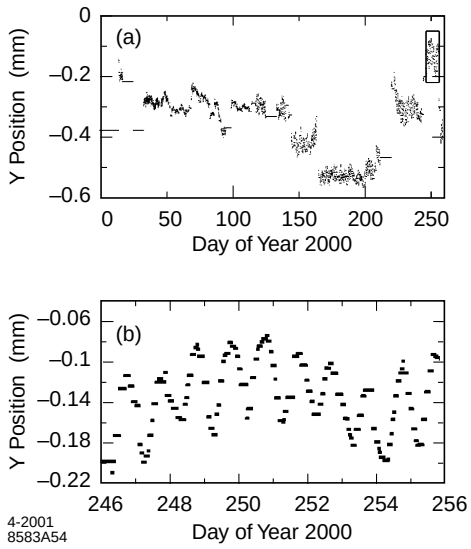

Figure 2.12: Global alignment of the SVT relative to the DCH based on e^+e^- and $\mu^+\mu^-$ events: changes in the relative vertical placement measured a) over the entire ten-month run in the year 2000, and b) a ten-day period, illustrating diurnal variations.

obtained in a given run are then used to reconstruct the data in the subsequent run. This procedure, known as *rolling calibration*, ensures that track reconstruction is always performed with up-to-date global alignment constants.

A record of the changes in the relative position of the SVT as determined by rolling calibrations is shown in Figure 2.12. The position is stable to better than $\pm 100\,\mu$m over several weeks, but changes abruptly from time to time, for instance, during access to the detector. The calibrations track diurnal variations of typically $\pm 50\,\mu$m that have been correlated with local changes in temperature of about $\pm 2°C$. Movements within a single run are small compared to the size of the beam.

Performance

The SVT efficiency can be calculated for each half-module by comparing the number of associated hits to the number of tracks crossing the active area of the module. As can be seen in Figure 2.13, a combined hardware and software efficiency of 97% is measured, excluding defective readout sections (9 out of 208), but employing no special treatment for other defects, such as broken AC coupling capacitors or dead channels on front-end chips. Actually, since most of the defects affect a single channel, they do not contribute to the inefficiency, because most tracks deposit charge in two or more strips due to track crossing angles, and charge diffusion.

The spatial resolution of SVT hits is determined by measuring the distance (in the plane of the sensor) between the track trajectory and the hit, using high-momentum tracks in two prong events. The uncertainty due to the track trajectory is subtracted from the width of the residual distribution to obtain the hit resolution. Figure 2.14 shows the SVT hit resolution for z and ϕ side hits as a function of track incident angle, for each of the five layers. The measured resolutions are in excellent agreement with expectations from Monte Carlo simulations.

Initial studies have shown that hit reconstruction efficiency and spatial resolution are effectively independent of occupancy for the occupancy levels observed so far.

Measurement of the ToT value by the ATOM ICs enables one to obtain the pulse height, and hence the ionization dE/dx in the SVT sensor. The values of ToT are converted to pulse height using a lookup table computed from the pulse shapes obtained in the bench measurements. The pulse height is

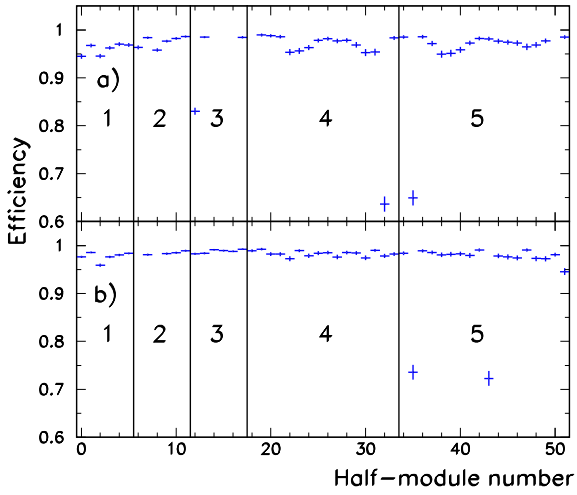

Figure 2.13: SVT hit reconstruction efficiency, as measured on $\mu^+\mu^-$ events for a) forward half-modules and b) backward half-modules. The plots show the probability of associating both a ϕ and z hit to a track passing through the active part of the detector. The horizontal axis corresponds to the different modules, with the vertical lines separating the different layers as numbered. Missing values correspond to non-functioning half-modules.

corrected for track length variation. The double-sided sensors provide up to ten measurements of dE/dx per track. For every track with signals from at least four sensors in the SVT, a 60% truncated mean dE/dx is calculated. The cluster with the smallest dE/dx energy is also removed to reduce sensitivity to electronics noise. For MIPs, the resolution on the truncated mean dE/dx is approximately 14%. A 2σ separation between the kaons and pions can be achieved up to momentum of 500 MeV/c, and between kaons and protons beyond 1 GeV/c.

2.4.7 New effects observed

After six years of operation, some unexpected affects have appeared. In particular, a shift in the pedestal for the channels of the AToM readout chips more exposed to radiation, and an anomalous increase of the bias leakage current for the modules of the outer layers, have been observed. In both cases the reason has been understood and reproduced.

Pedestal shift in AToM chips

As stated, a shift in the pedestal of the AToM readout chips for mid-plane modules has appeared. A shift in the value of the pedestal for the channels of the AToM chips has been observed, as it can be see in Figure 2.15.

The values plotted in Figure 2.15 correspond to a zero charge injection performed during a so-called "Noise calibration".

After a very detailed study of the structure of the AToM chip, we found that the effect is radiation-induced and it is due to a well-identified component of the chip.

The effect of this pedestal shift was a loss of efficiency for those channels. The net effect for the affected inner layer module was around 10%. We have raised the threshold for the AToM chip to cope with the problem. The efficiency has gone back to the original value.

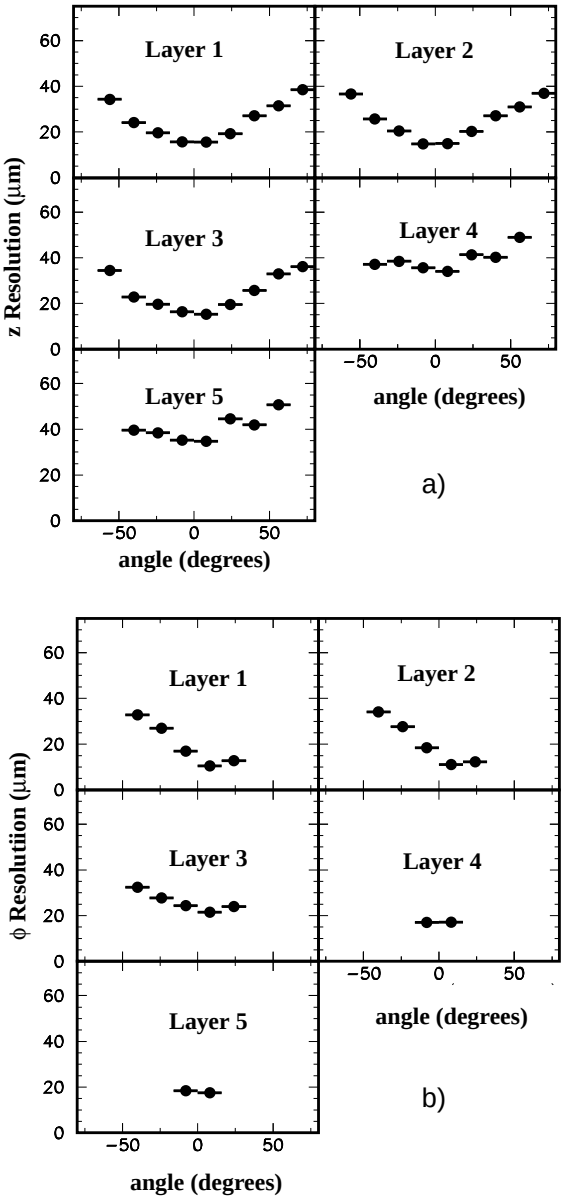

Figure 2.14: SVT hit resolution in the a) z and b) ϕ coordinate in microns, plotted as a function of track incident angle in degrees. Each plot shows a different layer of the SVT. The plots in the ϕ coordinate for layers 1-3 are asymmetric around $\phi = 0$ because of the "pinwheel" design of the inner layers. There are fewer points in the ϕ resolution plots for the outer layers as they subtend smaller angles than the inner layers.

Increase in bias leakage current

An anomalous increase in the bias leakage current has been observed since spring 2004. This increase was affecting only some modules of the layer 4. In Figure 2.16 we show an example of the increase of the bias leakage current as a function of time. It was clearly not a simple background related effect due to the absence of the effect in inner layers. Moreover, no one layer 5 module was affected, even if they were only a few millimeters far away from layer 4 ones. A series of analyses and tests were performed to try to understand the origin of the problem and some conclusions have been drawn. First of all, the

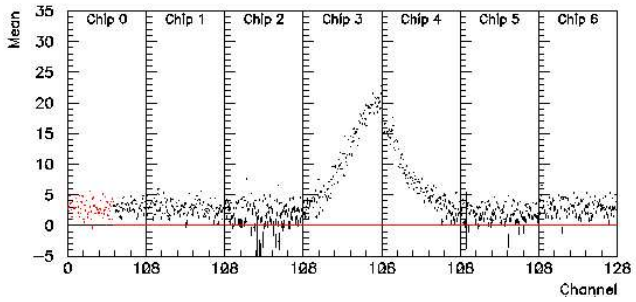

Figure 2.15: Average noise per channel with zero charge injected. It can be seen the increase in noise for chip 3 and 4.

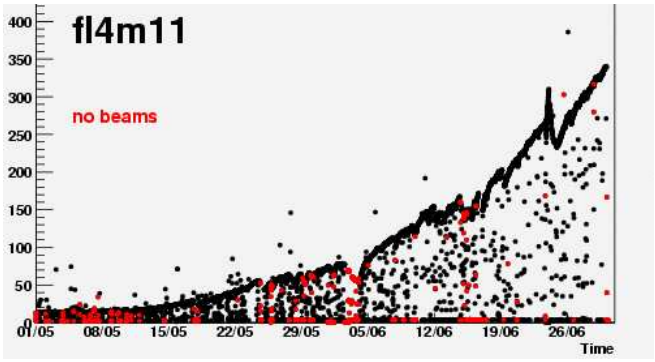

Figure 2.16: Bias leakage current as a function of time for one half module.

presence of the beams have an effect: a couple of hours without beams in the machine has determined a stop in the bias leakage current increase. Then the increase of a few percent of the relative humidity of the air in the detector have helped in order to halt the increase. Moreover, there was a non-zero voltage drop across the space between layer 4 and 5. Varying this voltage drop we were able to stop the effect. All these hints pointed to the existence of charges, induced by the beam presence, on the passivated surface of the sensors. The charge drifts toward the sensors due to the electrical field present in the space region between different layers. When deposited on the surface of the sensors, the charge accumulation modifies the internal field in the silicon, inducing a beginning of breakdown effect. A simulation of the effect has been performed and the results are in Figure 2.17.

The modification of the reference voltage for layer 4 and 5 modules and the increase of relative humidity of the air in the detector volume (from roughly 2% to about 5%) has helped in stopping the effect, limiting the drift of the charges toward the sensors and the helping the discharge of the charges on the passivated surfaces. We were eventually able to decrease the bias leakage current to the former values.

2.4.8 Summary and Outlook

The SVT has been operating efficiently since its installation in the *BABAR* experiment in May 1999. The five layer device, based on double-sided silicon sensors, has satisfied the original design goals, in particular the targets specified for efficiency, hit resolution, and low transverse momentum track

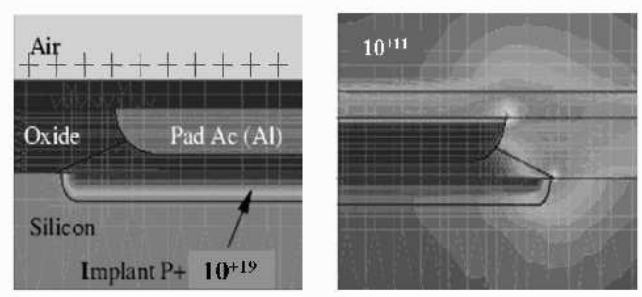

Figure 2.17: Simulation to map the electric field inside the silicon in the junction region in presence of additional positive charge on the surface passivation. The intense electric field at the tip of the p^+ implant can induce a breakdown, which is responsible for the increase in the measured leakage current.

reconstruction. With this plan for the currents an extrapolation for dose is computed. The Signal to Noise ratio has to be greater than 10. This translates into a radiation budget of about 5 MRad. Relying on the computed extrapolation, SVT will be operated smoothly until 2008. No modules so far have failed due to radiation damage. The performance of the SVT modules at high radiation dose have been studied. Results indicate that the sensors will continue to function after type inversion (at 1–3 MRad). Studies on possible deterioration of measurements of physics parameter indicate a 2-4% loss in efficiency for the mode $B^0 \to J/\psi K^0_S$ and a 2-10% effect for slow pions when you assume pessimistic scenarios (most of the chips dead in inner layers).

2.5 The Drift Chamber (DCH)

The DCH's reconstruction of track trajectories dominates *BABAR*'s measurement of charge particle momenta. It is 3 m long, inner diameter is 24 cm and outer diameter is 84 cm; it has 7104 hexagonal cells; each cell consists of one grounded tungsten-rhenium sense wire surrounded by six aluminum field wires held at more than 1900 V. The cells are grouped into 40 layers, which are in turn grouped into 10 superlayers, with the wires in each superlayer oriented as either axial (directly parallel to the z-axis) or "stereo" (at a small angle in with respect to the z-axis, in order to obtain longitudinal position information). See Figure 2.18

Each cell is able to detect traversing charge particles' ionization of a 80:20 mixture of helium:isobutane gas which is held at 4 mbar above atmospheric pressure. This choice of wire and gas minimizes multiple Coulomb scattering, presenting less than 0.2% of the radiation length (X_0) to tracks. The readout electronics, mounted on the backward end-plate in order to minimize the material in front of the forward calorimeter end-cap, measure the drift time from ionization and the integrated charge, and provide a single bit to the L1 trigger. The time-to-distance relationship within the cells, as well as calibrations for determining the deposited charge are performed offline. The time-to-distance relationship is determined from two prong events (e^+e^- and $\mu^+\mu^-$ events). The total deposited charge in each cell is used to determine the specific energy loss $\mathrm{d}E/\mathrm{d}x$, which in turn is used for particle identification (see Figure 2.19).

The dE/dx resolution for Bhabha events is typically 7.5%.

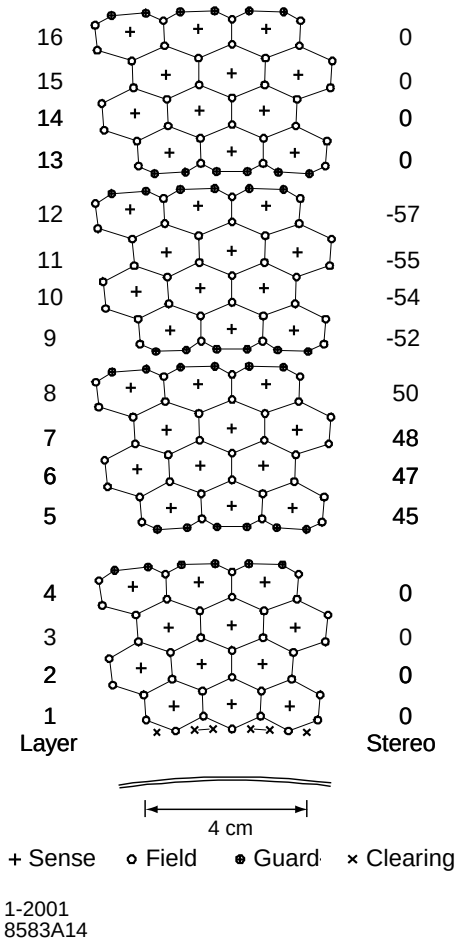

Figure 2.18: Schematic layout of drift cells for the four innermost superlayers. Lines have been added between field wires to aid in visualization of the cell boundaries. The numbers on the right side give the stereo angles (mrad) of sense wires in each layer. The 1 mm-thick beryllium inner wall is shown inside of the first layer.

2.6 Track Reconstruction

Most of the B decay modes are very dependent on precise determination of track parameters. The decay $B^0 \to \overline{D}^{(*)0} h^0$ involves pions and kaons in some of the channels and requires precise determination of mass and energy in order to separate these events from combinatoric background; thus, it is dependent on good charged particle tracking.

The reconstruction of charged particle tracks relies on the data obtained from the SVT and DCH. Charged tracks are defined by five parameters $(d_0, \phi_0, \omega, z_0, s)$ and their associated error matrix [68]:

d_0 the distance in the $x-y$ plane from the origin to the orbit (cm);

ϕ_0 the azimuthal angle corresponding to the track direction in the $x-y$ plane (rads);

ω the signed geometrical curvature: $\omega = 1/r$ (cm^{-1});

z_0 the z position of the orbit at the point of closest approach in the $x-y$ plane (cm);

s $= \tan\lambda$, the tangent of the dip angle, $\lambda = \pi/2 - \theta$ (θ is the polar angle in the lab frame).

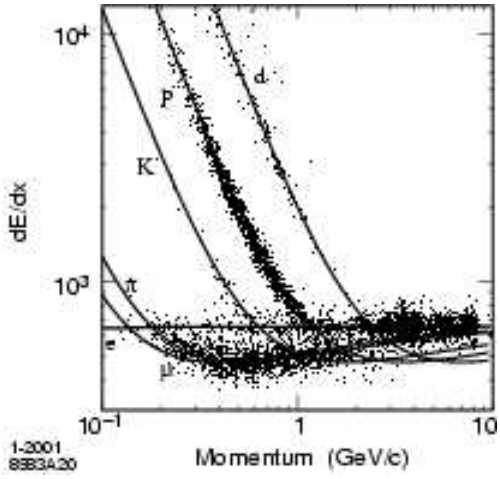

Figure 2.19: Measurement of dE/dx in the DCH as a function of track momenta. The data include large samples of beam background triggers, as evident from the high rate of protons. The curves show the Bethe-Bloch predictions with parameter derived from selected control samples of particles of different masses.

These parameters are measured at the point of closest approach to the z-axis; d_0 and z_0 are the distances of this point from the origin in the $x-y$ plane. The angle ϕ_0 is the azimuth of the track, λ the dip angle $(\pi/2-\theta)$ relative to the transverse plane, and $\omega = 1/p_t$ is its curvature. Track reconstruction is done offline and builds tracks from information initially provided by the L3 trigger. L3 provides an estimate of the time at which the e^+e^- interaction occurred, called t_0 as well as four-hit track segments in the DCH superlayers. Tracks are selected by performing a helix fit to these track segments, and a search for additional hits in the DCH that may belong to these tracks is performed; t_0 is improved by using only hits associated with tracks. Next, the L3 DCH tracks are refitted using the more precise time-to-distance calibration, while two other sophisticated pattern-finding algorithms are used to find tracks that do not pass through the entire DCH or do not originate from the IP. At the end of this procedure, tracks are again fit using a Kalman filter method [69] that takes into account the detailed distribution of material in the detector and the full map of the magnetic field.

The resulting tracks are extrapolated into the SVT, and SVT track segments are added, provided they are consistent with the expected error through the intervening material and inhomogeneous magnetic field. Among the possible SVT segments, those with the smallest residuals and the largest number of SVT layers are retained and a Kalman fit is performed to the full set of DCH and SVT hits. Any remaining SVT hits are passed to two complementary stand-alone track finding algorithms. The first of these forms "space-points" from combinations of ϕ and $z-hits$ from opposite sides of a wafer in layers 1, 3 and 5, and then adding consistent space points from the other layers. This algorithm is efficient over a wide range of d_0 and z_0 values. The second algorithm starts with circle trajectories from hits and then adds z hits to form helices. This algorithm is less sensitive to large combinatorics and to the missing z information in the few defective SVT modules. These two stand-alone SVT tracking algorithms have a high efficiency for tracks with low transverse momentum. This feature is important for the detection of the soft pion in D^* decays. In fact, the SVT significantly extends the capability of the charged particle detection down to transverse momenta as low as 50 MeV/c.

2.7 The DIRC and Particle Identification

The *BABAR* physics program has stringent requirements for $\pi - K$ separation over a large momentum range. At low momenta, below 1 GeV/c, flavor tagging using kaons form cascade decays is an efficient way of determining B flavor. At the high end of the range, reconstructing $B^0 \to \pi^+\pi^-$ and $B^0 \to K^\pm\pi^\mp$ requires separation at momenta up to 4.2 GeV/c in the laboratory frame. At intermediate energies, reducing background in charm decays such as $D^0 \to \pi^+\pi^-$, $D^0 \to KK$ and $D^0 \to K^\pm\pi^\mp$.

2.7.1 DIRC

The DIRC (Detector of Internally Reflected Cerenkov light) principle uses internal reflection within quartz bars to propagate Cerenkov light to readout phototubes while preserving the Cerenkov angle θ_C. A schematic of the DIRC principle is shown in Figure 2.20.

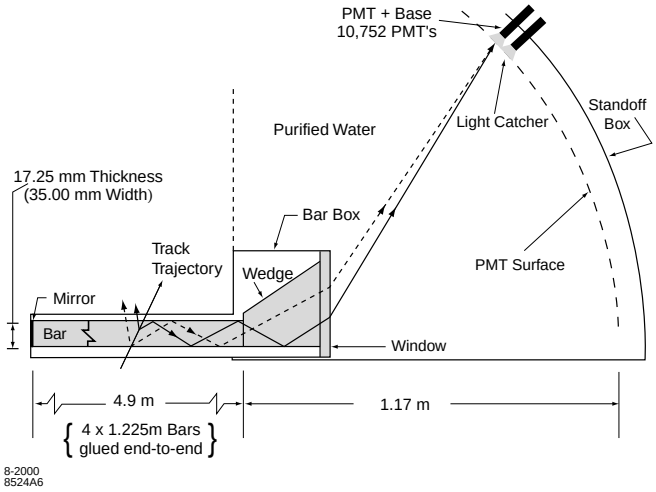

Figure 2.20: Schematics of the DIRC fused silica radiator bar and imaging region. Not shown is a 6 mrad angle on the bottom surface of the wedge (see text).

The propagation of photons and the preservation of θ_C requires extremely flat surfaces in order to avoid dispersion of the reflected angles. Fused, synthetic silica quartz is used due to the excellent optical surface it allows through polishing, as well as other favorable properties such as long attenuation length, low chromatic dispersion, small radiation length, and radiation hardness. As shown in Figure 2.20, the light is internally reflected to a wedge to reflect photons into a water-filled *standoff box*. The standoff box is enclosed by an array of 10752 photomultiplier tubes, which are each 29mm in diameter. The Cerenkov light from a particle passing through the DIRC forms a ring (essentially a conic section) imaged on the phototubes. The opening angle of this conic section contains information on particle type via the typical relation $\cos\theta_C = 1/n\beta$, where $\beta = v/c$, and n is the mean index of refraction (= 1.473 for fused silica).

Data from the phototubes is read out to front-end electronics, which performs the amplification, digitization, and buffering. Reduction of data from out-of-time or noisy PMTs is performed in in the external electronics and reduces the data volume by 50% using rough timing cuts. Online calibration of PMT efficiency, timing response, and electronics delays is provided by a light pulser system which generates precise 1 ns flashes from blue LEDs inside the standoff box.

The emission angle and the arrival time of the Cherenkov photons are reconstructed from the observed space-time coordinates of the PMT signals and then transformed into the Cherenkov coordi-

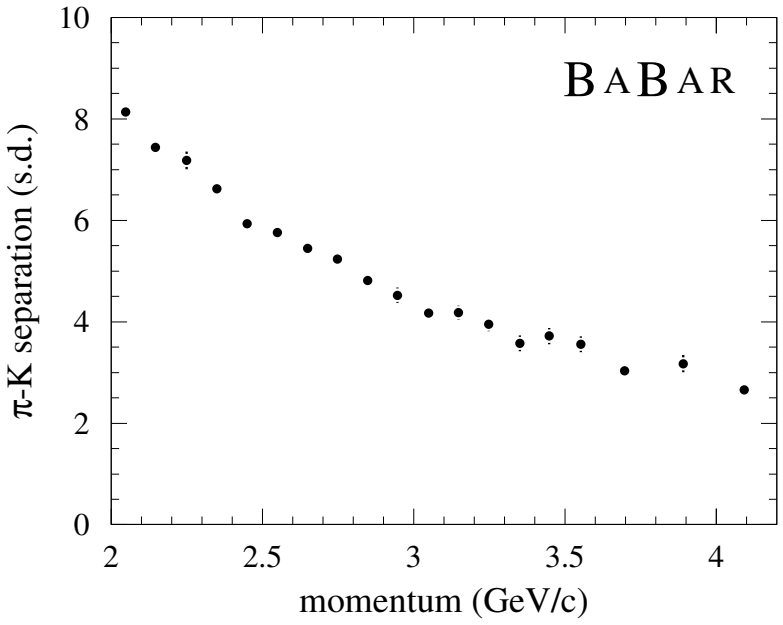

Figure 2.21: DIRC $\pi - K$ separation versus track momentum measured in $D^0 \to K^-\pi^+$ decays selected kinematically from inclusive D^* production

nates (θ_C, ϕ_C and δ_t) via a maximum likelihood fit. Both efficiency and the timing of the electronics are critical for DIRC performance. Timing accuracy is necessary for background hit rejection, and more importantly, for the exclusion of other tracks in the same event as the source of the photon.

The Cerenkov angle resolution for dimuon events is 2.5 mrad, close to the design goal of 2.2 mrad. This results in $\pi - K$ separation at 3 GeV/c of 4.2; this is shown in Figure 2.21. The mean kaon selection efficiency and pion mis-identification for a "loose" selection (see appendix B) are 96.2% and 2.1% respectively.

2.7.2 Other Particle ID

Measurements of energy loss ($\mathrm{d}E/\mathrm{d}x$) by the tracking system also allow charged particle identification at low momenta and allow separation of pions and kaons with momentum lower than 700 MeV. In the SVT, ≈ 10 ToT measurements are converted to $\mathrm{d}E/\mathrm{d}x$ using a lookup table and a 60% truncated mean is calculated. In the DCH, an 80% truncated mean of the 40 ionization loss measurements for each track provide a 7.5% $\mathrm{d}E/\mathrm{d}x$ determination (see Figure 2.19).

2.8 Electromagnetic Calorimeter

2.8.1 Purpose and Design

The electromagnetic calorimeter (EMC) is designed to measure electromagnetic showers with excellent efficiency, and energy and angular resolution over the energy range from 20 MeV to 9 GeV. This capability allows the detection of photons from π^0 and η decays as well as from electromagnetic and radiative processes. By identifying electrons, the EMC contributes to the flavor tagging of neutral B mesons via semi-leptonic decays, to the reconstruction of vector mesons like J/ψ, and to the study of

semi-leptonic and rare decays of B and D mesons, and τ leptons. The upper bound of the energy range is set by the need to measure QED processes, like $e^+e^- \to e^+e^-(\gamma)$ and $e^+e^- \to \gamma\gamma$, for calibration and luminosity determination. The lower bound is set by the need for highly efficient reconstruction of B-meson decays containing multiple π^0 mesons and η^0s.

Requirements

The measurement of extremely rare decays of B mesons containing π^0s (*e.g.,* $B^0 \to \pi^0\pi^0$) poses the most stringent requirements on energy resolution, namely of order 1–2%. Below energies of 2 GeV, the π^0 mass resolution is dominated by the energy resolution. At higher energies, the angular resolution becomes dominant, and therefore it is required to be of the order of a few mrad.

To achieve excellent resolution, stable operating conditions have to be maintained. Temperatures and the radiation exposure must be closely monitored, and precise calibrations of the electronics and energy response over the full dynamic range must be performed frequently.

Design Considerations

The requirements stated above led to the choice of a hermetic, total-absorption calorimeter, composed of a finely segmented array of thallium-doped cesium iodide (CsI(Tl)) crystals. The crystals are read out with silicon photodiodes that are matched to the spectrum of scintillation light.

The energy resolution of a homogeneous crystal calorimeter can be described empirically in terms of a sum of two terms added in quadrature

$$\frac{\sigma_E}{E} = \frac{a}{\sqrt[4]{E(\,\mathrm{GeV})}} \oplus b, \tag{2.5}$$

where E and σ_E refer to the energy of a photon and its rms error, measured in GeV. The energy dependent term a arises primarily from the fluctuations in photon statistics, but it is also impacted by electronic noise of the photon detector and electronics. Furthermore, beam-generated background will lead to large numbers of additional photons that add to the noise. This term is dominant at low energies. The constant term, b, is dominant at higher energies (> 1 GeV). It arises from non-uniformity in light collection, leakage or absorption in the material between and in front of the crystals, and uncertainties in the calibrations. Most of these effects can be influenced by design choices, and they are stable with time. Others will be impacted by changes in the operating conditions, like variations in temperature, electronics gain, and noise, as well as by radiation damage caused by beam-generated radiation.

The angular resolution is determined by the transverse crystal size and the distance from the interaction point. It can also be empirically parameterized as a sum of an energy dependent and a constant term,

$$\sigma_\theta = \sigma_\phi = \frac{c}{\sqrt{E(\,\mathrm{GeV})}} + d, \tag{2.6}$$

where the energy E is measured in GeV. The design of the EMC required a careful optimization of a wide range of choices, including the crystal material and dimensions, the choice of the photon detector and readout electronics, and the design of a calibration and monitoring system. These choices were made on the basis of extensive studies, prototyping and beam tests [70], and Monte Carlo simulation, taking into account limitations of space and the impact of other *BABAR* detector systems.

Under ideal conditions, values for the energy resolution parameters a and b close to 1–2% could be obtained. A position resolution of a few mm will translate into an angular resolution of a few mrad; corresponding parameter values are $c \approx 3$ mrad and $d \approx 1$ mrad.

Table 2.6: Properties of CsI(Tl) .

Parameter	Values
Radiation Length	1.85 cm
Molière Radius	3.8 cm
Density	4.53 g/cm^3
Light Yield	50,000 γ/ MeV
Light Yield Temp. Coeff.	0.28%/°C
Peak Emission $\lambda_{\max}$	565 nm
Refractive Index ($\lambda_{\max}$)	1.80
Signal Decay Time	680 ns (64%)
	3.34 μs (36%)

However in practice, such performance is very difficult to achieve in a large system with a small, but unavoidable amount of inert material and gaps, limitations of electronics, and background in multi-particle events, plus contributions from beam-generated background.

Though in CsI(Tl) the intrinsic efficiency for the detection of photons is close to 100% down to a few MeV, the minimum measurable energy in colliding beam data is expected to be about 20 MeV, a limit that is largely determined by beam- and event-related background and the amount of material in front of the calorimeter. Because of the sensitivity of the π^0 efficiency to the minimum detectable photon energy, it was extremely important to keep the amount of material in front of the EMC to the lowest possible level.

Results for the achieved energy and angular resolutions are reported in 2.8.4.

CsI(Tl) Crystals

Its properties are listed in Table 2.6. The high light yield and small Molière radius allow for excellent energy and angular resolution, while the short radiation length allows for shower containment at *BABAR* energies with a relatively compact design. Furthermore, the high light yield and the emission spectrum permit efficient use of silicon photodiodes which operate well in high magnetic fields. The transverse size of the crystals is chosen to be comparable to the Molière radius achieving the required angular resolution at low energies while appropriately limiting the total number of crystals (and readout channels).

2.8.2 Layout and Assembly

The EMC consists of a cylindrical barrel and a conical forward end-cap. It has full coverage in azimuth and extends in polar angle from 15.8° to 141.8° corresponding to a solid-angle coverage of 90% in the c.m. system (see Figure 2.22). The barrel contains 5,760 crystals arranged in 48 distinct rings with 120 identical crystals each. The end-cap holds 820 crystals arranged in eight rings, adding up to a total of 6,580 crystals. The crystals have a tapered trapezoidal cross section. The length of the crystals increases from 29.6 cm in the backward to 32.4 cm in the forward direction to limit the effects of shower leakage from increasingly higher energy particles.

To minimize the probability of pre-showering, the crystals are supported at the outer radius, with only a thin gas seal at the front. The barrel and outer five rings of the end-cap have less than 0.3–0.6X_0 of material in front of the crystal faces. The SVT support structure and electronics, as well as the B1 dipole shadow the inner three rings of the end-cap, resulting in up to 3.0X_0 for the innermost ring. The principal purpose of the two innermost rings is to enhance shower containment for particles close

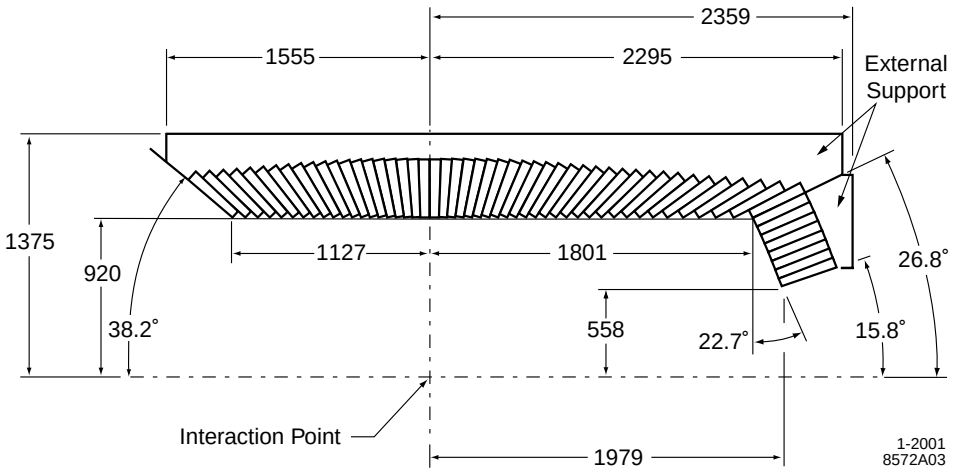

Figure 2.22: A longitudinal cross section of the EMC (only the top half is shown) indicating the arrangement of the 56 crystal rings. The detector is axially symmetric around the z-axis. All dimensions are given in mm.

to the acceptance limit.

The crystals were grown in boules from a melt of CsI salt doped with 0.1% thallium [71]. They were cut from the boules, machined into tapered trapezoids (Figure 2.23) to a tolerance of $\pm 150\,\mu$m, and then polished [72]. The transverse dimensions of the crystals for each of the 56 rings vary to achieve the required hermetic coverage. The typical area of the front face is $4.7 \times 4.7\,\mathrm{cm}^2$, while the back face area is typically $6.1 \times 6.0\,\mathrm{cm}^2$. The crystals act not only as a total-absorption scintillating medium, but also as a light guide to collect light at the photodiodes that are mounted on the rear surface.

The photon detector consists of two $2 \times 1\,\mathrm{cm}^2$ silicon PIN diodes glued to a transparent 1.2 mm-thick polysterene substrate that, in turn, is glued to the center of the rear face of the crystal by an optical epoxy [73] to maximize light transmission [74]. The surrounding area of the crystal face is covered by a plastic plate coated with white reflective paint [75]. The plate has two 3 mm-diameter penetrations for the fibers of the light pulser monitoring system.

Each of the diodes is directly connected to a low-noise preamplifier. The entire assembly is enclosed by an aluminum fixture as shown in Figure 2.23. This fixture is electrically coupled to the aluminum foil wrapped around the crystal and thermally coupled to the support frame to dissipate the heat load from the preamplifiers.

The crystals are inserted into modules that are supported individually from an external support structure. This structure is built in three sections, a cylinder for the barrel and two semi-circular structures for the forward end-cap. The barrel support cylinder carries the load of the barrel modules plus the forward end-cap to the magnet iron through four flexible supports. These supports decouple and dampen any acceleration induced by movements of the magnet iron during a potential earthquake.

The barrel section is divided into 280 separate modules, each holding 21 crystals (7×3 in $\theta \times \phi$).

The end-cap is constructed from 20 identical modules (each with 41 crystals), individually aligned and bolted to one of two semi-circular support structures. The end-cap is split vertically into two halves to facilitate access to the central detector components. The entire calorimeter is surrounded by a double Faraday shield composed of two 1 mm-thick aluminum sheets so that the diodes and preamplifiers are further shielded from external noise. This cage also serves as the environmental barrier, allowing the slightly hygroscopic crystals to reside in a dry, temperature controlled nitrogen atmosphere. The EMC is maintained at constant, accurately monitored temperature. Of particular concern are the stability of the photodiode leakage current which rises exponentially with temperature, and the large number

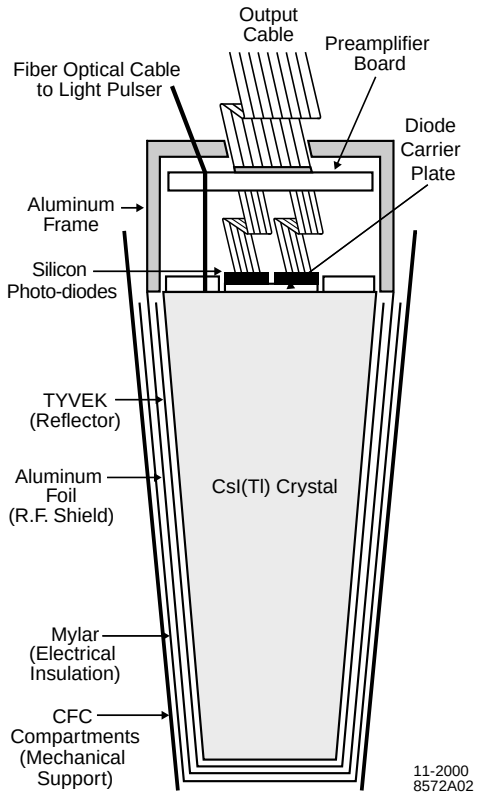

Figure 2.23: A schematic of the wrapped CsI(Tl) crystal and the front-end readout package mounted on the rear face. Also indicated is the tapered, trapezoidal CFC compartment, which is open at the front. This drawing is not to scale.

of diode-crystal epoxy joints that could experience stress due to differential thermal expansion. In addition, the light yield of CsI(Tl) is weakly temperature dependent.

The ENC ("Equivalent Noise Charge") is minimized by maximizing the light yield and collection, employing a highly efficient photon detector, and a low-noise electronic readout. The PIN silicon photodiodes [76] have a quantum efficiency of 85% for the CsI(Tl) scintillation light [77]. At a depletion voltage of 70 V, their typical dark currents were measured to be 4 nA for an average capacitance of 85 pF; the diodes are operated at a voltage of 50 V.

Electronics Calibration and Linearity

To measure pedestal offsets, determine the overall gain, and to remove non-linearities the FEE are calibrated by precision charge injection into the preamplifier input. Initially, residual non-linearities of up to 12% in limited regions near each of the range changes were observed and corrected for offline [78]. These non-linearities were traced to oscillations on the ADC cards that have since been corrected. The correction resulted in markedly improved energy resolution at high energies. Residual non-linearities (typically 2–4%) arise primarily from cross-talk, impacting both the electronics calibrations and the colliding-beam data. The effect is largest at about 630 MeV (950 MeV) in a high (low) gain preamplifier channel, inducing a 2 MeV (6 MeV) cross-talk signal in an adjacent channel. The implementation of an energy dependent correction is expected to significantly reduce this small, remaining effect, and lead to a further improvement of the energy resolution.

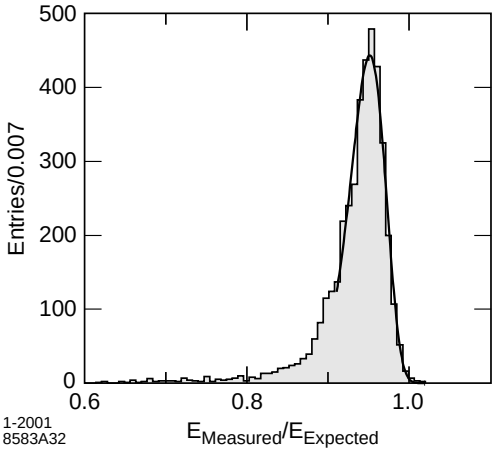

Figure 2.24: The ratio of the EMC measured energy to the expected energy for electrons from Bhabha scattering of 7.5 GeV/c. The solid line indicates a fit using a logarithmic function.

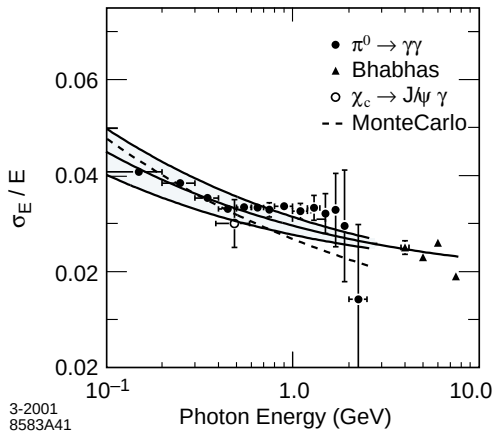

Figure 2.25: The energy resolution for the EMC measured for photons and electrons from various processes. The solid curve is a fit to Equation 2.5 and the shaded area denotes the rms error of the fit.

2.8.3 Energy Calibration

The energy calibration of the EMC proceeds in two steps. First, the measured pulse height in each crystal has to be translated to the actual energy deposited. Second, the energy deposited in a shower spreading over several adjacent crystals has to be related to the energy of the incident photon or electron by correcting for energy loss mostly due to leakage at the front and the rear, and absorption in the material between and in front of the crystals, as well as shower energy not associated with the cluster.

2.8.4 Performance

Energy Resolution

At low energy, the energy resolution of the EMC is measured directly with the radioactive source yielding $\sigma_E/E = 5.0 \pm 0.8\%$ at 6.13 MeV (see Figure 2.26). At high energy, the resolution is derived from Bhabha scattering, where the energy of the detected shower can be predicted from the polar angle

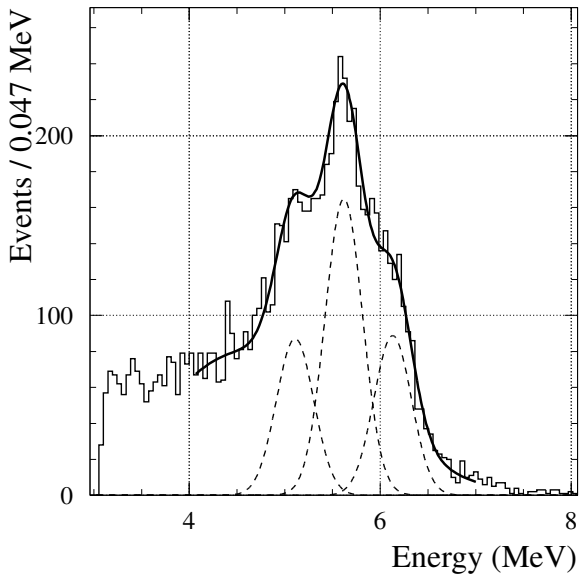

Figure 2.26: A typical pulse-height spectrum recorded with the radioactive source to calibrate the single-crystal energy scale of the EMC. The spectrum shows the primary 6.13 MeV peak and two associated escape peaks at 5.62 MeV and 5.11 MeV. The solid line represents a fit to the total spectrum, the dotted lines indicate the contributions from the three individual photon spectra.

of the $e^{\pm}$. The measured resolution is $\sigma_E/E = 1.9 \pm 0.07\%$ at 7.5 GeV (see Figure 2.24). Figure 2.25 shows the energy resolution extracted from a variety of processes as a function of energy. Below 2 GeV, the mass resolution of π^0 and η mesons decaying into two photons of approximately equal energy is used to infer the EMC energy resolution [79]. The decay $\chi_{c1} \to J/\psi\,\gamma$ provides a measurement at an average energy of about 500 MeV, and measurements at high energy are derived from Bhabha scattering. A fit to the energy dependence results [80] in

$$\frac{\sigma_E}{E} = \frac{(2.30 \pm 0.30)\%}{\sqrt[4]{E(\,\mathrm{GeV})}} \oplus (1.35 \pm 0.2)\%. \tag{2.7}$$

Values of these fitted parameters are higher than the somewhat optimistic design expectations, but they agree with detailed Monte Carlo simulations which include the contributions from electronic noise and beam background, as well as the impact of the material and the energy thresholds.

Angular Resolution

The measurement of the angular resolution is based on the analysis of π^0 and η decays to two photons of approximately equal energy. The result is presented in Figure 2.27. The resolution varies between about 12 mrad at low energies and 3 mrad at high energies. A fit to an empirical parameterization of the energy dependence results [80] in

$$\begin{aligned} \sigma_\theta &= \sigma_\phi \\ &= \frac{(4.16 \pm 0.04)\ \mathrm{mrad}}{\sqrt{E(\,\mathrm{GeV})}}). \end{aligned} \tag{2.8}$$

These fitted values are slightly better than would be expected from detailed Monte Carlo simulations.

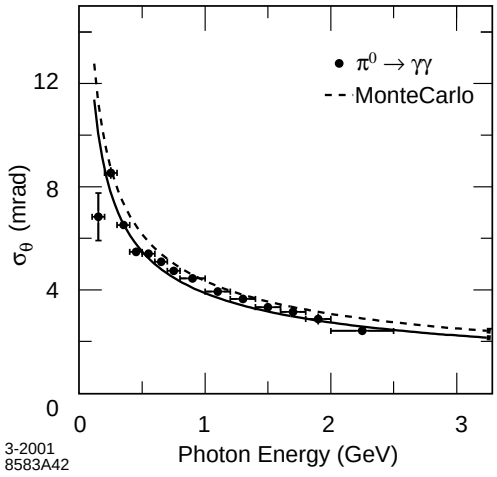

Figure 2.27: The angular resolution of the EMC for photons from π^0 decays. The solid curve is a fit to Equation 2.6.

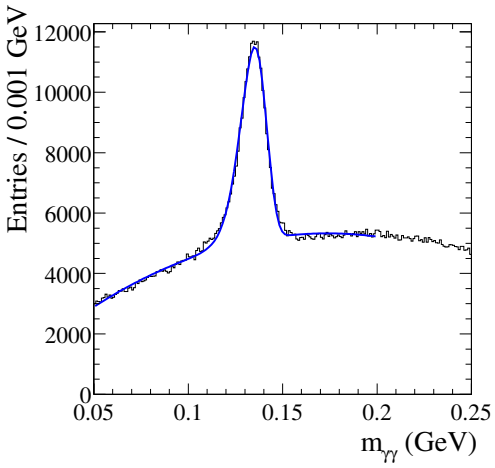

Figure 2.28: Invariant mass of two photons in $B\overline{B}$ events. The energies of the photons and the π^0 are required to exceed 30 MeV and 300 MeV, respectively. The solid line is a fit to the data.

π^0 Mass and Width

Figure 2.28 shows the two-photon invariant mass in $B\overline{B}$ events. The reconstructed π^0 mass is measured to be 135.1 MeV/c^2 and is stable to better than 1% over the full photon energy range. The width of 6.9 MeV/c^2 agrees well with the prediction obtained from detailed Monte-Carlo simulations. In low-occupancy $\tau^+\tau^-$ events, the width is slightly smaller, 6.5 MeV/c^2, for π^0 energies below 1 GeV. A similar improvement is also observed in analysis using selected isolated photons in hadronic events.

Electron Identification

Electrons are separated from charged hadrons primarily on the basis of the shower energy, lateral shower moments, and track momentum. In addition, the dE/dx energy loss in the DCH and the DIRC Cherenkov angle are required to be consistent with an electron. The most important variable

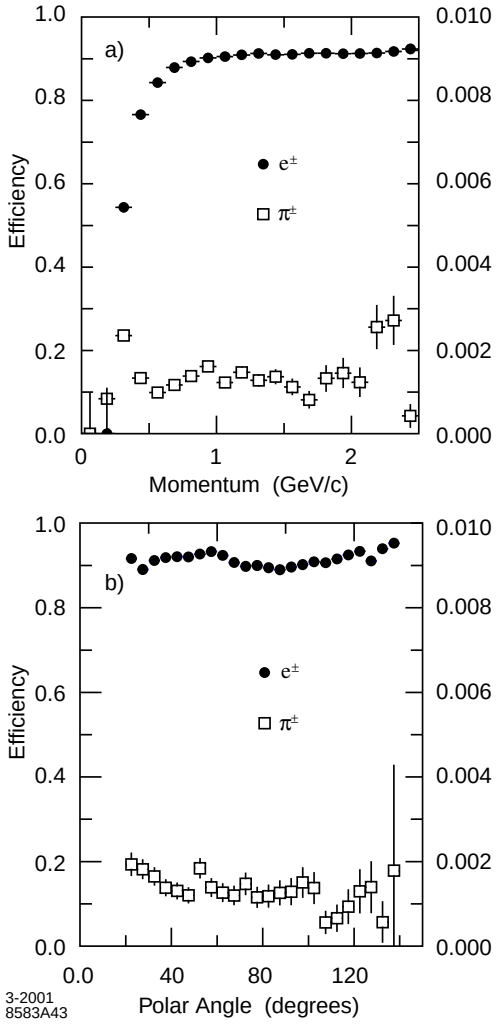

Figure 2.29: The electron efficiency and pion mis-identification probability as a function of a) the particle momentum and b) the polar angle, measured in the laboratory system.

for the discrimination of hadrons is the ratio of the shower energy to the track momentum (E/p). Figure 2.29 shows the efficiency for electron identification and the pion mis-identification probability as a function of momentum for two sets of selection criteria. The electron efficiency is measured using radiative Bhabha events and $e^+e^- \to e^+e^-e^+e^-$ events. The pion mis-identification probability is measured for selected charged pions from K^0_S decays and three-prong τ decays. A "tight" ("very tight") selector (see appendix A) results in an efficiency plateau at 94.8% (88.1%) in the momentum range $0.5 < p < 2\,\mathrm{GeV}/c$. The pion mis-identification probability is of order 0.3% (0.15%) for the tight (very tight) selection criteria.

2.9 Detector for Muons and Neutral Hadrons

2.9.1 Physics Requirements and Goals

The Instrumented Flux Return (IFR) was designed to identify muons with high efficiency and good purity, and to detect neutral hadrons (primarily K^0_L and neutrons) over a wide range of momenta and angles. Muons are important for tagging the flavor of neutral B mesons via semileptonic decays, for

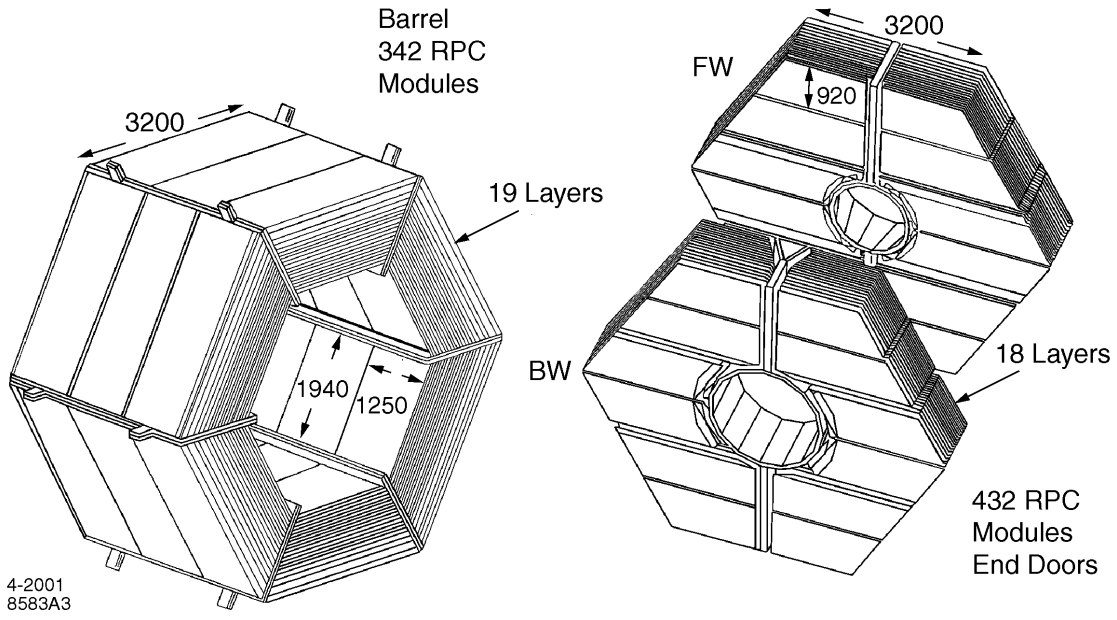

Figure 2.30: Overview of the IFR: Barrel sectors and forward (FW) and backward (BW) end doors; the shape of the RPC modules and their dimensions are indicated.

the reconstruction of vector mesons, like the J/ψ, and for the study of semileptonic and rare decays involving leptons of B and D mesons and τ leptons. K_L^0 detection allows the study of exclusive B decays, in particular CP eigenstates. The IFR can also help in vetoing charm decays and improve the reconstruction of neutrinos.

The principal requirements for IFR are large solid angle coverage, good efficiency, and high background rejection for muons down to momenta below 1 GeV/c. For neutral hadrons, high efficiency and good angular resolution are most important. Because this system is very large and difficult to access, high reliability and extensive monitoring of the detector performance and the associated electronics plus the voltage distribution are required.

2.9.2 Overview and RPC Concept

The IFR uses the steel flux return of the magnet as a muon filter and hadron absorber. Single gap resistive plate chambers (RPCs) [81] with two-coordinate readout have been chosen as detectors.

The RPCs are installed in the gaps of the finely segmented steel (see Section 2.3) of the barrel and the end doors of the flux return, as illustrated in Figure 2.30. The steel is segmented into 18 plates, increasing in thickness from 2 cm for the inner nine plates to 10 cm for the outermost plates. The nominal gap between the steel plates is 3.5 cm in the inner layers of the barrel and 3.2 cm elsewhere. There are 19 RPC layers in the barrel and 18 in the endcaps. In addition, two layers of cylindrical RPCs are installed between the EMC and the magnet cryostat to detect particles exiting the EMC.

RPCs detect streamers from ionizing particles via capacitive readout strips. They offer several advantages: simple, low cost construction and the possibility of covering odd shapes with minimal dead space. Further benefits are large signals and fast response allowing for simple and robust front-end electronics and good time resolution, typically 1–2 ns. The position resolution depends on the segmentation of the readout; a value of a few mm is achievable.

The construction of the planar and cylindrical RPCs differ in detail, but they are based on the same concept. A cross section of an RPC is shown schematically in Figure 2.31.

The planar RPCs consist of two bakelite (phenolic polymer) sheets, 2 mm-thick and separated by a

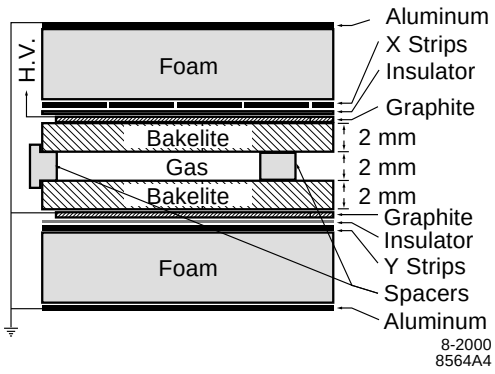

Figure 2.31: Cross section of a planar RPC with the schematics of the high voltage (HV) connection.

gap of 2 mm. The gap is enclosed at the edge by a 7 mm wide frame. The gap width is kept uniform by polycarbonate spacers (0.8 cm^2) that are glued to the bakelite, spaced at distances of about 10 cm. The bulk resistivity of the bakelite sheets has been especially tuned to 10^{11}–$10^{12}\,\Omega$ cm. The external surfaces are coated with graphite to achieve a surface resistivity of $\sim 100\,k\Omega$/square. These two graphite surfaces are connected to high voltage (~ 8 kV) and ground, and protected by an insulating mylar film. The bakelite surfaces facing the gap are treated with linseed oil. The RPCs are operated in limited streamer mode and the signals are read out capacitively, on both sides of the gap, by external electrodes made of aluminum strips on a mylar substrate.

The cylindrical RPCs have resistive electrodes made of a special plastic composed of a conducting polymer and ABS plastic. The gap thickness and the spacers are identical to the planar RPCs. No linseed oil or any other surface treatments have been applied. The very thin and flexible electrodes are laminated to fiberglass boards and foam to form a rigid structure. The copper readout strips are attached to the fiberglass boards.

In original setup, the IFR detectors cover a total active area of about 2,000 m^2. There are a total of 806 RPC modules, 57 in each of the six barrel sectors, 108 in each of the four half end doors, and 32 in the two cylindrical layers.

The RPCs operate with a non-flammable gas mixture, typically 56.7% Argon, 38.8% Freon 134a (1,1,1,2 tetrafluoroethane), and 4.5% isobutane. This mixture is drawn from a 760 liter tank that is maintained at an absolute pressure of 1500–1600 Torr. The mixing tank is filled on demand with the three component gases under control of mass-flow meters. Samples are extracted from the mixing tank periodically and analyzed to verify the correct mixture.

The mixed gas is distributed at a gauge pressure of approximately 6.5 Torr. Return flow of gas from each chamber is monitored by a second oil bubbler which creates a back pressure of about 0.2 Torr. The total flow through the entire system is approximately 5 ℓ/minute and corresponds on average to two gas exchanges per day.

2.9.3 Efficiency Measurements and Performance

The efficiency of the RPCs is evaluated both for normal collision data and for cosmic ray muons recorded with the IFR trigger. Every week, cosmic ray data are recorded at different voltage settings and the efficiency is measured chamber-by-chamber as a function of the applied voltage. The absolute efficiency at the nominal working voltage (typically 7.6 kV) is stored in the database for use in the event reconstruction software.

Following the installation and commissioning of the IFR system, all RPC modules were tested with

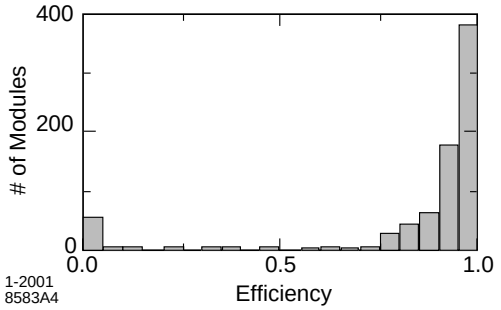

Figure 2.32: Distribution of the efficiency for all RPC modules measured with cosmic rays in June 1999. Some 50 modules were not operational at that time.

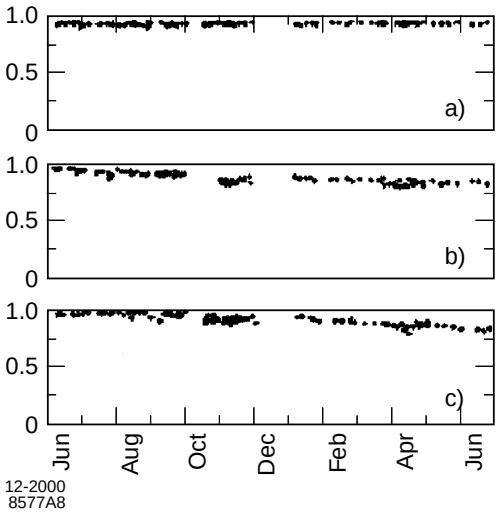

Figure 2.33: Efficiency history for 12 months starting in June 1999 for RPC modules showing different performance: a) highly efficient and stable; b) continuous slow decrease in efficiency; c) more recent, faster decrease in efficiency.

cosmic rays and their efficiency was measured. The results are presented in Figure 2.32. Of the active RPC modules, 75% exceeded an efficiency of 90%.

Early tests indicated that the RPC dark current was very temperature dependent, specifically, the current increases 14–20% per °C. Because the IR experimental hall does not have temperature regulation this presents a serious problem. The FECs that are installed in the steel gaps dissipate 3 W each, generating a total power of 3.3 kW in the barrel and 1.3 kW in the forward end door.

During the first summer of operation, the daily average temperature in the IR hall was 28°C and the maximum hall temperature frequently exceeded 31°C. The temperature inside the steel rose to more than 37°C and the dark currents in many modules exceeded the capabilities of the HV system and some RPCs had to be temporarily disconnected.

During operation at high temperatures, a large fraction of the RPCs (>50%) showed not only very high dark currents, but also some reduction in efficiency compared to earlier measurements [82]. After the cooling was installed and the RPCs were reconnected, some of them continued to deteriorate while others remained stable, some of them ($> 30\%$) at full efficiency. (see Figure 2.33).

In the end most of the RPCs were substituted with Limited Streamer Tubes (LSTs). Two out of six

sextants were upgraded to LSTs in 2004 and in 2006 the barrel upgrade has been completed. See 2.9.4 for further details.

Some of the chambers in the forward endcap have been switched to avalanche mode. This has been done in order to cope with high rate (induced by beam backgrounds) and low efficiency of inner radius chambers. Switch to avalanche mode, the charge/avalanche will be several times less than streamer mode. Therefore the RPC chambers can last longer, also the rate capability can be improved. Avalanche mode is operated using a R134A/Ar/Isobutane (42/50/8) mixture while for streamer it was R134A/Ar/Isobutane/SF6 (73.1/22/4.4/0.5).

Very preliminary results indicate a reduction of a factor of 5 in dark current decrease. Operating chambers at voltages greater than 9.6 kV indicate full efficiency recover for inner radius chambers. Plans are to continue upgrade of forward end-cap region.

2.9.4 LSTs

A "standard" LST configuration [83] consists of a silver plated wire 100 μm in diameter, located at the center of a cell of 9x9 mm^2 section. A plastic (PVC) extruded structure, or profile, contains 8 such cells, open on one side (see Figure 2.34). The profile is coated with a resistive layer of graphite, having a typical surface resistivity between 0.1 and 1 M$\Omega/\Box$. The profiles, coated with graphite and strung with wires, are inserted in plastic tubes ("sleeves") of matching dimensions for gas containment. The signals for the measurement of one coordinate can be read directly either from the wires or from external strip planes attached on both side of the sleeve.

A 15x17 mm^2 cell design is used where each tube is composed by 7 or 8 cells and assembled in modules. We use wire readout for the azimuthal coordinate, ϕ, and strips plans for the z coordinate (along the beam direction). In order to obtain high performances and to respect the safety requirements it has been chosen a ternary gas mixture of $Ar/C_4H_{10}/CO_2$ (3/8/89)% [84].

BABAR experiment began RUN5 on March 2005 and after 8 months of operation LSTs are showing very good performances concerning number of dead channels, plateau curves, efficiency, muon identification and pion rejection.

Results for whole IFR system will be presented in what follows.

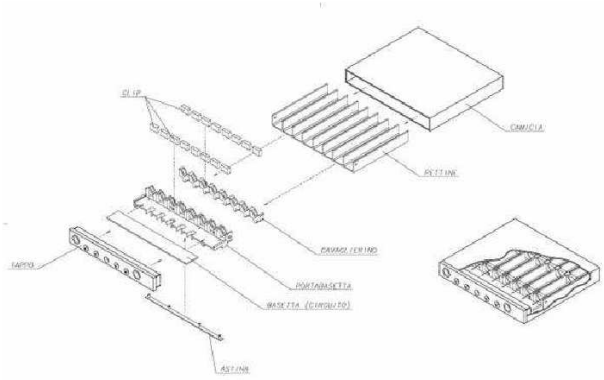

Figure 2.34: Schematic of the "standard" Limited Streamer Tube configuration

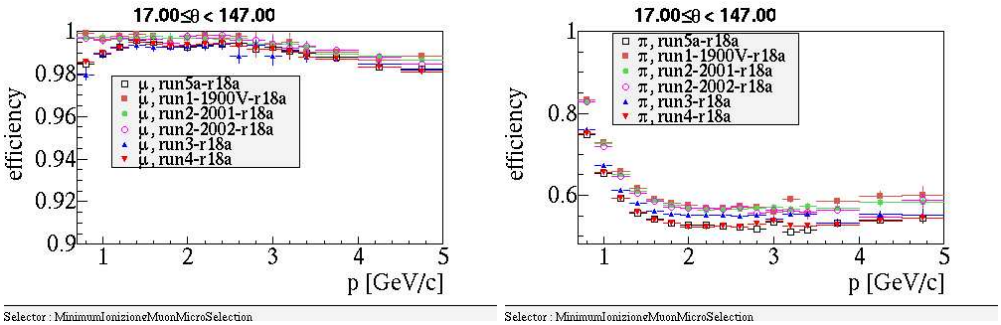

Figure 2.35: Muon efficiency (left plot) and pion mis-identification probability (right right) as a function of the laboratory track momentum obtained with loose selection criteria.

2.9.5 Muon Identification

While muon identification relies almost entirely on the IFR, other detector systems provide complementary information. Charged particles are reconstructed in the SVT and DCH and muon candidates are required to meet the criteria for minimum ionizing particles in the EMC. Charged tracks that are reconstructed in the tracking systems are extrapolated to the IFR taking into account the non-uniform magnetic field, multiple scattering, and the average energy loss. The projected intersections with the RPC planes are computed and for each readout plane all clusters detected within a predefined distance from the predicted intersection are associated with the track.

A number of variables are defined for each IFR cluster associated with a charged track to discriminate muons from charged hadrons: 1) the total number of interaction lengths traversed from the IP to the last RPC layer with an associated cluster, 2) the difference between this measured number of interaction lengths and the number of interaction lengths predicted for a muon of the same momentum and angle, 3) the average number and the rms of the distribution of RPC strips per layer, 4) the χ^2 for the geometric match between the projected track and the centroids of clusters in different RPC layers, and 5) the χ^2 of a polynomial fit to the two-dimensional IFR clusters. Selection criteria based on these variables are applied to identify muons.

The performance of muon identification has been tested on samples of muons from $\mu\mu ee$ and $\mu\mu\gamma$ final states and pions from three-prong τ decays and $K_S \to \pi^+\pi^-$ decays. The selection of these control samples is based on kinematic variables, and not on variables used for muon identification. As illustrated in Figure 2.35, a muon detection efficiency of close to 98% has been achieved in the momentum range of $1.0 < p < 5.0\,\mathrm{GeV}/c$ with a fake rate for pions of less than 1%.

2.9.6 K_L^0 and Neutral Hadron Detection

K_L^0's and other neutral hadrons interact in the steel of the IFR and can be identified as clusters that are not associated with a charged track.

Since a significant fraction of hadrons interact before reaching the IFR, information from the EMC and the cylindrical RPCs is combined with the IFR cluster information. Neutral showers in the EMC are associated with the neutral hadrons detected in the IFR, based on a match in production angles. For a good match, a χ^2 probability of $\geq 1\%$ is required.

K_L^0 efficiency roughly increases linearly with momentum and varies between 20% and 40% between 1 and 4 GeV.

2.10 The Online System

BABAR's electronics, trigger, data acquisition (DAQ), and online computing systems are composed of tightly coupled hardware and software. A brief overview of the trigger system and online monitoring is presented here.

2.10.1 Trigger

The basic requirement for the trigger system is the selection of events of interest (see Table 2.7) with a high, stable, and well-understood efficiency while rejecting background events and keeping the total event rate under 120 Hz.

The total trigger efficiency was required to exceed 99% for all $B\overline{B}$ events and at least 95% for continuum events. Less stringent requirements apply to other event types, *e.g.,* $\tau^+\tau^-$ events should have a 90-95% trigger efficiency, depending on the specific $\tau^\pm$ decay channels.

The trigger system must be robust and flexible in order to function even under extreme background situations. It must also be able to operate in an environment with dead or noisy electronics channels. The trigger should contribute no more than 1% to dead time.

The trigger is implemented as a two-level hierarchy, the Level 1 (L1) in hardware followed by the Level 3 (L3) in software.

During normal operation, the L1 is configured to have an output rate of typically 1 kHz. Triggers are produced within a fixed latency window of 11–12 μs after the e^+e^- collision, and delivered to the Fast Control and Timing System (FCTS). Data used to form the trigger decision are preserved with each event for efficiency studies.

The L3 receives the output from L1, performs a second stage rate reduction for the main physics sources, and identifies and flags the special categories of events needed for luminosity determination, diagnostic, and calibration purposes. At design luminosity, the L3 filter acceptance for physics is ∼90 Hz, while ∼30 Hz contain the other special event categories. The L3 algorithms comply with the same software conventions and standards used in all other *BABAR* software, thereby simplifying its design, testing, and maintenance.

The L1 trigger decision is based on charged tracks in the DCH above a preset transverse momentum, showers in the EMC, and tracks detected in the IFR. Trigger data are processed by three specialized hardware processors. The drift chamber trigger (DCT) and electromagnetic calorimeter trigger (EMT) both satisfy all trigger requirements independently with high efficiency, and thereby provide a high degree of redundancy, which enables the measurement of trigger efficiency. The instrumented flux return trigger (IFT) is used for triggering $\mu^+\mu^-$ and cosmic rays, mostly for diagnostic purposes.

The overall structure of the L1 trigger is illustrated in Figure 2.36.

Table 2.7: Cross sections, production and trigger rates for the principal physics processes at 10.58 GeV for a luminosity of $3 \times 10^{33}\,\mathrm{cm}^{-2}\mathrm{s}^{-1}$. The e^+e^- cross section refers to events with either the e^+, e^-, or both inside the EMC detection volume.

Event type	Cross section (nb)	Production Rate (Hz)	Level 1 Trigger Rate (Hz)
$b\overline{b}$	1.1	3.2	3.2
other $q\overline{q}$	3.4	10.2	10.1
e^+e^-	∼53	159	156
$\mu^+\mu^-$	1.2	3.5	3.1
$\tau^+\tau^-$	0.9	2.8	2.4

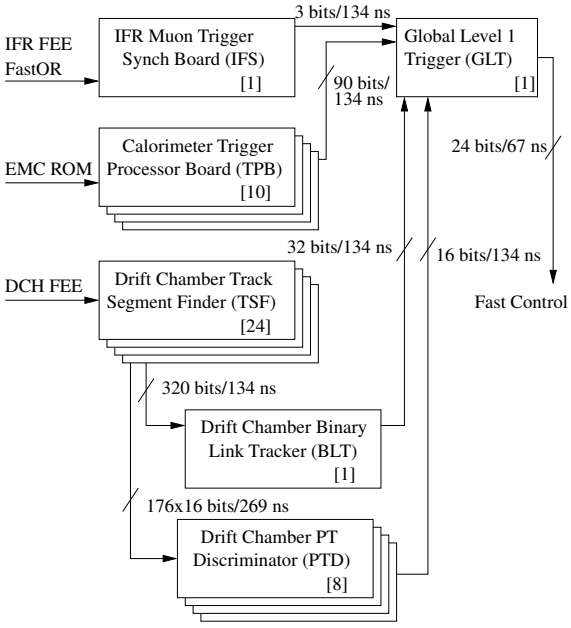

Figure 2.36: Simplified L1 trigger schematic. Indicated on the Figure are the number of components (in square brackets), and the transmission rates between components in terms of total signal bits.

The DCT algorithms are executed in three types of modules. First, track segments, their ϕ positions and drift time estimates are found using a set of 24 Track Segment Finder (TSF) modules. These data are then passed to the Binary Link Tracker (BLT) module, where segments are linked into complete tracks. In parallel, the ϕ information for segments found in axial superlayers is transmitted to eight transverse momentum discriminator (PTD) modules, which search for tracks above a set transverse momentum (p_T) threshold. All of this information is output to the GLT.

The calorimeter trigger (EMT) divides the EMC into 280 towers of 24 crystals each (22 for the endcap). All crystal energies within a tower which are above a 20 MeV threshold are summed and supplied to the EMT trigger processor boards (TPBs). The TPBs digitally filter the energy deposition and compare neighboring towers to look for clusters which span more than one tower. Again this data corresponding to the energy and placement of found clusters is passed to the GLT.

The GLT receives the trigger line "primitives" (bytes corresponding to trigger type and information) from the EMT and DCT, as well as information from the IFT (which is used for $\mu^+\mu^-$ and cosmic ray triggering), and performs a timing alignment of these input data. The GLT does some rudimentary matching between DCT tracks and EMT clusters, and performs a logical AND of the input trigger primitives. The combined L1 trigger efficiency is greater than 99.9% for $B\overline{B}$ events, about 99% for continuum events, and 94.5% for $\tau^+\tau^-$ events.

The L3 trigger software comprises event reconstruction and classifications, a set of event selection filters, and monitoring. This software runs on the online computer farms within the Online Event Processing (OEP) framework. Many events which pass L1 but must be rejected by L3 are beam-induced charged particle background that are produced in material close to the IP. The Level 3 trigger combines DCT tracks (from the TSF system) and EMT clusters with the full DCH and EMC information. The L3 DCH algorithm performs fast pattern recognition and fits L1 tracks to helices and is able to determine the z_0 of tracks, which is important for rejecting the above mentioned background. The L3 EMC based trigger identifies energy clusters with a higher sensitivity than L1 and filters events with either high energy deposits of high cluster multiplicity. The output of both the DCH and EMC L3 filters is dominated by Bhabha events with are mostly rejected but are also prescaled in L3 for calibration and

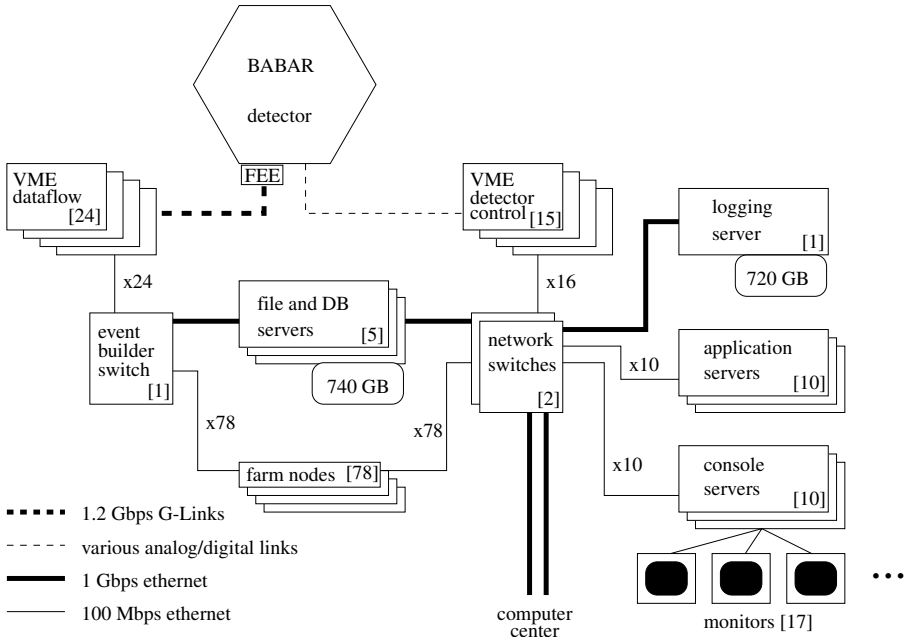

Figure 2.37: Physical infrastructure of the *BABAR* online system, including VME crates, computers, and networking equipment.

luminosity online monitoring and offline measurements.

Data Flow and Detector Monitoring

Online Data-flow (ODF), which provides data transport, buffering, and event building is implemented in a set of VME crates which house 157 Readout Modules (ROMs) running real-time operating system. Configuration and readout of the FEEs are performed through 1.2 Gbits/s fiber links to the ROMs. These specialized VME-based processors handle Feature Extraction (FEX) of physics signals, perform gain and pedestal corrections, as well as data specification and formatting. The calibration data is stored in a dedicated conditions database. Using a Fast Control and Timing System (FCTS), events are built from data from the individual subsystems and shipped from the ROM modules to the Online Event Processing (OEP) workstations via 100 Mb Ethernet. No dedicated counters are employed to associate events with beam crossings. Instead absolute timing is determined offline using DCH track segment timing, waveforms from EMC, and accelerator timing fiducials. Figure 2.37 presents a schematic diagram of the DAQ system.

Running on a farm of Unix workstations, the OEP software collects and processes data from the ODF event builders, partially reconstructing the event in order to apply the Level3 (L3) trigger algorithms and provide fast monitoring for the data taking personnel on shift. The L3 software examines the complete event information, categorizing and flagging physics, diagnostic, and calibration events for logging into 0.8 TB immediate storage. Online Prompt Reconstruction (OPR) of the collected events occurs in as little as few hours after logging by farms of several hundred Unix workstations running in parallel. Using the raw detector signals and the partially reconstructed events of the L3 trigger, OPR performs full reconstruction of all physics events and select calibration events. These algorithms categorize potentially interesting events before storing the results into an object database for further analysis. Monitoring and rolling calibration of reconstructed parameters is also applied at this stage. The Online Detector Control (ODC) system controls and monitors the electronics and environment of the detector and its support systems for safety assurance. Monitoring of machine status, injection

inhibition, and beam aborting is achieved through links to PEP-II systems. All collected data is archived into a browsable ambient database. The online machinery is tied together by the Online Run Control (ORC) system whose logic manages the state of all systems and provides a user interface for calibrations and starting/stopping runs. Detector configurations are stored in a configurations database for reference during reconstruction.

Chapter 3

Color suppressed $B \to \overline{D}^{(*)0}$light meson decay

In Chapter 1 we motivated the study of B mesons and the specific decay of $B^0 \to \overline{D}^{(*)0}h^0$ in the context of understanding *CP* violation as well as furthering our knowledge of B meson physics. We now focus on procedures and methods to extract *CP* violating parameters from $B^0 \to \overline{D}^{(*)0}h^0$ decays, discussing on data selection and the determination of event yields in this chapter. In Chapter 4 we will describe time-dependent fit techniques. Finally, in Chapter 5 we will present fit functions and results.

3.1 Overview

The measurements introduced in Chapter 1 are based on the reconstruction of D^0 in *CP* eigenstates, and of the "bachelor" h^0mesons. Since *CP* violation in $B^0 \to \overline{D}^{(*)0}h^0$ occurs via interference between mixing and decay (see 1.2.1), time-dependent analysis using flavor information from the other B, is needed. The ingredients of the analysis are:

- clearly identification of D^0 decays, and
- unambiguous reconstruction of h^0mesons, to
- fully reconstruct one B^0 meson decay;
- identification of the flavor of the other B^0 meson;
- measurements of the separation of the decay vertices of the two B^0 mesons.

The corresponding methods and procedures are described in the following; for the last two points more details are given in Sections 4.2 and in 4.3.1 respectively.

3.2 Data Sample

In this analysis, we used the data sample containing approximately 384×10^6 $B\bar{B}$ pairs, corresponding to an integrated luminosity of 349 fb^{-1}, and about 22.9 fb^{-1} of off-resonance data.

These data were collected by *BABAR* during the November 1999 - August 2006 periods.

We analyzed also fully simulated MonteCarlo (MC) events, both pure signal events (Table 3.2) and generic $B\overline{B}$ and $q\overline{q}$ ones (Table 3.1). In Table 3.2 there is the breakdown of the analyzed MC events; not all possible 154 modes were included in the final fit (we will discuss it in Section 3.4); so this Table provide only used channels information.

Table 3.1: "Generic" Monte Carlo samples, used in this analysis. Equivalent luminosity is also listed.

SP8 Sample	Events ($\times 10^6$)	σ(nb)	equiv.Lumi (fb^{-1})
$u\overline{u}$ $d\overline{d}$ $s\overline{s}$	696	2.09	333
$c\overline{c}$	591	1.30	455
$B^0\overline{B}^0$	552	0.525	1052
B^+B^-	555	0.525	1058

Table 3.2: Signal Monte Carlo samples, used in this analysis. The branching fractions of $\overline{B}^0 \to D^{(*)0}h^0$ are taken from the PDG 2006 [16] and multiplied by the branching fractions of the corresponding $\overline{D}^{*0}$, $\overline{D}^0$, h^0 and other decay modes. n$(B\overline{B})_{eqv}$ stands for the number of $B\bar{B}$ pairs, corresponding to the generated number of signal events.

$\overline{B}^0$ decay	Events ($\times 10^3$)	$\mathcal{B}(10^{-6})$	n$(B\overline{B})_{eqv}$ ($\times 10^9$)	n$(B\overline{B})_{eqv}$/n$(B\overline{B})_{data}$
$D^0_{KK}\pi^0$	173	1.1	157	408
$D^0_{K^0_S\omega}\pi^0$	193	2.3	100	261
$D^0_{KK}\eta_{\gamma\gamma}$	193	0.34	580	1512
$D^0_{KK}\eta_{3\pi}$	193	0.19	1019	2655
$D^0_{KK}\omega$	166	0.87	196	251
$D^0_{K^0_S\pi^0}\omega$	178	1.7	104	271
$D^0_{K^0_S\omega}\omega$	168	1.8	114	297
$D^{*0}_{KK}\pi^0$	288	1.1	281	733
$D^{*0}_{K^0_S\omega}\pi^0$	288	2.2	161	420
$D^{*0}_{KK}\eta_{\gamma\gamma}$	390	0.40	992	2586
$D^{*0}_{KK}\eta_{3\pi}$	339	0.22	1514	3946

3.3 Preselection of the data

The measurement of the *CP* violating parameters of $B^0 \to \overline{D}^{(*)0}h^0$ decays requires the selection of a sample of events with high purity. In order to achieve this goal we should maximize the efficiency of selection of the decay of our interest and, on the other hand, we should minimize the number of background events that can mimic our decay final state.

The selection was performed in several steps, first of all to reduce the number of events and then to maximize the significance of signal events.

3.3.1 Event shape discriminating variables

In the first step of the initial selection, the so called *skim* stage, we try to reject non-$B\overline{B}$ events. As reported in Table 2.1, $q\overline{q}$ cross Sections are comparable with those of $B\overline{B}$ one. Luckily the event topology of $q\overline{q}$ decays (and also of QED processes like $e^+e^- \to e^+e^-, \mu^+\mu^-, \tau^+\tau^-and\gamma\gamma$) is different from that of $B\overline{B}$ events; in Table 3.3 a summary the main topological features of each process is given.

Table 3.3: Main characteristics of the physics processes at the $\Upsilon(4S)$ energy, in the center of mass frame

Event type	Main characteristics
$e^+e^- \to e^+e^-(\gamma)$	Two high-momentum back-to back tracks and associated energy deposit in the EMC
$e^+e^- \to \mu^+\mu^-(\gamma)$	Two high-momentum back-to back tracks
$e^+e^- \to \tau^+\tau^-$	Back-to-back topology with large missing energy
$e^+e^- \to q\overline{q}$	Large number of hadrons and jet-like topology, due to the hadronization of the quarks that are produced back-to-back
$e^+e^- \to B\overline{B}$	Large number of hadrons and isotropic topology, due to the B decays

Several variables are used to minimize the $q\overline{q}$ and QED backgrounds. Relying on their different topology, we use the R_2 variable to discriminate among $B\overline{B}$ and $q\overline{q}$ events. The normalized second Fox-Wolfram momentR_2 [85] is the ratio of second to zeroth Fox-Wolfram moment $\mathcal{H}_l$; each moment $\mathcal{H}_l$ is the momentum-weighted sum of Legendre polynomial of ℓ^{th} order, computed from the cosine of the angle all pairs of tracks. The quadrupole moment $\mathcal{H}_2$ can discriminate events with a jet-like structure of momentum ($q\overline{q}$ events) from those with a more spherically symmetric topology ($B\overline{B}$ events).

The normalized ratio $R_2 = \mathcal{H}_2/\mathcal{H}_0$ is therefore very close to unity for events with back-to-back tracks such as QED events, and approaches zero for isotropic events like $B\overline{B}$ events. R_2 is computed using both charged tracks and neutral particles and we require the event having R_2 less than 0.5.

Another topological variable is used to help reduce continuum background events. Since the continuum events have a jet-like distribution, the direction of the jets can be used to distinguish events from the more isotropic B decays. The vector $\vec{A}_B$ for a B candidate is found by maximizing the ratio V_T

$$V_T = \frac{\sum_i^{1,N} |\vec{A}_B \cdot \vec{p_i^*}|}{\sum_i^{1,N} \sqrt{\vec{p_i^*} \cdot \vec{p_i^*}}} \tag{3.1}$$

where the sum is over the all the charged and neutral particles in the event, that were not used to reconstruct the B candidate, and $\vec{p_i^*}$ are their three-momentum vectors in the $\Upsilon(4S)$ rest frame. The cosine of the thrust angle θ_T between the three-momentum $\vec{p_B^*}$ of the B candidate and the thrust axis $\vec{A}_B$:

$$\cos\theta_T = \frac{\vec{p_B^*} \cdot \vec{A}_B}{|\vec{p_B^*}||\vec{A}_B|} \tag{3.2}$$

peaks at ± 1 in the jet-like $q\overline{q}$ events, but is uniformly distributed in the isotropic $B\overline{B}$ events. $\cos\theta_T < 0.9$ is required for $B^0 \to \overline{D}^{(*)0}h^0$ decays.

3.3.2 Preselection of decay chain particles

In addiction to event shape variables we use also variables related to the particles in the decay chain, to minimize backgrounds.

For each possible particle in our final states we apply a set of selection criteria, starting from charged tracks and neutral clusters up to composite objects. A list of all skim-level selection criteria is given in what follows; they will be refined in following selection stages.

We reconstruct B^0 meson decaying into $\overline{D}^{(*)0}$ h^0. We look for $\overline{D}^{*0} \to \overline{D}^0\pi^0$. As already stated we are interested in $\overline{D}^0$ going to *CP* eigenstates; so we reconstruct $\overline{D}^0$ going in to *CP*-even modes: K^+K^- and $\pi^+\pi^-$; and going to *CP*-odd modes: $K^0_S\pi^0$, $K^0_S\eta$, $K^0_S\omega$, $K^0_S\eta'$ and $K^0_S\phi$. Light bachelor meson h^0can be π^0, η, ω or η'.

Here is a list of preselection criteria for the decay-chain particles. More details and particles lists definition can be found in appendix B.

- π^0 was made from `pi0AllLoose` list which is a combination of `MergedPi0Loose` , and $\pi^0 \to \gamma\gamma$ (`pi0LooseMass`) with photon energy in the laboratory frame $E_\gamma^{lab} > 30$ MeV, lateral momentum $LAT < 0.8$ [86], invariant mass from 100 to 160 MeV/c^2 and energy in the laboratory frame $E_{lab} > 200$ MeV, with mass constraint applied.

- K^0_S was derived from the `KsDefault` list with an additional requirement of ± 15 MeV/c^2 window around its nominal mass. Each candidate was composed of $\pi^+\pi^-$ (with no Particle Identification applied), with a requirement of χ^2 vertex fit probability greater than 0.001. No cut on the displacement of K^0_S from the beam spot was applied.

- η was made from `etaDefault`, which combines $\eta \to \gamma\gamma$ and $\eta \to \pi^+\pi^-\pi^0$. For the $\eta \to \gamma\gamma$ the mass window is from 470 to 620 MeV/c^2, with photon energy in the laboratory frame $E_\gamma^{lab} >$ 50 MeV, $LAT < 0.8$, and energy in lab frame for η candidate $E_\eta^{lab} > 200$ MeV. $\eta \to \gamma\gamma$ was mass constrained. For $\eta \to \pi^+\pi^-\pi^0$ the mass window was from 515 to 575 MeV (with no energy selection and no mass constraint). Same selection applied for bachelor and D^0's η.

- ω was reconstructed in $\pi^+\pi^-\pi^0$ final state (`omegaDefault` list). Both charged pions were from `GTVL` list. The mass window was ± 50 MeV/c^2 around ω nominal mass. This selection was identical for both the bachelor ω and the one inside D^0.

- η' was made from `etaPDefault` which combined $\eta' \to \eta\pi^+\pi^-$ and $\eta' \to \rho^0\gamma$. The preselection mass window for η' was from 900 to 1010 MeV/c^2. $\rho^0 \to \pi^+\pi^-$ was selected inside ± 300 MeV/c^2 mass window, and both its pions were from the `GTVL` list. The photon was taken from `GoodPhotonLoose` with the requirements of $LAT < 0.8$ and $E_\gamma^{lab} > 100$ MeV. Same selection applied both for the bachelor and D^0's η'.

- All D^0 candidates were required to have momentum in center of mass frame $p_{CMS} > 1.1$ GeV.

- $D^0 \to K^+K^-$ was from `D0ToKKLoose` list. Mass window was ± 90 MeV/c^2. No Particle Identification on kaons: one is `GTL`, the other is `GTVL`.

- $D^0 \to \pi^+\pi^-$, same requirements as for $D^0 \to K^+K^-$, except that pions were `GTVL`.
- $D^0 \to K^0_S\pi^0$ was from `D0ToKsPi0Loose` list, which was composed out of `pi0AllLoose` and K^0_S coming from `KsDefault` list with a ± 15 MeV/c^2 mass window around nominal mass [16]. D^0 mass window was ± 160 MeV/c^2.
- $D^0 \to K^0_S\eta$ was from `D0ToKsEtaLoose` list. D^0 mass window was ± 160 MeV/c^2.
- $D^0 \to K^0_S\eta'$ was from `D0ToKsEtaPLoose` list. D^0 mass window was ± 160 MeV/c^2.
- $D^0 \to K^0_S\omega$ was from `D0ToKsOmegaLoose` list. D^0 mass window was ± 160 MeV/c^2.
- $D^0 \to K^0_S\phi$ was from `D0ToKsPhiLoose` list. D^0 mass window was ± 90 MeV/c^2. ϕ was from `phiDefault` list, kaons were `GTL` and `GTVL`, ϕ mass window was ± 30 MeV/c^2.
- D^{*0} was reconstructed in two modes: $D^0\pi^0$ and $D^0\gamma$. The mass window for $D^{*0} \to D^0\pi^0$ was from 132 to 153 MeV/c^2, for $D^{*0} \to D^0\gamma$ the window was from 110 to 175 MeV/c^2. For D^{*0}, π^0 was from `pi0SoftDefaultMass`, which was $\pi^0 \to \gamma\gamma$, π^0 mass 115$< m_{\pi^0} <$150 MeV/c^2, center of mass momentum $p^{\pi^0}_{CMS} < 450$ MeV, and and γ energy in lab frame $E^{lab}_\gamma > 30$ MeV, $LAT < 0.8$ for γ from π^0. For γ from D^{*0}, $E^{lab}_\gamma > 100$ MeV, $LAT < 0.8$.

3.3.3 B meson reconstruction

B meson candidates are reconstructed by combining one $\overline{D}^{(*)0}$ and a h^0candidate; both mesons should have passed the criteria listed in 3.3.2 and the whole event must satisfy requirements presented in 3.3.1.

The variables [87] used to separate our signal from background are $m_{\rm ES}$ and ΔE, defined as:

- the beam-energy substituted mass $m_{\rm ES}$:

$$m_{\rm ES} = \sqrt{E^{*2}_{\rm beam} - p^{*2}_B} \tag{3.3}$$

  where $E^{*2}_{\rm beam}$ is the beam energy and p^{*2}_B is the measured momentum of the B candidate in the $\Upsilon(4S)$ center-of-mass frame. The RMS spread of $m_{\rm ES}$ is given by [87]:

$$\sigma^2(m_{\rm ES}) \approx \sigma^2_B + \left(\frac{p_B}{M_B}\right)^2 \sigma^2_p \tag{3.4}$$

  where σ_B is the spread of the true B meson energy and σ_p is the uncertainty on the measured momentum. The uncertainty is dominated by the beam-energy spread σ_B.

  We select candidates with $m_{\rm ES}$ within the window from 5.115 to 5.300 GeV/c^2;

- the difference in energy ΔE:

$$\Delta E = E^*_B - E^*_{\rm beam} \tag{3.5}$$

  where $E^*_{\rm beam}$ is the beam energy and E^*_B is the energy of the reconstructed B meson (both energies are calculated in $\Upsilon(4S)$ rest frame). Expected ΔE value is zero for signal candidates. The RMS spread $\sigma(\Delta E)$ is given by the uncertainty σ_E on the measured energy and by the spread σ_B of the true B meson energy:

$$\sigma^2(\Delta E) = \sigma^2_B + \sigma^2_E \tag{3.6}$$

The measured spread in the beam energies results in variations of the $\Upsilon(4S)$ energy and is the main contribution to σ_B. The beam-energy spread is of the order of a few MeV and therefore $\sigma(\Delta E)$ is dominated by σ_E.

We select candidates having ΔE within the interval from -0.38 to +0.28 GeV.

It is important to stress that $m_{\rm ES}$ and ΔE variables are nearly uncorrelated, so we can define independent selection windows for each variable. We will fit $m_{\rm ES}$ projection to extract signal and background yields; on the contrary we will narrow ΔE window to optimize event selection.

3.4 Selection Optimization

We focus the analysis on those decay channels that, based on their known branching fractions, could give a significant number of signal events (typically greater than 5), with good decay vertex determination and reasonably low background. We initially considered 154 different decay trees. Only most of them are expected to yield a small number of signal events based on signal simulation and a set of crude event selection cuts. Some of the modes, e.g. $B^0 \to D^0\pi^0,\ D^0 \to \pi^+\pi^-$, were dropped since their corresponding fractions of peaking background, carrying *CP* asymmetry, were found to be significant (more details in 3.5). Some modes, e.g., $B^0 \to D^0\pi^0,\ D^0 \to K^0_S\pi^0$, do not have a well reconstructed B vertex, since the charmed meson D^0 has decay length of order $c\tau$ 125 μm and $\pi^0 \to \gamma\gamma$ cannot provide valuable vertex position and are not used. Also, vector-vector final states like $D^{*0}\omega$ are not used. Finally, the decays in Table 3.4 were included in the sample for the time dependent *CP* asymmetry fit.

Table 3.4: $B^0 \to \overline{D}^{(*)0}h^0$ modes selected for the final *CP* fit, with the corresponding *CP*-parity η_f *CP*.

η_f *CP*	B^0 decay mode	D^0 decay mode
-1	$\overline{B}^0 \to D^0\pi^0$	$D^0 \to KK$
$+1$	$\overline{B}^0 \to D^0\pi^0$	$D^0 \to K^0_S\omega$
-1	$\overline{B}^0 \to D^0\eta, \eta \to \gamma\gamma$	$D^0 \to KK$
-1	$\overline{B}^0 \to D^0\eta, \eta \to 3\pi$	$D^0 \to KK$
-1	$\overline{B}^0 \to D^0\omega$	$D^0 \to KK$
$+1$	$\overline{B}^0 \to D^0\omega$	$D^0 \to K^0_S\pi^0$
$+1$	$\overline{B}^0 \to D^0\omega$	$D^0 \to K^0_S\omega$
$+1$	$\overline{B}^0 \to D^{*0}\pi^0$	$D^0 \to KK$
$+1$	$\overline{B}^0 \to D^{*0}\eta, \eta \to \gamma\gamma$	$D^0 \to KK$
$+1$	$\overline{B}^0 \to D^{*0}\eta, \eta \to 3\pi$	$D^0 \to KK$
-1	$\overline{B}^0 \to D^{*0}\pi^0$	$D^0 \to K^0_S\omega$

The final state *CP*-parity η_f depends on the angular momentum L of the final states and on the *CP*-parity of $h^0$and $D^{(*)0}$. For $D^0\ h^0$with h^0= π^0 or η, $L = 0$, giving $\eta_f = (-1)^0 \cdot \eta_{h^0} \cdot \eta_{D^0} = -\eta_{D^0}$. For $D^0\omega$, $L = 1$, $\eta_\omega = 1$, therefore $\eta_f = (-1)^1 \cdot \eta_\omega \cdot \eta_{D^0} = -\eta_{D^0}$. For $D^{*0}h^0$ with $h^0 = \pi^0$ or η, $L = 1$, $\eta_{h^0} = -1$, and in $D^{*0} \to D^0\pi^0$, the angular momentum $L' = 1$, therefore $\eta_f = (-1)^L \cdot \eta_{h^0} \cdot (-1)^{L'} \cdot \eta_{\pi^0} \cdot \eta_{D^0} = +\eta_{D^0}$.

For the modes listed in Table 3.4 we perform further selections in order to maximize the signal significance, defined as $S/\sqrt{S+B}$, where $S(B)$ is number of signal (background) events. The selection

requirements for these modes are summarized in Tables 3.5 and 3.6. In what follows we will present requirements for particles in the decay chain and selection criteria.

3.4.1 Selection of charged tracks

All tracks used for reconstruction (charged pions and kaons) were taken from the `ChargedTracks` (see appendix A) list and required to be `GoodTrackVeryLoose` except for the kaons from $D^0 \to KK$ which were of type `GoodTrackLoose`. In the decay mode $D^0 \to KK$, kaons must pass the Particle Identification criteria `KLHVeryLoose` and fail `piLHVeryTight`, which resulted in the efficiency for kaons of about $\sim 88\%$ and an approximate pion mis-identification (mis-id) rate of 0.25%.

3.4.2 Selection of photons and π^0 candidates

Candidate π^0 mesons were reconstructed from photon pairs; at this level of analysis we drop merged π^0 (merged π^0 is a π^0 candidate where γ daughters are "merged" in only one EMC cluster, defined in appendix B). The photons were taken from the `GammaForPi0` and `GammaForEta` lists (see appendix B). To improve signal purity we impose more stringent cuts on π^0 mass than those used in the preliminary skim selection. For π^0 candidates coming from B^0 meson decays we require the candidate to have mass within 25 MeV/c^2 of the nominal π^0 mass [16], independently of the D^0 decay. The invariant mass cuts, imposed after the skim selection requirements, are also shown in Tables 3.5 and 3.6. For π^0 coming from D^0 decay ($D^0 \to K^0_S\pi^0$) and those coming from η and ω we apply no further refinements than those at skim level.

3.4.3 Selections of η, ω candidates

We select the η and ω candidates using decay modes $\eta \to \gamma\gamma$, $\pi\pi\pi^0$ and $\omega \to \pi\pi\pi^0$. The decay $\overline{B}^0 \to D^0\omega$ is of the type $S \to SV$ (S: scalar, V: vector). We define the "normal angle" θ_N to be the angle between the B^0 flight direction in the c.m. frame and the normal to the decay plane of the ω in the ω rest frame. For the decay $\omega \to \pi\pi\pi^0$, we defined a "Dalitz angle" θ_D to be the angle between the direction of one pion in the rest frame of the remaining pion pair and the direction of the pion pair. The distributions of these two angles using the signal MC $\overline{B}^0 \to D^0\omega$ are displayed in the Figure 3.1. In order to reduce the background from π^0 photons in η candidates, we construct a π^0 veto variable which is applied whenever it allows to increase the signal significance (see Tables 3.5 and 3.6). This variable is the minimum difference from the π^0 nominal mass of all the combinations of each of the photons from the η with any other photon in the same event. Those temporary $\gamma\gamma$ combinations are required to have $p_{CMS} > 500$ MeV.

3.4.4 Selection of K^0_S candidates

K^0_S mesons are reconstructed using pairs of charged pions, whose invariant mass was required to be within ± 15 MeV/c^2 their nominal mass [16], after refitting the pion tracks. The probability of a common vertex was required to be greater than 0.1%. The flight length in the detector of the K^0_S is about 4 cm on average, thus we didn't require the daughter pions to be of the type `GoodTrackLoose`, substituting it with less restrictive `ChargedTracks` list. We also required the flight length significance of the K^0_S candidates, defined as the ratio of the reconstructed flight length L and its uncertainty σ_L, to exceed 2. The flight length L, defined as the distance between the K^0_S decay vertex and the D^0 vertex, is projected on the x-y plane.

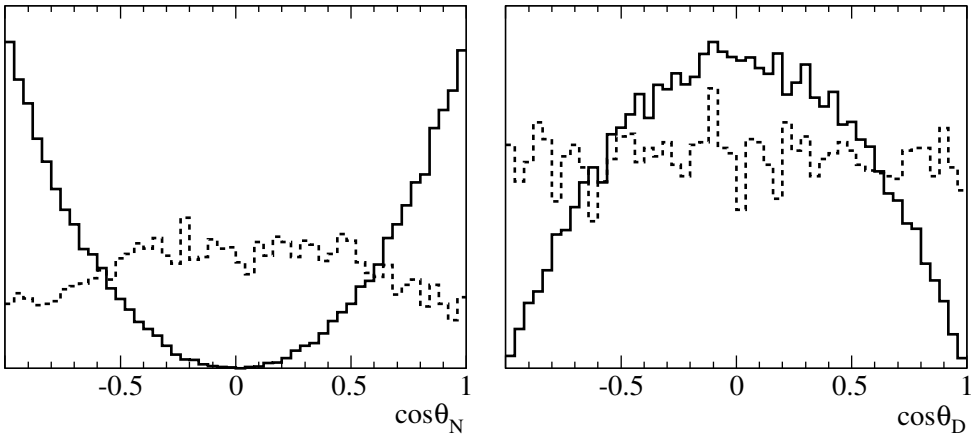

Figure 3.1: Distributions of $\cos\theta_N$ (left) and $\cos\theta_D$ (right); the angles $\cos\theta_N$ and $\cos\theta_D$ are defined in the text. Solid histograms correspond to the signal, dashed histograms to the background distributions.

3.4.5 Selection of D^0 candidates

D^0 candidates were reconstructed in 3 modes: $D^0 \to KK$, $D^0 \to K^0_S\pi^0$ and $D^0 \to K^0_S\omega$. We required the fit probability of D^0 vertex to be greater than 0.5% for KK mode, and greater than 1% for $K^0_S\pi^0$ and $K^0_S\omega$ given to the presence in these last modes of neutrals which degrade the precision on vertexing. Requirements on the invariant masses of the D^0 candidates are summarized in Tables 3.5 and 3.6.

3.4.6 Selection of D^{*0} candidates

D^{*0} candidates were reconstructed in decay mode $D^{*0} \to D^0\pi^0$. We required the difference between the mass of the $D^0\pi^0$ combination (where D^0 was mass constrained) and the reference D^{*0} [16] mass to be less than 2.7 MeV/c^2. In some of the modes, we also used a selection based on the D^{*0} helicity angle, which is defined as the angle between the π^0 and h^0 momenta in the D^{*0} rest frame (see Tables 3.5 and 3.6).

3.4.7 Selection of B^0 candidates

We reconstruct the B^0 candidates using eleven decay modes listed in Table 3.4. B^0 candidates were subject to the requirement on the probability of vertex fit and on ΔE, the difference between the energy of the B^0 and the beam energy in the $\Upsilon(4S)$ frame. Selection criteria for each decay mode are listed in Tables 3.5 and 3.6.

The Fisher discriminant technique [88] is widely used to combine linearly several discriminant variables and provide a separation or classification of events in two classes. In this analysis, we form a Fisher discriminant ($\mathcal{F}$) for continuum background suppression by using:

1. the ratio L_2/L_0 of Wolfram moments [85] $L_i = \sum_j p^*_j |\cos\theta^*_j|^i$, summed over the remaining particles j in the event, where θ^*_j and p^*_j are the angle with respect to the B^0 thrust and the momentum in the c.m. frame;

2. $\cos\theta_T$, where θ_T is the angle between the B thrust [47] and the thrust of the rest of the event;

3. $\cos^2\theta^*_B$, where θ^*_B is the angle between the beam direction (z) and the direction of B^0 candidate in the c.m. frame;

4. T, the total event thrust magnitude;

5. S, the total event sphericity [47];

The distributions of these variables for signal MC and off-peak data are shown in Fig. 3.2. The Fisher discriminant functional form that maximally separates the off-peak data from the signal MC is found to be

$$\mathcal{F} = 2.96 + 4.70\frac{L_2}{L_0} + 0.75|\cos\theta_T| + 0.85\cos^2\theta_B^* - 2.70S - 5.85T; \quad (3.7)$$

coefficients are determined indeed from training on off-peak data and signal MC samples. The Fisher discriminant distributions for signal MC, generic background and on/off-peak data are shown in Fig. 3.3.

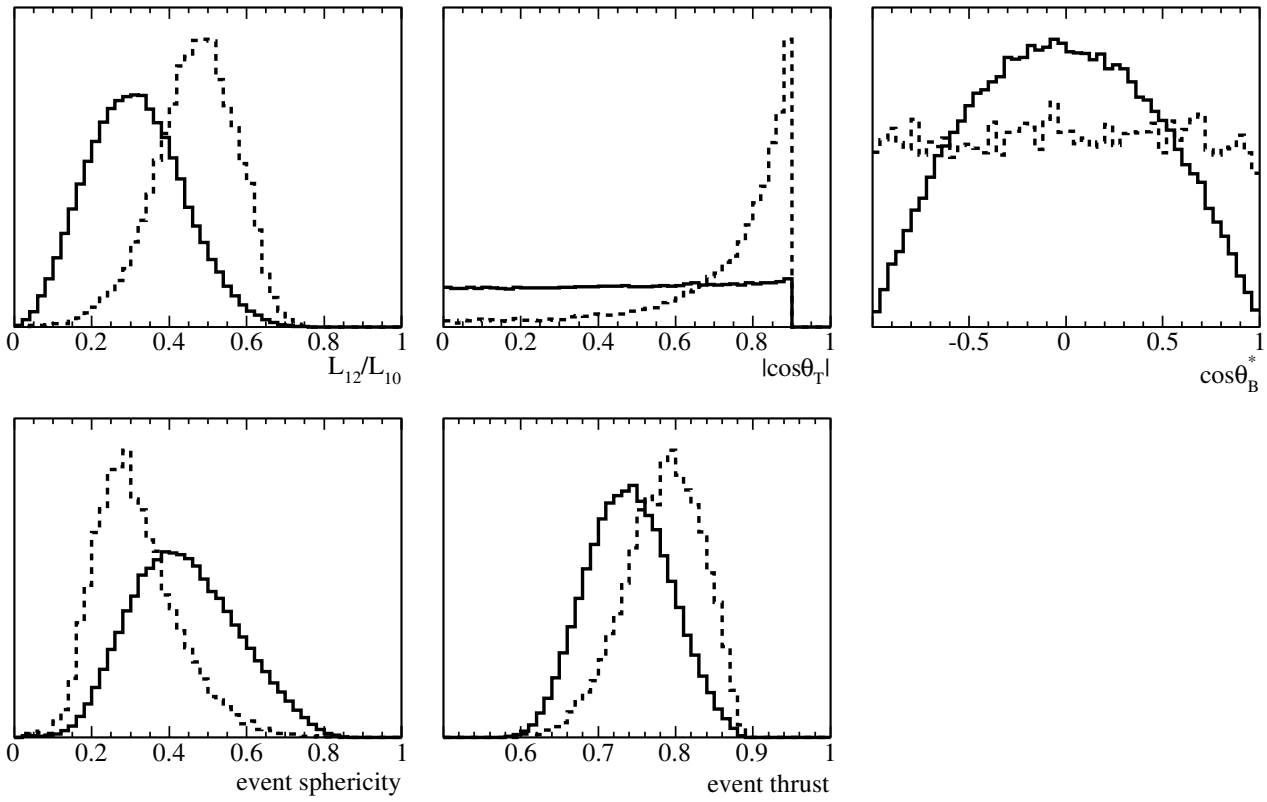

Figure 3.2: Event shape variables used in the Fisher discriminant as described in the text for signal MC (solid histograms) and off-peak data (dashed histograms).

We used a different Fisher formula for $\overline{B}^0 \to D^0\omega$ ($\omega \to \pi^+\pi^-\pi^0$) decays, adding two more variables:

1. $\cos\theta_N$, where θ_N is the angle between the B^0 direction in the c.m. frame and the normal to the decay plane of the ω in the ω rest frame;

2. $\cos\theta_D$, where θ_D is the angle between the direction of one pion in the rest frame of the remaining pion pair and the direction of the pion pair.

Since ω is a vector meson, it is fully polarized in $\overline{B}^0 \to D^0\omega$ decays and so we can use this property to discriminate against background. In Figure 3.1 the distributions of $\cos\theta_N$ and $\cos\theta_D$. For $\cos\theta_N$ signal is distributed as $\cos^2\theta_N$ and background distribution is close to $1 + \sin^2\theta_N$; for $\cos\theta_D$ signal follows $1 - \cos^2\theta_D$ and for background is flat.
The Fisher discriminant that maximally separates off-peak data and signal MC was found to be

$$\mathcal{F}_\omega = 2.59 + 3.13\frac{L_2}{L_0} + 0.50|\cos\theta_T| + 0.70\cos^2\theta_B^* - 2.22S - 3.29T + 0.49|\cos\theta_D| - 1.86|\cos\theta_N|\,. \quad (3.8)$$

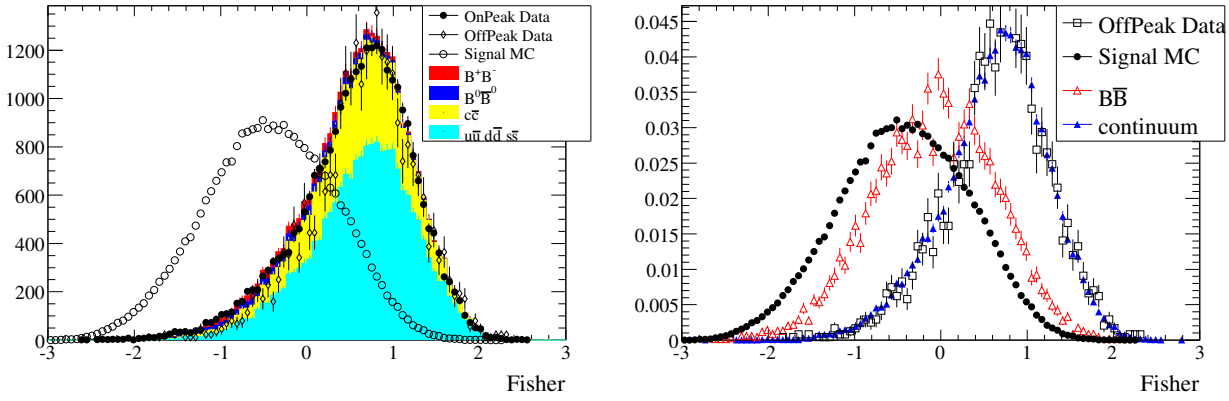

Figure 3.3: Fisher discriminant for modes with $h^0 \neq \omega$ as described in the text for signal MC, generic background and on/off-peak data. Left: the histograms of generic background sources are summed on top of each other. Both generic background and off-peak data are scaled to the on-peak luminosity; the signal MC histogram is scaled to the same integral of the on-peak distribution. Right: all histograms are scaled to have the same integral.

The Fisher discriminant distributions for signal MC, generic background and on/off-peak data are shown in Figure 3.4.

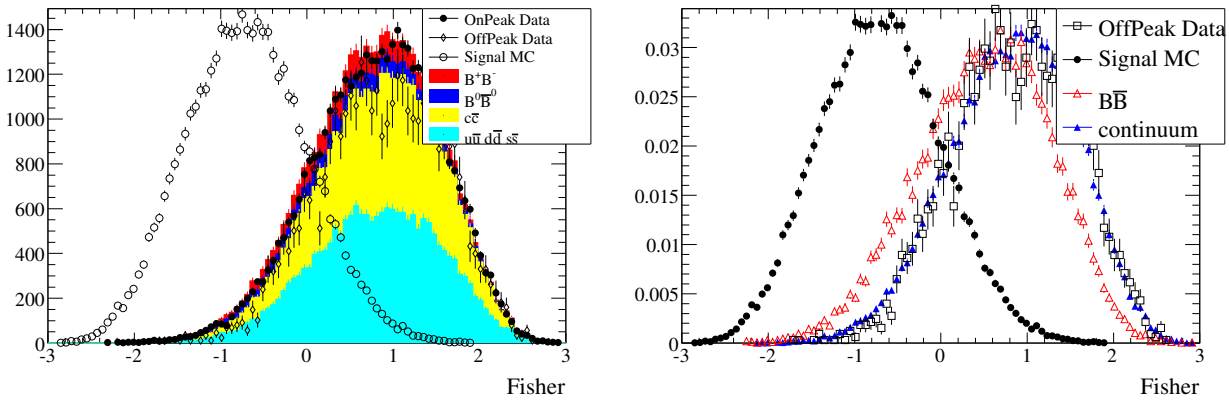

Figure 3.4: Fisher discriminant for modes with $h^0 = \omega$ as described in the text for signal MC, generic background and on/off-peak data. Left: histograms related to generic background sources are stacked on top of each other. Both generic background and off-peak data are scaled to the on-peak luminosity; signal MC histogram is scaled to the same integral of on-peak distribution. Right: all histograms are scaled to have the same integral.

The selection values on the Fisher discriminant for each mode are obtained by maximizing the statistical significance in the signal region with Monte-Carlo signal and generic Monte-Carlo $q\overline{q}$ (q = u, d, s, c). The signal region was defined as the $\{\Delta E; m_{\rm ES}\}$ region: $m_{\rm ES} > 5.27$ GeV/c^2 and $|\Delta E| < \Delta E_{cut}$; the values of ΔE_{cut} are shown Tables 3.5 and 3.6. The distributions of Fisher and of the statistical significance for the Monte Carlo signal $B^0 \to D^0\eta$, $D^0 \to KK$ and generic $q\overline{q}$ are shown as an example in Figure 3.5.

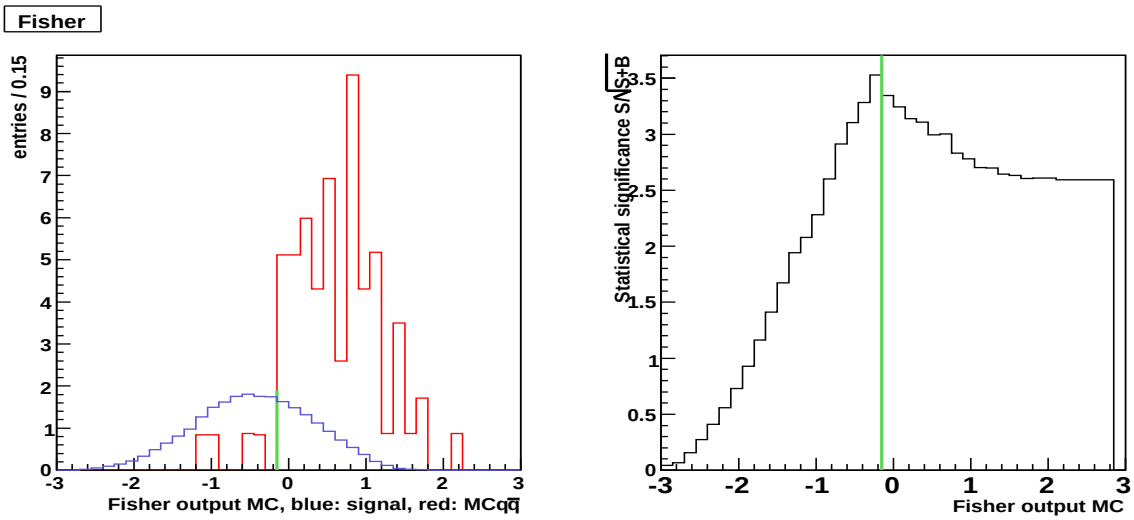

Figure 3.5: Left hand plot: distributions in the "signal box" of the Fisher discriminant for the simulated signal mode $B^0 \to D^0\eta$, $D^0 \to KK$ (red histogram) and generic quark-antiquark (blue histogram) . Right hand plot: the statistical significance $N_{signal}/\sqrt{N_{signal} + N_{q\bar{q}}}$ depending on the selection on $\mathcal{F}$. The vertical line indicates the cut position.

Table 3.5: Selection requirements, imposed on $B^0 \to D^0 h^0$ candidates (in addition to the skim selection). $|\Delta m_X|$ is the mass difference between the reconstructed invariant mass and the world-average measured value for particle X. The units are MeV and MeV/c^2 for energies and invariant masses respectively.

selection criteria	$D^0_{KK}\pi^0$	$D^0_{K^0_S\omega}\pi^0$	$D^0_{KK}\eta_{\gamma\gamma}$	$D^0_{KK}\eta_{3\pi}$	$D^0_{KK}\omega$	$D^0_{K^0_S\pi^0\omega}$	$D^0_{K^0_S\omega}\omega$
$\mathcal{F}$ <	0.26	−0.4	0.21	0.31	−0.37	−0.45	−0.24
$\lvert\Delta m_{h^0}\rvert$	25	25	27	7	24	21	24
$\lvert\Delta m_{D^0}\rvert$	14	18	14	14	14	29	18
High ΔE	85	50	55	40	40	40	40
Low ΔE	−95	−85	−80	−40	−45	−50	−55
$\lvert\Delta m_\omega\rvert$	–	20	–	–	–	–	20
$\lvert\cos\theta_D\rvert$ <	–	0.9	–	–	–	–	0.9
$\lvert\cos\theta_N\rvert$ >	–	0.4	–	–	–	–	0.4
π^0 veto	–	–	5	–	–	–	–

3.4.8 Comparison of real and simulated data

As a consistency check of the selection described above we compare real data and simulated events in some relevant distributions.

We apply the same selections criteria to real data and to Monte Carlo simulation; we used for each of the 11 selected modes (see Table 3.4) its own set of simulated signal events; we also added samples of

Table 3.6: Selection requirements, imposed on $B^0 \to D^{*0}h^0$ candidates (in addition to the skim selection). $|\Delta m_X|$ means the mass difference from the nominal value for the particle X. The unit for mass, π^0 veto and ΔE is MeV/c^2.

selection criteria	$D^{*0}_{KK}\pi^0$	$D^{*0}_{K^0_S\omega}\pi^0$	$D^{*0}_{KK}\eta_{\gamma\gamma}$	$D^{*0}_{KK}\eta_{3\pi}$
$\mathcal{F}$ <	0.55	0.79	−0.1	0.55
$\lvert\Delta m_{D^{*0}}\rvert$	2.7	2.7	2.7	2.7
$\lvert\Delta m_{h^0}\rvert$	skim	skim	32	10
$\lvert\Delta m_{D^0}\rvert$	30	30	30	30
$\lvert\Delta E\rvert$	65	65	60	35
$\lvert\Delta m_\omega\rvert$	–	20	–	–
$\lvert\cos\theta_D\rvert$ <	–	0.9	–	–
$\lvert\cos\theta_N\rvert$ >	–	0.4	–	–
π^0 veto	–	–	–	–
$\lvert\cos\theta_H\rvert$ > ...	0.0	0.4	0.0	0.0

generic $B\overline{B}$ events and of continuum $q\overline{q}$ events. Each category of events was scaled by a proper factor to account for the cross sections (see 2.1) and branching ratios; the factor f is the defined as:

$$f \equiv \frac{1}{\mathcal{L}^{\text{OnPeak}}\sigma\mathcal{B}} \tag{3.9}$$

where $\mathcal{L}^{\text{OnPeak}}$ is the luminosity corresponding to the recorded real data, σ is the cross section for the relevant process ($e^+e^- \to B\overline{B}, q\overline{q}$) and $\mathcal{B}$ is the Branching Ratio for the decay channel (e.g. $B^0 \to D^0\pi^0$).

The comparisons of m_{ES} and ΔE distributions between the real data and simulated data, after imposing all the selection requirements, are shown in Figure 3.6; we select events in a m_{ES} (ΔE) window when projecting on the ΔE (m_{ES}) variable.

Points correspond to real data and histograms to different Monte Carlo samples (signal, B^+B^-, $B^0\overline{B}^0$, $c\overline{c}$ and $u\overline{u}$,$d\overline{d}$,$s\overline{s}$). The agreement is pretty good; minor discrepancies can be attributed to statistical fluctuations.

Looking both at m_{ES} and ΔE projections we can clearly see an enhancement in the signal region (defined by $m_{\text{ES}} > 5.27\,\text{GeV}/c^2$ and ΔE within values reported in Tables 3.5 and 3.6).

We can also see a large number of events with ΔE lower than signal region lower limit. We anticipate here that this is expected and it is mainly due to modes in which a low momentum particle can be lost resulting in some missing energy. On the contrary their m_{ES} value is really close to m_B. Events of his kind are called as "peaking backgrounds"; more details on this are given in Section 3.5.

We can group modes by *CP* parity and also put all eleven modes together. Result is shown in Figure 3.7; now agreement is better.

Figure 3.8 shows the m_{ES} distribution for real (points) and simulated data (histogram), adding all eleven decay modes: the possible fluctuations of individual modes averaged out. The comparison of the two distributions gives $\chi^2/\text{nDOF} = 31.95/22$, where nDOF is the number of degrees of freedom; the χ^2 probability for this result is 7.8%, indicating a reasonable agreement.

At the beginning of this Section we anticipated that a particular mode $\overline{B}^0 \to D^0\pi^0$, $D^0 \to \pi^+\pi^-$ suffered from a higher "peaking background" contamination. This can be seen in Figure 3.9, that shows

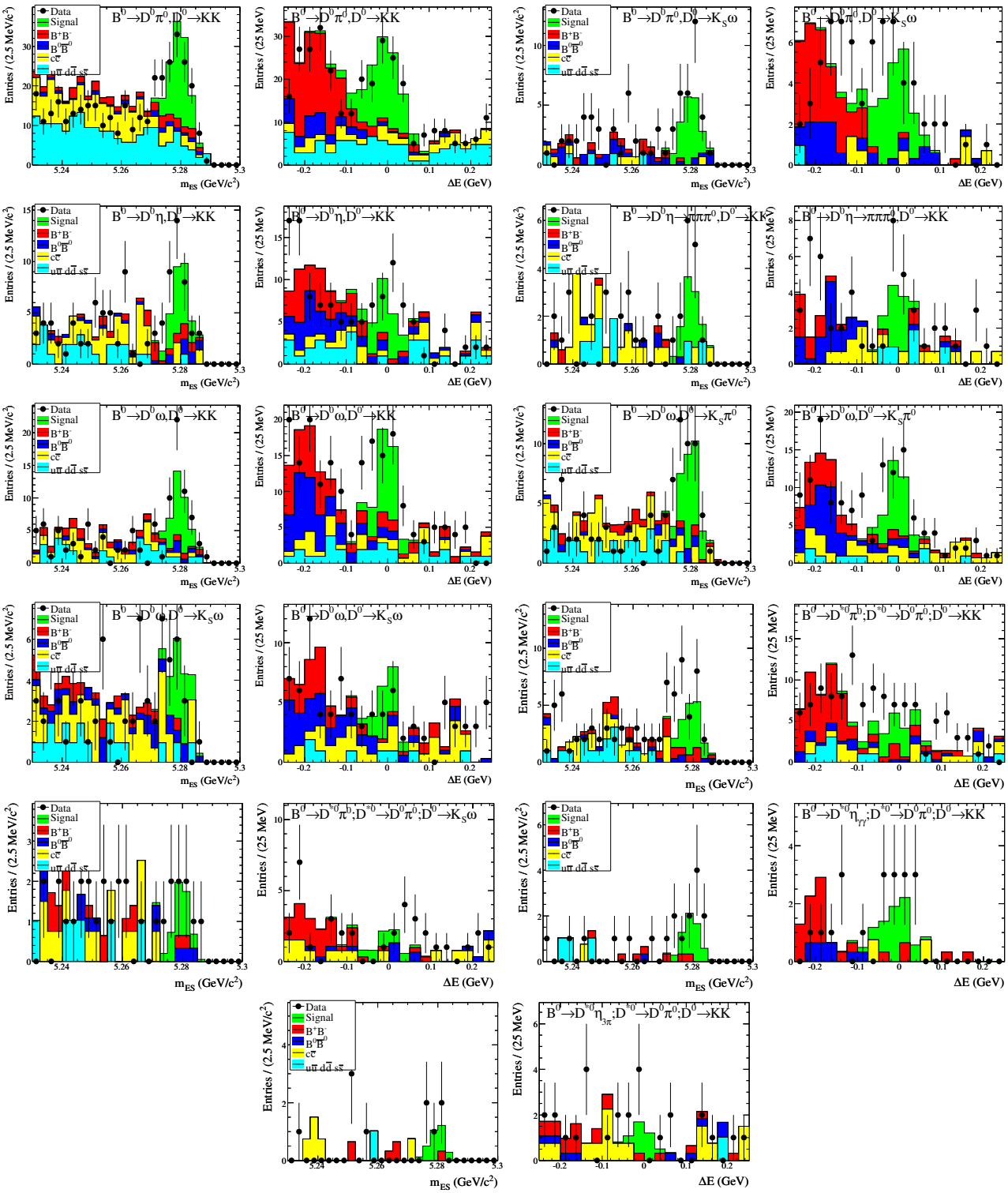

Figure 3.6: $m_{\rm ES}$ and ΔE distributions from the data (points) and generic MC (histograms) for seven D^0 $h^0$and four D^{*0} h^0modes. The color code for the simulated signal and background events is also displayed.

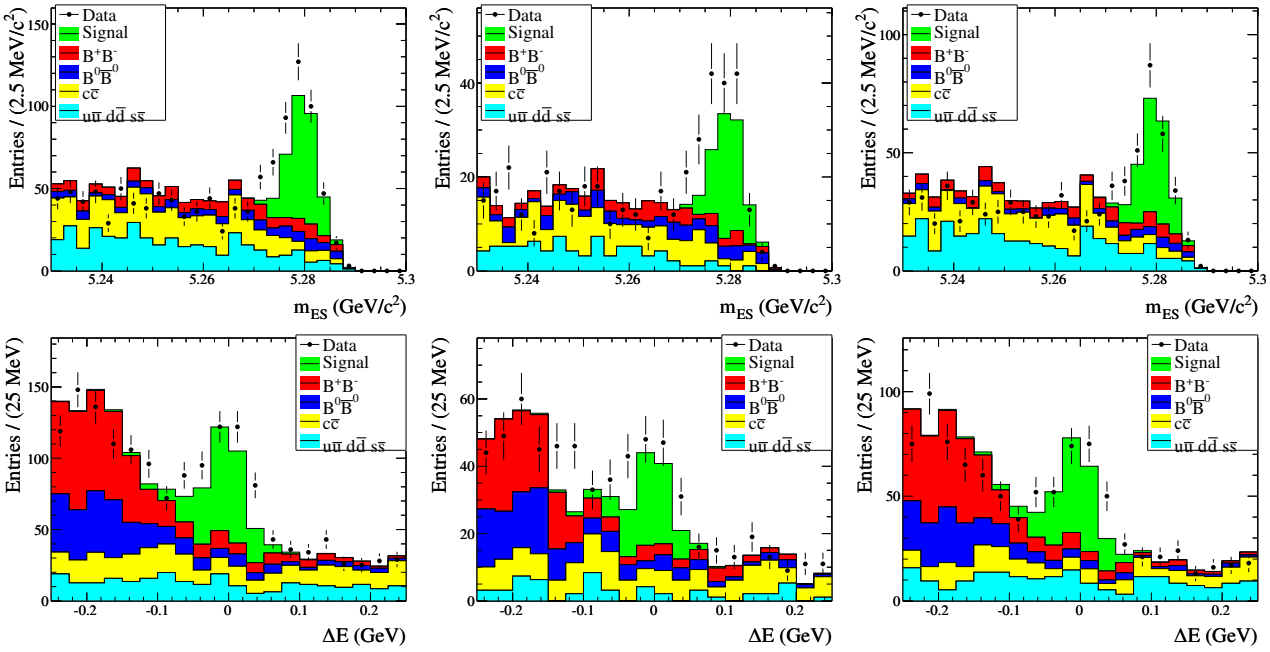

Figure 3.7: Comparison between real and simulated data. Top: $m_{\rm ES}$ distributions with all selection criteria applied. Bottom: ΔE distributions with $m_{\rm ES} > 5.27$ GeV/c^2 plus final cuts except ΔE cuts. Left: all modes combined. Middle: *CP*-even modes. Right: *CP*-odd modes.

$m_{\rm ES}$ and ΔE distribution for data and Monte Carlo events for this channel. This mode is not included in the final time-dependent fit due to high background contamination in signal region, as discussed in the following Section where signal and background yields extraction are described.

3.5 Estimate of signal and background yields

In this Section we describe methods and results for the estimate of signal and background yields from a fit to the $m_{\rm ES}$ projection. In 3.5.1 events that mimic $B^0 \to \overline{D}^{(*)0} h^0$ decays in the $m_{\rm ES}$ projections are described.

The $m_{\rm ES}$ distribution is well described by a single Gaussian with centered value m_B and standard deviation σ for the peak and an `Argus` [89] function for the combinatorial background; combinatorial background is made of mis-reconstructed decays and it is well described by an Argus [89] function:

$$\mathcal{A}(m_{\rm ES}, m_0, \xi, N_{\rm combinatorial}) = N_{\rm combinatorial} \cdot m_{\rm ES} \sqrt{1 - \left(\frac{m_{\rm ES}}{m_0}\right)^2} \cdot e^{\xi\left(1-\left(\frac{m_{\rm ES}}{m_0}\right)^2\right)} \tag{3.10}$$

The end-point parameter m_0 is fixed to 5.29 GeV/c^2 and we fit the shape parameter ξ and the normalization $N_{\rm combinatorial}$. Regarding the Gaussian distribution, the mean and the width are fixed to the values obtained from the fit of Monte-Carlo signals. The numbers of signal $N_{\rm signal}$ (combinatorial background $N_{\rm combinatorial}$) events are then the integral of the Gaussian (Argus). The signal and background shape parameters obtained from the m_{ES} fit of all modes combined are summarized in Table 3.7.

We fit the eleven modes simultaneously. All distributions share the same signal and background shape. The results of the fits of $m_{\rm ES}$ distributions obtained using the on-peak data (with all the selections applied) are shown in Table 3.8, and the $m_{\rm ES}$ projection plots are shown in Figures 3.10, 3.11 and 3.12.

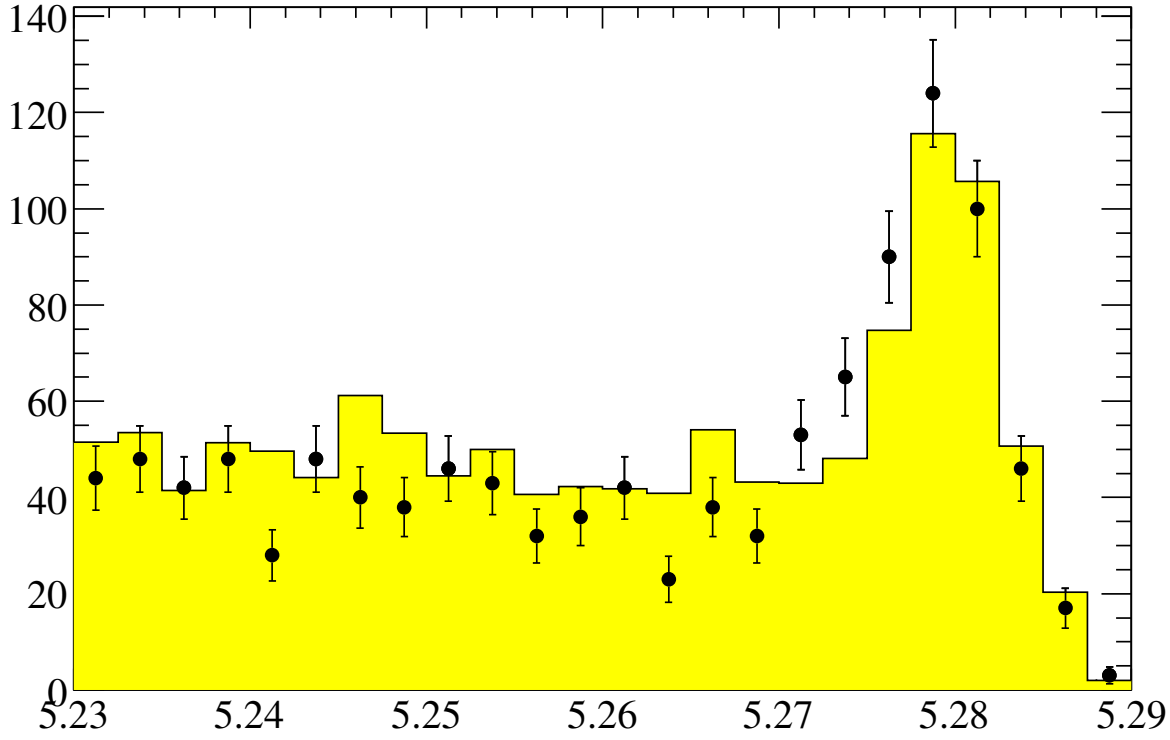

Figure 3.8: $m_{\rm ES}$ distribution from the data (points) and Monte Carlo (histogram) for seven D^0 $h^0$and four D^{*0} h^0modes. Signal MC events are embedded in generic Monte Carlo simulation.

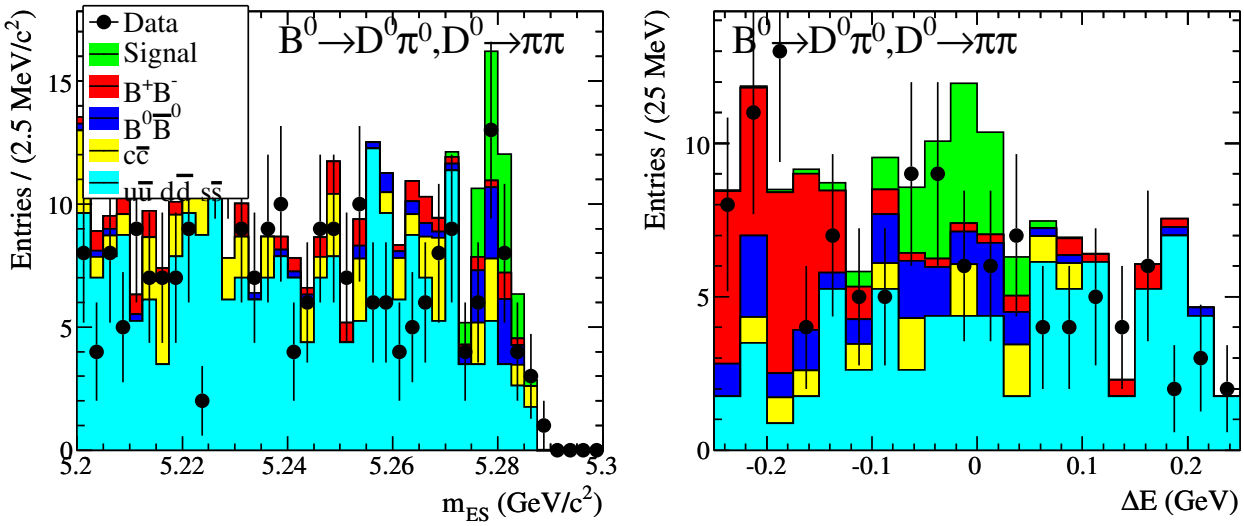

Figure 3.9: $m_{\rm ES}$ and ΔE distributions for the data (points) and generic MC (histograms) for $\overline{B}^0 \to D^0\pi^0$ where $D^0 \to \pi^+\pi^-$. High background contamination can be seen in the signal region. For this reason this mode was excluded from the time-dependent final fit.

Table 3.7: Signal and background shape parameters obtained from the m_{ES} fit of all modes combined.

Fit parameters	ξ	m_B [MeV/c^2]	σ [MeV/c^2]
Fitted values	-16 ± 10	5278.6 ± 0.3	3.4 ± 0.3

The yield of the six (five) *CP*-even(odd) modes combined is $131 \pm 16 (209 \pm 23)$ for a total of 340 ± 32. The following analysis of *CP* asymmetry is based on this sample.

Table 3.8: Signal yields obtained from the fits to the $m_{\rm ES}$ distributions of the selected data.

η_f	Mode	N_{signal}
$+1$	$D^0_{K^0_S\omega}\pi^0$	26.2 ± 6.3
	$D^0_{K^0_S\pi^0\omega}$	40.0 ± 8.0
	$D^0_{K^0_S\omega}\omega$	23.2 ± 6.8
	$D^{*0}_{KK}\pi^0$	23.2 ± 6.3
	$D^{*0}_{KK}\eta_{\gamma\gamma}$	9.8 ± 3.5
	$D^{*0}_{KK}\eta_{3\pi}$	6.8 ± 2.9
-1	$D^0_{KK}\pi^0$	103.7 ± 17.3
	$D^0_{KK}\eta_{\gamma\gamma}$	28.9 ± 6.5
	$D^0_{KK}\eta_{3\pi}$	14.2 ± 4.7
	$D^0_{KK}\omega$	51.2 ± 8.5
	$D^{*0}_{K^0_S\omega}\pi^0$	5.5 ± 3.3
	CP-even combined	131 ± 16
	CP-odd combined	209 ± 23
	All modes combined	340 ± 32

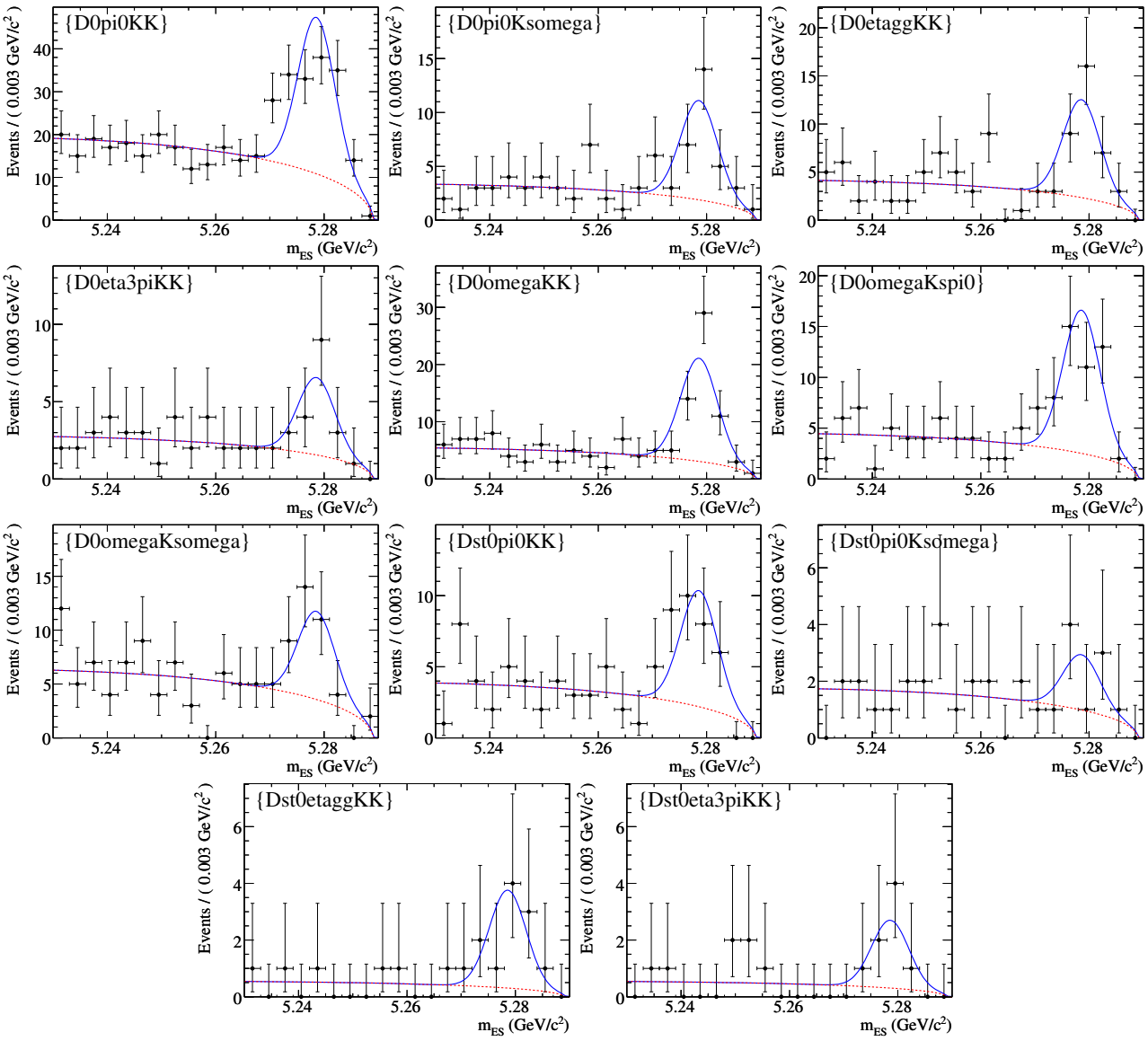

Figure 3.10: $m_{\rm ES}$ distributions with a simultaneous fit to the seven D^0h^0 and four $D^{*0}h^0$ modes in "on-peak" data.

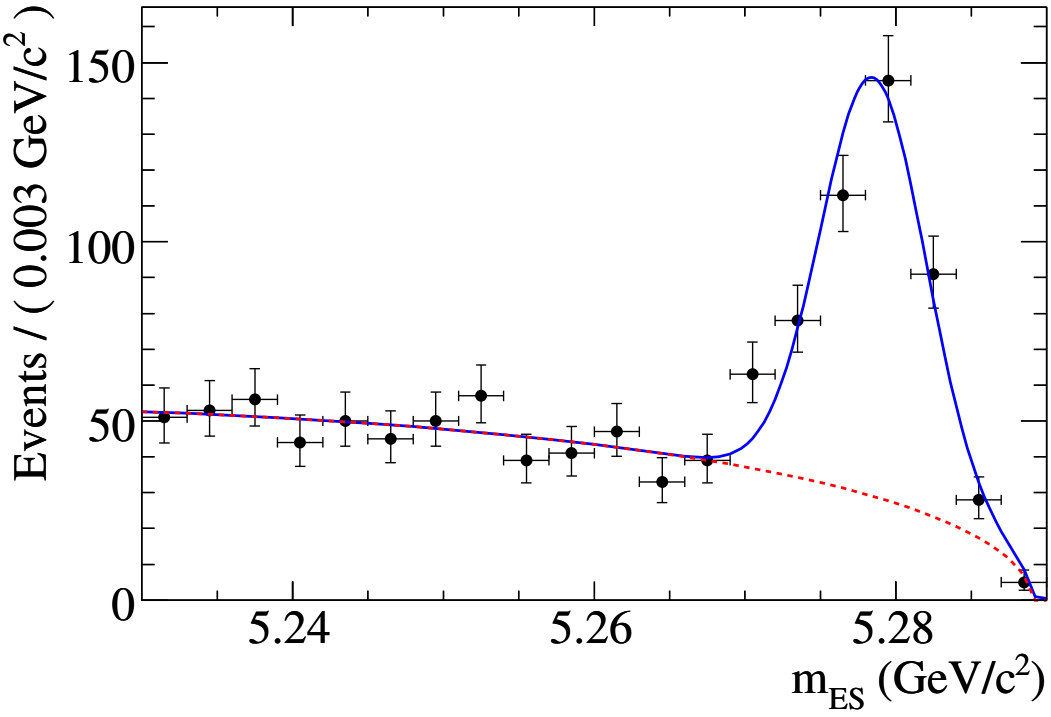

Figure 3.11: $m_{\rm ES}$ distribution with a fit to the seven D^0h^0 and four $D^{*0}h^0$ modes combined in "on-peak" data.

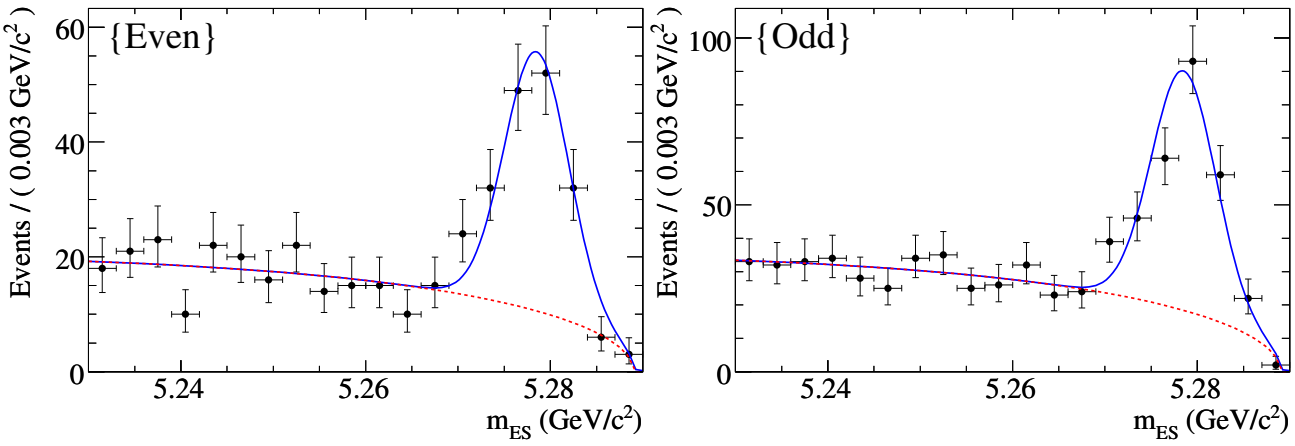

Figure 3.12: $m_{\rm ES}$ distributions with a fit to the *CP*-even and *CP*-odd modes combined in "on-peak" data.

3.5.1 "Peaking background" study

"Peaking backgrounds" were defined in Section 3.4 as backgrounds originated from mis-reconstructed B decays to non-signal channels, with reconstructed invariant mass peaking in the $m_{\rm ES}$ signal region. Such events are statistically indistinguishable from the signal and may affect the measurement of *CP* asymmetries. To estimate the fraction of the measured signal yields that should be attributed to this background source, two different methods, using both simulated events and a control sample of real data, were adopted.

In the first approach, the selection criteria discussed in the previous Section were applied also to a large sample of simulated events including all known B decay models except the signal channels ("generic $B\overline{B}$" sample, see Section 3.2); the peaking background contribution was then estimated from the $m_{\rm ES}$ distributions of the selected events, as described in the following. An extended maximum likelihood fit to the $m_{\rm ES}$ distribution, using the same PDF as for the data (see Section 3.5), was performed. The width of the Gaussian was fixed to 2.8 MeV/c^2, the MC value for the signal resolution, and the central value was fixed to 5279.3 MeV/c^2. All other parameters were free in the fit. We rescale the obtained values from the fit to the data luminosity, according to the Table 3.1. The results of the fit are presented in Table 3.9 (as $N^{MC}_{\rm peak}$). About 45% of the peak yield are from charged B decays, the other 55% are from neutral B. The $m_{\rm ES}$ projection plots are shown in Figures 3.13, 3.14 and 3.15.

In the second method a control sample of real data was defined as "D^0 sideband", in which the reconstructed D^0 candidate has an invariant mass value outside the signal region (see Tables 3.5 and 3.6); we looked in the D^0 sideband for possible charmless events as peaking background. Events from on-peak data with $m_{D^0} - m^{\rm PDG}_{D^0}$ between -70 and -30 MeV/c^2 or between $+20$ and $+60$ MeV/c^2 for $D^0 \to K^+K^-$ mode, and select between -140 and -50 MeV/c^2 or between $+40$ and $+140$ MeV/c^2 for $D^0 \to K^0_S\omega$ or $K^0_S\pi^0$ modes were selected. All the other selection criteria are unchanged. A simultaneous fit to $m_{\rm ES}$ distribution for all 11 modes are shown in Fig. 3.17. The peak yields, after scaled to the rates in the corresponding m_{D^0} selection windows, are shown in Table 3.9 ($N_{\rm SB}$).

The peaking component estimate based on D^0 sideband method appears to be somewhat larger than that determined from simulated data. We then use signal MC to study the decay modes that could contribute to the peaking component observed in D^0 sideband. As can be seen in Fig. 3.16, a small fraction of signal events can be selected from D^0 sideband. We compare the fit to $m_{\rm ES}$ distributions of signal MC samples selected from D^0 sideband and from the nominal selection. We find that for $D^0 \to K^+K^-$ modes, yield from D^0 sideband is about 5.5% of yield from the nominal selection. For $D^0 \to K^0_S\omega$, this ratio is about 11% and for $D^0 \to K^0_S\pi 0$ about 15.5%. Using these ratios, we estimate the number of signal events in D^0 sideband, as shown in Table 3.9 ($N^{\rm sig}_{\rm SB}$), scaled to the corresponding m_{D^0} selection windows.

Non-CP events such as $D^0 \to K^-\pi^+$ also contribute to peaking component. We use signal MC in $\overline{B}^0 \to D^{(*)0}\pi^0$ with $D^0 \to K^-\pi^+$, $K^-\pi^+\pi^0$, and $K^-\pi^+\pi^-\pi^+$ to estimate the peaking events in $m_{\rm ES}$ selected from D^0 sideband. They only contribute as background to $D^0 \to K^+K^-$ modes. The contributions are shown in Table 3.9 ($N^{\rm NonCP}_{\rm SB}$).

From Table 3.9, for *CP*-even modes all the peaking contributions determined by the D^0 sideband method are accounted for. Therefore we believe the estimate from generic MC is reasonable. For *CP*-odd modes, however, out of 22.5 events estimated from D^0 sideband, 4.4 are signal and 2.9 are from Non-*CP* events, according to simulation. The remaining 15.2 events are not accounted for. A scenario in which all these events (15/23≈65% of total peaking background component) have the same *CP* content is assumed for systematics studies, in the most conservative approach. More details will be given in Section 5.8.

In conclusion that for *CP*-even, the peaking background estimate is 1.1 ± 3.4 events, corresponding to (0.8 ± 2.6)%. For *CP*-odd, with 5.1 ± 3.2 events from $B^\pm$ and 2.9 events are from B^0 to non-*CP* decays, 15 ± 11 events are from possible *CP*-eigenstates. If this is the case, there are in total for *CP*-odd

23 ± 12 peaking events, corresponding to $(11 \pm 6)\%$ of the reconstructed signal.

In Figure 3.18 the $m_{\rm ES}$ distribution for selected on-peak events (*CP*-even on the left, *CP*-odd on the right); red-dashed line represents total (combinatorial plus peaking) background contribution.

Table 3.9: Peaking background yields obtained from the $m_{\rm ES}$ fits to the generic $B\overline{B}$ samples ($N^{\rm MC}_{\rm peak}$;) the numbers are scaled to the data luminosity. Scaled yield based on D^0 sideband data ($N_{\rm SB}$). Scaled yield from signal MC in D^0 sideband ($N^{\rm sig}_{\rm SB}$). Scaled yield from non-CP signal MC in D^0 sideband ($N^{\rm NonCP}_{\rm SB}$).

η_f	Mode	$N^{\rm MC}_{\rm peak}$	$N_{\rm SB}$	$N^{\rm sig}_{\rm SB}$	$N^{\rm NonCP}_{\rm SB}$
$+1$	$D^0_{K^0_S\omega}\pi^0$	0.0 ± 1.1	2.0 ± 1.5	0.55	-
	$D^0_{K^0_S\pi^0\omega}$	1.7 ± 1.8	0.2 ± 1.8	1.89	-
	$D^0_{K^0_S\omega}\omega$	0.0 ± 6.0	2.3 ± 2.0	0.48	-
	$D^{*0}_{KK}\pi^0$	0.7 ± 1.3	-2.3 ± 2.3	0.96	0.72
	$D^{*0}_{KK}\eta_{\gamma\gamma}$	0.2 ± 0.5	0	0.41	0.30
	$D^{*0}_{KK}\eta_{3\pi}$	0.0 ± 0.4	1.1 ± 1.4	0.28	0.20
-1	$D^0_{KK}\pi^0$	4.5 ± 2.8	9.3 ± 4.8	2.00	1.51
	$D^0_{KK}\eta_{\gamma\gamma}$	3.5 ± 1.9	6.5 ± 2.5	0.54	0.41
	$D^0_{KK}\eta_{3\pi}$	0.0 ± 1.3	2.0 ± 1.5	0.27	0.20
	$D^0_{KK}\omega$	5.1 ± 2.3	3.2 ± 2.5	0.99	0.74
	$D^{*0}_{K^0_S\omega}\pi^0$	0.0 ± 2.8	1.4 ± 1.0	0.58	-
	CP-even	1.1 ± 3.4	3.3 ± 4.1	4.6	1.2
	CP-odd	11.5 ± 4.7	22.5 ± 11.7	4.4	2.9
	All modes	12.6 ± 5.8			

3.6 Summary

The analysis of the time-dependent *CP* asymmetry presented in Chapter 5 is based on data selected according to criteria presented in this Chapter; the total number of selected events is 1137. *CP*-violating parameters are extracted from a simultaneous fit to $m_{\rm ES}$, Δt and $\sigma_{\Delta t}$; peaking backgrounds fractions are fixed at the valued determined from $m_{\rm ES}$ fit to D^0 mass sideband as described in this Chapter; $m_{\rm ES}$ peak fractions and shape parameters (m, σ and ξ) are free parameters in the fit.

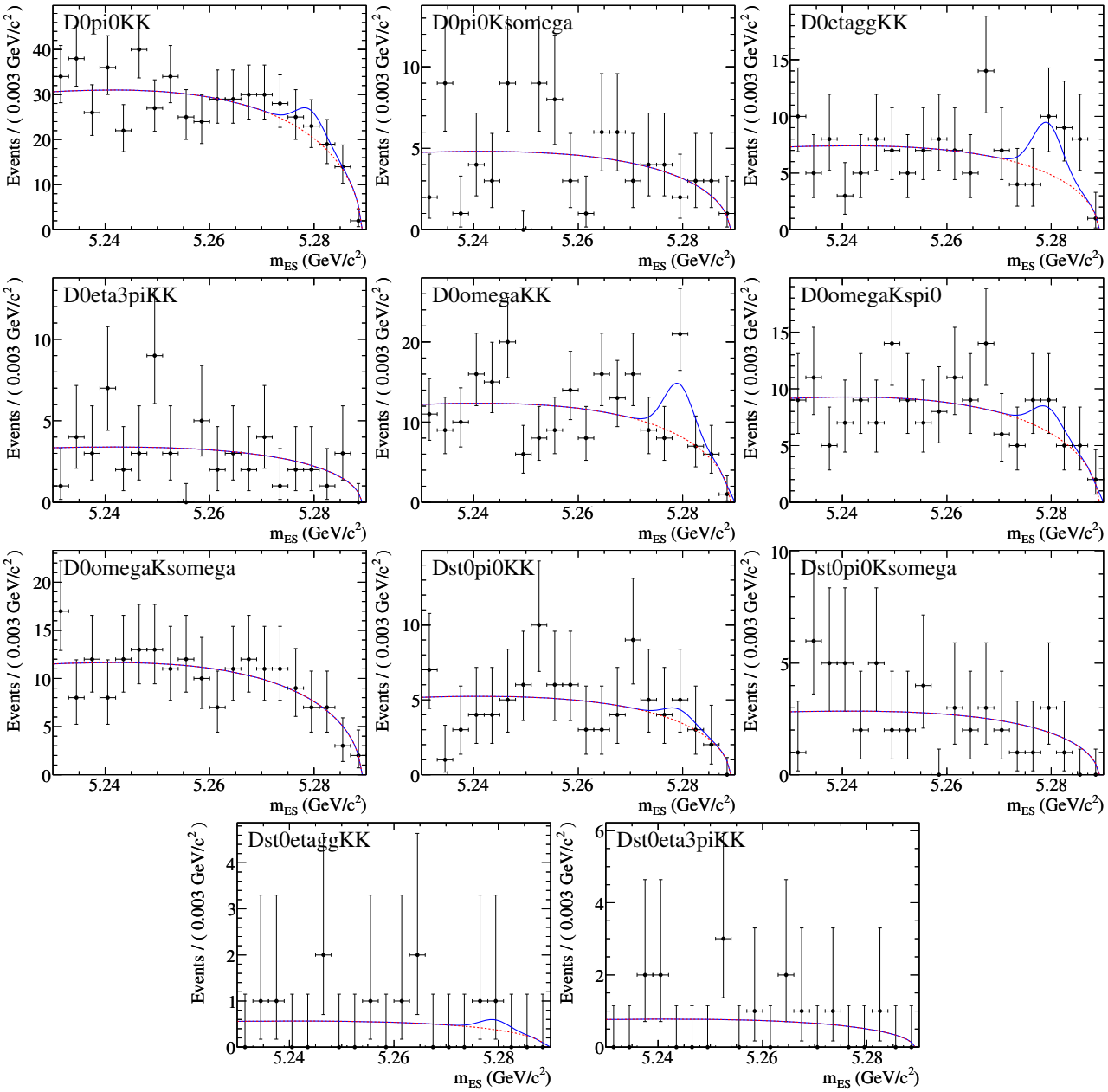

Figure 3.13: $m_{\rm ES}$ distributions from generic $B\overline{B}$ MC with a simultaneous fit to the seven D^0h^0 and four $D^{*0}h^0$ modes.

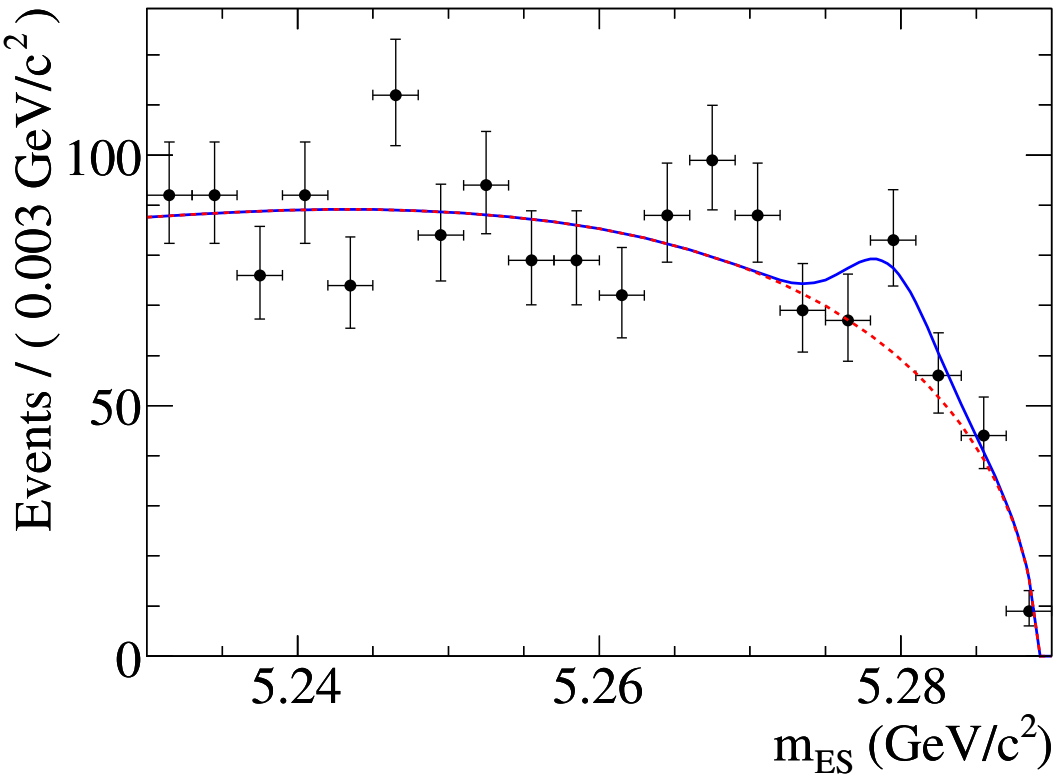

Figure 3.14: $m_{\rm ES}$ distribution from generic $B\overline{B}$ MC with a fit to the seven D^0h^0 and four $D^{*0}h^0$ modes combined.

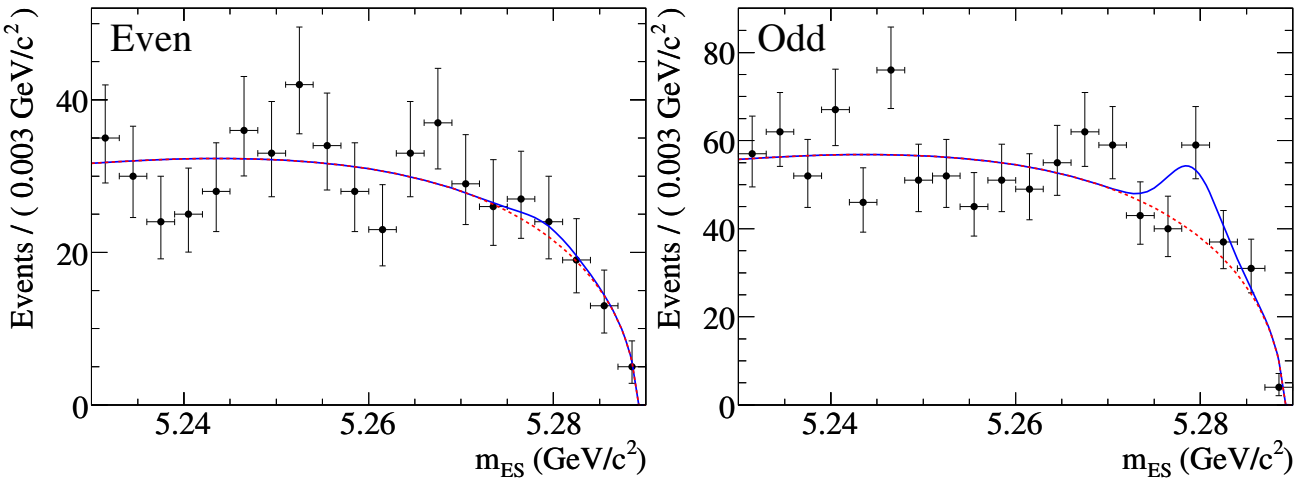

Figure 3.15: $m_{\rm ES}$ distributions from generic $B\overline{B}$ MC with a fit to the *CP*-even and *CP*-odd modes combined.

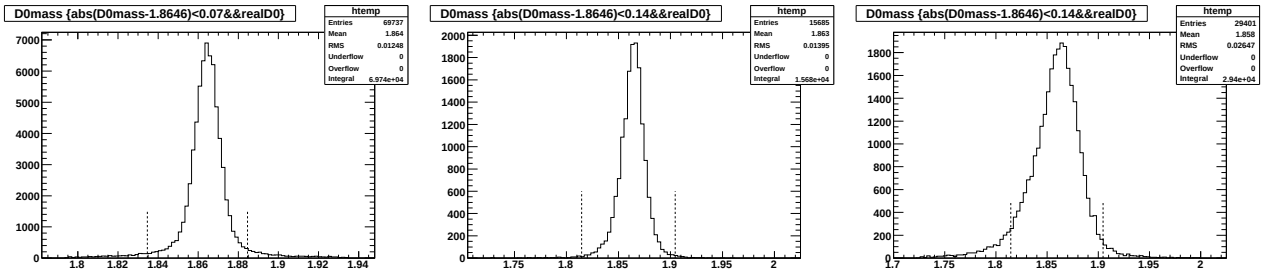

Figure 3.16: D^0 mass distribution of correctly reconstructed candidates in signal MC samples. Left: $D^0 \to K^+K^-$, middle: $D^0 \to K^0_S\omega$, right: $D^0 \to K^0_S\pi^0$. Vertical dashed lines indicate the cut for D^0 sideband selection.

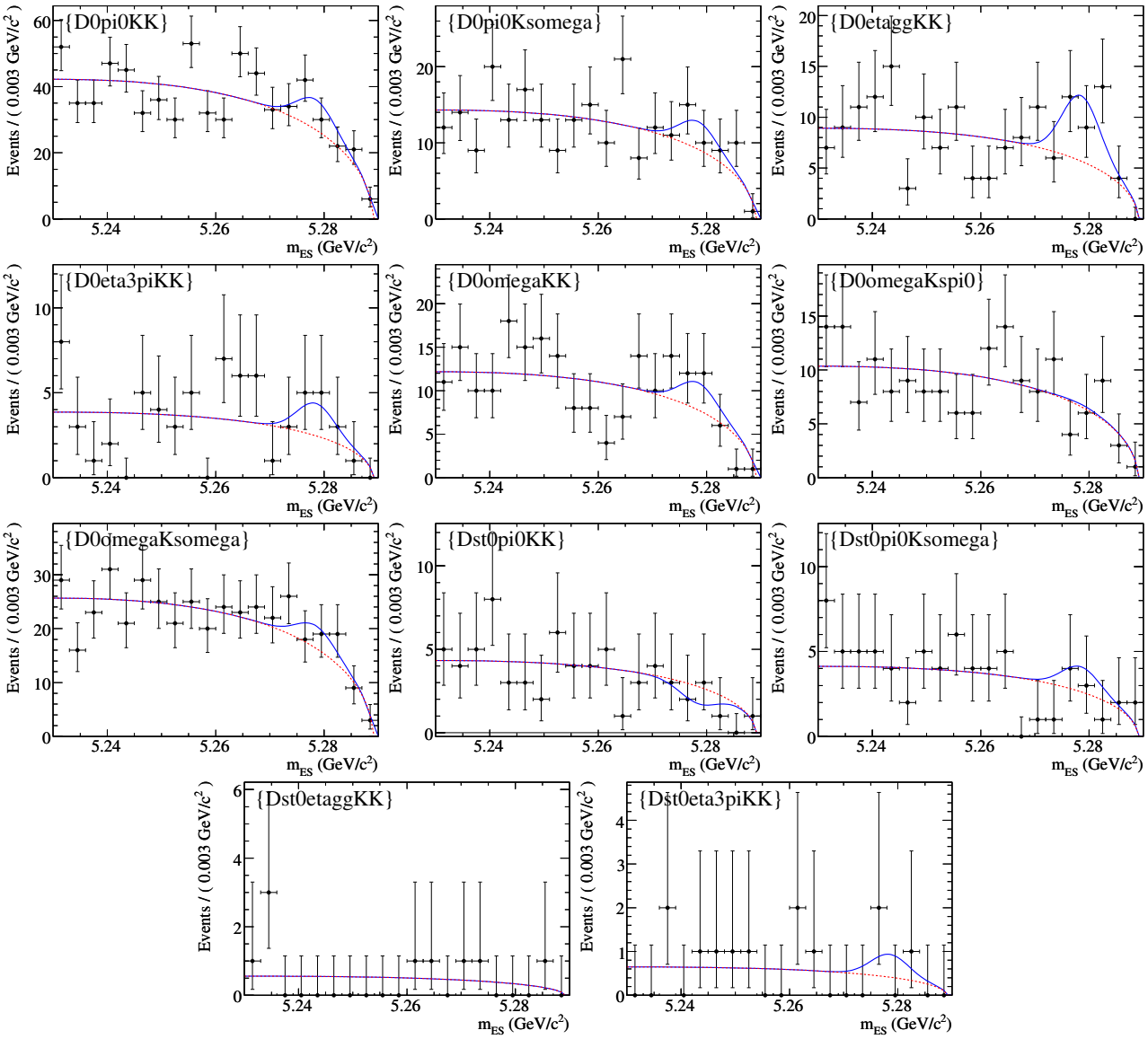

Figure 3.17: $m_{\rm ES}$ distributions from "on-peak" data in D^0 sideband with a simultaneous fit to the seven D^0h^0 and four $D^{*0}h^0$ modes.

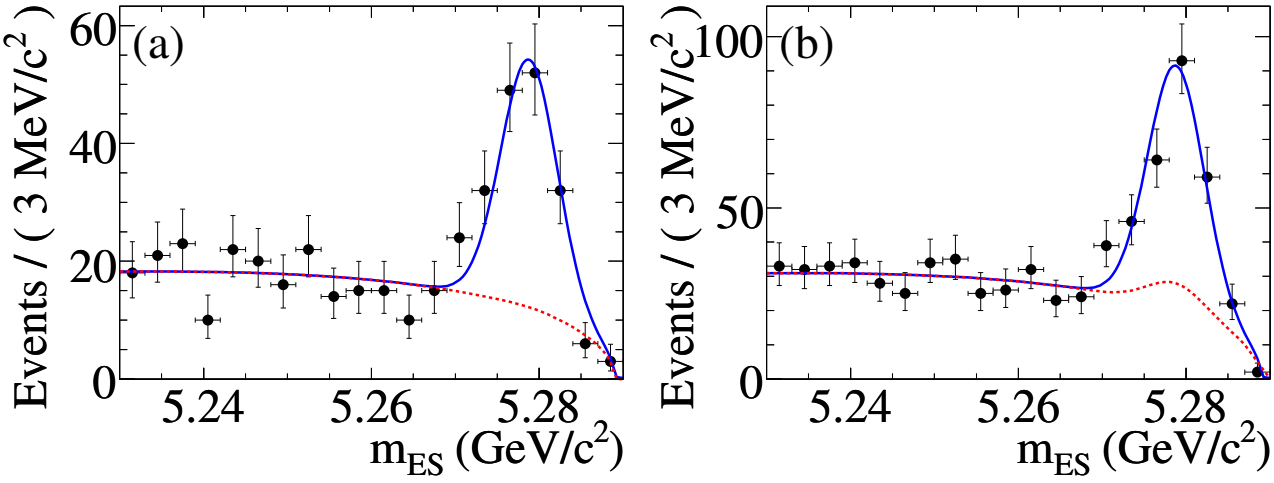

Figure 3.18: $m_{\rm ES}$ distributions with a fit to the *CP*-even and *CP*-odd modes combined in on peak data. Red line represents total (combinatorial and peaking) background contribution.

Chapter 4

Time-dependent CP analysis

The theoretical framework of CP violation and the motivation for measuring CP asymmetries in the decays of B mesons was discussed in Chapter 1. The $B^0 \to J/\psi K^0_S$ decay provides a direct measurement of the parameter sin2β; the decay $B^0 \to \overline{D}^{(*)0} h^0$ is also sensitive to the same quantity and provides an independent test of CP violation in the Standard Model. The measurement of time-dependent CP-violating asymmetries with $B^0 \to \overline{D}^{(*)0} h^0$ decays requires several experimental ingredients. We begin this chapter with an overview of the analysis and the components of the measurement.

4.1 Analysis overview

The PEP-II collider, as described in Chapter 2, is a high luminosity e^+e^- storage ring operating at $\Upsilon(4S)$ resonance energy. The $\Upsilon(4S)$ is a $b\bar{b}$ bound state which decays to a $B^0\overline{B}^0$ or B^+B^- pair. Since the $\Upsilon(4S)$ has spin $S = 1$, and therefore total angular momentum $J = L \oplus S = 1$, , the two pseudoscalar mesons must be in an $L = 1$ anti-symmetric state. The time evolution of the $B^0\overline{B}^0$ state is derived from the relations in Equation 1.23 and represents an example of quantum coherence. The decay of one of the two mesons as a B^0, for example, forces the other meson to necessarily be a $\overline{B}^0$ at the time of the first decay. If one B, referred to as $B_{\rm rec}$, is fully reconstructed in a CP eigenstate then its flavor cannot be determined from its decay products. However, the coherence property of the $\Upsilon(4S)$ decay can be used to correlate its flavor with the flavor of the other B, referred to as $B_{\rm tag}$, at the time at which one of them decays first. The time-dependent probability distributions of $B_{\rm rec}$ (see also Equation 1.26 and 1.27) are given by:

$$\begin{aligned} f_{B_{\rm tag}=\overline{B}^0}(t_{\rm tag}, t_{\rm rec}) &\propto e^{-\Gamma(t_{\rm rec}-t_{\rm tag})}\{1 + \frac{1-|\lambda|^2}{1+|\lambda|^2}\cos[\Delta m_d(t_{\rm rec}-t_{\rm tag})] \\ &- \frac{2\Im\lambda}{1+|\lambda|^2}\sin[\Delta m_d(t_{\rm rec}-t_{\rm tag})]\} \end{aligned} \tag{4.1}$$

$$\begin{aligned} f_{B_{\rm tag}=B^0}(t_{\rm tag}, t_{\rm rec}) &\propto e^{-\Gamma(t_{\rm rec}-t_{\rm tag})}\{1 - \frac{1-|\lambda|^2}{1+|\lambda|^2}\cos[\Delta m_d(t_{\rm rec}-t_{\rm tag})] \\ &+ \frac{2\Im\lambda}{1+|\lambda|^2}\sin[\Delta m_d(t_{\rm rec}-t_{\rm tag})]\} \end{aligned} \tag{4.2}$$

where $t_{\rm rec}$ is the time of decay of the fully reconstructed CP eigenstate, $B_{\rm rec}$, and $t_{\rm tag}$ is the time of the decay of $B_{\rm tag}$. A CP-violating asymmetry can be constructed from the time-dependent evolution

of $B_{\rm rec}$. We define the time-dependent asymmetry $a_{f_{CP}}$ as the ratio of the difference and the sum of the decay rates 4.1 and 4.2:

$$a_{f_{CP}} = \frac{1-|\lambda|^2}{1+|\lambda|^2}\cos(\Delta m_d \Delta t) - \frac{2\Im\lambda}{(1+|\lambda|^2)}\sin(\Delta m_d \Delta t) \tag{4.3}$$

where $\Delta t = t_{\rm rec} - t_{\rm tag}$ is the appropriate time variable for time- dependent measurements in the $\Upsilon(4S) \rightarrow B^0\overline{B}^0$ coherent decays. Relations 4.1 and 4.2 are illustrated in Figure 4.1 and are visibly different for events in which $B_{\rm tag}$ is a B^0 and those where $B_{\rm tag}$ is a $\overline{B}^0$.

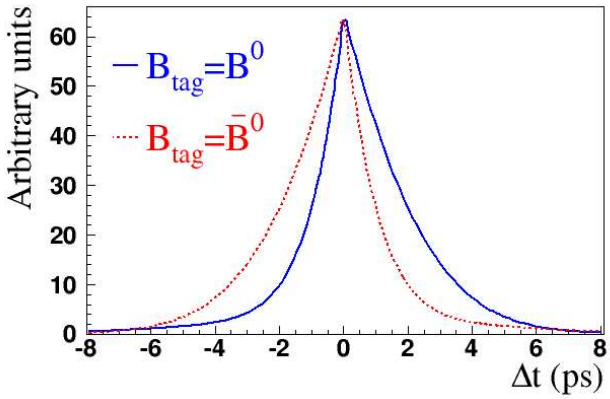

Figure 4.1: Time-dependent rates $f_{B_{\rm tag}=B^0}$ and $f_{B_{\rm tag}=\overline{B}^0}$. The values of $|\lambda|$ and $\Im\lambda$ are chosen to be 1.0 and 0.75, respectively.

The $|\lambda|$ and $\Im\lambda$ parameters can be measured experimentally, and are related to different types of *CP* violation, as already discussed in 1.2.1. In the Standard Model, $|\lambda|$ is expected to be very close to 1. Since the sine term in Equation 4.3 is an odd function of Δt, $\int_{-\infty}^{+\infty} a_{f_{CP}} {\rm d}\Delta t = 0$. Therefore $\Im\lambda$ can only be measured with a time-dependent analysis of the Δt distribution.

Experimentally the value of Δt can be measured from the spatial displacement of B^0 meson decay vertices. In the $\Upsilon(4S)$ rest frame, B mesons are separated by $\sim 30\,\mu$m on average. Measuring such a small distance is technologically challenging and the problem is solved by the asymmetric-energy configuration of the PEP-II beams. The $\Upsilon(4S)$ is produced by colliding a 9 GeV electron beam with a 3.1 GeV positron beam, and therefore has a Lorentz boost of $\beta\gamma = 0.55$ (see Section 2.1). As a result, the average separation of the two B mesons is about 250 μm along the collision axis (z) in the laboratory frame and can be measured with a precision sufficient for a time-dependent analysis.

The time-dependent measurement of the asymmetry a_{CP} with $B^0 \rightarrow \overline{D}^{(*)0}h^0$ decays therefore requires:

- the flavor of $B_{\rm tag}$; it must be determined to correlate the flavor of $B_{\rm rec}$ at time $t = t_{\rm tag}$. In practice, the flavor-tagging procedure will incorrectly assign the flavor of $B_{\rm tag}$ for a fraction of the events; wrong-tag fraction must also be measured;
- the decay vertices of $B_{\rm rec}$ and $B_{\rm tag}$; they must be determined in order calculate the time difference Δt. The experimental resolution of the Δt measurement must also be determined and parameterized and convoluted with the time-dependent asymmetry (see Section 4.3).

These ingredients are represented in Figure 4.2 (here $B_{\rm rec}$ is reconstructed in $J/\psi\ K^0_S$, in our case it will be reconstructed in $\overline{D}^{(*)0}\ h^0$). The effect of non-perfect tagging and finite Δt resolution on the

true Δt didtribution is shown in Figure 4.4.

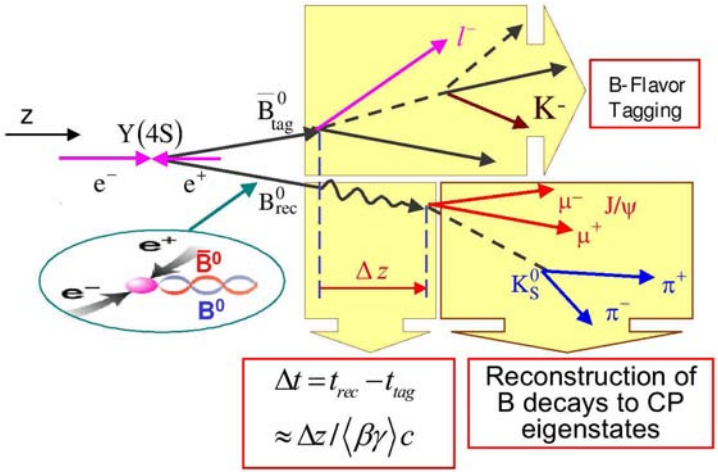

Figure 4.2: An illustration of the $B^0\overline{B}^0$ decays used to extract time-dependent *CP* asymmetries. $B_{\rm rec}$ is fully reconstructed and the remaining particles are used to infer the flavor of $B_{\rm tag}$. The time-difference between the two B decays is determined from the separation of the decay vertices.

In what follows we will present techniques to determine the flavor of $B_{\rm tag}$ and to measure the Δt decay time difference.

4.2 B flavor tagging techniques

To perform the time-dependent analysis we need to determine flavor of $B_{\rm tag}$ at its $t_{\rm tag}$ decay time. The flavor of $B_{\rm tag}$ is correlated with the charge of leptons, kaons and pions in its decay chain. Using particle identification and kinematical quantities we can "tag" the flavor of $B_{\rm tag}$.

For this purpouse, the *BABAR* collaboration developed a "flavor-tagging" algorithm, maximizing the fraction of "tagged events" (tagging efficiency ϵ), and minimizing non-zero probability of choosing the wrong flavor based on the final state particle. We define then an "effective tagging power" $Q = \epsilon(1-2w)^2$ where ϵ is the efficiency for determining the flavor and w is the fraction of candidates with a wrong flavor assignment. The quantity Q directly affects the statistical uncertainty on $\Im\lambda$ (since only flavor-tagged events are used, the statistical power of the sample is dependent on the tagging efficiency and the mis-tag fractions).

The output of the algorithm is a classification of events into six hierarchical mutually-exclusive tagging categories: `Lepton`, `KaonI` and `KaonII`, `Pion` and `KaPi` and an inclusive category `Other`. Events where there is no $B_{\rm tag}$ meson will enter in `NoTag` category. Details are given in [97].

4.2.1 Tagging performance

A large sample of fully reconstructed B-flavor eigenstates is used to estimate the performance of the tagging algorithms as well as estimate its mis-tagging rates. The "$B_{\rm flav}$" sample is composed of the decays $D^{*-}\pi^+/\rho^+/a_1^+$ and $J/\psi K^{*0}(K^+\pi^-)$. This sample is also used to measure the Δt resolution function in data and used as a control sample for the *CP*-violation asymmetry measurements [95]. An example of $m_{\rm ES}$ distribution for $B_{\rm flav}$ sample is shown in Figure 4.3.

A total of more than one hundred and thousand B decays have been selected and analyzed. Results are shown in Table 4.1.

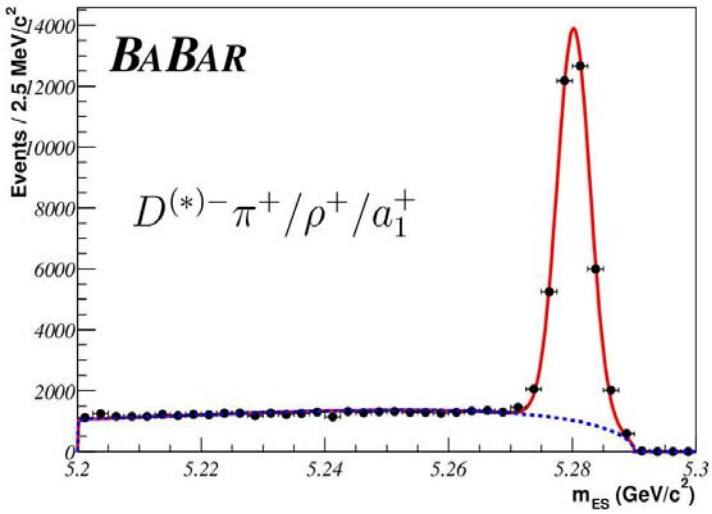

Figure 4.3: Distribution of $m_{\rm ES}$ for selected B^0 candidates in flavor eigenstates in the data sample.

Table 4.1: The efficiency ϵ, average mistags w, differences in mistag rates Δw and effective tagging power Q.

Tag Category	$\epsilon(\%)$	$w(\%)$	$\Delta w(\%)$	Q (%)
`Lepton`	8.67±0.08	3.0±0.3	-0.2±0.6	7.67±0.13
`KaonI`	10.96±0.09	5.3±0.4	-0.6±0.7	8.74±0.16
`KaonII`	17.21±0.11	15.3±0.4	-0.4±0.7	8.21±0.19
`KaPi`	17.21±0.11	15.3±0.4	-0.4±0.7	8.21±0.19
`Pion`	14.38±0.10	33.0±0.5	5.2±0.8	1.67±0.10
`Other`	9.61±0.08	41.9±0.6	4.6±0.9	0.25±0.04
All	74.60±0.12			30.4±0.3

The fraction w of wrongly tagged B^0 mesons can be different from the fraction $\bar{w}$ of mistagged $\overline{B}^0$ mesons. For example, the response of the detector to positive pions and kaons differs from its response to negative pions and kaons due to differences in total and charge-exchange cross sections. In order to account for such a difference the average mistag fraction $\langle w\rangle = (w+\bar{w})/2$ and the difference $\Delta w = w-\bar{w}$ are measured [96].

The observed Δt distributions for B^0 and $\overline{B}^0$-tagged events are derived form Equations 4.1 and 4.2 by including the fractions w and $\bar{w}$ and are given by:

$$f'_{B_{\rm tag}=\overline{B}^0}(\Delta t; w, \bar{w}) = (1-w) f(B_{\rm tag} \equiv \overline{B}^0, \Delta t) + \bar{w} f(B_{\rm tag} \equiv B^0, \Delta t) \quad (4.4)$$

$$f'_{B_{\rm tag}=B^0}(\Delta t; w, \bar{w}) = w f(B_{\rm tag} \equiv \overline{B}^0, \Delta t) + (1-\bar{w}) f(B_{\rm tag} \equiv B^0, \Delta t) \quad (4.5)$$

It is useful to rearrange terms in a way one can see the effect of the the mistag rate on the the time-dependent analysis. We define then the dilution term $\mathcal{D}$, average mistag rates and mistag differences:

$$\begin{aligned}
\langle w \rangle &= \frac{1}{2}(w + \bar{w}) \\
\Delta w &= (w - \bar{w}) \\
\mathcal{D} &= 1 - 2w \\
\bar{\mathcal{D}} &= 1 - 2\bar{w} \\
\langle \mathcal{D} \rangle &= \frac{1}{2}(\mathcal{D} + \bar{\mathcal{D}}) \\
\Delta \mathcal{D} &= (\mathcal{D} - \bar{\mathcal{D}})
\end{aligned} \tag{4.6}$$

After inserting relations 4.6 in Equations 4.5 and 4.4 we obtain:

$$f'_{B_{\rm tag}=\bar{B}^0}(\Delta t; \langle \mathcal{D} \rangle, \Delta \mathcal{D}) = \frac{\Gamma}{4} e^{-\Gamma|\Delta t|} \{(1 + \frac{1}{2}\Delta \mathcal{D}) - \langle \mathcal{D} \rangle [\mathcal{S} \sin(\Delta m_d \Delta t) - \mathcal{C} \cos(\Delta m_d \Delta t)]\} \tag{4.7}$$

$$f'_{B_{\rm tag}=B^0}(\Delta t; \langle \mathcal{D} \rangle, \Delta \mathcal{D}) = \frac{\Gamma}{4} e^{-\Gamma|\Delta t|} \{(1 - \frac{1}{2}\Delta \mathcal{D}) + \langle \mathcal{D} \rangle [\mathcal{S} \sin(\Delta m_d \Delta t) - \mathcal{C} \cos(\Delta m_d \Delta t)]\} \tag{4.8}$$

where $\mathcal{S}$ and $\mathcal{C}$ are the coefficients of the sine and cosine Δt terms respectively. In the $B^0 \to \overline{D}^{(*)0} h^0$ analysis we determine the mistag rates from $B_{\rm flav}$ sample, to avoid dependence on Monte Carlo simulation. It is reasonable to assume that mistag rates do not depend on the particular reconstructed channel [96].

4.3 Time decay difference Δt measurement

Another ingredient for time-dependent analysis is the measurement of decay time difference Δt between reconstructed B meson $B_{\rm rec}$, at time $t_{\rm rec}$, and of tagged B meson $B_{\rm tag}$, at time $t_{\rm tag}$. If $\Upsilon(4S)$ decays at $t = t_0$ in two B^0 meson, for $t > t_0$ there will be only one B^0 and one $\overline{B}^0$, till one of the two decays. Identifying then the flavor of $B_{\rm tag}$ meson $B_{\rm rec}$ at $t = t_{\rm tag}$ give us the flavor correlation among the two mesons at $t = t_{\rm tag}$.

The value of Δt can be measured by reconstructing the decay vertices of the B mesons, and measuring the spatial separation between them, without reconstructing the $\Upsilon(4S)$ decay point. The distance is then converted to Δt by using the boost factor $\beta\gamma$ that is known from the beam energies. An approximate determination of Δt is given by the relation

$$\Delta z = \beta\gamma \Delta t \tag{4.9}$$

where $\beta\gamma = 0.55$ is the $\Upsilon(4S)$ Lorentz boost factor, which is known with a precision of 0.1%. Its value is calculated from the measured beam energies.

4.3.1 Determination of B vertices

The decay vertex of the $B_{\rm rec}$ meson is reconstructed using all its decay daughters; the momenta of the particles are then re-fitted with mass constraints.

The decay vertex of $B_{\rm tag}$ is reconstructed with an inclusive technique, using charged tracks not used in the reconstruction of $B_{\rm rec}$. Charged tracks originating from long-lived particles, K^0_S and Λ^0s, are removed, and replaced by the reconstructed composite candidates in order to reduce potential biases. These composite candidates and the remaining charged tracks are used as input in a geometrical fit

to determine a common decay vertex. Since the three-momentum $\vec{p}_{rec}$ and the decay vertex of the $B_{\rm rec}$ candidate are measured with good precision, the three-momentum of $B_{\rm tag}$ can be constrained kinematically by using the measured momentum of the $\Upsilon(4S)$ and $\vec{p}_{rec}$. Since D^0 and D^+ mesons have decay lengths $c\tau$ of about $125\,\mu$m and $315\,\mu$m, respectively, the determination of the $B_{\rm tag}$ vertex will typically be biased. Hence the vertex is determined with an iterative procedure, where tracks with a large contribution to the fit χ^2 ($\Delta\chi^2 > 6$) are removed until no track fails the χ^2 requirement or only two tracks remain.

The value of Δz is determined directly in the $B_{\rm tag}$ vertex fit. The fit also provides a correct estimate of the uncertainty $\sigma_{\Delta z}$ by taking into account the correlation between the $B_{\rm tag}$ and $B_{\rm rec}$ vertices (which originates from the use of the three-momentum of $B_{\rm rec}$ as a constraint on the $B_{\rm tag}$ vertex).

4.3.2 Δt Resolution

The measured and true values of Δt differ due to the finite resolution of the detector in the measurement of decay vertices. The detector response for Δt, called the Δt resolution function, is parameterized with a sum of three Gaussian distributions (core, tail and outlier components) as a function of the residual $\delta_t \equiv \Delta t_{\rm meas} - \Delta t_{\rm true}$, and in terms of a set of parameters $\hat{a} \equiv (f_k, \mu_k, \sigma_k)$, as

$$\mathcal{R}(\delta_t;\hat{a}) = \sum_k^{\rm core,tail} \frac{f_k}{\sigma_k\sigma_{\Delta t}\sqrt{2\pi}} \exp\Big(-\frac{(\delta_t - \mu_k\sigma_{\Delta t})^2}{2(\sigma_k\sigma_{\Delta t})^2}\Big) + \frac{f_{\rm outl}}{\sigma_{\rm outl}\sqrt{2\pi}} \exp\Big(-\frac{\delta_t^2}{2\sigma_{\rm outl}^2}\Big); \tag{4.10}$$

f_k is the fraction of events in each component. The width S of the core and tail components can be written as

$$S_{\rm core} = \sigma_{\rm core}\sigma_{\Delta t} \quad , \quad S_{\rm tail} = \sigma_{\rm tail}\sigma_{\Delta t} \tag{4.11}$$

where $\sigma_{\Delta t}$ is the measured uncertainty on Δt, determined for every event, and $\sigma_{\rm core}$ and $\sigma_{\rm tail}$ are scale parameters. These factors accomodate possible under(over) estimation of the uncertainty on Δt.

The core and tail Gaussian are allowed to have non-zero offset δ_0 to account for residual charm decay products included in the $B_{\rm tag}$ vertex which tend to bias the Δt determination. These offsets are proportional to the uncertainty $\sigma_{\Delta t}$ and therefore parameterized as

$$\delta_{\rm core} = \mu_{\rm core}\sigma_{\Delta t} \quad , \quad \delta_{\rm tail} = \mu_{\rm tail}\sigma_{\Delta t} \tag{4.12}$$

The outliers component has a fixed width of 8 ps and no offset and accounts for 0.3% of selected events, which have mis-reconstructed vertices. All parameters of the Δt resolution function are measured from the $B_{\rm flav}$ sample in data.

The finite resolution Δt PDF, obtained by convolving 4.7 and 4.8 with Δt resolution function $\mathcal{R}(\delta_t;\hat{a})$, are:

$$\mathcal{F}_{B_{\rm tag}=\overline{B}^0}(\Delta t;\langle\mathcal{D}\rangle,\Delta\mathcal{D},\hat{a}) = f'_{B_{\rm tag}=\overline{B}^0}\big(\Delta t_{\rm true};\langle\mathcal{D}\rangle,\Delta\mathcal{D}\big) \otimes \mathcal{R}(\delta_t;\hat{a}) \tag{4.13}$$

$$\mathcal{F}_{B_{\rm tag}=B^0}(\Delta t;\langle\mathcal{D}\rangle,\Delta\mathcal{D},\hat{a}) = f'_{B_{\rm tag}=B^0}\big(\Delta t_{\rm true};\langle\mathcal{D}\rangle,\Delta\mathcal{D}\big) \otimes \mathcal{R}(\delta_t;\hat{a}) \tag{4.14}$$

Values of resolution parameters are given in Section 5.6.1.

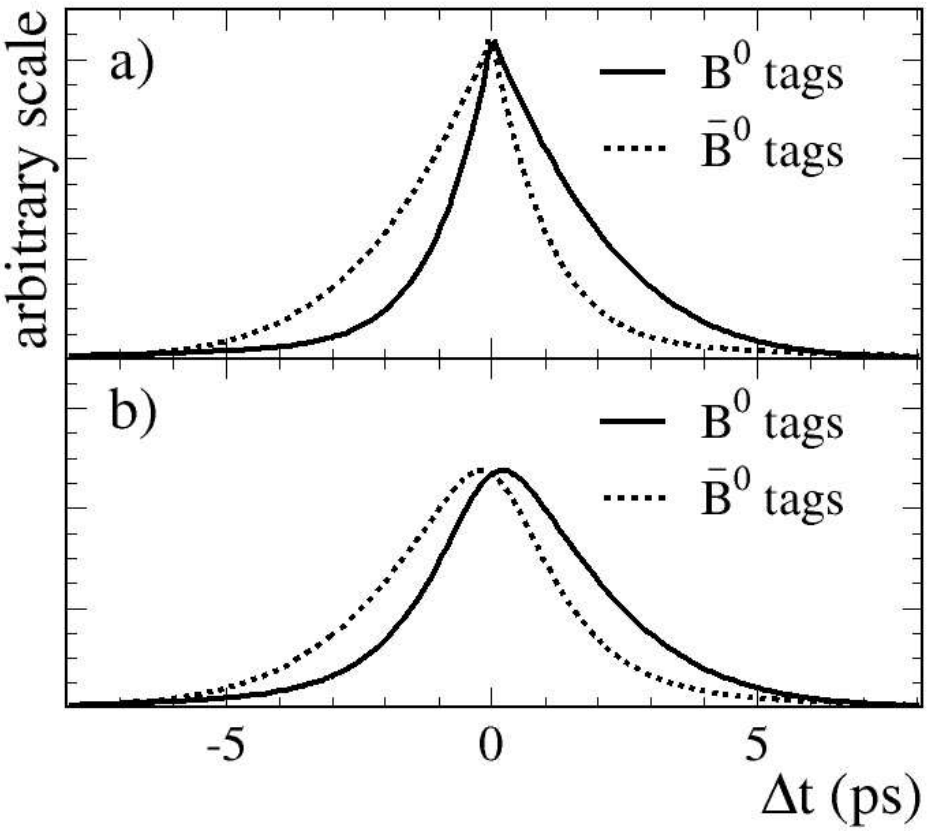

Figure 4.4: Expected Δt distribution for B^0 and $\overline{B}^0$ tagged *CP* events with a) perfect tagging and Δt resolution, and b) typical mistag fractions and finite Δt resolution. The scale is arbitrary but the same for the two plots.

Chapter 5

CP Asymmetry Fit and Results

We describe here the measurement of the *CP*-violating of parameters $\mathcal{S}$ and $\mathcal{C}$ in $B^0 \to \overline{D}^{(*)0} h^0$ decays: this is the first measurement of *CP*-asymmetry ever performed in this channel.

In the next Sections we describe the fit strategy (5.1) and the methods (5.2), the Probability Density Function (PDF) determination (5.3-5.5) and the consistency check of the assumption for the PDFs models. The validation of the total PDF for the Δt distribution is discussed in Section 5.6 before the fit on real data to extract *CP*-violating parameters; the results are presented in Section 5.7. The evaluation of systematic uncertainties affecting the measurement are discussed in 5.8.

5.1 Fit strategy

The determination of the *CP*-violating parameters $\mathcal{S}$ and $\mathcal{C}$ was performed by a fit to time-dependent asymmetry ("time-dependent fit") on real data selected according to the criteria presented in Chapter 3. A total of 1137 events has been selected ("final sample"); from these events the signal yields were estimated to be 340 ± 32 ("signal yields", see Section 3.5).

We also retain events outside the $m_{\rm ES}$ (the beam-energy substituted mass; see Subsection 3.3.3) signal region; these events have $m_{\rm ES} < 5.27\,{\rm GeV}/c^2$ and they populate the "$m_{\rm ES}$ sideband". The PDFs for background events will be modeled using those real events, avoiding to rely only on simulated events; moreover, in this way, in the final fit the correlations are taken into account properly.

The selected events contain one B^0 meson candidate ($B_{\rm rec}$) that is reconstructed in its decay to $D^{(*)0}h^0$; a total of 1137 events is selected. We also require that the flavor of the other B^0 meson candidate ($B_{\rm tag}$) is identified; a subsample of 755 events was then retained. This is called the *CP*-sample; this sample is used to extract the *CP*-violating parameters.

The ingredients and methods of the time-dependent fit have been presented in Chapter 4. The *CP*-violating parameters are extracted from the fit to the $m_{\rm ES}$ and the decay time difference Δt distributions on *CP*-sample (Δt was defined in Section 4.1). The fit is performed once the PDFs have been defined and validated using events from different control samples: the *CP*-sample in the $m_{\rm ES}$ sideband; events satisfying regular selection criteria but having D^0-candidate invariant mass value outside the signal region ("D^0 sideband"; see Subsection 3.5.1); real events in which one B meson is reconstructed in a flavor eigenstate ("$B_{\rm flav}$ sample", see Subsection 4.2.1); 157891 signal simulated events ("signal MC"; see Section 3.2); and 1573 $B\overline{B}$ and $q\overline{q}$ simulated events ("generic MC"), in which final states are generated according to known Branching Ratios. Both signal and generic MC events are selected according to the criteria presented in Chapter 3.

A summary of the samples used in the final fit is given in table 5.1.

The fit is performed simultaneously on *CP*-sample for the eleven selected modes reported in Table 3.4; data is divided by its *CP*-parity. The *CP*-sample is also divided by the tagging category

Table 5.1: List of samples used in the fit to time-dependent *CP*-asymmetry; number of events N_{evts} are listed.

sample	N_{evts}
final sample	1137
CP-sample	755
D^0 sideband	114823
signal MC	157891
generic MC	1573

presented in Section 4.2: `Lepton`, `KaonI`, `KaonII`, `KaPi`, `Pion`, and `Other`. The total number of mutually exclusive subsamples in the simultaneous fit was therefore $2 \times 6 = 12$.

We have identified three main components in our data sample: signal events, peaking and combinatorial events (see Section 3.5). A detailed description of the shapes of $m_{\rm ES}$ and Δt distributions for each component have been identified and checked using both control samples on data and different simulated events; parameters of resolution functions (introduced in Subsection 4.3.2) have been determined from the $B_{\rm flav}$ sample (presented in Subsection 4.2.1).

Besides *CP*-violating parameters ($\mathcal{C}$ and $\mathcal{S}$), some other parameters were allowed to vary in the final "standard" fit configuration, in particular the three shape parameters of the $m_{\rm ES}$ distribution, twelve peak fraction parameters for *CP*-even and *CP*-odd channels in different $B_{\rm tag}$-categories, and eight parameters related to the combinatorial background. In total, 25 parameters were simultaneously determined in the final fit.

5.2 Likelihood Fit method

In order to extract the *CP*-violating parameters, a fit to the joint distribution of the measured quantities $\vec{x} \equiv (m_{\rm ES}, \Delta t, \sigma_{\Delta_t})$ was performed maximizing a log-likelihood function $\ln \mathcal{L}$; the likelihood $\mathcal{L}$ was defined as the product of the Probability Density Function (PDF) values, evaluated for each event j in the twelve selected subsamples , identified by an index k, corresponding to different *CP*-parities and tag categories;

$$\mathcal{L} = \prod_j \Big[f_{{\rm peak},k} P_{\rm peak}(\vec{x}_j; \vec{\theta}_{\rm peak}) + (1 - f_{{\rm peak},k}) P_{\rm comb}(\vec{x}_j; \vec{\theta}_{\rm comb}) \Big]. \tag{5.1}$$

In this expression, the parameters $f_{{\rm peak},k}$ are the twelve relative fractions of "peak" (signal plus peaking background) components in the $m_{\rm ES}$ distribution discussed in Section 3.5, to be determined separately for channels with different *CP*-parities and tags, that are affected by different combinatorial ("comb") background levels.

The $P_{\rm peak}$ and $P_{\rm comb}$ PDFs model the signal plus background ("peak") and the combinatorial ("comb") respectively:

$$\begin{aligned} P_{\rm peak} &= \mathcal{G}(m_{\rm ES}; \vec{\alpha}_{\rm peak}) \Big[\mathcal{T}(\Delta t; \vec{\beta}^{\rm (phys)}_{\rm peak}) \otimes \mathcal{R}(\Delta t, \sigma_{\Delta_t}; \vec{\beta}^{\rm (res)}_{\rm peak}) \Big] \\ P_{\rm comb} &= \mathcal{A}(m_{\rm ES}; \vec{\alpha}_{\rm comb}) \Big[\mathcal{T}(\Delta t; \vec{\beta}^{\rm (phys)}_{\rm comb}) \otimes \mathcal{R}(\Delta t, \sigma_{\Delta_t}; \vec{\beta}^{\rm (res)}_{\rm comb}) \Big]. \end{aligned} \tag{5.2}$$

They are both written as the product of a PDF describing the $m_{\rm ES}$ projection (identified by $\mathcal{G}(\mathcal{A})$ for "peak"("comb") part), with a PDF $\mathcal{T}$, modelling the Δt distribution, convoluted with a resolution function $\mathcal{R}$.

The $m_{\rm ES}$ distribution function was defined in Section 3.5, as a single Gaussian $\mathcal{G}$ for the "peak" component with parameters $\vec{\alpha}_{\rm peak} \equiv (m, \sigma)$, and an Argus [89] function $\mathcal{A}$ with parameters $\vec{\alpha}_{\rm comb} \equiv (\xi, m_0)$ for the "comb" component.

The Δt distribution and resolution require different models $\mathcal{T}_{\rm peak}, \mathcal{T}_{\rm comb}$ and $\mathcal{R}_{\rm peak}, \mathcal{R}_{\rm comb}$ for the "peak" and "comb" components. In particular, in the $\mathcal{T}_{\rm peak}$ PDF the signal is modelled by an exponential times the oscillating function, as described in in Equations 4.7 and 4.8 (see Section 5.3), and peaking background is described by an exponential function (Section 5.5). In $\mathcal{T}_{\rm comb}$, different functions of Δt are assumed for $q\overline{q}$ and $B\overline{B}$ events (Section 5.5).

The corresponding $\vec{\beta}_{\rm peak}(\vec{\beta}_{\rm comb})$ can be logically grouped in "physical" parameters, labelled by the "phys" superscript (*CP*-violating parameters, lifetime, mixing, wrong tag rates) and Δt resolution parameters, labelled by "res".

Some of these parameters, for instance $\vec{\beta}^{\rm (res)}_{\rm peak}$ were fixed from from previous analyses, not described here, of time-dependent mixing in the $B_{\rm flav}$ sample (Subsection 4.2.1), some others were fixed after specific studies, performed on simulated and real data, and reported in this Chapter. In the final "standard" fit, described in Subsections 5.6.1 and 5.7.1, 25 parameters including $\mathcal{S}$ and $\mathcal{C}$ were allowed to vary.

Details of the different components for the Δt PDF are in the following; the consistency checks for individual components and for the the total Δt PDF will be given too.

5.3 Signal and peaking background Δt model

The $\mathcal{T}_{\rm peak}$ PDF is the sum of two parts, describing the signal and peaking background components respectively:

$$\mathcal{T}_{\rm peak} = f_{\rm Pb}\mathcal{F}_{\rm Pb} + (1 - f_{\rm Pb})\mathcal{F}_{\rm Signal}, \tag{5.3}$$

where $f_{\rm Pb}$ is the fraction of peaking background events (Subsection 3.5.1), that is fixed in the final fit; $\mathcal{F}_{\rm Signal}$ models the signal and is described here; $\mathcal{F}_{\rm Pb}$ takes into account the peaking background and is discussed in Section 5.4.

As defined in Section 4.2, is:

$$\mathcal{F}_{\rm Signal} \equiv f'_{\pm} = \frac{e^{-|\Delta t|/\tau_B}}{4}[1 \mp \Delta w \mp (1-2w)\mathcal{C}\cos(\Delta m \Delta t) \pm (1-2w)\eta_f \mathcal{S}\sin(\Delta m \Delta t)] \,, \tag{5.4}$$

where the upper (lower) sign represents B^0 ($\overline{B}^0$)-tagged events; w is the average mistag rate, Δw the difference in mistag rate between B^0 and $\overline{B}^0$; η_f is the *CP* eigenvalue of the final state, $\mathcal{C} = (1-|\lambda|^2)/(1+|\lambda|^2)$, and $\mathcal{S} = (2\Im(\lambda))/(1+|\lambda|^2)$. To a good approximation, $|\lambda| = 1$ and $\Im(\lambda) = -\sin 2\beta$: therefore, $\mathcal{C} \simeq 0$ and $\mathcal{S} \simeq -\sin 2\beta$, up to corrections discussed in 1.3.2.

Here we simplified the original PDF definitions 4.7 and 4.8 assuming that $\Delta\mathcal{D} \approx \Delta w$ and $\langle\mathcal{D}\rangle \approx \mathcal{D} = (1-2w)$ (see Equations 4.6); this simplification is supported by experimental evidence.

To take into account the vertex resolution, the signal Δt PDF is convoluted with the resolution function $\mathcal{R}$ described in Section 4.3.2.

5.3.1 Signal MC: Δt fit

A first validation of the fitting code was performed on the signal MC sample, implementing the Δt PDF $f'_{\pm}$ described above.

In the simultaneous time-dependent fit, all tagging categories share the same resolution function parameters except for the mean $\mu_{\rm core}$ and scale factor $\sigma_{\rm core}$ in the core Gaussian, for which the `Lepton` tag was allowed to have a different value from the non-`Lepton` tag. We fixed w and Δw to the values obtained by using the correctly reconstructed MC events.

The generated input values were: $\mathcal{C} = 0$, $\mathcal{S} = -0.703$, $\Delta m = 0.489$ ps^{-1} and $\tau_{B^0} = 1.541$ ps [16]. The results of the simultaneous fit are shown in Table 5.2 and in Figures 5.1-5.2, where they are separated according to the D^0-decay *CP*-parity. The Table also shows the fits to $h^0 \to \gamma\gamma$ modes and $h^0 \to 3\pi$ modes separately, and a fit using the resolution function parameters obtained from the $B_{\rm flav}$ MC sample [96], that is made of simulated events of the same kind of the $B_{\rm flav}$ sample. The two h^0decay modes were analyzed separately, to check the consistency because they have different event topology ($h^0 \to \gamma\gamma$ does not contribute to vertexing).

The values of the physical parameters obtained from the fit are consistent with the input MC parameters within the errors, except for the τ_B, that differs by about 2.6σ. However, since the correlation between the B^0 lifetime and the other fitted physics quantities is very small, this discrepancy is not considered as an indication of a problem with the *CP* asymmetry fit.

Table 5.2: Results of the *CP* asymmetry fit to the signal MC data. Fits to $h^0 \to \gamma\gamma$ and $h^0 \to 3\pi$ modes, and the fit using the resolution function determined from `BFlav` MC sample [96] are also shown. Indices C, T, O stand for the core, tail and outlier part of the resolution function, respectively; Lepton(Hadr) indicates tagged events using `Lepton`(non-`Lepton`) tag category.

Fit par.	Input	Fit result	$h^0 \to \gamma\gamma$	$h^0 \to 3\pi$	Use `BFlav` MC
$\mathcal{S}$	-0.703	-0.711 ± 0.009	-0.713 ± 0.012	-0.710 ± 0.014	-0.720 ± 0.009
$\mathcal{C}$	0	-0.003 ± 0.006	-0.002 ± 0.008	-0.006 ± 0.010	-0.001 ± 0.006
Δm (ps^{-1})	0.489	0.481 ± 0.006	0.481 ± 0.007	0.481 ± 0.009	0.480 ± 0.006
τ_B (ps)	1.540	1.561 ± 0.008	1.562 ± 0.012	1.553 ± 0.012	1.533 ± 0.006
$\mu_{C;\rm Hadr}$	–	-0.199 ± 0.011	-0.187 ± 0.013	-0.219 ± 0.020	-0.2472 ± 0.0028
$\mu_{C;\rm Lepton}$	–	-0.061 ± 0.023	-0.056 ± 0.027	-0.073 ± 0.045	-0.0618 ± 0.061
f_C	–	0.923 ± 0.009	0.934 ± 0.010	0.890 ± 0.017	0.8894 ± 0.0019
$\sigma_{C;\rm Hadr}$	–	1.13 ± 0.02	1.153 ± 0.020	1.066 ± 0.035	1.0898 ± 0.0047
$\sigma_{C;\rm Lepton}$	–	1.06 ± 0.03	1.09 ± 0.04	0.992 ± 0.074	0.9952 ± 0.0098
μ_T	–	-1.30 ± 0.18	-1.166 ± 0.21	-1.442 ± 0.25	-1.178 ± 0.029
f_O	–	$(0.1 \pm 9.3) \cdot 10^{-5}$	0.0003 ± 0.0009	0.0000 ± 0.0016	0.0041 ± 0.0001

5.4 Δt model for the peaking background

A detailed description of peaking background events was given in Subsection 3.5.1. The fractions $f_{\rm Pb}$ (Equation 5.3) for peaking background were fixed to the values reported in the same Subsection.

The peaking background is modelled by a simple exponential decay:

$$\mathcal{F}_{\rm Pb} \propto e^{-|\Delta t|/\tau_{\rm Pb}}. \tag{5.5}$$

The default lifetime $\tau_{\rm Pb}$ is fixed to the mean value of the neutral and charged B meson lifetimes [16]. The resolution function is the same as the one used for the signal PDF.

5.5 Δt model for combinatorial background

The main background is combinatorial and does not peak in the $m_{\rm ES}$ distribution, where it is modeled by the Argus function $\mathcal{A}$. Continuum $q\overline{q}$ events form the major source of (about 80%, as estimated

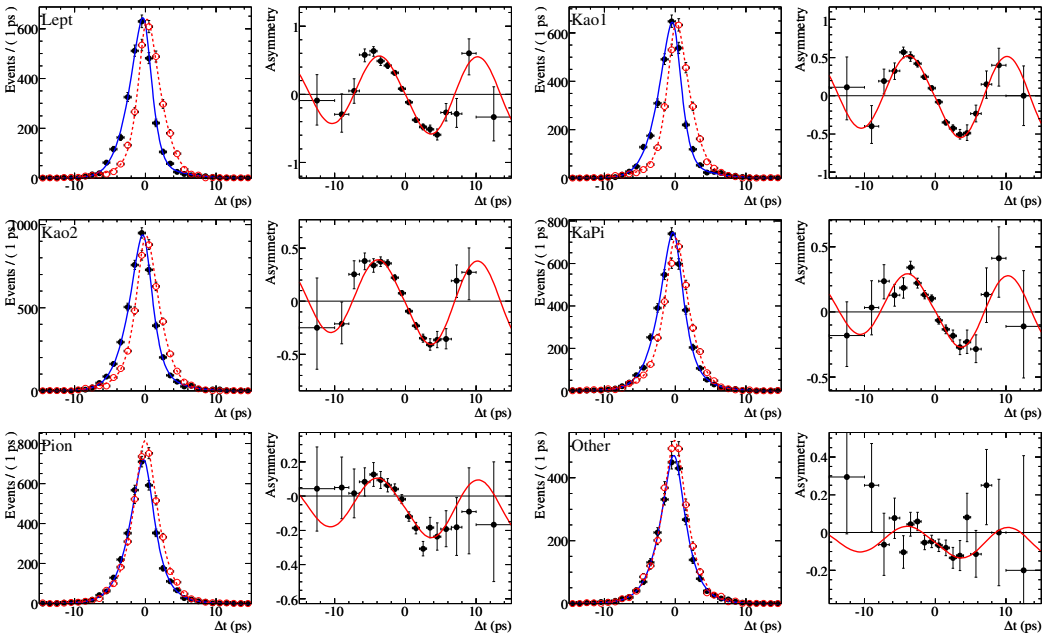

Figure 5.1: Signal MC Δt and asymmetry plots for D^0 decaying to *CP*-**even** eigenstates. The solid data points and solid curve in the first and third column are for B^0-tagged events. The open circles and dashed curve are for $\overline{B}^0$-tagged events; the used-`tag` selector is reported. As expected, different tag categories correspond to different dilutions $\mathcal{D}$ of the same asymmetry.

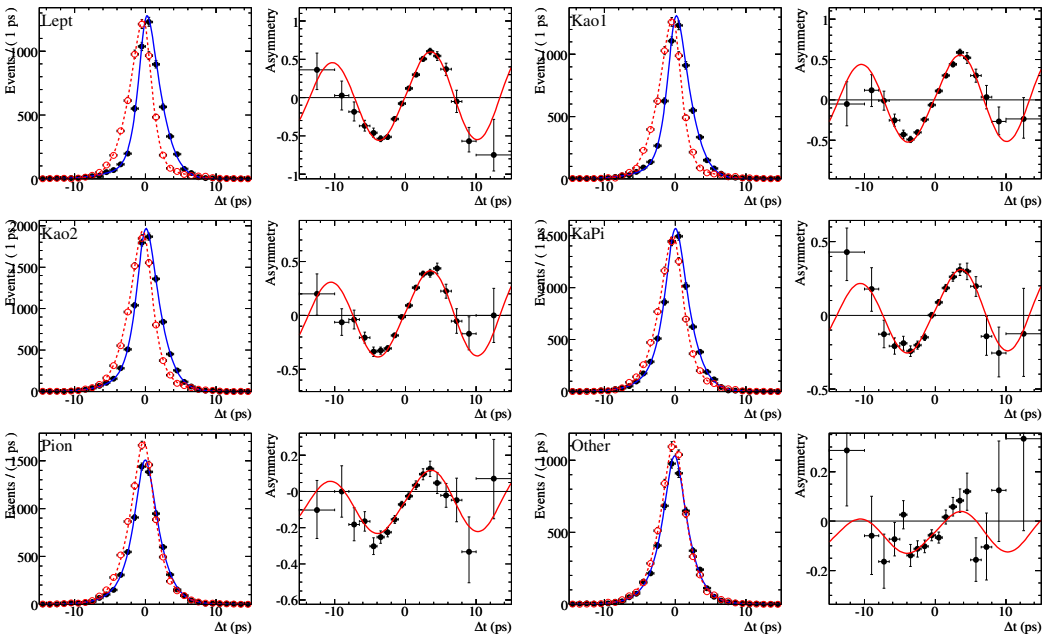

Figure 5.2: Signal MC Δt and asymmetry plots for D^0 decaying to *CP*-**odd** eigenstates. The solid data points and solid curve in the first and third column are for B^0-tagged events. The open circles and dashed curve are for $\overline{B}^0$-tagged events; the used-`tag` selector is reported. As expected, different tag categories correspond to different dilutions $\mathcal{D}$ of the same asymmetry.

using generic MC); $B\overline{B}$ events account for the remaining 20%. The continuum $q\overline{q}$ events ("prompt" component) are modeled with a Dirac-δ function (since there is no oscillation for these events); for B decay component, *CP*-asymmetry is allowed to be non-zero: an exponential time an oscillating function, just like the signal, is assumed. The overall Δt PDF for combinatorial background is:

$$\mathcal{T}_{\rm comb,i} = F_{\pm}^{\rm Cb} = f_{{\rm pmt},i}\delta(\Delta t) + (1 - f_{{\rm pmt},i}) \frac{e^{-|\Delta t|/\tau^{\rm Cb}}}{4}[1 \mp \Delta w \mp (1-2w)(C^{\rm Cb}\cos(\Delta m \Delta t) - \eta_f S^{\rm Cb}\sin(\Delta m \Delta t))] \quad (5.6)$$

where subscript "pmt" means prompt and "Cb" means combinatorial. The prompt fractions $f_{{\rm pmt},i}$ are splitted according to tag category i, `Lepton` or not (labelled has "Hadron"). The PDF is convoluted with a double-Gaussian resolution function instead of the usual triple Gaussian form described in Subsection 4.3.1; we do not use the tail gaussian but only the "core" and the "outlier" ones.

This PDF was tested using the "$m_{\rm ES}$ sideband" control sample (see Section 5.1). The mistag and Δ-mistag were split according to the tagging categories. For the prompt fraction $f_{\rm pmt}$, the `Lepton`-tagged events were treated separately from the rest. The mistag rates w, the difference in mistag rates Δw, and the mixing Δm frequency were fixed at the same values as in the signal. The prompt fractions, the effective lifetime, the $\mathcal{S}^{\rm Cb}$ and $\mathcal{C}^{\rm Cb}$ parameters, as well as the resolution function bias $\mu_{\rm core}$, the scale factor $\sigma_{\rm core}$, and the core fraction $f_{\rm core}$, were free parameters. The result of the fit to the data sideband ($m_{\rm ES} < 5.27$ GeV/c^2) is shown in Table 5.3 and in Figure 5.3. No evidence of *CP*-violation was found as expected.

Table 5.3: Result of the Δt fit to the $m_{\rm ES}$ sideband. $f_{\rm pmt;Lepton}$ is the fraction of prompt events $f_{\rm pmt}$ that are tagged under `Lepton`-tag category; $f_{\rm pmt;Hadron}$ is the fraction of prompt events $f_{\rm pmt}$ that have tagged under all the remaining tag categories.

Parameter	Value
$\mathcal{C}^{\rm Cb}$	-0.13 ± 0.29
$\mathcal{S}^{\rm Cb}$	0.18 ± 0.42
$\mu_{\rm core}^{\rm Cb}$	-0.18 ± 0.11
$f_{\rm core}^{\rm Cb}$	0.924 ± 0.031
$\sigma_{\rm core}^{\rm Cb}$	1.35 ± 0.15
$f_{\rm pmt;Hadron}$	0.56 ± 0.15
$f_{\rm pmt;Lepton}$	0.00 ± 0.99
$\tau^{\rm Cb}$ (ps)	1.30 ± 0.37

5.6 Test of the time dependent fit

We looked for a possible undesidered bias by fitting both pure signal simulated events with the signal PDF and samples of Monte Carlo events including background with the total PDF described above. We present techniques and results in the following.

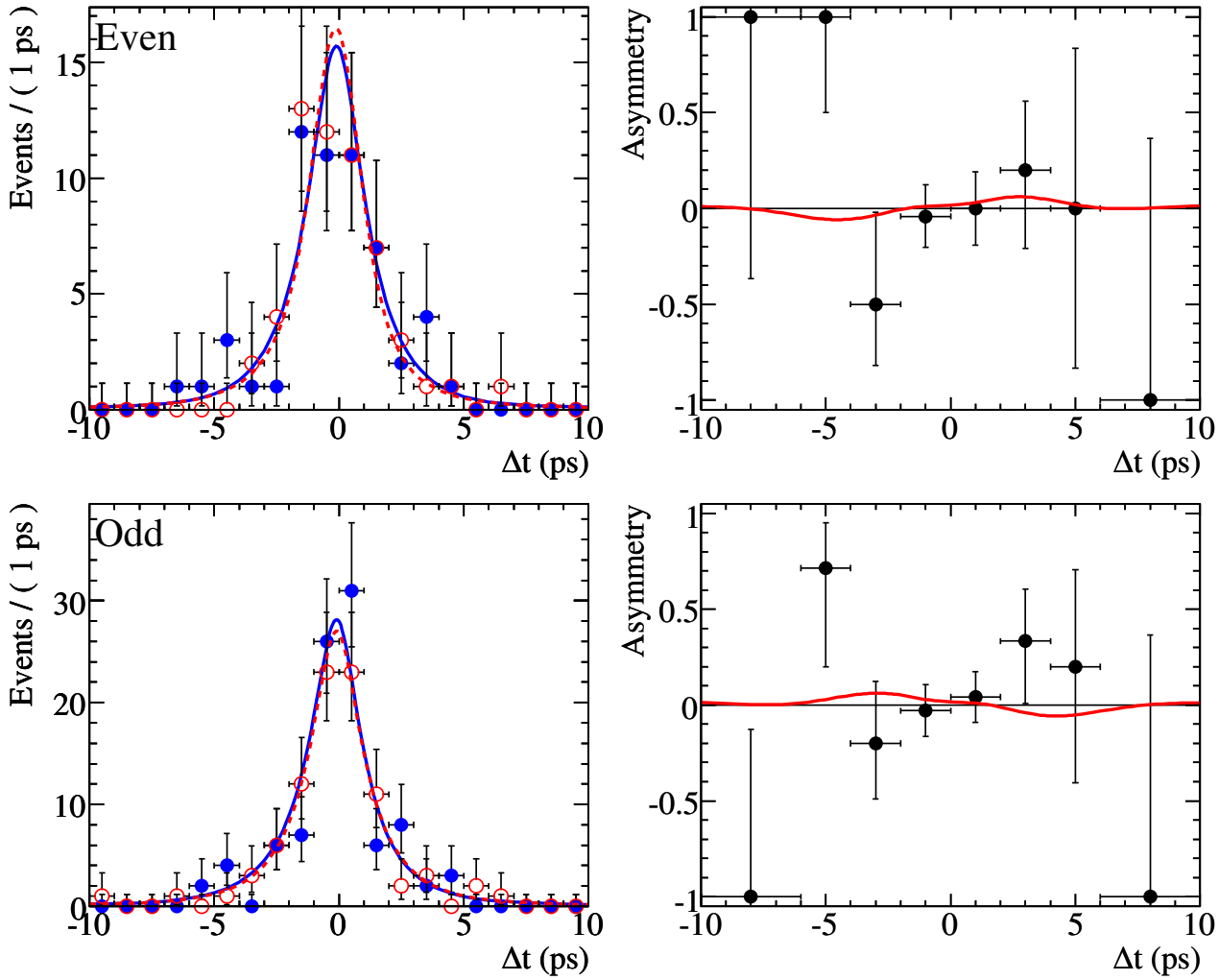

Figure 5.3: Δt projection and asymmetry plots for $m_{\rm ES}$ sideband data. Solid dots/curves are for the B^0 tag, open dots/dashed curves - for the $\overline{B}^0$ tag.

5.6.1 Standard *CP* fit configuration

The standard *CP* fit model is a simultaneous fit to $m_{\rm ES}$, Δt and $\sigma_{\Delta t}$. In addition to physics quantities ($\mathcal{S}$, $\mathcal{C}$, Δm, τ_B), the parameters that are shared among all decay modes and tagging categories are: $(\mathcal{S}^{\rm Cb},\mathcal{C}^{\rm Cb})$ in combinatorial background, $(\mathcal{S}^{\rm Pb},\mathcal{C}^{\rm Pb})$ in peaking background, resolution function parameters (core Gaussian fraction $f_{\rm core}$, tail Gaussian bias $\mu_{\rm tail}$ and scale factor $\sigma_{\rm tail}$, outlier Gaussian fraction $f_{\rm outlier}$) for signal, resolution function parameters (core Gaussian bias $\mu^{\rm Cb}_{\rm core}$, fraction $f^{\rm Cb}_{\rm core}$ and scale factor $\sigma^{\rm Cb}_{\rm core}$) for combinatorial background, Δm in combinatorial and peaking background, outlier Gaussian shape, effective lifetimes in combinatorial and peaking background ($\tau^{\rm Cb}$ and $\tau^{\rm Pb}$).

All mistag rates w and Δ-mistag Δw rates are split according to the tagging categories. The core Gaussian bias $\mu_{\rm core}$ and scale factor $\sigma_{\rm core}$, and the prompt fraction $f_{\rm pmt}$ in the combinatorial PDF are allowed to be different for the `Lepton` tag. The peaking background fraction $f_{\rm Pb}$ is fixed at a different value for *CP*-even and *CP*-odd events (see Section 3.5). The twelve peaking fractions $f_{\rm peak,k}$ in $m_{\rm ES}$ are allowed to be different according to the tagging category and *CP*-eigenvalue.

The mistag values and the signal resolution function parameters are obtained from `BFlav` sample and

are fixed. The outlier Gaussian shape is fixed ($\mu_{\rm outlier} = 0$, $\sigma_{\rm outlier} = 8ps$). The $(\mathcal{S}^{\rm Pb}, \mathcal{C}^{\rm Pb})$ for the peaking background are fixed to zero. Δm and τ_{B^0} are fixed to their world average values [16]. Peaking background fractions $f_{\rm Pb}$ is fixed at the values reported in Subsection 3.5.1. The effective lifetime for the peaking background $\tau_{\rm Pb}$ is fixed to the mean value of τ_{B^0} and τ_{B^+} [16].

5.6.2 Fit bias test in signal MC

In order to check for a possible bias in the time-dependent fit, and to make sure that the uncertainties are estimated correctly, the fitting procedure was tested on 100 MC samples of about the same size of final sample (order of 1100 events). For the signal part, we create eleven signal MC samples (one for each signal mode, see Table 3.4) splitted into 100 statistically independent subsamples each of about the same size of the signal sample (order of 300 events). Each of the 100 subsamples from each of the 11 signal modes are then mixed together according to the fitted signal yield in data (see Table 3.4).

For the background, there are not enough MC events to split them into 100 independent samples. Instead, we randomly select events from the generic MC mixing them according to the luminosity scale factors: 0.33 for $B\bar{B}$, 0.75 for $c\bar{c}$ and 1.0 for $q\bar{q}$ (where $q = u, d, s$). It is therefore by definition that the background components are highly correlated across the samples.

First, we fit the samples containing signal events only (using the signal Δt PDF only). The results are shown in Figure 5.4. No bias is observed. The spread of $\mathcal{S}$ (RMS= 0.166) is a little smaller than the average error (0.187). The $\mathcal{S}$-pull distribution (defined as the difference between the fitted $\mathcal{S}_{\rm fit}$ value minus the input $\mathcal{S}_{\rm gen}$ value, divided by the estimated error $\sigma_{\mathcal{S}}$, $\mathcal{S}_{\rm fit} - \mathcal{S}_{\rm gen}/\sigma_{\mathcal{S}}$) is reasonably Gaussian (as expected) with an Root Mean Square (RMS) just above 0.9.

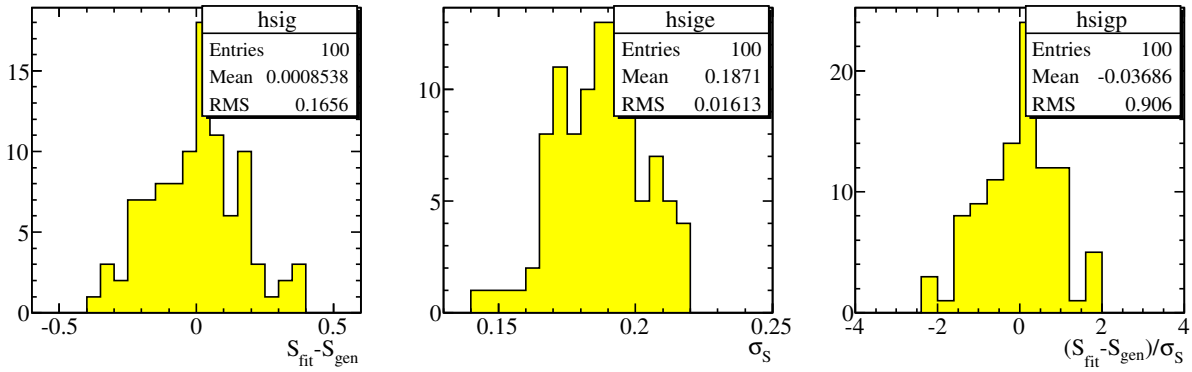

Figure 5.4: Results of the time-dependent *CP* asymmetry fit using 100 samples containing simulated signal events. The plots show (left to right) $\mathcal{S}$ residuals ($\equiv \mathcal{S}_{\rm fit} - \mathcal{S}_{\rm gen}$), fit errors $\sigma_{\mathcal{S}}$ and pulls (defined in text).

5.6.3 Fit bias check in MC with background

We proceed by using the standard *CP* fit model to fit the samples containing the signal and background events mixed in the correct proportions. The resolution function parameters, used in these fits are taken from the fit to the combined signal MC sample. The mistag rates are taken from the MC correctly reconstructed events. The free parameters of the fits are: $\mathcal{S}, \mathcal{C}$, $m_{\rm ES}$ shape parameters (m, σ, ξ) and peak fractions $f_{\rm peak,k}$, the fraction of the prompt component $f_{\rm pmt,i}$ and the parameters of the combinatorial background resolution function. The prompt fraction is split according to the tag category (`Lepton` and everything else).

The results are shown in Figure 5.5. A small bias was observed in the pull distribution, corresponding to approximately 40% of the statistical error. The interpretation of this observation is not straightforward due to the fact that the background events in the 100 samples are not independent. So the reason for observing the bias may be a fluctuation due to low statistics of the background sample (which was replicated 100 times to create the samples for the test fit).

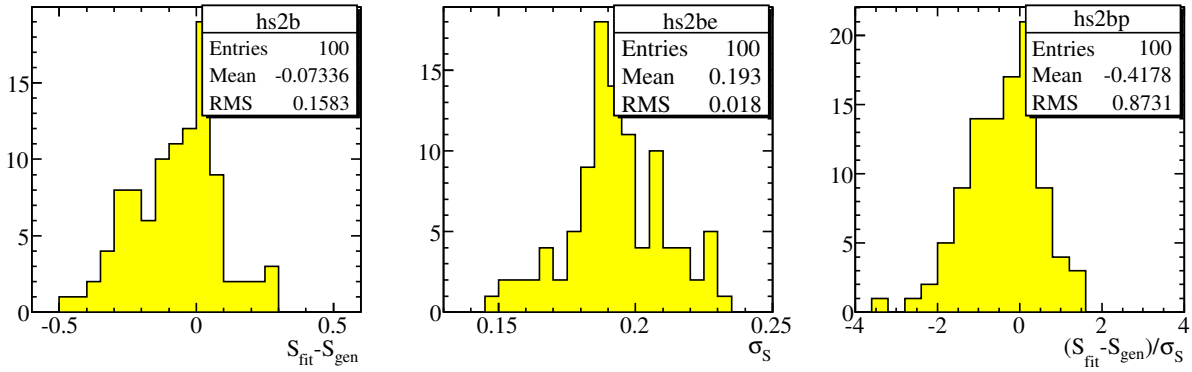

Figure 5.5: Results of the time-dependent *CP* asymmetry fit using 100 samples containing signal and background events. The plots show (left to right) $\mathcal{S}$ residuals ($\equiv \mathcal{S}_{\rm fit} - \mathcal{S}_{\rm gen}$), fit errors $\sigma_{\mathcal{S}}$ and pulls (defined in text). $\mathcal{S}$ residuals, fit errors and pulls (defined in text).

In order to investigate this bias further, we increase the background sample size by removing the selection criteria applied to Fisher discriminant (see Subsection 3.4.7) in the generic MC sample. This change increases the generic MC sample size from 1573 to 9626. Based on the fit to data, the total number of combinatorial background events is 772, about 8% of 9626. We then again randomly select 100 subsamples of generic MC background from 9626 events. Each of the 9626 events has a probability of 8% being selected into one subsample. These 100 samples are still highly correlated, but the situation is improved. In these subsamples, about 30% of the events are $B\overline{B}$. In the generic MC sample using the default selection, the $B\overline{B}$ fraction is about 25%.

We then repeat the exercise by fitting these 100 subsamples of signal MC plus the generic MC with no selection applied on Fisher discriminant. The resulting distributions are shown in Fig. 5.6. A scatter plot of $\mathcal{S}$ from full fits versus signal only fits, and the histogram of their difference are shown in Fig. 5.7. The mean of the $\mathcal{S}$ distribution (minus the generated value) is -0.012 ± 0.020 (assuming the subsamples are independent), with an RMS of 0.199, consistent with the mean of the error on $\mathcal{S}$. We found that the bias is not significant, so we conclude that the bias shown in Fig. 5.5 is most likely due to statistical fluctuations in the background sample.
An illustration of the fit performance, using just one sample out of 100, is shown in Figure 5.8. The fit results using that particular sample are $\mathcal{S} = -0.82 \pm 0.20$, $\mathcal{C} = -0.05 \pm 0.14$.

5.7 Fit results

In this Section we present the results of the time-dependent fit along with consistency check of the fitted values.

5.7.1 Fit result

The fit to data was performed at first with the results of the $\mathcal{S}$ and $\mathcal{C}$ parameters kept "blind": the central values were randomly shifted and the sign was allowed to be flipped. No plot was available of the signal region for the Δt distribution. This was done to avoid to be biased by preliminary results. This

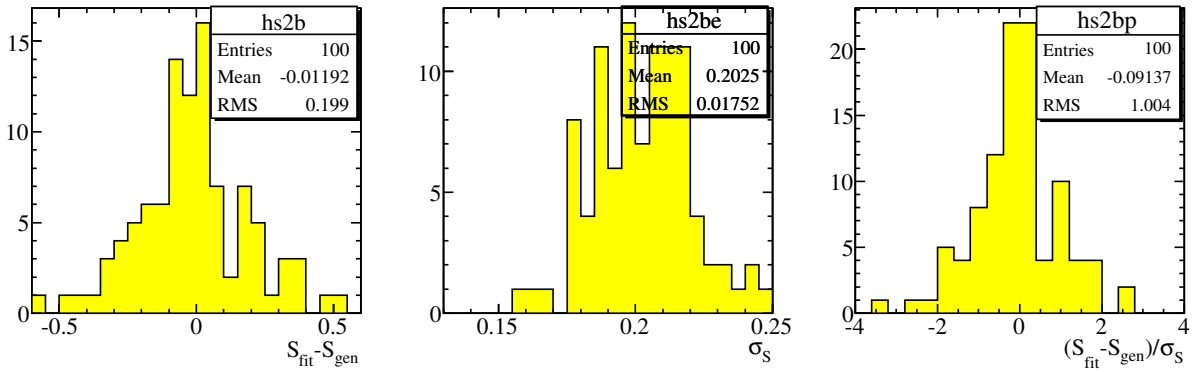

Figure 5.6: Results of the time-dependent *CP* asymmetry fit using 100 samples containing signal and background events, where the background events are from generic MC without applying the selection criteria for the Fisher discriminant. The plots show (left to right) $\mathcal{S}$ residuals ($\equiv \mathcal{S}_{\rm fit} - \mathcal{S}_{\rm gen}$), fit errors $\sigma_{\mathcal{S}}$ and pulls (defined in text).

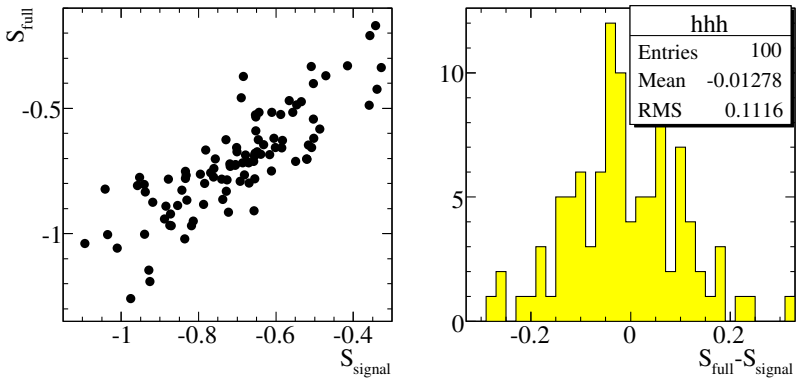

Figure 5.7: . Scatter plot of $\mathcal{S}$ from the fits to signal and background events (no selection applied to Fisher discriminant to the background events) versus signal only fits, and the histogram of their difference.

is a standard procedure in *BABAR* experiment. We "unblinded" the results when an internal Review Committee approved the overall analysis procedure as reliable.

The time-dependent fit has been performed using the standard fit-configuration described in Section 5.6.1. The fitted parameters are: the *CP*-violating terms $\mathcal{S}$ and $\mathcal{C}$; the $m_{\rm ES}$-PDF shape parameters m, σ and ξ; the peak fractions $f_{CP-{\rm parity};\texttt{tag}}$ (splitted according to *CP*-parity and tag category); the *CP*-violating terms $\mathcal{S}^{\rm Cb}$ and $\mathcal{C}^{\rm Cb}$ and effective lifetime $\tau^{\rm Cb}$ for combinatorial background; resolution parameters $(f, \mu, \sigma)_{\rm core}$ for combinatorial background; prompt fraction of $f_{{\rm pmt};\texttt{tag}}$ combinatorial background (splitted according to `Lepton`(non-`Lepton`) tag category). The results for the 25 free parameters are shown in Table 5.4 along with correlation coefficients between free parameters and $\mathcal{S}$ and $\mathcal{C}$. The Δt projection plots and asymmetry ones are shown in Fig. 5.9 for signal region ($m_{\rm ES} > 5.27\,{\rm MeV}/c^2$) and in Fig. 5.11 for sideband region ($m_{\rm ES} > 5.27\,{\rm MeV}/c^2$). In Figure 5.10 the Δt projection and asymmetry plots are shown for *CP*-even and *CP*-odd events merged together.

We measure:

$$\begin{aligned} \mathcal{S} &= -0.56 \pm 0.23 \\ \mathcal{C} &= -0.23 \pm 0.16 \end{aligned} \tag{5.7}$$

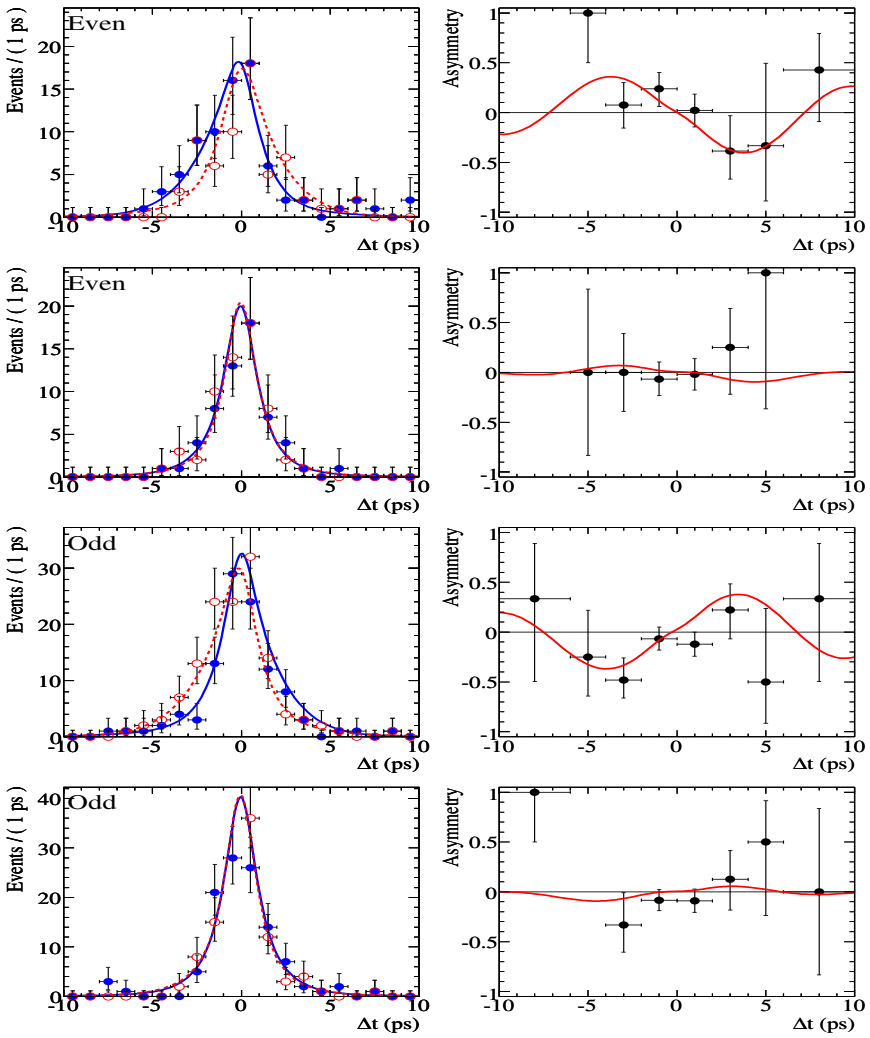

Figure 5.8: Results of the time-dependent fit using one sample out of 100 test MC samples. The first and the third pairs of plots are for events in the peak region $m_{\rm ES} > 5.27\,{\rm GeV}/c^2$; the second and the fourth pairs are for the sideband $m_{\rm ES} < 5.27\,{\rm GeV}/c^2$.

The errors on $\mathcal{S}$ and $\mathcal{C}$ are consistent with those in the MC fits. The correlation between $\mathcal{S}$ and $\mathcal{C}$ is 2.4%. Most correlation coefficients between $\mathcal{S}$, $\mathcal{C}$ and the rest of free parameters are at a few percent level, except for the correlation of about -20% between $\mathcal{S}$ (or $\mathcal{C}$) in signal and in combinatorial background, which is roughly consistent with the oscillating component in the combinatorial background.

5.7.2 Consistency checks

Different consistency checks of the fitted results was performed; the results of these checks are presented here and comments are added.

Subsample consistency

We split up the *CP*-sample according to the their *CP*-parity, and the h^0decay mode; a fit to the sub-sample is performed separately to check consistency. The results are shown in Table 5.5.

- *CP* even and *CP* odd states: the difference in $\mathcal{S}$ is about 1.3σ.

Table 5.4: Result of the fit to data: parameter values and correlations with $\mathcal{S}$ or $\mathcal{C}$.

Parameter	Value	corr($\mathcal{S}$,p)	corr($\mathcal{C}$,p)
$\mathcal{C}$	-0.23 ± 0.16	-0.024	1.000
$\mathcal{S}$	-0.56 ± 0.23	1.000	-0.024
m ($m_{\rm ES}$) (GeV/c^2)	5.27881 ± 0.00032	-0.038	-0.042
σ ($m_{\rm ES}$) (GeV/c^2)	0.00337 ± 0.00029	0.042	0.014
ξ	-23.6 ± 11	0.044	0.041
$f_{\rm Even;Lepton}$	0.68 ± 0.14	0.024	0.026
$f_{\rm Even;KaonI}$	0.537 ± 0.095	0.053	0.019
$f_{\rm Even;KaonII}$	0.319 ± 0.072	0.003	0.002
$f_{\rm Even;KaPi}$	0.159 ± 0.088	0.010	0.048
$f_{\rm Even;Pion}$	0.224 ± 0.078	0.016	0.029
$f_{\rm Even;Other}$	0.213 ± 0.094	0.015	0.021
$f_{\rm Odd;Lepton}$	0.775 ± 0.093	0.032	-0.005
$f_{\rm Odd;KaonI}$	0.370 ± 0.089	0.005	0.028
$f_{\rm Odd;KaonII}$	0.215 ± 0.056	0.038	0.006
$f_{\rm Odd;KaPi}$	0.388 ± 0.066	0.025	0.027
$f_{\rm Odd;Pion}$	0.296 ± 0.060	0.009	0.016
$f_{\rm Odd;Other}$	0.276 ± 0.066	0.019	0.020
$\mathcal{C}^{\rm Cb}$	0.16 ± 0.34	0.017	-0.197
$\mathcal{S}^{\rm Cb}$	0.03 ± 0.38	-0.176	0.009
$\tau_{\rm Cb}$	1.88 ± 0.59	-0.015	-0.007
$\mu^{\rm Cb}_{\rm core}$	-0.193 ± 0.083	0.006	-0.013
$f^{\rm Cb}_{\rm core}$	0.961 ± 0.029	-0.021	0.006
$\sigma^{\rm Cb}_{\rm core}$	1.33 ± 0.10	-0.025	-0.010
$f_{\rm pmt;Hadron}$	0.705 ± 0.087	-0.010	-0.015
$f_{\rm pmt;Lepton}$	0.00 ± 0.96	0.000	-0.001

- Modes with $h^0 \to \gamma\gamma$ and modes with $h^0 \to 3\pi$: the reason for this splitting is that modes with $h^0 \to \gamma\gamma$ only use D^0 for vertexing information, while $h^0 \to 3\pi$ contributes directly to the vertex determination. As shown in Section 5.3, we have already done this check using signal MC. They yielded consistent results.

MonteCarlo-simulated experiments study

We generate 1000 MonteCarlo-simulated experiments ("toy MC") to study the consistency of the fit model: events are simulated according to the fitted PDF parameters. The variables generated by the toy MC are Δt, $m_{\rm ES}$ and the flavor tag. The rest of variables, $\sigma_{\Delta t}$, tagging category and decay modes are taken from the *CP*-sample. We use the parameters from the fit result on the *CP*-sample to generate the 1000 samples. Only ten out of 1000 fits fail. The distributions of the fitted values, uncertainties, and pull distributions of $\mathcal{S}$ and $\mathcal{C}$ are shown in Fig. 5.12. The pull distributions are consistent with the expected normal distribution and the uncertainties of $\mathcal{S}$ and $\mathcal{C}$ in data are consistent with the error distributions in toy MC.

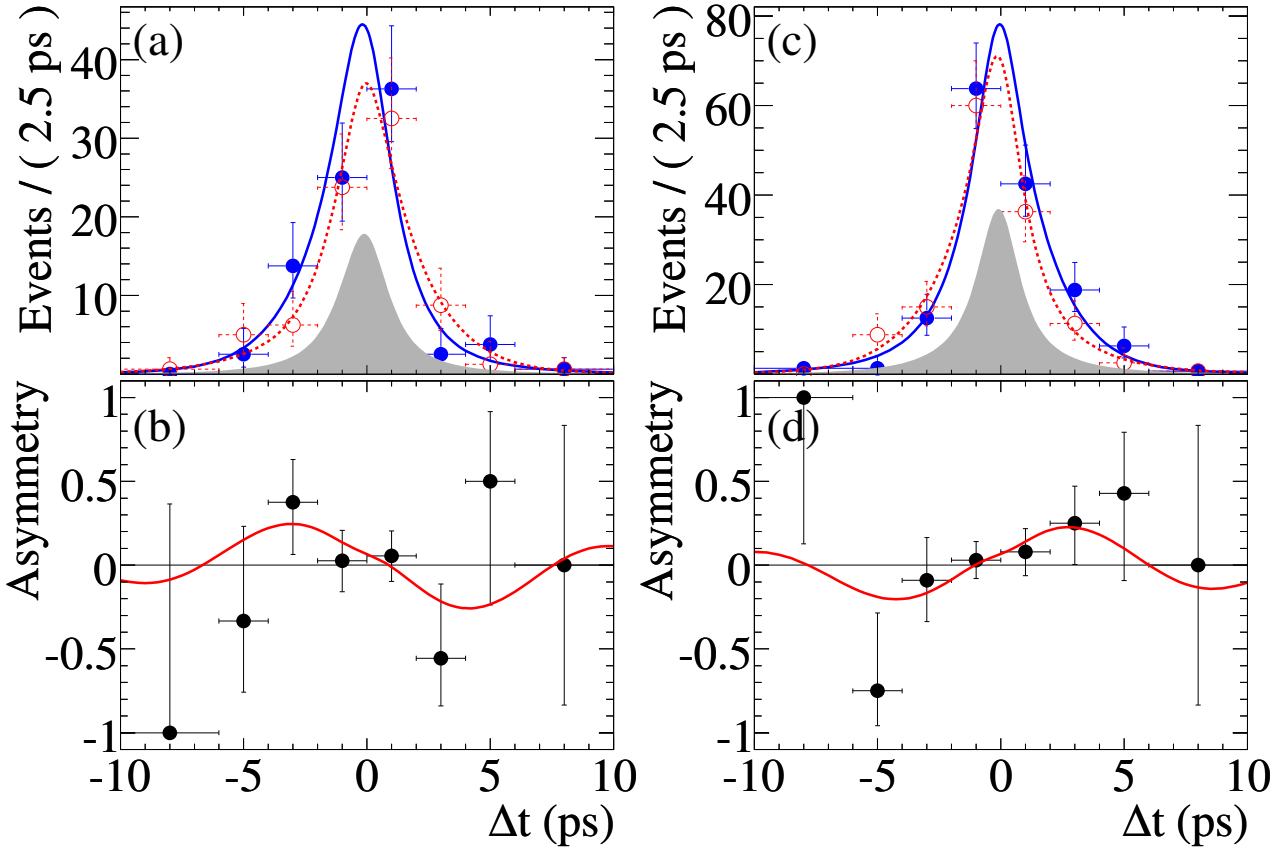

Figure 5.9: The Δt and asymmetry plots for (a,b) *CP*-even and (c,d) *CP*-odd events in $m_{\rm ES}$ signal region ($m_{\rm ES} > 5.27$ GeV/c^2). The solid blue points and curve (red dashed circles and curve) are B^0-tagged ($\overline{B}^0$-tagged) data points and Δt projection curves. Shaded areas are background distributions.

Table 5.5: Fit result comparison different event categories.

Configuration	$\mathcal{S}$	$\mathcal{C}$
Standard fit	$\mathcal{S} = -0.56(\equiv \mathcal{S}_0) \pm 0.23$	$\mathcal{C} = -0.23(\equiv \mathcal{C}_0) \pm 0.16$
CP even	$\mathcal{S}_0 + 0.38 \pm 0.37$	$\mathcal{C}_0 + 0.01 \pm 0.25$
CP odd	$\mathcal{S}_0 - 0.22 \pm 0.26$	$\mathcal{C}_0 + 0.02 \pm 0.19$
Difference	0.60 ± 0.45	0.01 ± 0.31
Average	$\mathcal{S}_0 - 0.01 \pm 0.22$	$\mathcal{C}_0 + 0.02 \pm 0.15$
$h^0 \to \gamma\gamma$ modes	$\mathcal{S}_0 + 0.03 \pm 0.27$	$\mathcal{C}_0 + 0.08 \pm 0.19$
$h^0 \to 3\pi$ modes	$\mathcal{S}_0 - 0.08^{+0.41}_{-0.37}$	$\mathcal{C}_0 + 0.06 \pm 0.30$
Difference	0.11 ± 0.47	0.02 ± 0.36
Average	$\mathcal{S}_0 - 0.0 \pm 0.22$	$\mathcal{C}_0 + 0.08 \pm 0.16$

5.8 Systematic uncertainties

This Section describes the sources of systematic uncertainties and the procedure used to evaluate their effect on the time-dependent *CP* asymmetry measurement.

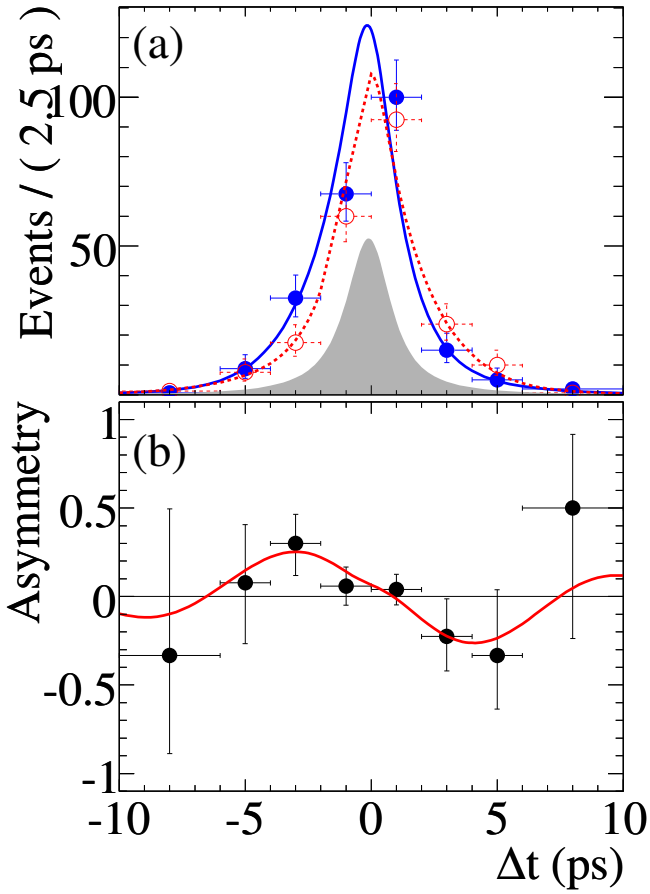

Figure 5.10: The Δt (a) and asymmetry (b) plot for *CP*-even and *CP*-odd events merged together; only signal region ($m_{\rm ES} > 5.27$ GeV/c^2) is shown. The solid blue points and curve (red solid circles and dashed curve) are B^0-tagged ($\overline{B}^0$-tagged) data points and Δt projection curves. Shaded region corresponds to background contribution.

We evaluate the effect of fixed parameters in the fit and also of the assumption made on Probability Density Functions (PDFs).

5.8.1 Mistag rates

In the final fit we used mistag rates w and the differences in mistag rates Δw provided by the `Tagging` group [97]. The values (Table 5.6) are determined by fitting a large (112878 events) `BFlav` sample from full *BABAR* dataset. The signal component, as well as the oscillation component of the peaking and combinatorial backgrounds, are assigned the same w and Δw values and are fixed in the fit. We vary each parameter within its statistical uncertainty and repeat the fit in order to estimate the effect on $\mathcal{S}$ and $\mathcal{C}$. The sum in quadrature of the variation is 0.0032 for $\mathcal{S}$ and 0.0052 for $\mathcal{C}$; the effect is of order of 0.5% of the fitted $\mathcal{S}$ and $\mathcal{C}$ values.

We also checked the difference between using mistag values as determined from `BFlav` sample and mistag values from signal MC. The differences are found to be 0.0106 for $\mathcal{S}$ and 0.0129 for $\mathcal{C}$; this corresponds to a 2% effect.

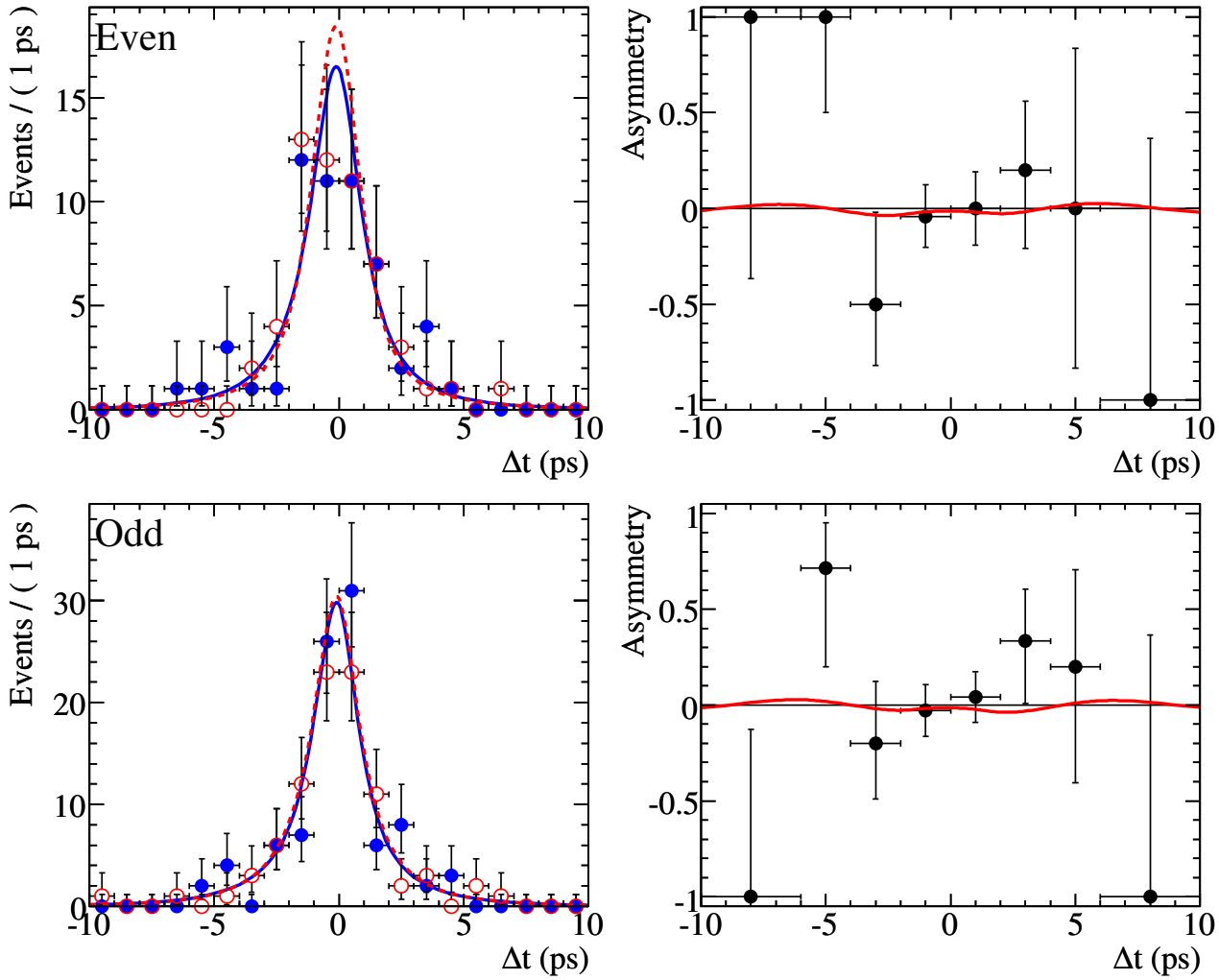

Figure 5.11: The Δt and asymmetry plots for (a,b)*CP*-even and (c,d)*CP*-odd events in $m_{\rm ES}$ sideband ($m_{\rm ES} < 5.27$ GeV/c^2). The solid blue points and curve (red solid circles and dashed curve) are B^0-tagged ($\overline{B}^0$-tagged) data points and Δt projection curves.

Table 5.6: Mistag rate w and mistag rate difference Δw for each `tag` category

.

`Tag` category	w	Δw
`Lepton`	0.0297 ± 0.0033	-0.0015 ± 0.0064
`KaonI`	0.0535 ± 0.0038	-0.0057 ± 0.0071
`KaonII`	0.1546 ± 0.0039	-0.0044 ± 0.0066
`KaPi`	0.2349 ± 0.0048	-0.0237 ± 0.0078
`Pion`	0.3295 ± 0.0051	0.0524 ± 0.0078
`Other`	0.4193 ± 0.0063	0.0459 ± 0.0094

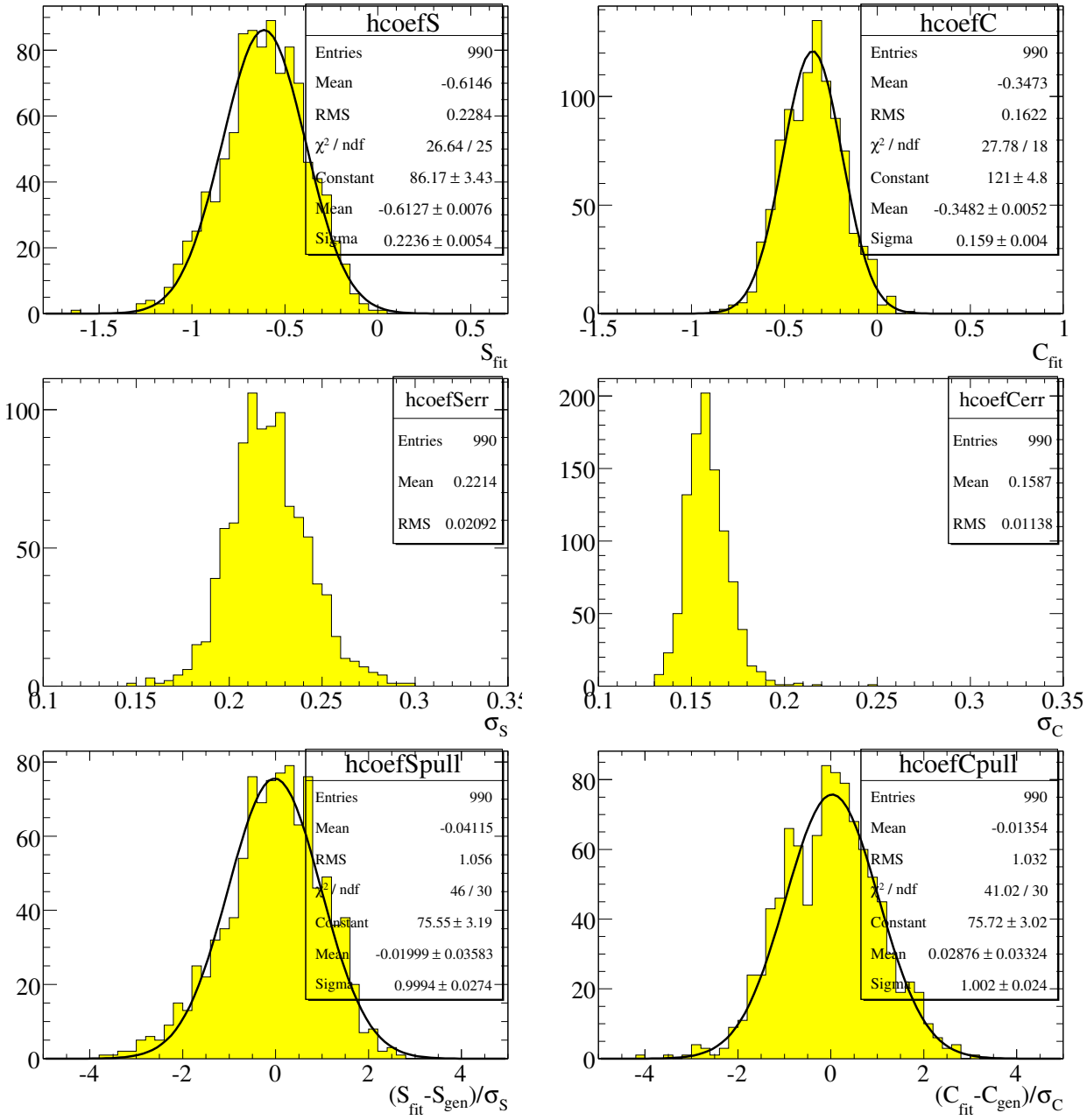

Figure 5.12: Distributions of fitted values, uncertainties, and pull distributions of $\mathcal{S}$ and $\mathcal{C}$ in the toy MC study.

5.8.2 Δt resolution function

The signal (and peaking background) Δt resolution function is the sum of three Gaussians denoted as "core", "tail" and "outlier". The combinatorial background Δt resolution function is the sum of two Gaussians, "core" and "outlier". The outlier Gaussian shares its parameters among all three data components (signal, peaking and combinatorial background). The Gaussian form of resolution functions $\mathcal{R}$ has one set of parameters for signal and peaking background, and another for the combinatorial background. Parameters of the signal resolution functions are determined from the fit to the `Bflav` sample. The outlier offset μ_{outlier} and resolution σ_{outlier} are fixed to 0 and 8 ps respectively; the tail

Gaussian scale factor $f_{\rm tail}$ is fixed to 3.

We vary fractions, offsets and scale factors in ranges determined by their statistical uncertainties. For the outlier Gaussian offset $\mu_{\rm outlier}$ and sigma $\sigma_{\rm outlier}$, we vary them by ± 2 ps and by ± 4 ps respectively. The tail Gaussian scale factor $\sigma_{\rm tail}$ is varied in the range from 2.0 to 5.0. For all these variations, we take the deviations from the central value of the resulting *CP* asymmetry fit as an estimate of the systematic error. We find that the total effects on $\mathcal{S}$ and $\mathcal{C}$ are 0.0104 and 0.0131, respectively.

We also check for the effect of the possible difference between the real resolution in our decay modes and the `BFlav` sample resolution function using signal MC. As shown in Table 5.2, the difference between floating resolution function and using `BFlav` MC sample resolution is 0.0090 in $\mathcal{S}$ and is 0.0024 in $\mathcal{C}$. We add these in quadrature to the ones in the previous paragraph and obtain $\sigma(\mathcal{S}) = 0.0138$ and $\sigma(\mathcal{C}) = 0.0133$; the shift is of order of 2%.
The resolution function parameters for the combinatorial background are free in the fit. Therefore there is no systematic uncertainty associated with it. (More about the combinatorial background is discussed later.)

5.8.3 Signal PDF

For the signal, Δt PDF is the one shown in eq. 5.4, where we fix Δm, τ_{B^0}, w, and Δw. Δm is fixed to its world average value [16] and in order to evaluate the systematic error we vary it within the uncertainty region ($\delta\mathcal{S} = 0.0022$, $\delta\mathcal{C} = 0.0011$). The same procedure is applied to B^0 lifetime τ_{B^0} and the effect is negligible. The mistag rate uncertainties are taken into account as described above.

Instead of Gaussian, we also use Crystal Ball [92] line-shape for the $m_{\rm ES}$ peak shape. Crystal Ball function $\mathcal{CB}$ is defined as:

$$\mathcal{CB}(x;\alpha,n,\bar{x},\sigma) = N \cdot \begin{cases} exp(-\dfrac{(x-\bar{x})^2}{2\sigma^2}), & \text{for} \dfrac{(x-\bar{x})^2}{2\sigma^2} > -\alpha \\ A \cdot (B - \dfrac{(x-\bar{x})}{\sigma}) & \text{for} \dfrac{(x-\bar{x})^2}{2\sigma^2} \leq -\alpha \end{cases} \tag{5.8}$$

where:

$$\begin{aligned} A &= \Big(\frac{n}{|\alpha|}\Big)^n \cdot exp\Big(-\frac{|\alpha|^2}{2}\Big) \\ B &= \frac{n}{|\alpha|} - |\alpha|; \end{aligned} \tag{5.9}$$

The exponent was fixed in the fit: $n = 5$. The changes in $\mathcal{S}$ and $\mathcal{C}$ are 0.0231 and 0.0226, respectively.

We assume the $m_{\rm ES}$ peak width σ and Argus $\mathcal{A}$ parameters m_0 and ξ (see Section 3.5) are the same for all decay modes in the standard fit. To check that this assumption is reasonable, a fit to the $m_{\rm ES}$ distribution in signal MC events is performed, separately for each of the eleven signal modes. We find the $m_{\rm ES}$ Gaussian widths σ are in the range of 2.6–2.9 MeV/c^2 ($\sim \pm 6\%$ range). The fit to data shows the width σ of 3.4 ± 0.3 MeV/c^2 ($\sim \pm 9\%$ for standard deviation). The results are reported in Table 5.7 and in Figure 5.13. So assuming the same $m_{\rm ES}$ peak width σ is quite reasonable given our data statistics. To check the effects of a possible difference in data, we perform a fit allowing the $m_{\rm ES}$ peak widths and Argus $\mathcal{A}$ parameters be different among the 11 decay modes. The changes in $\mathcal{S}$ and $\mathcal{C}$ are 0.0074 and 0.0084; the effect is of order of 1.5%.

5.8.4 Peaking background PDF

The PDF of the peaking background component is identical to the signal PDF with the exception that no *CP*-violating term is assigned to the peaking background. The other parameters are subject to the

Table 5.7: Mean m and width σ of a single Gaussian fit for $m_{\rm ES}$ distribution for each of the eleven modes; the fit has been performed on signal Monte Carlo events.

signal mode	m MeV/c^2	σ MeV/c^2
$B^0 \to D^{*0}\eta_{3\pi}D^0 \to KK$	5279.39 ± 0.02	2.60 ± 0.02
$B^0 \to D^{*0}\eta_{\gamma\gamma}D^0 \to KK$	5279.39 ± 0.02	2.78 ± 0.02
$B^0 \to D^{*0}\pi^0 D^0 \to KK$	5279.21 ± 0.03	2.85 ± 0.02
$B^0 \to D^{*0}\pi^0 D^0 \to K_S\omega$	5279.09 ± 0.08	2.92 ± 0.05
$B^0 \to D^0\eta_{3\pi}D^0 \to KK$	5279.40 ± 0.02	2.57 ± 0.01
$B^0 \to D^0\eta_{\gamma\gamma}D^0 \to KK$	5279.37 ± 0.02	2.77 ± 0.01
$B^0 \to D^0\omega D^0 \to KK$	5279.41 ± 0.02	2.58 ± 0.01
$B^0 \to D^0\omega D^0 \to K_S\omega$	5279.45 ± 0.05	2.65 ± 0.03
$B^0 \to D^0\omega D^0 \to K_S\pi^0$	5279.37 ± 0.03	2.65 ± 0.02
$B^0 \to D^0\pi^0 D^0 \to KK$	5279.31 ± 0.02	2.91 ± 0.01
$B^0 \to D^0\pi^0 D^0 \to K_S\omega$	5279.30 ± 0.04	2.85 ± 0.03

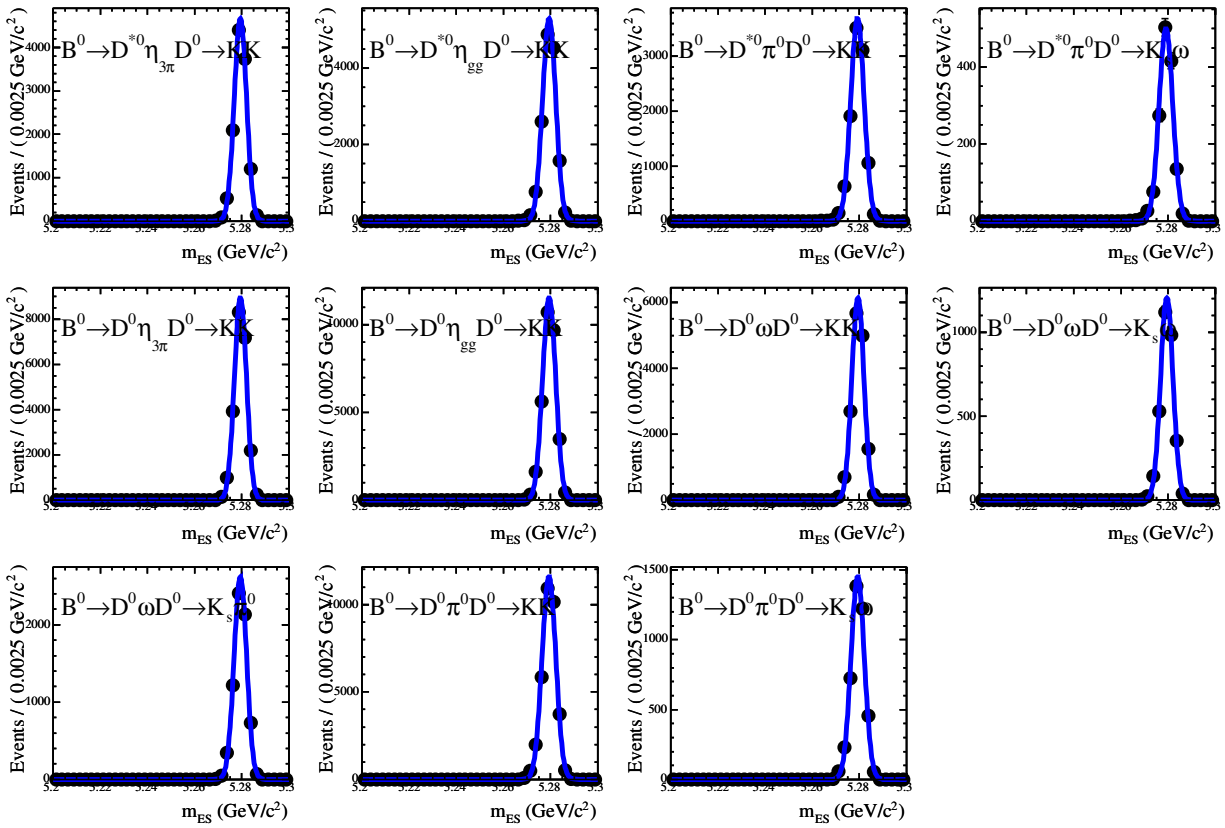

Figure 5.13: $m_{\rm ES}$ Gaussian fit to 11 signal Monte Carlo samples. Each fit has its own set of parameters.

variations described above. We vary the peaking background fractions $f_{\rm Pb}$, separately for *CP*-even and *CP*-odd modes, in the ranges from 0.0 to 0.034 and from 0.053 to 0.167 (see the discussion in

Section 5.4) respectively, and sum the average variation in quadrature. This results in the variation in $\mathcal{S}$ and $\mathcal{C}$ by 0.0118 and 0.0082, respectively.

As mentioned in Section 5.4, we estimate that the possible peaking component with *CP* content is about 65% of the total peaking background and we assume that the maximum effective $\mathcal{S}$ is 0.7. So on average the maximum effective $\mathcal{S}$ in the peaking background is $65\% \times 0.7 = 0.45$. For effective $\mathcal{C}$, we choose ± 0.1 because the direct *CP* asymmetry in B^0 decay channels that have been discovered is only about 10% level (see for example [93]). The uncertainty in the *CP* content of the peaking background is accounted for by including the terms with $\mathcal{S}^{\rm Pb}$ and $\mathcal{C}^{\rm Pb}$ set equal to (± 0.45, ± 0.10). The variations in $\mathcal{S}$ and $\mathcal{C}$ are 0.0319 and 0.0067, respectively; the effect is of order of 5%.

The $m_{\rm ES}$ shape is assumed to be the same as the signal. But by experience the peaking background has a wider $m_{\rm ES}$ shape. To account for this effect we increase the $m_{\rm ES}$ width for the peaking background from 3.4 MeV/c^2 to 5 MeV/c^2 and let the mean float. We find that $\mathcal{S}$ changes by 0.0111 and $\mathcal{C}$ by 0.0003; the effect is of order of 2%.

The lifetime in the peaking background is fixed at the mean of B^0 and B^+ lifetimes. We vary peaking background lifetime $\tau^{\rm Pb}$ from B^0 lifetime to B^+ lifetime. The effect on the fitted $\mathcal{S}$ and $\mathcal{C}$ values due to this switch is negligible.

5.8.5 Combinatorial (non-peaking) background PDF

Combinatorial background PDF is a sum of a Dirac δ-function (representing the prompt component, originating from the primary vertex) and eq. 5.4. We fix Δm to PDG [16] value and mistag fractions (see Table 5.6); *CP* violating term are floated in the fit. By varying all the fixed parameters within their uncertainty ranges, we obtain a total systematic error due to the combinatorial background of 0.0006 for $\mathcal{S}$ and 0.0007 for $\mathcal{C}$.
We also check the effect of allowing $\mathcal{S}$ and $\mathcal{C}$ to be different for *CP*-even and *CP*-odd modes. $\mathcal{S}$ changes by 0.0021 and $\mathcal{C}$ changes by 0.0024. The sum in quadrature are shown in Table 5.8; the effect is of order of 0.5%.

5.8.6 SVT misalignment

The default condition for simulated signal events in *BABAR* is to have a perfect SVT alignment. In order to estimate effect of a realistic SVT alignment we would need to generate events with realistic SVT alignment and fit the sample. This has been done for $J/\psi K^0_S$ [96] *BABAR* analysis, and the resulting deviation is really small. We believe that the effect in our analysis is comparable so we don't repeat the study and we quote their result, that is a shift of 0.0005 for $\mathcal{S}$ and 0.0003 for $\mathcal{C}$.

5.8.7 Absolute z scale and boost uncertainty

The formula for vertices separation Δz given in Equation 4.9:

$$\Delta z = \beta\gamma\Delta t \tag{5.10}$$

is an approximation. The effect due to this approximation on boost has been evaluated through scaling the measured Δt and its error by 0.6%; that is the estimated uncertainty on Δt and $\sigma_{\Delta t}$ due to this approximation [96]. The change in $\mathcal{S}(\mathcal{C})$ is measured to be 0.0017 (0.0009), which we take as a systematic uncertainty; the effect is of order of 0.3%.

5.8.8 Beam spot position

Tag vertex is reconstructed using a constraint from the beam spot position. The strongest constraint comes from the y position of the beam spot. In order to evaluate the effect due to this constraint, the

y position is varied to ± 20 μm and the error on the y position is separately blown up to 20 μm as well. This has been done for $J/\psi K^0_S$ [96] analysis, and the resulting deviation is small. We believe that the effect in our analysis is comparable so we don't repeat the study and we quote their result, that is a shift of 0.0081 for $\mathcal{S}$ and 0.0041 for $\mathcal{C}$.

5.8.9 Tag-side interference

The interference between the doubly CKM-suppressed $\overline{b} \to \overline{u}c\overline{d}$ and CKM-favored $b \to c\overline{u}d$ amplitudes for some tag-side decay modes [94] is studied with simulation. The effect has been evaluated in 0.0018 and 0.014 for $\mathcal{S}$ and $\mathcal{C}$, respectively; the effect is of order of 0.3%.

5.8.10 $m_{\rm ES}$ endpoint

We assume the standard center-of-mass (c.m.) energy $\sqrt{s} = 10.58$ GeV and fix the $m_{\rm ES}$ endpoint m_0 at $\sqrt{s}/2 = 5.29$ GeV/c^2. However, the true c.m. energy is not constant over the entire time period of data taking due to fluctuations in the beam energies; in principle $m_{\rm ES}$ endpoint should be a moving variable. Our selected event statistics is not high enough to be sensitive the changing $\sqrt{s}$. We check the effect of ignoring the changing endpoint by letting the endpoint m_0 be a free parameter in the fit. We find that the resulting endpoint is 5.2879 ± 0.0004 GeV/c^2 and $\mathcal{S}$ and $\mathcal{C}$ shift by 0.0093 and 0.0115, respectively; the effect is of the order of 1.6%.

5.8.11 Fisher discriminant

The Fisher discriminant is used only as a selection variable and does not enter the fit. Given that we partly rely on the simulation when determining the peaking background fraction, the possible discrepancy between the Fisher discriminant distribution between data and simulation could only affect the peaking background.
We compare the Fisher discriminant in the `BFlav` sample from data and in signal Monte Carlo samples. The comparison can be seen in the left plot in Fig. 5.14. The `BFlav` sample is selected with $|\Delta E| < 30$ MeV and $m_{\rm ES} > 5.27$ GeV/c^2. The background contribution is subtracted using the $m_{\rm ES}$ sideband. The Fisher selection efficiency ratio of `BFlav` to signal MC is shown in the right plot. Our Fisher criteria take values between -0.5 and 1, where the discrepancy between data and MC is only a few percent. As mentioned above, this can only affect the peaking background fraction $f_{\rm Pb}$ in the $m_{\rm ES}$ peak PDF. A few percent of change in the peaking background fraction has negligible effect to the physical quantities $\mathcal{S}$ and $\mathcal{C}$.

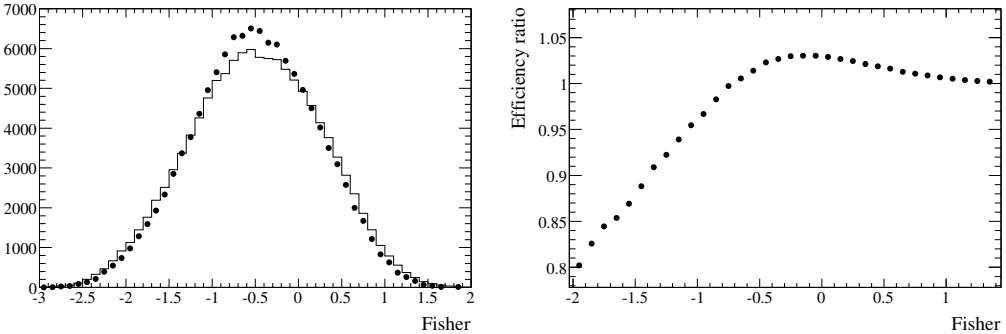

Figure 5.14: Left: Fisher discriminant comparison between signal MC (histogram) and `BFlav` sample (data dots). Right: The Fisher selection efficiency ratio of `BFlav` to signal MC.

5.8.12 Summary of systematic uncertainties

In Table 5.8 a summary of the sources of systematic uncertainties is given, together with their effect on *CP*-violating parameters $\mathcal{S}$ and $\mathcal{C}$. The total systematic uncertainty, that is the sum in quadrature of all the different contributions, is also reported, and it is of order of 0.05 and 0.04 for $\mathcal{S}$ and $\mathcal{C}$ respectively. The systematic uncertainties are of order of 8.7% for $\mathcal{S}$ and of 16% for $\mathcal{C}$. As it can be seen from Table 5.8, the major systematic uncertainty contribution comes from the uncertainty on peaking background and $m_{\rm ES}$ signal PDF, when a Crystal Ball [92] function is chosen instead of Gaussian.

Table 5.8: Summary of the absolute contributions to the total systematic uncertainty; total systematic uncertainties is also given.

Parameter	$\mathcal{S}$	$\mathcal{C}$
Mistag	0.0111	0.0139
Signal Δt resolution function	0.0138	0.0133
Δm, τ_B^0	0.0023	0.0011
Crystal Ball $m_{\rm ES}$ peak	0.0231	0.0226
Sharing of $m_{\rm ES}$ shape	0.0074	0.0084
Peaking background *CP*	0.0319	0.0067
Peaking background fractions	0.0118	0.0082
Peaking background $m_{\rm ES}$ width	0.0111	0.0003
Combinatorial background	0.0025	0.0022
SVT Alignment	0.0005	0.0003
z scale	0.0017	0.0009
Beamspot	0.0081	0.0041
Tag-side interference	0.0018	0.0140
$m_{\rm ES}$ endpoint	0.0093	0.0115
Total	0.0485	0.0376

5.9 Results

We have measured the time-dependent *CP* asymmetry coefficients $\mathcal{S}$ and $\mathcal{C}$ in $B^0 \to \overline{D}^{(*)0} h^0$ decays to be

$$\begin{aligned} \mathcal{S} &= -0.56 \pm 0.23 \pm 0.05 \\ \mathcal{C} &= -0.23 \pm 0.16 \pm 0.04; \end{aligned} \tag{5.11}$$

the measurement is dominated by statistical uncertainties. Note that in our formalism $\mathcal{S} = -\sin 2\beta$, so $\sin 2\beta = 0.56 \pm 0.23 \pm 0.05$.

This is the first measurement of this kind of decay modes. The result is consistent with the Standard Model expectation and is 2.5 standard deviations from *CP*-conserved hypothesis $\mathcal{S} = 0$ and $\mathcal{C} = 0$. The significance is determined by comparing the log-likelihoods of the nominal fit and a fit with $\mathcal{S}$ and $\mathcal{C}$ fixed at -0.05 and -0.04 (the systematic uncertainties), respectively. This result is consistent with world average: $\sin 2\beta = 0.675 \pm 0.026$

Conclusions

The analysis reported in this thesis was aimed at observing *CP* violation in $B^0 \to \overline{D}^{(*)0} h^0$ decays, with D^0 decaying to *CP* eigenstates, and h^0 being a light meson; this was never tried before.

CP-violation was well established in B meson physics looking at $b \to c\bar{c}s$ transitions; the predicted theoretical uncertainties for these modes are relatively small. Once the *CP*-violation is established, it is crucial to test its mechanism and its agreement with SM expectations, measuring other decays. The $b \to s$ channels are interesting because they have only penguin diagrams contribuiting to decay amplitude. On the contray, the $B^0 \to \overline{D}^{(*)0} h^0$ amplitude receive no contribution from any penguin diagram; measuring *CP*-asymmetry in $B^0 \to \overline{D}^{(*)0} h^0$ decays is therefore an indipendet test of the flavor sector of the Standard Model. The $B^0 \to \overline{D}^{(*)0} h^0$ decays are also really interesting because the Standard Model predictions have limited uncertainties and there could be fairly large New Physics effects due to possible tree diagrams from Supersymmetric models with R-parity violation. The results of measured *CP*-asymmetry using $b \to c\bar{c}s$, $b \to sq\overline{q}$ and $B^0 \to \overline{D}^{(*)0} h^0$ decays could indicate a pattern that allows to determine which New Physics is likely to be correct.

The time dependent asymmetry in $B^0 \to \overline{D}^{(*)0} h^0$ decays was measured using data collected by the *BABAR* experiment using events produced at the e^+e^- PEP-II asymmetric collider operating at the $\Upsilon(4S)$ resonance. We analyzed about $384{\times}10^6$ $B\overline{B}$ pairs, corresponding to a luminosity of $349\,\mathrm{fb}^{-1}$. Useful decay chains, and background sources that could mimic our signal were identified, together with discriminant variables enhancing signal significance over background. The analysis selected $B^0\overline{B}^0$ pairs in which one neutral B meson was reconstructed in our decay modes and the other one was tagged as B^0 or $\overline{B}^0$ in an inclusive way. We eventually selected roughly 1100 events, with an estimated signal yield of 340±32 signal events. The fit to time-dependent *CP*-asymmetry indicated that:

$$\mathcal{C} = -0.23 \pm 0.16 \pm 0.04$$
$$\mathcal{S} = -0.56 \pm 0.23 \pm 0.05$$

where the first error is statistical and the second is systematic.

Assuming $\mathcal{S} = -\sin 2\beta$, then $\sin 2\beta = 0.56 \pm 0.23 \pm 0.05$. This is the first measurement for these decay modes. The result is consistent with the Standard Model expectation and is 2.5 standard deviation away from *CP*-conserved hypothesis $\mathcal{C} = \mathcal{S} = 0$. This result is consistent with world average ("WA"): $\sin 2\beta = 0.675 \pm 0.026$.

In Figure 5.15 a comparison of $\mathcal{S}$ measurements from different decay modes and different experiments is shown.

The results presented in this thesis are dominated by statistical uncertainties, therefore there is room to improve the analysis using more data. *BABAR* data taking will continue until the end of 2008 with the plans to increase peak luminosity and to almost triplicate the dataset used in this analysis. On the other hand one can also envisage the possibility of including more channels. For example $\overline{B}^0 \to D^0\pi^0$ with $D^0 \to K^0_S\pi^0$ might be added, trading the large $D^0 \to K^0_S\pi^0$ branching ratio against the poorer primary vertex information. Overall, a decrease of the statistical uncertainty by a factor between 1.5 and 2. can be envisaged in the near future. Measurements at the proposed future "Super

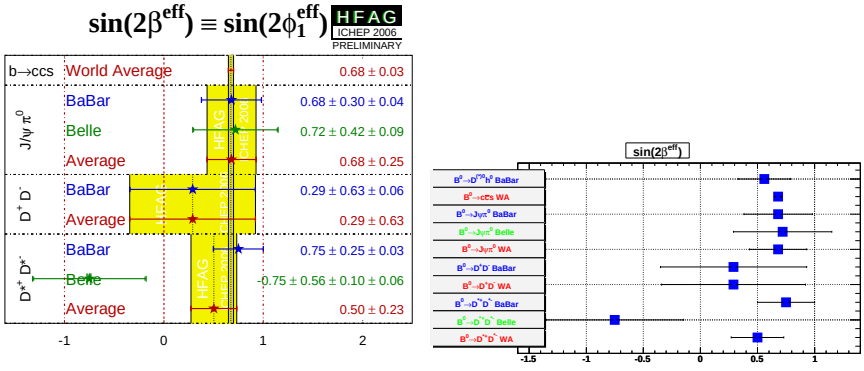

Figure 5.15: Comparison between different $-\eta\mathcal{S} \equiv \sin(2\beta^{\rm eff})$ measurement using $b \to c$ transitions; measurements from *BABAR* and BELLE collaboration for the reference charmonium $c\bar{c}s$ and other modes are listed, and also the World Average (WA) is reported. Left: official averages from `HFAG` [98]; right: this analysis' measurement is added.

B factory" [99], with very large luminosity should be able to push the uncertainty to the systematic limit. In any case, a comparison of statistical uncertainties with the other measurements using $b \to c$ transitions in Figure 5.15 shows that this channel is one of the most promising in this domain.

Looking at $b \to s$ penguin transitions, at the moment the results for these modes, reported in Figure 5.16, are individually compatible with the $b \to c\bar{c}s$ result, takens as a reference; however, they appear to be systematically on the low side, and their average is lower than the reference by 2.6 standard deviations. This is interesting, but cannot yet be considered as an indication of a discrepancy with respect to the SM predictions.

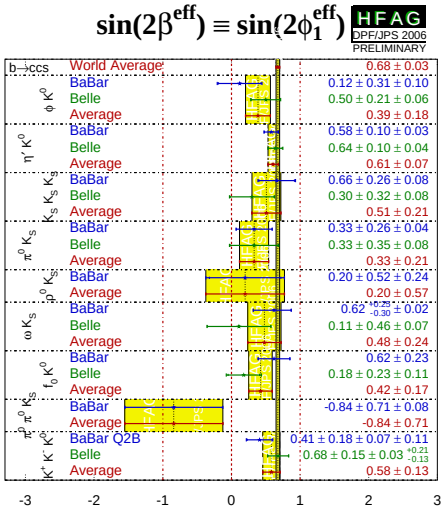

Figure 5.16: Comparison between different $-\eta \times \mathcal{S} \approx \sin(2\beta^{\rm eff})$ measurements using $b \to s$-penguin decays. The averaged $b \to c\bar{c}s$ result is reported too.

Recent theoretical efforts [23–25] to calculate the difference of *CP*-asymmetries between

penguin-dominated and tree-dominated modes, using different methods, indicate that differences $\Delta\mathcal{S} = \sin2\beta^{\rm eff} - \sin2\beta$ should be within a few %, predicting mostly the positive shifts, to be compared with the observed negative differences.

Therefore $B^0 \to \overline{D}^{(*)0}h^0$ decays can shed some light into this situation, adding an independent measurement of the mixing phase β that will contribute to constrain contributions to physics beyond the Standard Model.

Appendix A

Charged tracks, neutral objects and Particle Identification in *BABAR*

This Appendix summarizes the criteria used to form lists of reconstructed charged track candidates and lists reconstructed "object" (candidates); the criteria used to clarify charged particle candidates considered are also discussed.

Charged Tracks classification

ChargedTracks are charged reconstructed tracks candidates with

- $\theta \in [0.410, 2.54]$, where θ is the polar angle

GoodTracksVeryLoose (GTVL) same as ChargedTracks with:

- momentum lower than 10 GeV/c;
- *DOCA*[1] in XY plane lower than 1.5 cm;
- *DOCA* along z axis lower than 10 cm;
- *DOCA* along z axis greater than -10 cm;

GoodTracksLoose (GTL) same as GoodTracksVeryLoose with:

- minimum transverse momentum p_T equal to 0.1 GeV/c;
- at least 12 DCH hits.

GoodTracksTight (GTT) same as GTL with:

- at least 20 DCH hits;
- *DOCA* in XY plane lower than 1 cm;
- *DOCA* along z axis lower than -3 cm;
- *DOCA* along z axis greater than 3 cm;

GoodTracks (GT) same as GTL with:

- *DOCA* in XY plane lower than 0.1 cm;
- *DOCA* along z lower than 2.5 cm.

[1] Distance Of Closest Approach, see Section 2.5

Neutral objects classification

CalorNeutral candidates which are single EMC bumps not matched with any track. Photon mass hypothesis assigned.

CalorClusterNeutral candidates that are multi-bump neutral clusters or single bumps which are not part of a cluster which is matched with a track.

Particle Identification

See [91] for more details on Particle Identification (PId) *BABAR*. In what follows the list of used criteria.

charged K and pion selectors charged K and pion identification is mainly based on information coming from DIRC, SVT and DCH (for the latter ones we use $\mathrm{d}E/\mathrm{d}x$):

- SVT is able to discriminate pions and kaons at more than 2 standard deviations in a range of momentum up to 0.6 GeV/c;
- DCH is able to discriminate pions and kaons at more than 2 standard deviations in a range of momentum up to 0.7 GeV/c;
- DCH is able to discriminate pions and kaons at more than 2 standard deviations in a range of momentum from 1.5 GeV/c;

selection is then based on likelihood (LH) hypothesis; the idea of the LH selector is to calculate a Likelihood L_{ipart} for each particle hypothesis $ipart$: $L_{ipart} = L^{Drc}_{ipart} * L^{Dch}_{ipart} * L^{Svt}_{ipart}$, where L^{j}_{ipart} is the Likelihood based on the information coming from the detector j. Finally, the LH selectors consist of different cuts on the relevant likelihood ratios: likeKvsPi=$L_K/(L_K + L_\pi) >$ cut.

- KLHVeryLoose: likeKvsPi > 0.5 and likeKvsPro > 0.018; moreover momentum should be lower than 0.40 or it should be inconsistent with electron hypothesis
- piLHVeryTight: likeKvsPi < 0.2 and likeProvsPi < 0.5; moreover it should be inconsistent with electron hypothesis and muon hypothesis

Appendix B

Particle candidates in *BABAR*

Here we present the lists of particle candidates used in the analysis. For more basic lists, such like tracks, neutral cluster and also for Particle Identification requirements see appendix A.

γ Lists

GoodPhotonLoose is a CalorNeutral object with

- γ energy greater than 0.03 GeV
- LAT lower than 0.8

GammaForPi0 is a GoodPhotonLoose with

- γ energy $\in [0.03, 10.0]$ GeV

GammaForEta is a GoodPhotonLoose with

- γ energy $\in [0.05, 10.0]$ GeV

π^0 Lists

Mergedpi0Loose are CalorClusterNeutral

- $\theta \in [0.410, 2.54]$, where θ is the polar angle

pi0LooseMass is made with 2 GammaForPi0 with

- π^0 mass $\in [0.1, 0.160]$ GeV/c^2
- π^0 energy $\in [0.2, 10.]$ GeV
- refitted with Mass, Momentum and Primary vertex constraints

pi0SoftDefaultMass is made with 2 GammaPhotonLoose with

- π^0 mass $\in [0.115, 0.150]$ GeV/c^2
- π^0 momentum in CMS lower than 0.45 GeV/c
- refitted with Mass, Momentum and Primary vertex constraints

pi0DefaultMass is made with 2 GammaForPi0 with

- π^0 mass $\in [0.115, 0.150]$ GeV/c^2

- π^0 energy $\in [0.2, 10.]$ GeV

pi0AllDefault is a merged list of Mergedpi0Loose and pi0DefaultMass

η **Lists**

etaDefault is a merged list of etaggDefault and etagg3piDefault

etaggDefault is made with two GammaForEta with

- η mass $\in [0.470, 0.620]$ GeV/c^2
- η momentum in lab frame $\in [0.200, 10.0]$ GeV/c
- refitted with Mass, Momentum and Primary vertex constraints

etagg3piDefault is made with two GoodTracksLoose and one pi0AllLoose with

- η mass $\in [0.515, 0.575]$ GeV/c^2
- η momentum in lab frame $\in [0.200, 10.0]$ GeV/c
- refitted with Primary vertex constraint

ρ **Lists**

rho0Defaut is made with two GoodTracksVeryLoose with

- ρ mass ± 0.3 GeV/c^2 from pdg [16] value

ω **Lists**

omegaDefault is made with two GoodTracksVeryLoose and one pi0AllDefault with

- ω mass ± 0.05 GeV/c^2 from pdg [16] value
- ω momentum in lab frame $\in [0.200, 10.0]$ GeV/c

η' **Lists**

etaPDefault is merged list of etaPeppDefault and etaPrgDefault

etaPeppDefault is made with two GoodTracksLoose and one etaDefault with

- η' mass $\in [0.90, 1.01]$ GeV/c^2

etaPrgDefault is made with one rho0Default and one GammaForEtaPrime with

- η' mass $\in [0.90, 1.01]$ GeV/c^2

ϕ **Lists**

phieppDefault is made with one GoodTracksLoose and one GoodTracksVeryLoose with

- ϕ mass ± 0.07 GeV/c^2 from pdg [16] value

D^0 Lists

D0ToKKLoose is made with one GoodTrackLoose and one GoodTrackVeryLoose with

- D^0 mass within 0.09 GeV/c^2 from pdg [16] value

D0ToPiPiLoose is made with two GoodTracksVeryLoose with

- D^0 mass within 0.09 GeV/c^2 from pdg [16] value

D0ToKsPi0Loose is made with one pi0AllLoose and one KsDefault with

- D^0 mass within 0.16 GeV/c^2 from pdg [16] value

D0ToKsEtaLoose is made with one EtaDefault and one KsDefault with

- D^0 mass within 0.16 GeV/c^2 from pdg [16] value

D0ToKsEtaPLoose is made with one etaPDefault and one KsDefault with

- D^0 mass within 0.16 GeV/c^2 from pdg [16] value

D0ToKsPhiLoose is made with one phiDefault and one KsDefault with

- D^0 mass within 0.16 GeV/c^2 from pdg [16] value

Acknowledgements

A *Philosophiae Doctor* course is a part of my life that lasted three years. It started for me one week after master graduation, solving physics problems and hoping to be good enough to deserve a chance to continue the only work that I love, physics researches.

New chapter of my life started thanks to efforts and dedication to work; for this I have to thank my parents, *Luciano e Daniela*: they taught me love for work and dedication to excellence. They also were enthusiastic of my achievements and supported me during these three years. My brother *Alberto* has been also really important: his interest about science made me feel important. It was always a great pleasure talking with him about sports, comics, music, movie, *etc...* All my relatives (they are a lot...) have played important role, making me feel special.

I've met lot of people working for *BABAR* that I will never forget. *Tina, Antonio, Marcello, Baffetto, Alessia, Elisa, Loredana, Vir, Sir Sacco, Silvano, Matteo, Gigi, Mirco, Diego, Maurizio, Vincenzo, Alberto, Giovanni, Riccardo, Shane, Adam, etc...*

I want to say *grazie Peppino, Francesca e Matteo!* I had great time with you in Spain in 2004 and also in Pisa, Rome and San Francisco.

I've met in Trieste special people. *Bartolo*, your genuine interest in science has been delightful for me: I loved spending time discussing on mathematics and physics but also on movie, human behaviours and social attitudes. You've been a really good friend also when we were far away. Keep on trying on what you really love and one day we will hear: "Best director: Bartolo Ansaldi".

I've had great time with my room-mates *Andrea, Silvia, Duccio e Paolo*. I've had great birthday party and we spent some funny days in California and Las Vegas. *Grazie ragazzi!*

I've discovered the pleasure of singing in a chorus; and also some special persons: *Lara, Anto, Vinz, Toffy, Momo, Luca, Thomas* and all the other chorists. I've had great time with you and I will continue to sing with you my friends.

A special *ciao ragazzi!* also to my friends *Ilaria, Maribel, Mirco, Elisa, Claudio, Stefano, Federica, Laura, Mauro, Elena, Fabio, Emanuele*.

Greetings to all HT community! *HT, Alò!*

Many thanks to Doctor *Vitaly* and Doctor *Chih-hsiang* for the wonderful work we put together and for many useful discussions. A special thank to Professor Antani from Sbiliguda University. Many thanks to *Lorenzo* for interesting discussions.

I want really to thank *Professor Paolo Poropat*: my first steps in physics career are due to his dedication to physics and passion for teaching.

Bibliography

[1] See for example Section 2.2 in [2]

[2] M. Peskin and D. Shroeder, *An Introduction to Quantum Field Theory*, Perseus Books, Massachussetts (1995)

[3] C.S. Wu, E. Ambler, E. Haywood, R.W. Hoppes, R.P. Hudson (1957) Phys. Rev.**105**, 1413.

[4] M. Goldhaber, L. Grodzis, and A. Sunyar, (1958) Phys. Rev.**109**, 1015.

[5] J.H. Christensen, J.W. Cronin, V.L. Fitch, Phys. Rev. Lett.**13**, 138 (1964).

[6] *BABAR* Collaboration, B. Aubert *et al*, Phys. Rev. Lett.**87**, 091801 (2001).

[7] BELLE Collaboration, K. Abe *et al*, Phys. Rev. Lett.**87**, 091802 (2001).

[8] S.L. Glashow, Nucl. Phys. **B22** (1961) 579.
S. Weinberg, Phys. Rev. Lett. **19** (1967) 1264.
A. Salam, *Elementary Particle Theory*, Almquits e Wiksell, Stockolm, 1968.

[9] AMS Collaboration, J. Alcarez *et al*, Phys. Lett. B **461**, 387-396 (1999); M. Aguilar *et al*, Physics Reports **366** (2002), pp.331-404.

[10] F. Halzen and A.D. Martin,

[11] A.D. Sakharov, ZhETF Pis. Red. **5**, 32 (1967); JETP Lett. **5**, 24 (1967).

[12] Y. Grossman, M.P. Worah, Phys. Lett. **5** (1997) 241-249

[13] R. Barbier *et al*, Phys. Rep. **420** (2004) 1-202

[14] P.W. Higgs, Phys. Lett. **12** (1964) 232 e **13** (1964) 509.

[15] D.J. Gross e F. Wilczek, Phys. Rev. Lett. **30** (1973) 1343. H.D. Politzer Phys. Rev. Lett. **30** (1973) 1346.

[16] W.-M. Yao *et al*, J. Phys. **G33**, 1 (2006)

[17] N. Cabibbo, Phys. Rev. Lett. **10**, 531 (1963).

[18] M. Kobayashi and T. Maskawa, Prog. Th. Phys. **49**, 652 (1973).

[19] N. Cabibbo, Phys. Rev. Lett. **10**, 531 (1963); M. Kobayashi and T. Maskawa, Prog. Th. Phys. **49**, 652 (1973).

[20] L. Wolfenstein, Phys. Rev. Lett. **51** (1983) 1945.

[21] C. Jarlskog , Phys. Rev. Lett. **55**, 1039 (1985).

[22] M. Ciuchini *et al*, JHEP **0107** (2001) 013.

[23] M. Beneke, Phys. Lett. B **620** (2005) 143 [arXiv:hep-ph/0505075].

[24] H. Y. Cheng, C. K. Chua and A. Soni, Phys. Rev. D **72** (2005) 094003 [arXiv:hep-ph/0506268].

[25] A. R. Williamson and J. Zupan, Phys. Rev. D **74** (2006) 014003 [Erratum-ibid. D **74** (2006) 03901] [arXiv:hep-ph/0601214].

[26] The most recent public results are: B. Aubert *et al.* (*BABAR* Collaboration), BABAR-CONF-06-036 [hep-ex/0607107] ($\sin 2\beta = 0.710 \pm 0.034 \pm 0.019$); BELLE Collaboration, BELLE-CONF-0647 [hep-ex/0608039] ($\sin 2\beta = 0.642 \pm 0.031 \pm 0.017$).

[27] K. Wilson, Phys. Rev.179, 1499 (1969).

[28] M. Bauer, B. Stech, and M. Wirbel, Z. Phys. C **34**, 103 (1987).

[29] A. Deandrea, N. Di Bartolomeo, R. Gatto, and G. Nardulli, Phys. Lett. B **318**, 549 (1993); A. Deandrea *et al*, *ibid.* **320**, 170 (1994).

[30] M. Neubert and B. Stech, in *Heavy Flavours II*, eds. A.J. Buras and M. Lindner (World Scientific, Singapore, 1998), p. 294 [hep-ph/9705292].

[31] M. Neubert and A.A. Petrov, Phys. Lett. B **519**, 50 (2001).

[32] M. Beneke, G. Buchalla, M. Neubert, and C.T. Sachrajda, Nucl. Phys. B **591**, 313 (2000).

[33] H.J. Lipkin, Phys. Rev. Lett. **44**, 710 (1980).

[34] J.L. Rosner, Phys. Rev. D **60**, 074029 (1999).

[35] A. Deandrea and A.D. Polosa, Eur. Phys. Jour. **22**, 677 (2002).

[36] C-K. Chua, W-S. Hou, and K-C. Yang, Phys. Rev. D 65, 096007 (2002).

[37] C-K. Chua and W-S. Hou, Phys. Rev. D 72, 036002 (2005).

[38] C-W. Chiang and J.L. Rosner, Phys. Rev. D 67, 074013 (2003).

[39] T. E. Coan *et al.*, Phys. Rev. Lett. **88**, 062001 (2002)

[40] K. Abe *et al.* Phys. Rev. Lett. **88**, 052002 (2002)

[41] R. Fleischer, Phys. Lett. B **562**, 234 (2003)

[42] Y. Grossman, Z. Ligeti, Y. Nir, H. Quinn, Phys. Rev. D **68** (2003) 015004

[43] B. Aubert *et al.* [BABAR Collaboration], arXiv:hep-ex/0607112.

[44] K. F. Chen *et al.* [Belle Collaboration], Phys. Rev. Lett. **98** (2007) 031802 [arXiv:hep-ex/0608039].

[45] PEP-II - An Asymmetric B Factory, Conceptual Design Report, SLAC-418, LBL-5379 (1993).

[46] J. Seeman *et al.*, SLAC-PUB-12023 *Contributed to European Particle Accelerator Conference (EPAC 06), Edinburgh, Scotland, 26-30 Jun 2006*

[47] P. F. . Harrison and H. R. . Quinn [BABAR Collaboration], SLAC-R-0504 *Papers from Workshop on Physics at an Asymmetric B Factory (BaBar Collaboration Meeting), Rome, Italy, 11-14 Nov 1996, Princeton, NJ, 17-20 Mar 1997, Orsay, France, 16-19 Jun 1997 and Pasadena, CA, 22-24 Sep 1997*

[48] The *BABAR* Collaboration, Letter of Intent for the Study of *CP* Violation and Heavy Flavor Physics at PEP-II, SLAC-443 (1994).

[49] J. Seeman *et al.,* The PEP-II Storage Rings, SLAC-PUB-8786 (2001), submitted to Nucl. Instr. and Methods .

[50] J. Seeman *et al.,* Status Report on PEP-II Performance, *Proceeedings of the 7th European Particle Accelerator Conference (EPAC 2000)*, Vienna, Austria (2000).

[51] S.E. Csorna *et al.,* (CLEO Collaboration), Phys. Rev. 61 (2000) 111101.

[52] T. Mattison *et al.,* Background Measurements during PEP-II Commissioning, *Proceedings of the IEEE Particle Accelerator Conference (PAC99)*, New York, NY, USA (1999).

[53] W. Kozanecki, Nucl. Instr. and Methods A **446** (2000) 59.

[54] C. Hast *et al.,* Report of the High-Luminosity Background Task Force, *BABAR* Note 522 (2000).

[55] F.Kircher, *et al.,* IEEE Transactions on Applied Superconductivity, 9 #2 (1999) 847.

[56] Europa Metali SpA, Fornaci di Barga, Italy. Alcatel Swiss Cable (now Nexans), Cortaillod, Switzerland.

[57] E. Antokhin *et al.,* Nucl. Instr. and Methods A **432** (1999) 24.

[58] UBE Industries, Japan. see also [59]

[59] C. Bozzi *et al.,* Nucl. Instr. and Methods A **447** (2000) 20.

[60] D. Barbieri *et al.,* Nuo. Cim. **A112** (1999) 113.

[61] MICRON Semiconductor Ltd., Lancing, U.K.

[62] L. Bosisio, INFN Trieste, Italy, *private communication.*

[63] G. Della Ricca *et al.,* Nucl. Instr. and Methods A **409** (1998) 258.

[64] V. Re *et al.,* Nucl. Instr. and Methods A **409** (1998) 354.

[65] J. Beringer *et al.,* The Data Transmission System for the *BABAR* Silicon Vertex Tracker, *BABAR* Note 518 (2000).

[66] R. Claus *et al.,* SLAC-PUB-8134 (1999).

[67] CAEN, Costruzioni Apparecchiature Elettroniche Nucleari, Viareggio, Italy.

[68] G. Lynch, "*BABAR* Drift Chamber Tracking Conventions", *BABAR* note 488 (2001)

[69] R. Kalman, Journal of Basic Engineering, 35 (1960).

[70] R.J. Barlow *et al.,* Nucl. Instr. and Methods A **420** (1999) 162.

[71] Aldrich-APL, Urbana, IL, USA. Chemetall GmbH, Frankfurt, Germany.

[72] Shanghai Institute of Ceramics, Shanghai, P.R.China; Beijing Glass Research Institute, Beijing, P.R.China; Hilger Analytical, Margate, Kent, UK; Crismatec, Nemours, France; Amcrys-H, Kharkov, Ukraine.

[73] EPILOX A17-01 manufactured by Leunaer Harze GmbH, Leuna, Germany.

[74] J. Brose, G. Dahlinger, K.R. Schubert, Nucl. Instr. and Methods A **417** (1998) 311;
C. Jessop *et al.,* Development of Front End Readout for the *BABAR* CsI(Tl) Calorimeter, *BABAR* Note 216 (1995);
C. Jessop *et al.,* Development of Direct Readout for CsI Calorimeter, *BABAR* Note 270 (1995).

[75] NE-561 manufactured by Nuclear Enterprises, Sighthill, Edinburgh, Scotland.

[76] S-2744-08 PIN diode by Hamamatsu Photonics, K. K., Hamamatsu City, Japan. Dark current $< 5\ nA$, capacitance $< 105\ pF$ at the depletion voltage of 70 V.

[77] J. Harris, C. Jessop, Performance Tests of Hamamatsu 2774-08 Diodes for the *BABAR* Electromagnetic Calorimeter Front End Readout and Proposal for Reliability Issues, *BABAR* Note 236 (1995).

[78] S. Menke, Offline Correction of Non-Linearities in the *BABAR* Electromagnetic Calorimeter, *BABAR* Note 527 (2000).

[79] S. Menke *et al.,* Calibration of the *BABAR* Electromagnetic Calorimeter with π^0s, *BABAR* Note 528 (2000).

[80] *BABAR* Collaboration EMC Group IEEE Nucl.Sci.Symp.Conf.Rec. **2**, 1038-1042 (2006).

[81] R. Santonico, R. Cardarelli, Nucl. Instr. and Methods A **187** (1981) 377.

[82] A. Zallo *et al.,* Nucl. Instr. and Methods A **456** (2000) 117.

[83] G. Battistoni, E. Iarocci, M.M. Massai, G. Nicoletti and L. Trasatti, *Operation of Limited Streamer Tubes*, Nucl. Instr. and Methods **164** (1979) 57.

[84] G.D. Alekseev, N.A. Kalinina, V.V. Karpukhin, D.M. Khazins and V.V. Kruglov, *Investigation of Selfquenching Streamer discharge in a wire chamber*, Nucl. Instr. and Methods **177** (1980) 385.

[85] G.C. Fox and S. Wolfram, Phys. Rev. Lett. **41**, 1581 (1978).

[86] A. Drescher, *et al.*, Nucl. Instr. and Methods A **237**, 464(1985).

[87] J. Smith, A. Soffer, and R. Waldi, *Reccomendation for Exclusive B Reconstruction Analysis Variables*, BABAR Note 497 (1999).

[88] R.A. Fisher, Annals of Eugenics 7, 179 (1936).

[89] ARGUS Collaboration, H. Albrecht *et al.*, Phys. Lett. **B185**, 218 (1987).

[90] M. Simard, *Charged Track Studies in Tau decays,*
`http://www.slac.stanford.edu/BFROOT/www/Physics/Analysis/tauqed/`

[91] `http://www.slac.stanford.edu/BFROOT/www/Physics/Tools/Pid/pid.html`

[92] J.E. Gaiser, Appendix-F "Charmonium Spectroscopy from Radiative Decays of the J/ψ and Ψ'", Ph.D. Thesis, SLAC-R-255, (1982).

[93] B. Aubert *et al.* [BaBar Collaboration], Phys. Rev. Lett. **93** (2004) 131801 [arXiv:hep-ex/0407057].

[94] O. Long *et al.*,, Phys. Rev. D**68**, 034010 (2003).

[95] S. Rahatlou *Observation of Matter-Antimatter Asymmetry in the B^0 Meson System*, SLAC-R-677 (2002).

[96] B. Aubert *et al.* [BABAR Collaboration], Phys. Rev. D **66** (2002) 032003 [arXiv:hep-ex/0201020].

[97] See for example:
B. Aubert *et al.* [BABAR Collaboration], Phys. Rev. D **66**, 032003 (2002) [arXiv:hep-ex/0201020].
B. Aubert *et al.* [BABAR Collaboration], Phys. Rev. Lett. **94** (2005) 161803 [arXiv:hep-ex/0408127].

[98] `http://www.slac.stanford.edu/xorg/hfag/index.html`

[99] First Frascati workshop: November 11-12, 2005: `http://www.lnf.infn.it/conference/superbf05/`; M. Yamauchi, *In the Proceedings of Flavor Physics and CP Violation (FPCP 2003), Paris, France, 3-6 Jun 2003, pp JEU15.*

List of Figures

List of Tables